

## CONTENS

### ADDRESS OF PUBLISHER & EDITOR'S OFFICE:

GDAŃSK UNIVERSITY  
OF TECHNOLOGY

Faculty of Ocean Engineering  
& Ship Technology  
G. Narutowicza 11/12  
80-233 Gdańsk, POLAND

tel.: +48 58 347 13 66  
fax: +48 58 341 13 66

### EDITORIAL STAFF:

Jacek Rudnicki  
| Editor in Chief  
Rafał Szłapczyński  
| Associate Editor  
Jerzy Świryczuk  
| Associate Editor  
Przemysław Wierzchowski  
| Associate Editor  
Maciej Galik  
| Associate Editor  
Aleksander Kniat  
| Editor for international  
relations

Price:  
single issue: 25 PLN

Prices for abroad  
single issue:  
- in Europe EURO 15  
- overseas USD 20

### WEB:

[pg.edu.pl/pmr](http://pg.edu.pl/pmr)  
[degruyter.com/view/j/pomr](http://degruyter.com/view/j/pomr)

ISSN 1233-2585

3	<b>Marek Przyborski</b> <i>INFORMATION ABOUT DYNAMICS OF THE SEA SURFACE AS A MEANS TO IMPROVE SAFETY OF THE UNMANNED VESSEL AT SEA</i>
8	<b>Tomasz Cepowski</b> <i>APPROXIMATING THE ADDED RESISTANCE COEFFICIENT FOR A BULK CARRIER SAILING IN HEAD SEA CONDITIONS BASED ON ITS GEOMETRICAL PARAMETERS AND SPEED</i>
16	<b>Judyta Felicjancik, Sebastian Kowalczyk, Karol Felicjancik, Krzysztof Kawecki</b> <i>NUMERICAL SIMULATIONS OF HYDRODYNAMIC OPEN-WATER CHARACTERISTICS OF A SHIP PROPELLER</i>
23	<b>Parviz Ghadimi, Sasan Tavakoli, Abbas Dashtimanesh</b> <i>CALM WATER PERFORMANCE OF HARD-CHINE VESSELS IN SEMI-PLANING AND PLANING REGIMES</i>
46	<b>Hassan Ghassemi, Isar Ghamari, Arash Ashrafi</b> <i>NUMERICAL PREDICTION OF WAVE PATTERNS DUE TO MOTION OF 3D BODIES BY KELVIN-HAVELOCK SOURCES</i>
59	<b>Gang Xue, Yanjun Liu, Muqun Zhang, Wei Zhang, Jian Zhang, Huaqing Luo, Rui Jia</b> <i>OPTIMAL DESIGN AND NUMERICAL SIMULATION ON FISH-LIKE FLEXIBLE HYDROFOIL PROPELLER</i>
67	<b>Marek Dzida, Jerzy Girtler</b> <i>OPERATION EVALUATION METHOD FOR MARINE TURBINE COMBUSTION ENGINES IN TERMS OF ENERGETICS</i>
73	<b>Zhang Zhiyang, Ma Yong, Jiang Jin, Liu Weixing, Ma Qingwei,</b> <i>3-D SIMULATION OF VERTICAL-AXIAL TIDAL CURRENT TURBINE</i>
84	<b>Grzegorz Grzeczka, Paweł Szymak</b> <i>THE HARDWARE IMPLEMENTATION OF DEMONSTRATOR AIR INDEPENDENT ELECTRIC SUPPLY SYSTEM BASED ON PEM FUEL CELL</i>
93	<b>Zygmunt Paszota</b> <i>ON POWER STREAM IN MOTOR OR DRIVE SYSTEM</i>
99	<b>Jerzy Sawicki</b> <i>FERROMAGNETIC FLOW OF VISCOUS FLUID IN A SLOT BETWEEN FIXED SURFACES OF REVOLUTION</i>
105	<b>Łukasz Muślewski, Michał Pająk, Bogdan Landowski, Bogdan Żółtowski</b> <i>A METHOD FOR DETERMINING THE USABILITY POTENTIAL OF SHIP STEAM BOILERS</i>
112	<b>Wei Wang, Na Li, Fang Zhang, Aizhao Zhou, Snow Chi</b> <i>EXPERIMENTAL AND MATHEMATICAL INVESTIGATIONS ON UNCONFINED COMPRESSIVE BEHAVIOUR OF COSTAL SOFT SOIL UNDER COMPLICATED FREEZING PROCESSES</i>
117	<b>Magdalena Kaup, Wojciech Jurczak, Janusz Kaup</b> <i>DESIGN METHODOLOGY OF STRENGTH VERIFICATION OF PLATFORM DURING LOAD OUT OF THE ARKUTUN DAGI SE-TOPSIDE 43,800 MT</i>
129	<b>Przemysław Strzelecki, Janusz Sempruch</b> <i>EXPERIMENTAL METHOD FOR PLOTTING S-N CURVE WITH A SMALL NUMBER OF SPECIMENS</i>
138	<b>Grzegorz Szala</b> <i>APPLICATION OF TWO-PARAMETER FATIGUE CHARACTERISTICS IN FATIGUE PERSISTENCE CALCULATIONS OF STRUCTURAL COMPONENTS UNDER CONDITIONS OF A BROAD SPECTRUM OF LOADS</i>

## Editorial

---

POLISH MARITIME RESEARCH is a scientific journal of worldwide circulation. The journal appears as a quarterly four times a year. The first issue of it was published in September 1994. Its main aim is to present original, innovative scientific ideas and Research & Development achievements in the field of :

### **Engineering, Computing & Technology, Mechanical Engineering,**

which could find applications in the broad domain of maritime economy. Hence there are published papers which concern methods of the designing, manufacturing and operating processes of such technical objects and devices as : ships, port equipment, ocean engineering units, underwater vehicles and equipment as well as harbour facilities, with accounting for marine environment protection.

The Editors of POLISH MARITIME RESEARCH make also efforts to present problems dealing with education of engineers and scientific and teaching personnel. As a rule, the basic papers are supplemented by information on conferences , important scientific events as well as cooperation in carrying out international scientific research projects.

---

### Scientific Board

**Chairman : Prof. JERZY GIRTLEK - Gdańsk University of Technology, Poland**

**Vice-chairman : Prof. MIROSLAW L. WYSZYŃSKI - University of Birmingham, United Kingdom**

---

<b>Dr POUL ANDERSEN</b> Technical University of Denmark Denmark	<b>Prof. HASSAN GHASSEMI</b> Amirkabir University of Technology Iran	<b>Prof. EUGEN NEGRUS</b> University of Bucharest Romania
<b>Dr MEHMET ATLAR</b> University of Newcastle United Kingdom	<b>Prof. STANISŁAW GUCMA</b> Maritime University of Szczecin Poland	<b>Prof. YASUHIKO OHTA</b> Nagoya Institute of Technology Japan
<b>Prof. GÖRAN BARK</b> Chalmers University of Technology Sweden	<b>Prof. ANTONI ISKRA</b> Poznań University of Technology Poland	<b>Dr YOSHIO SATO</b> National Traffic Safety and Environment Laboratory Japan
<b>Prof. SERGEY BARSUKOV</b> Army Institute of Odessa Ukraine	<b>Prof. JAN KICIŃSKI</b> Institute of Fluid-Flow Machinery of PASci Poland	<b>Prof. KLAUS SCHIER</b> University of Applied Sciences Germany
<b>Prof. MUSTAFA BAYHAN</b> Süleyman Demirel University Turkey	<b>Prof. ZBIGNIEW KORCZEWSKI</b> Gdańsk University of Technology Poland	<b>Prof. FREDERICK STERN</b> University of Iowa, IA, USA
<b>Prof. VINCENZO CRUPI</b> University of Messina, Italy	<b>Prof. JANUSZ KOZAK</b> Gdańsk University of Technology Poland	<b>Prof. ILCEV DIMOV STOJCE</b> Durban University of Technology South Africa
<b>Prof. MAREK DZIDA</b> Gdańsk University of Technology Poland	<b>Prof. JAN KULCZYK</b> Wrocław University of Technology Poland	<b>Prof. JÓZEF SZALA</b> Bydgoszcz University of Technology and Agriculture Poland
<b>Prof. ODD M. FALTINSEN</b> Norwegian University of Science and Technology Norway	<b>Prof. NICOS LADOMMATOS</b> University College London United Kingdom	<b>Prof. WITALIJ SZCZAGIN</b> State Technical University of Kaliningrad, Russia
<b>Prof. PATRICK V. FARRELL</b> University of Wisconsin Madison, WI USA	<b>Prof. JÓZEF LISOWSKI</b> Gdynia Maritime University Poland	<b>Prof. BORIS TIKHOMIROV</b> State Marine University of St. Petersburg, Russia
<b>Prof. WOLFGANG FRICKE</b> Technical University Hamburg-Harburg Germany	<b>Prof. JERZY MATUSIAK</b> Helsinki University of Technology Finland	<b>Prof. DRACOS VASSALOS</b> University of Glasgow and Strathclyde United Kingdom
	<b>Prof. JERZY MERKISZ</b> Poznań University of Technology Poland	

# INFORMATION ABOUT DYNAMICS OF THE SEA SURFACE AS A MEANS TO IMPROVE SAFETY OF THE UNMANNED VESSEL AT SEA

Marek Przyborski, Prof.  
Gdansk University of Technology, Poland

## ABSTRACT

*One of the fundamental states of the sea surface is its heave. Despite of years of the intense scientific inquiry, no clear understanding of the influence of this aspect on the dynamics of the sea environment has emerged. The separation of two nearby fluid elements which one may observed for example as a free floating of small objects on the sea surface (rescuers on the rough sea or small research vessels) is caused by the interaction of different components. On the other hand one may say that the heave of the sea is also a summary interaction of a few components describing the dynamics of the sea. Therefore it is the most important aspect, which influenced the dispersion phenomenon. This observation has important consequences for many different problems as for example conducting Search and Rescue missions and using unmanned ships. We would like to present results of our experiment focused on finding the answer to question about nature of the heave of the sea and its influence on safety of Unmanned Surface Vessels (USV).*

**Keywords:** hypothesis testing, nonlinearity, sea dynamics, USV

## INTRODUCTION

Heave of the sea is one of the most important factors that influenced the ship's movement especially at the open sea but also at the shallow waters. We may see its influence on the behavior of small boats, research vessels and unmanned surface vessels doing bathymetric tasks, laser scanning of the cliffs or infrastructure of harbor facilities [7,9,11,14,17,18]. The mathematical description of that phenomenon gives us the possibility to improve the quality of the data [22] dedicated to the spatial information systems and electronical navigational charts [16,20] integrating information about shore infrastructure, shape of the sea bottom and waterways in the vicinity of the ports [12,13,15,21].

One may say that it is the fusion of different components

like sea currents, wind, atmospheric pressure, salinity, water temperature and so on. It influenced such a complex phenomenon like dispersion of small objects on the high seas. If this kind of behavior has a deterministic component then we may use deterministic methods like time series analysis to investigate its influenced on process of small objects dispersion. If it is not true then the heave of the sea might be considered simply as a disturbance, which influenced dispersion as a stochastic component.

Measuring of the heave of the sea is very difficult there are no clear and simple recording methods of this phenomenon. By using semiconductor accelerometer we have attempt a trial of collecting some measurements describing different states of natural sea environment. As a result of our experiment we

have obtained a collection of time series of acceleration in three dimensions. When looking at this time series immediately one critical question has emerged - are there any deterministic components? If the distribution of this accelerations is totally random then heave of the sea should have also stochastic component and all the attempts to investigate this phenomenon by using deterministic methods must fail due to the stochastic nature of this process. If otherwise, searching for deterministic signatures we can answer the question about the nature of the heave of the sea and then, this would substantiate using nonlinear time series analysis methods to investigate such important phenomenon. So far many attempts have been made to detect behavior characteristic for deterministic systems in the data coming from the real world. Finite number of points as well as finite resolution of those kind of data makes this investigation difficult to obtain satisfactory results. In this particular case we would like to use the method of surrogate data [5,6,19], which provides statistical test for the null hypothesis that the data has been generated by a linear stochastic process. If this null hypothesis cannot be rejected, then results of using nonlinear methods of analysis are not correct. This kind of test is based on comparing the value of nonlinear measure for the original data and a number of surrogates.

In this paper we will present results of applying such a test to seek for signatures of determinism in the samples of accelerations measured at high seas by the accelerometer mounted on small drifter.

## EXPERIMENT DESCRIPTION

The null hypothesis, which is suitable for our investigation, states that the interesting us data was generated by a stationary Gaussian linear stochastic process. Computing nonlinear observable on the data allows distinguishing deviations from the null hypothesis, our main purpose is to show that the original data  $x_n^0$ , differs significantly from the surrogates which are realizations of the null hypothesis. Our original data consists of samples of accelerations recorded in 3-dimensions

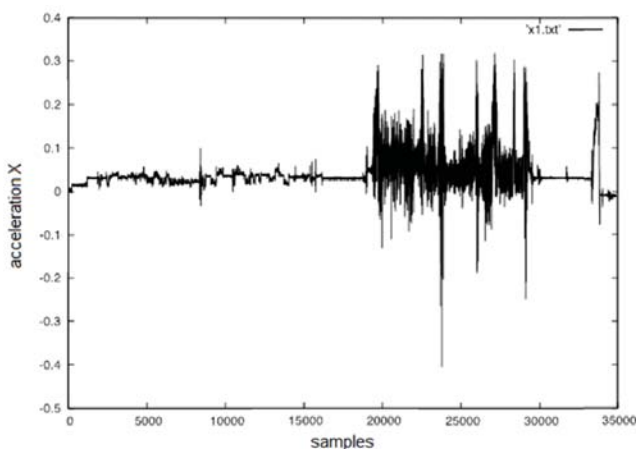


Fig. 1. Acceleration in X direction

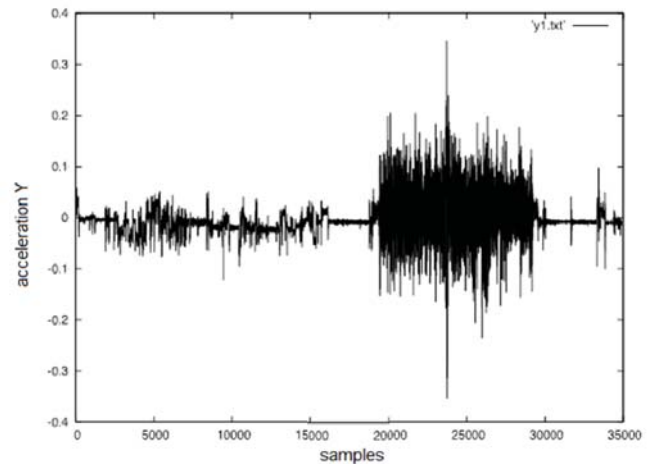


Fig. 2. Acceleration in Y direction

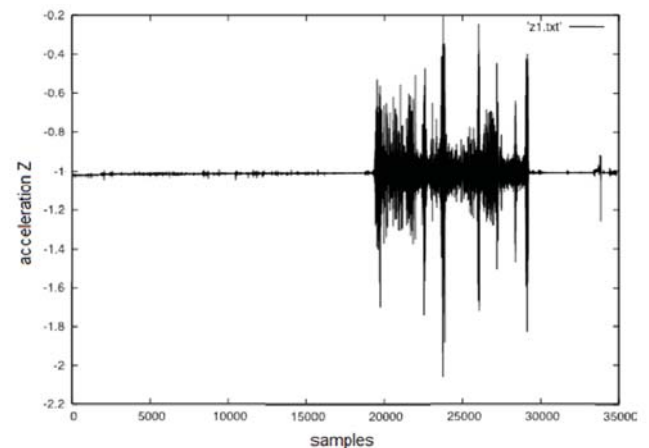


Fig. 3. Acceleration in Z direction

while the drifter was moving on the sea surface. We have used system of drifters equipped with GPS and radio link with the main station on board the research vessel. This technique has been used for the first time for tracking the position of drifters in order to find the distribution of the sea currents. The laboratory equipment consist of 5 drifters with mass about 80 kg each one. We may assume that the dimensions of the drifters are small comparable to the open sea. During our previous experiments we have come to the conclusion that the distribution of the sea currents in the Baltic Sea is extremely difficult to describe. The heave of the sea is one of the most important factors when considering dynamics of the sea environment. By recording the accelerations we tried to describe the specific state of the interested us environment. When talking about the analysis, first we have to answer the question about the nature of collected data. Is it deterministic or not? If yes, then we may use all the methods coming from the time series analysis in particular some methods form deterministic chaos. In our search for nonlinearity in those data we used method of surrogate data.

The surrogate data is a set of data which mimic the original one, however consistent with the null hypothesis. For a given conjecture we generated  $\{x_n^k\}$ ,  $k = 1, \dots, B$  surrogates of the

specific type, in our case they should be realization of the Gaussian linear stochastic process.

As an example of the data, Fig. 1, 2, 3 presents the accelerations recordings, this particular segment comes from the first sea trial. The Fig. 4 presents an example of surrogate data created to mimic accelerations in X direction.

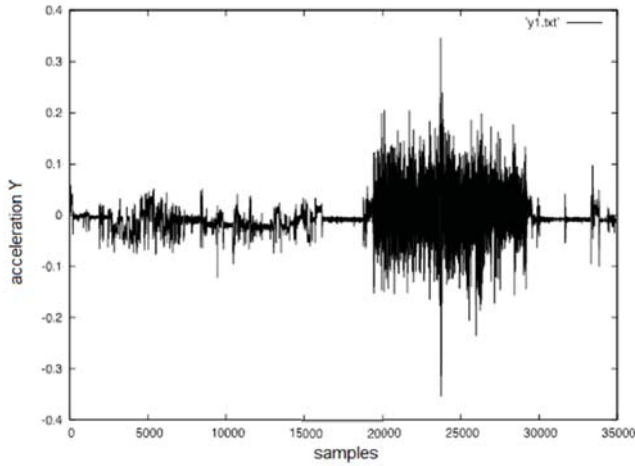


Fig. 4. Surrogates of the data presented on the Fig. 1

When creating tests for nonlinearity we should take into account two parameters. The first one, is its *size*  $\alpha$ , which is the probability that the null hypothesis is rejected although it is in fact true. And the second, called *level of significance*  $1 - p$  (usually the value of  $p$  is specify a priori, and then test is design with accordance to its value).

### TESTING FOR NONLINEARITY WITH SURROGATE DATA

The null hypothesis which is suitable for our investigation states that the data was generated by a stationary Gaussian linear stochastic process. Computing nonlinear observable on the data allows distinguishing deviations from the null hypothesis, our main purpose is to show that the original data  $x_n^0$ , differs significantly from the surrogates which are realizations of the null hypothesis. Our original data (Fig. 1, 2, 3) consists of samples of accelerations measured on the high seas. Recordings were done on the standard PC computer equipped with the RS-232 card and downloaded into the hard disk as a .txt files. We have collected recordings from 4 sea trails. Each one of them consists of about 300.000 samples. Due to the length of the recording, we split it, and for further considerations we have used only segments of length 10000 points. We decided to choose this length, due to stationarity requirement.

### MEASURES OF NONLINEARITY

There exists several examples of different statistical methods (see for instance Ref. [1,2,6]) which have been developed in order to reveal the nature of the considered time series.

We decided to apply two types of nonlinear statistics  $t = t(\{x_n\})$ :

1. As a first one, nonlinear prediction error with respect to a locally constant predictor  $F$  defined by

$$t^1(m, \tau, \epsilon) = \left( \sum [x_{n+1} - F(x_n)]^2 \right)^{1/2}$$

The prediction is performed over one time step and it is done by averaging over the future values of all neighboring delay vectors closer than  $\epsilon$  in  $m$  dimensions.

2. The second quantity it is cross-prediction errors, which can be expressed by the following formula

$$\sigma_{X,Y}^2 = \frac{1}{L'} \sum_{k=(m-1)\tau+1}^{L-1} \|\vec{y}_{k+1} - F_X(\vec{y}_k)\|^2$$

where:  $L' = L - ((m - 1)\tau + 1)$ - number of delay vectors, and  $F$  zero-th order model as it is proposed in the Ref. 7].

Calculating those nonlinear observable require using time delay embedding according to the following scheme, where embedding vectors in  $m$  dimensions are created by:  $\vec{x}_n = (x_{n-(m-1)\tau}, \dots, x_n)$ , -  $\tau$  is the delay time.

## RESULTS

We generated the surrogate data according to the null hypothesis which states that a Gaussian linear stochastic process has generated the data. This is the simplest description of a purely stochastic process, therefore we decided to applied this hypothesis. The method is based on the phase randomized surrogate series  $S = \{s_n, n = 1, \dots, N\}$  which has the same power spectrum as the time series  $X = \{x_n, n = 1, \dots, N\}$ . The temporal correlations in the original data are not preserved in the surrogates. The surrogate is obtained by determine the Fourier transform of the original data  $X$ , randomizing the phases, and inverting the transform. The probability distributions of the nonlinear statistic  $t = t(\{x_n\})$  remains unknown to us, therefore we applied a non-parametric, rank-based test. If the data deviates from the surrogates in a specific direction then we can reject the null hypothesis (one-side test). According to the size of the test  $\alpha$ , we create  $B = 1/\alpha - 1$  surrogate sets and then compute the test statistic  $t_0$  on the original data and on each of the surrogates ( $t_k, k = 1, \dots, B$ ). For the prediction error, we expect nonlinearity in the data to appear in the lower values. Thus in this case we perform one-sided tests. All tests were carried out at the 95% level of significance, it means that for one-sided test we have created 19 surrogates. Our data is a typical example of field measurement, it is strongly contaminated by the noise. In this particular case the nature of noise can have dual substance, the first source is a measurement noise, and the second one as we have already said is the influence of for example wind.

Assuming that the second type of noise and the samples of accelerations can be well described by the Gaussian linear

stochastic process [3] we can expect that those features should be reflected in the results of the test. Simply in the presence of the stochastic components in our data test for nonlinearity should fail. Conducted tests reveal that for one-sided test we achieved the 95% level of significance each time, results of one of the tests are presented on the Fig. 5.

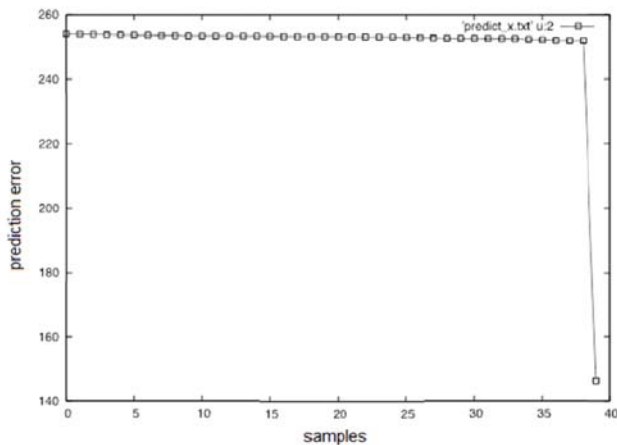


Fig. 5. Prediction error for the series of accelerations in X direction.

In order to precise our results we decided to apply method based on the clustering algorithm. The main idea of using this algorithm in the test for nonlinearity is to classify the total set of surrogates and original data, say  $K$  into two groups, from which one has only 1 element. As a dissimilarity measure cross-prediction errors were used. For conducting the test we used 9 surrogates and the original data, thus the probability that if the algorithm turned out the original data is  $1 / K = 0.1$ , if it is true then we can reject the null hypothesis with the  $(1 - (1 / K)) \times 100 = 90\%$  of significance. For each combination of surrogates and original data from the set of 30 segments we obtained the rejection of the null hypothesis with the 90% level of confidence. An example of the answer given by the clustering algorithm is presented on the Fig. 6.

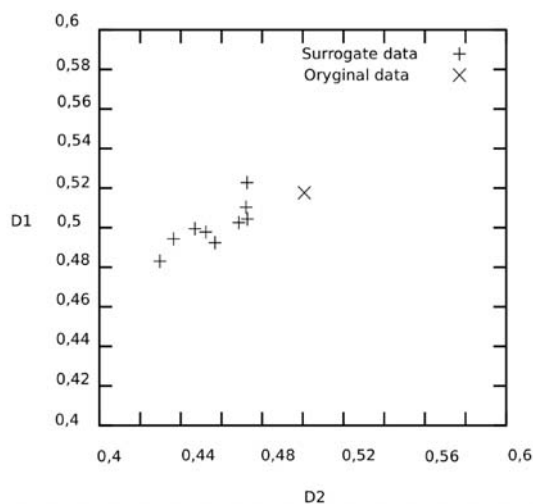


Figure 6. Results of clustering algorithm

As we have seen there are two clusters and one of them singled out the one element, which contain the original data.

## CONCLUSION

We applied two nonlinear statistics in order to reveal the possible nature of considered signals. Taking into account results of conducted tests we can conclude that the null hypothesis can be rejected because original data cannot be well described by the Gaussian linear stochastic process. It means that our assumption about the nature of samples of accelerations influenced the move of experimental drifter is false, thus its distribution can be predicted due to deterministic nature of that process.

The null hypothesis, which has been chosen, in fact is the simplest one, however in our opinion it presents the main drawback in the field of investigation such a complicated phenomenon like dynamics of the sea environment. The possibility to reject the hypothesis of stochastic nature of that signals opens the way to extract the most important features of the considered object by means, for example nonlinear time series analysis. This will allow us to characterize sea surface dynamics by the set of suitable parameters.

## ACKNOWLEDGEMENT

Publication of the above text and its language translation was funded by the Ministry of National Education of the Republic of Poland - the task BGC Innovation Forum Surveying in Geodesy, the contract 965 / P-DUN / 2016, allocated to the activities of disseminating science.

## REFERENCES

1. Diks, C., et al. Reversibility as a criterion for discriminating time series. *Phys. Lett. A.* 1995, p. 201:221, DOI: 10.1016/0375-9601(95)00239-Y.
2. Kantz, H. and Schreiber, T. *Nonlinear time series analysis.* Oxford : Cambridge University Press, 1997.
3. Percival, D. B. and Walden, A. T. *Spectral analysis for physical applications.* Cambridge : Cambridge University Press, 1993.
4. Thailer, J., et al. *Nonlinear modeling and forecasting. Using surrogate data to detect nonlinearity in time series.* Reading : Santa Fe Institute Studies in the Science of Complexity, Vol. Proc. Vol. XII, 1992
5. Schreiber, T. Constrained randomization of time series data. *Phys. Rev Lett.*, Vol. 80, 1998, DOI: 10.1103/PhysRevLett.80.2105
6. Theiler, J. and Prichard, D. Generating surrogate data for time series with several simultaneously measured variables.

- Phys. Rev. Lett., Vol. 73, 1994
7. Burdziakowski, P. et al. Maritime laser scanning as the source for spatial data. Polish Maritime Research, Vol. 22, Iss. 4, pp. 9-14, 2015, DOI: 10.1515/pomr-2015-0064
  8. Hejmanowska, B. et al. Modern remote sensing and the challenges facing education systems in terms of its teaching. 7th International Conference on Education and New Learning Technologies, Barcelona, Spain JUL 06-08, 2015, pp. 6549-6558, 2015
  9. Janowski, A. et al. Airborne and mobile laser scanning in measurements of sea cliffs on the southern Baltic. 15th International Multidisciplinary Scientific Geoconference (SGEM) Location: Albena, Bulgaria, JUN 18-24, 2015, SGEM 2015, pp. 17-24, 2015, DOI: 10.5593/SGEM2015/B12/S2.003
  10. Janowski, A. et al. Proprietary software in technical higher education. EDULEARN14: 6th International Conference On Education and New Learning Technologies, ISBN 978-84-617-0557-3, ISSN 2340-1117, pp. 1941-1949, 2014
  11. Jedrasik J. and Szymelfenig M.: Ecohydrodynamic model of the Baltic Sea. Part 2. Validation of the model, Oceanologia, Vol. 47, Iss. 4, pp. 543-566, 2005
  12. Kazimierski, W. and Stateczny, A. Radar and Automatic Identification System Track Fusion in an Electronic Chart Display and Information System. Journal of Navigation, Vol. 68, Iss. 6, pp. 1141-1154, 2015, DOI: 10.1017/S0373463315000405P
  13. Kazimierski, W. et al. Verification of multiple model neural tracking filter with ship's radar. 13th International Radar Symposium (IRS) Location: Warsaw, Poland, MAY 23-25, 2012, Book Series: International Radar Symposium Proceedings, pp. 549-553, 2012, DOI: 10.1109/IRS.2012.6233384
  14. Kedzierski, M. et al. Detection of gross errors in the elements of exterior orientation of low-cost UAV images. Baltic Geodetic Congress (Geomatics), Gdansk, Poland, JUN 2-4, 2016, pp. 95-100, 2016, DOI: 10.1109/BGC.Geomatics.2016.26
  15. Kozaczka, E. et al. Detection of Objects Buried in the Sea Bottom with the Use of Parametric Echosounder. Archives of Acoustics, Vol. 38, Iss. 1, pp. 99-104, 2013
  16. Kulawiak M., Chybicki A., Moszynski M.: Web-based GIS as a tool for supporting marine research. Marine Geodesy, Vol. 33, Iss. 2-3, pp. 135-153, Art. No. PII 923578807, 2010, DOI: 10.1080/01490419.2010.492280
  17. Liao Yu-lei, Su Yu-min, Cao Jian. Trajectory planning and tracking control for under actuated unmanned surface vessels. Journal of Central South University, Vol. 21, Iss. 2, pp. 540-549, 2014, DOI: 10.1007/s11771-014-1972-x
  18. Michoud, C. et al. Landslide detection and monitoring capability of boatbased mobile laser scanning along Dieppe coastal cliffs, Normandy. Landslides, Vol. 12, Iss. 2, pp. 403-418, 2014, DOI: 10.1007/s10346-014-0542-5
  19. Przyborski, M. Possible determinism and the real world data. Physica A-Statistical Mechanics and Its Applications, Vol. 309 Iss. 3-4, pp. 297-303, PII S0378-4371(02)00565-4, 2002
  20. Roberts, G. N. Trends in marine control systems. Annual Reviews in Control, Vol. 32, Iss. 2, pp. : 263-269, 2008, DOI: 10.1016/j.arcontrol.2008.08.002
  21. Stateczny, A. and Bodus-Olkowska, I. Hierarchical Hydrographic Data Fusion for Precise Port Electronic Navigational Chart Production. 14th Transport Systems Telematics Conference (TST) Location: Poland Date: OCT 22-25, 2014, Book Series: Communications in Computer and Information Science, Vol. 471, pp. 359-368, 2014, DOI: 10.1007/978-3-662-45317-9\_38
  22. Stateczny, A. and Bodus-Olkowska, I. Sensor data fusion techniques for environment modelling. 16th International Radar Symposium (IRS) Location: Dresden, Germany, JUN 24-26, 2015, Book Series: International Radar Symposium Proceedings, pp. 1123-1128, 2015, DOI: 10.1109/IRS.2015.7226263

#### CONTACT WITH THE AUTHOR

Marek Przyborski

*e-mail: marek.przyborski@pg.gda.pl*

Gdańsk University of Technology  
 Department of Geodesy  
 Faculty of Civil and Environmental Engineering  
 11/12 Narutowicza St.  
 80 - 233 Gdańsk

**POLAND**

# APPROXIMATING THE ADDED RESISTANCE COEFFICIENT FOR A BULK CARRIER SAILING IN HEAD SEA CONDITIONS BASED ON ITS GEOMETRICAL PARAMETERS AND SPEED

Tomasz Cepowski, Prof.  
Maritime University of Szczecin, Poland

## ABSTRACT

*The article presents the mathematical function to calculate the added wave resistance transfer function for bulk carriers. Based on this function, the statistical mean added wave resistance generated by an irregular head wave with arbitrary statistical parameters can be forecasted. The input parameters are: waterplane area, waterplane coefficient, ship speed, and frequency of the regular wave. The model has been developed based on the theory of artificial neural networks. The presented function can be used in design analyses, and for planning shipping routes in situations when basic geometrical parameters of the hull are only available and not the full technical documentation. The article presents sample cases of use of this function to calculate the added wave resistance transfer function and the statistical mean added wave resistance. Another presented application refers to waterplane coefficient optimisation taking into account the added wave resistance at the stage of preliminary bulk carrier design.*

**Keywords:** bulk carrier; resistance; added wave resistance; added resistance coefficient; regular wave; irregular wave; ship designing; preliminary design stage; artificial neural networks; approximation; forecasting; speed; waterplane area; waterplane coefficient, sample case, task, designing

## INTRODUCTION

Assumptions concerning the design of a floating object designed for arbitrary purposes usually include two basic groups of requirements, which are [9]:

- economic requirements,
- technical requirements.

Meeting the first group of requirements usually means realisation of ship function at minimal financial costs of building and maintenance of the object, while meeting the other group is equivalent to object's ability to keep afloat and possess other technical features which will secure safety of the performed operations. To meet the above requirements, a so-called design goal and design constraints are formulated.

For bulk carriers, the design goals are mainly the result of the transport study. According to [17], basic design goals for the bulk carrier refer to:

1. mass of the cargo to be transported,

2. operating speed of the ship, shipping route, and the distance between transshipment ports.

Reaching the assumed operating speed by the bulk carrier depends, among other factors, on operating parameters and conditions of the propulsion system, the efficiency of the propulsion system and hull, and the total hull resistance.

Among other components, the total hull resistance includes the added wave resistance, which [3, 10]:

- is connected with ship navigation in storm waves,
- can contribute to about 30-50% of total ship resistance,
- leads to remarkable drop of operating speed,
- depends on, among other factors, hull dimensions and shape.

That is why forecasting the added wave resistance of the ship is a considerable challenge for ship designers, due to economic aspects of selection of ship propulsion parameters and assessment of fuel consumption and time of voyage, as

well because of the need to improve energy efficiency of ship operation.

Forecasting the added wave resistance is also an important element of various shipping route planning systems. When the detailed data on ship resistance-propulsion characteristics taking into account the added wave resistance and hull geometry are missing, these characteristics are to be forecasted using simplified methods.

## THE ADDED WAVE RESISTANCE

Accounting methods used to assess the added wave resistance are limited to resistance calculations for the head wave. These methods base on the assumption that the added resistance has the nature of wave resistance and does not depend on the calm water resistance [10]. The mean added wave resistance is calculated using the function which initially describes the resistance contribution from a regular (sine) wave,  $R_{AW}(\omega_E)$ . Then, applying the superposition principle to the spectral distribution of the irregular wave (given by function  $S_{\zeta\zeta}(\omega_E)$ ), the increase of the statistical mean resistance  $R_w$  in irregular (statistical) wave is calculated as [10]:

$$R_w = \int_0^{\infty} \frac{R_{AW}(\omega_E)}{\zeta_a^2} S_{\zeta\zeta}(\omega) \quad (1)$$

where:

- $R_w$  – statistical mean wave resistance increase,
- $R_{AW}$  – added resistance from the regular wave,
- $\omega_E$  – encounter frequency of the harmonic wave,
- $\zeta_a$  – amplitude of the regular wave,
- $S_{\zeta\zeta}$  – wave energy spectrum density function.

The proportionality of the added resistance  $R_{AW}$  to the square of the regular wave amplitude  $\zeta_a$  makes it possible to calculate the dimensionless added wave resistance coefficient  $\rho_{AW}$  [10]:

$$\rho_{AW} = \frac{R_{AW}}{\zeta_a^2 \rho g \frac{B^2}{L}} \quad (2)$$

where:

- $\rho_{AW}$  – dimensionless added wave resistance coefficient,
- $B$  – ship breadth,
- $L$  – ship length,
- $\rho$  – seawater density,
- $g$  – acceleration due to gravity.

The added resistance from regular wave is calculated using various methods, most frequently the Gerritsma–Beukelman method [12] or the Boese method [10]. The former method is simpler and provides results which are relatively well in line with the experiment [10]. However, calculating the dimensionless added wave resistance coefficient with the aid of this method requires the use of numerical calculations and the knowledge of the geometrical shape of the hull.

Simplified methods to calculate the added wave resistance which are presented in [3,4,15] can only be applied to a given hull. They enable to calculate the added resistance from an irregular wave. In turn, the methods presented in [5,6,8] omit the effect of ship speed on the wave resistance and enable to

calculate the resistance contribution only from a so-called statistical wave.

In [7], in turn, a simplified method is presented which enables to calculate the added wave resistance coefficient as a function of design parameters of the ship. In this method, the added resistance coefficient is initially parameterised based on the simplified model [7]:

$$\rho_{AW} = \frac{a \cdot \omega}{\sqrt{\left(1 - \frac{\omega^2}{\omega_0^2}\right)^2 + \left(b \cdot \frac{\omega}{\omega_0}\right)^2}} \quad (3)$$

where:

- $\rho_{AW}$  – approximated dimensionless added wave resistance coefficient,
- $\omega$  – wave frequency,
- $a, b, \omega_0$  – parameters depending on geometrical parameters of the ship hull.

The results obtained using this method allow to assess, within the linear theory of rolling, statistical values of the added resistance from an arbitrary irregular wave described by the wave energy spectrum density function.

The dimensionless resistance coefficient is calculated using the method [7] in two stages:

1. calculating the values of the coefficients  $a, b, \omega_0$  in model (3) in such a way that the function (3) best fits the reference data,
2. calculating the functions which approximate the parameters  $a, b, \omega_0$  based on the design parameters of the ship.

Since the approximation is done in two stages, its accuracy is relatively low while the calculation model is complicated. Moreover, the method does not take into account the effect of speed change on this coefficient and only refers to container ships within a narrow range of dimensions.

## APPROXIMATING THE ADDED WAVE RESISTANCE COEFFICIENT

Taking into account the above discussed aspects, the goal of the research reported in the article was to develop an approximating function for the added wave resistance which will depend on:

- encounter frequency of the regular wave,
- ship speed,
- basic design parameters of the hull.

As the first step, making use of the method [12], the reference values of the added resistance coefficient were calculated for the group of hulls of bulk carriers collated in Table 1. The calculations were performed using the code SEAWAY which, based on the theory of 2D flow, calculates the ship motion in regular an irregular wave. The results presented in [13] testify to high accuracy of this code and compliance with the results of measurements recorded in the model basin.

The calculations were performed under the following assumptions:

- geometrical shape of each bulk carrier is given by theoretical lines,
- ship speed range is within:  $v = 0 - 8$  m/s,
- wave frequency is:  $w = 0,25 - 0,95$  s<sup>-1</sup>.

Table 1. Parameters describing hulls of bulk carriers for which the reference values of the dimensionless resistance coefficient were calculated:  $L_{pp}$  - length between perpendiculars,  $B$  - breadth,  $T$  - draught,  $F_w$  - waterplane area,  $CWL$  - waterplane coefficient,  $D$  - mass displacement.

Lp	$L_{pp}$ [m]	B [m]	T [m]	$F_w$ [m <sup>2</sup> ]	CWL [-]	D [t]
1	185	24,4	11,01	3938	0,8725	41849
2	140,1	22,3	10,95	2921	0,9348	25379
3	185	25,3	10,65	3987	0,8518	40837
4	187	29	10,95	4693	0,8653	48395
5	167	22,86	10,87	3381	0,8856	34334
6	172	23,1	7,86	3398	0,8553	26109
7	132	21	8,53	2309	0,833	18446
8	173	25,3	10	3526	0,8056	30385
9	210	32,26	10,5	5622	0,8299	46818
10	175,4	32,2	12	5067	0,8971	56232
11	160	25,3	10	3298	0,8148	27935

The reference data set created in the above way was used, along with various approximation methods, to develop the function approximating the added wave resistance coefficient. The above function depends on:

- waterplane area and waterplane coefficient,
- ship speed,
- regular wave frequency.

The approximation was done using the following methods: linear regression, nonlinear regression, artificial neural networks.

The approximations making use of linear and nonlinear regression turned out too inaccurate.

More accurate results were obtained using the method based on the theory of artificial neural networks. In many research activities in the fields of hydromechanics and ship designing [1, 2] for instance, this method brought very good solutions.

The tested neural network types included:

- multilayer perceptron MLP,
- generalized regression neural network GRNN,
- radial basis function network RBF,
- linear networks.

From among all those network types, the best solution was obtained using the neural network MLP having the following structure: 4 neurons in the input layer, 9 neurons in the hidden layer, and 1 neuron in the output layer. The structure of this network is graphically shown in Fig. 1, while its mathematical form is given by the following relations:

$$\rho_{AW} = \frac{c}{0,093} \quad (4)$$

where:

$\rho_{AW}$  - the approximated dimensionless added wave resistance coefficient [-],

$c$  - the variable calculated from the relation:

$$c = \frac{[4,2231 \quad -3,8588 \quad -0,7112 \quad -1,7356 \quad 1,0448 \quad 0,1661 \quad 0,9618 \quad -0,9952 \quad 1,0022] \times A + 0,1322}{1} \quad (5)$$

where:

$A$  - column matrix:

$$A = \begin{bmatrix} 1 \\ \frac{1+e^{-a_1}}{1} \\ \frac{1+e^{-a_2}}{1} \\ \frac{1+e^{-a_3}}{1} \\ \frac{1+e^{-a_4}}{1} \\ \frac{1+e^{-a_5}}{1} \\ \frac{1+e^{-a_6}}{1} \\ \frac{1+e^{-a_7}}{1} \\ \frac{1+e^{-a_8}}{1} \\ \frac{1+e^{-a_9}}{1} \end{bmatrix} \quad (6)$$

where:

$$\begin{bmatrix} a_1 \\ a_2 \\ a_3 \\ a_4 \\ a_5 \\ a_6 \\ a_7 \\ a_8 \\ a_9 \end{bmatrix} = \begin{bmatrix} 0,0486 & 0,1848 & 3,024 & 17,7772 \\ 0,5403 & 0,2205 & 2,6284 & 18,8042 \\ 1,3183 & -2,1168 & 1,100 & 3,0319 \\ -1,431 & 1,7161 & 0,636 & -0,3537 \\ -1,0826 & 1,4126 & 1,4063 & 2,968 \\ -0,3303 & -0,3019 & 2,075 & 0,2037 \\ -1,8584 & 0,375 & 1,5476 & 0,5624 \\ -1,8994 & 0,3979 & 0,7193 & 2,5233 \\ 0,2652 & -0,6208 & -0,828 & 1,4015 \end{bmatrix} \times \begin{bmatrix} b_1 \\ b_2 \\ b_3 \\ b_4 \end{bmatrix} = \begin{bmatrix} 10,2767 \\ 11,284 \\ 2,102 \\ -2,1791 \\ -0,7662 \\ -1,8044 \\ 0,0735 \\ -0,0256 \\ -0,626 \end{bmatrix} \quad (7)$$

where:

$$b_1 = F_w \cdot 0,0003 - 0,697 \quad (8)$$

$$b_2 = CWL \cdot 7,7399 - 6,2353 \quad (9)$$

$$b_3 = V \cdot 0,0667 \quad (10)$$

$$b_4 = \omega_E \cdot 1,4229 - 0,3486 \quad (11)$$

where:

$F_w$  - waterplane area [m<sup>2</sup>],

$CWL$  - waterplane coefficient [-],

$V$  - ship speed [w],

$\omega_E$  - wave encounter frequency [1/s],

Table 2 presents statistical parameters of the developed approximation with respect to the reference data, broken down by:

- data used for network teaching - teaching set,
- data used for network validation during its teaching - validation set,
- data used only for network testing - test set.

Of particular significance here are the statistics for the test values. The statistic values shown in Table 2 testify to high anticipatory ability of this network, even for test data which were not used for network development.

Table 2 Statistical parameters of artificial neural network described by Equation (4)

	Teaching set	Validation set	Test set
Mean absolute error [-]	0,39	0,46	0,39
Correlation coefficient [-]	0,96	0,95	0,96

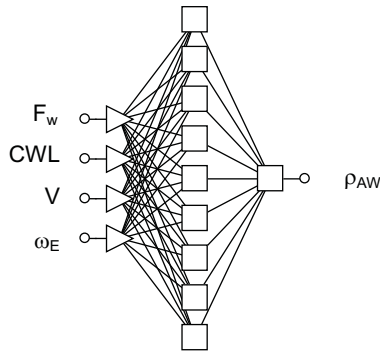


Fig. 1 Structure of the artificial neural network described by Equation (4):  $F_w$  – waterplane area,  $CWL$  – waterplane coefficient,  $V$  – ship speed,  $\omega_E$  – encounter frequency,  $\rho_{AW}$  – added resistance coefficient.

Figure 2 compares the reference data with the values calculated using formula (4), while Fig. 3 presents the reference values of the added resistance coefficient, calculated for the bulk carrier No. 4 from Table 1 and the values calculated using formula (4) within a wide ship speed range. Figure 4, in turn, compares the reference values of the added resistance coefficient obtained from formula (4) and using the methods [11,16] presented in the publication [14] for the bulk carrier “Stara Platina” having parameters:  $F_w = 4779 \text{ m}^2$ ,  $CWL = 0,9$  and the Froude number  $Fr = 0.2$ . It results from these diagrams that the approximation (4) reveals relatively high accuracy as compared to other methods, in particular to the method [16].

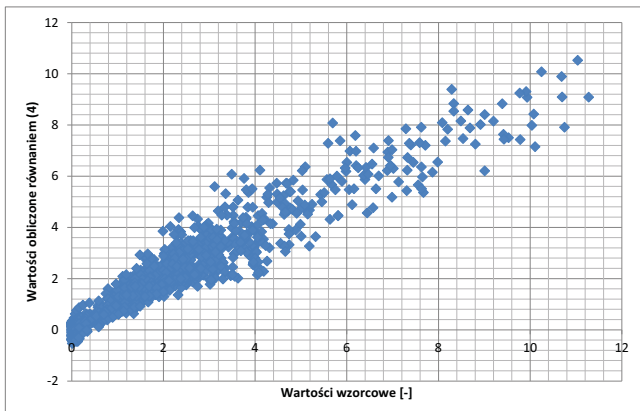


Fig. 2. Reference values of the added wave resistance coefficient vs. results obtained from Equation (4).

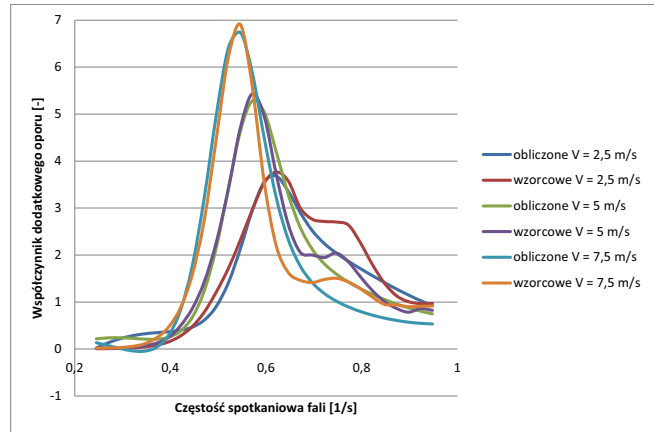


Fig. 3. Reference values of the added wave resistance coefficient vs. results obtained from Equation (4) for the bulk carrier having the parameters:  $F_w = 4693 \text{ m}^2$ ,  $CWL = 0,8653$

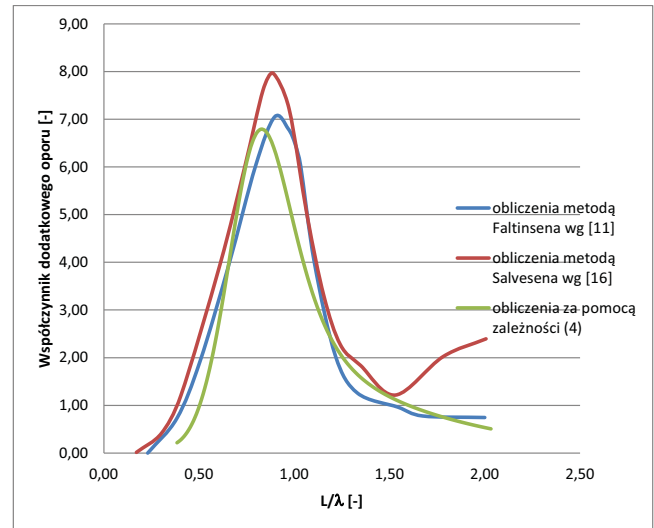


Fig. 4. Comparing the added wave resistance coefficient values obtained from Equation (4) and using methods [11,16] presented in publication [14] for the bulk carrier “Stara Platina” having the parameters:  $F_w = 4779 \text{ m}^2$ ,  $CWL = 0,9$ , Froude number  $Fr = 0.2$

The further part of the article presents examples of practical use of the developed formula (4) for:

- calculating the added wave resistance coefficient  $\rho_{AW}$  for constant encounter frequency  $\omega_E = 0,5 \text{ s}^{-1}$  – case 1,
- calculating the statistical mean wave resistance increase – case 2.

The calculations were performed under the following assumptions:

- the ship length between perpendiculars  $L_{pp} = 187 \text{ m}$ ,
- ship breadth  $B = 29 \text{ m}$ ,
- waterplane coefficient  $CWL = 0,85$
- ship speed  $V = 15 \text{ w}$ .

Case 1. Calculating the added wave resistance coefficient  $\rho_{AW}$  for constant encounter frequency  $\omega_E = 0,5 \text{ s}^{-1}$

In the first stage, using formulas (8) – (11) the values of coefficients  $b_p, \dots, b_4$  were calculated as:

$$b_1 = F_w \cdot 0,0003 - 0,697 = L_{pp} \cdot B \cdot CWL \cdot 0,0003 - 0,697 = 187 \cdot 29 \cdot 0,85 \cdot 0,0003 - 0,697 = 0,6859 \quad (12)$$

$$b_2 = CWL \cdot 7,7399 - 6,2353 = 0,85 \cdot 7,7399 - 6,2353 = 0,3436 \quad (13)$$

$$b_3 = V \cdot 0,0667 = 15 \cdot 0,0667 = 1,0005 \quad (14)$$

$$b_4 = \omega_E \cdot 1,4229 - 0,3486 = 0,5 \cdot 1,4229 - 0,3486 = 0,3629 \quad (15)$$

Then, using formula (7), the values of coefficients  $a_p, \dots, a_9$  were calculated as:

$$\begin{bmatrix} a_1 \\ a_2 \\ a_3 \\ a_4 \\ a_5 \\ a_6 \\ a_7 \\ a_8 \\ a_9 \end{bmatrix} = \begin{bmatrix} 0,0486 & 0,1848 & 3,024 & 17,7772 \\ 0,5403 & 0,2205 & 2,6284 & 18,8042 \\ 1,3183 & -2,1168 & 1,100 & 3,0319 \\ -1,431 & 1,7161 & 0,636 & -0,3537 \\ -1,0826 & 1,4126 & 1,4063 & 2,968 \\ -0,3303 & -0,3019 & 2,075 & 0,2037 \\ -1,8584 & 0,375 & 1,5476 & 0,5624 \\ -1,8994 & 0,3979 & 0,7193 & 2,5233 \\ 0,2652 & -0,6208 & -0,828 & 1,4015 \end{bmatrix} \times \begin{bmatrix} 0,6859 \\ 0,3436 \\ 1,0005 \\ 0,3629 \end{bmatrix} = \begin{bmatrix} 10,2767 \\ 11,284 \\ 2,102 \\ -2,1791 \\ -0,7662 \\ 1,0005 \\ 0,0735 \\ -0,0256 \\ -0,626 \end{bmatrix} = \begin{bmatrix} -0,7031 \\ -1,3839 \\ 0,2758 \\ 2,2952 \\ 2,9931 \\ 3,624 \\ 0,5332 \\ 0,4949 \\ 0,2748 \end{bmatrix} \quad (16)$$

Placing the values of coefficients  $a_p, \dots, a_9$  calculated using formula (16) to formula (6), we got the single column matrix A in the form:

$$A = \begin{bmatrix} 1 \\ 1+e^{-(-0,7031)} \\ 1 \\ 1+e^{-(-1,3839)} \\ 1 \\ 1+e^{-0,2758} \\ 1 \\ 1+e^{-2,2952} \\ 1 \\ 1+e^{-2,9931} \\ 1 \\ 1+e^{-3,624} \\ 1 \\ 1+e^{-0,5332} \\ 1 \\ 1+e^{-0,4949} \\ 1 \\ 1+e^{-0,2748} \end{bmatrix} = \begin{bmatrix} 0,3311 \\ 0,2004 \\ 0,5685 \\ 0,9085 \\ 0,9523 \\ 0,974 \\ 0,6302 \\ 0,6213 \\ 0,5683 \end{bmatrix} \quad (17)$$

Then, making use of Equation (5) we got the value of coefficient c:

$$c = [4,2231 \quad -3,8588 \quad -0,7112 \quad -1,7356 \quad 1,0448 \quad 0,1661 \quad 0,9618 \quad -0,9952 \quad 1,0022] \times \quad (18)$$

and making use of formula (4) we finally got:

$$\begin{bmatrix} 0,3311 \\ 0,2004 \\ 0,5685 \\ 0,9085 \\ 0,9523 \\ 0,974 \\ 0,6302 \\ 0,6213 \\ 0,5683 \end{bmatrix} + 0,1322 = 0,4903 \quad (19)$$

The formula (17) represents the value of the added wave resistance coefficient for the assumed encounter frequency equal to  $\omega_E = 0,5 \text{ s}^{-1}$ .

Case 2. Calculating the statistical mean wave resistance increase

Making use of the superposition principle applied to spectral representation of the irregular wave and transforming formulas (1) and (2) we can calculate the increase of the statistical mean wave resistance  $R_w$  coming from an irregular wave. For this purpose, we use the following formula:

$$R_w = \rho \cdot g \cdot \frac{B^2}{L} \int_0^\infty \rho_{AW}(\omega_E) \cdot S_{\zeta\zeta}(\omega_E) d\omega_E \quad (20)$$

where:

- $R_w$  – statistical mean wave resistance increase,
- $\omega_E$  – encounter frequency of the harmonic wave,
- $S_{\zeta\zeta}(\omega_E)$  – wave energy spectrum density function,
- $\rho_{AW}(\omega_E)$  – added wave resistance transfer function,
- $B$  – ship breadth,
- $L$  – ship length,
- $\rho$  – seawater density,
- $g$  – acceleration due to gravity.

The added wave resistance transfer function  $\rho_{AW}(\omega_E)$  was calculated in the same way as in Case 1, assuming that the encounter frequency values range within  $\omega_E = 0,4 - 1,0 \text{ s}^{-1}$  with the step of  $0,05 \text{ s}^{-1}$ .

The function  $S_{\zeta\zeta}$  was calculated under the following assumptions:

- wave parameters:
  - significant wave height  $H_s = 3 \text{ m}$ ,
  - characteristic wave period  $T_1 = 8 \text{ s}$ ,
- wave energy spectrum, according to ITTC:

$$S_{\zeta\zeta}(\omega) = A\omega^{-5} \exp(-B\omega^{-4}) \quad (21)$$

where:

$$A = \frac{173 \cdot H_s^2}{T_1^4} = \frac{173 \cdot 3^2}{8^4} = 0,38 \quad (22)$$

$$B = \frac{691}{T_1^4} = \frac{691}{8^4} = 0,169 \quad (23)$$

The calculated values of: the added wave resistance transfer function  $\rho_{AW}(\omega_E)$ , the wave energy spectrum density function  $S_{\zeta\zeta}(\omega_E)$ , and the product of these functions  $\rho_{AW}(\omega_E)S_{\zeta\zeta}(\omega_E)$  are given in Table 3. Additionally, Fig. 5 shows graphically the transfer function  $\rho_{AW}(\omega_E)$ .

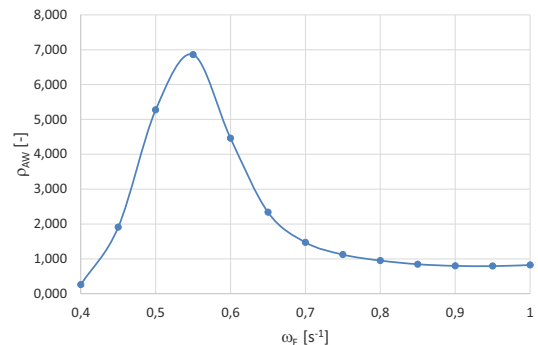


Fig. 5. The added wave resistance transfer function calculated for Case 2. Ship parameters were the following: length between perpendiculars  $L_{pp} = 187 \text{ m}$ , breadth  $B = 29 \text{ m}$ , waterplane coefficient  $CWL = 0,85$ , speed  $v = 15 \text{ w}$ .

Table 3. Sample results of calculations of: the added wave resistance transfer function  $\rho_{AW}$ , the wave energy spectrum density function  $S_{\zeta\zeta}$  and the product  $\rho_{AW} \times S_{\zeta\zeta}$ . The calculations were performed under the following assumptions: ship length between perpendiculars  $L_{pp} = 187$  m, ship breadth  $B = 29$  m, waterplane coefficient  $CWL = 0,85$ , ship speed  $V = 15$  w, significant wave height  $H_s = 3$  m, characteristic wave period  $T_1 = 8$  s.

(1)	$\omega_c$ [1/s]	0,4	0,45	0,5	0,55	0,6	0,65	0,7	0,75	0,8	0,85	0,9	0,95	1
(2)	$\rho_{AW}$ [-]	0,26	1,91	5,27	6,86	4,46	2,34	1,47	1,12	0,95	0,85	0,80	0,79	0,82
(3)	$S_{\zeta\zeta}$ [m <sup>2</sup> /s]	0,05	0,33	0,81	1,19	1,33	1,27	1,12	0,94	0,77	0,62	0,50	0,40	0,32
(4)	$\rho_{AW} \times S_{\zeta\zeta}$ [m <sup>2</sup> /s]	0,01	0,63	4,27	8,16	5,93	2,97	1,65	1,05	0,73	0,53	0,40	0,32	0,26

Then, making use of formula (20) and the values of  $\rho_{AW} \times S_{\zeta\zeta}$  from line (4) in Table 3, the statistical mean value of the added wave resistance  $R_w$  was calculated using the trapezoidal method:

$$R_w = 1,025 \cdot 9,81 \cdot \frac{29^2}{187} \cdot \left( \frac{0,01}{2} + 0,63 + 4,27 + 8,16 + 5,93 + 2,97 + 1,65 + 1,05 + 0,73 + 0,53 + 0,4 + 0,32 + \frac{0,26}{2} \right) \cdot 0,05 = 121,1 \text{ kN} \quad (24)$$

**Case 3. The use of the developed method for waterplane coefficient optimisation taking into account the added wave resistance at the preliminary bulk carrier design stage.**

This example presents the use of the method for finding, at the preliminary bulk carrier design stage, an optimal value of the waterplane coefficient which takes into account the added wave resistance. In the calculations the following assumptions were adopted:

- ship speed  $V = 15$  knots,
- length between perpendiculars  $L_{pp} = 187$  m,
- breadth  $B = 29$  m,

The aim of the design task was to calculate the waterplane coefficient value  $CWL$  within the range from 0,85 to 0,93 for which the wave resistance reaches the minimum.

The formula (20) allows to calculate the added wave resistance from a single wave of arbitrary statistical parameters. However, waves of different parameters can occur on the ship navigation route. To evaluate the ship design in a comprehensive way which takes into account a variety of waves, coefficients reflecting certain wave distributions are frequently used. An example of such a coefficient and its use in ship designing is given in [17].

In the present case the wave resistance was described using the coefficient  $RI$  which, like in [17], was defined as:

$$RI = \sum_{i=1}^8 R_w(H_s = 3 \text{ m}, T_1(i)) \cdot \frac{f_T(i)}{1000} \quad (25)$$

where:

$R_w$  – statistical mean added wave resistance, calculated according to formula (20) (and the sample formula (24)),

$H_s$  – significant wave height,

$T_1$  – characteristic period of the wave having parameters from Table 4,

$f_T$  – incidence rate of the wave of given period  $T_1$ . Its value was taken from Table 4, showing the data for the Atlantic [10, p. 373, Table 6.4]

$i$  – No. of line in Table 4.

The  $RI$  coefficient represents the statistical mean added wave resistance from the statistical wave having the following parameters:

- significant height  $H_s = 3$  m,
- characteristic period  $T_1 = 5 - 17$  s,
- different incidence rates.

Table 5 presents sample results of  $RI$  calculations for the assumed data and for the waterplane coefficient equal to  $CWL = 0,85$ .

Then the  $RI$  values were calculated for other  $CWL$  values ranging from 0,85 to 0,93 with the step of 0,1. The results are graphically shown in Fig. 6.

It results from the diagram in Fig. 6 that the optimal  $CWL$  value taking into account the added wave resistance is  $CWL = 0,90$ . For this value the  $RI$  coefficient is the lowest.

Table 4. Incidence rates  $f_T$  of waves of characteristic periods  $T_1$  adopted in calculations. The data for the North Atlantic taken from [10, p. 373, Table 6.4]

No.	Characteristic wave period $T_1$ [s]	Incidence in 1000 observations $f_T$ [-]
1	5	118,97
2	5 – 7	345,43
3	7 – 9	358,72
4	9 – 11	138,59
5	11 – 13	29,05
6	13 – 15	5,65
7	15 – 17	0,92
8	17	2,69

Table 5. Sample results of  $RI$  calculations for  $CWL = 0,85$ ;  $H_s$  – significant wave height,  $T_1$  – characteristic wave period,  $R_w$  – statistical mean added wave resistance,  $f_T$  – incidence rate of the wave of a given characteristic period.

No. (i)	$H_s$ [m]	$T_1$ [s]	$R_w$ [kN]	$f_T/1000$ [-]	$R_w \times f_T/1000$ [kN]
1	3	5	15,3	0,119	1,82
2	3	6	38,4	0,345	13,25
3	3	8	121,2	0,359	43,51
4	3	10	144,3	0,139	20,06
5	3	12	110,1	0,029	3,19
6	3	14	74,1	0,006	0,44
7	3	16	47,9	0,001	0,05
8	3	17	39,6	0,003	0,12
$RI = \Sigma$					82,4

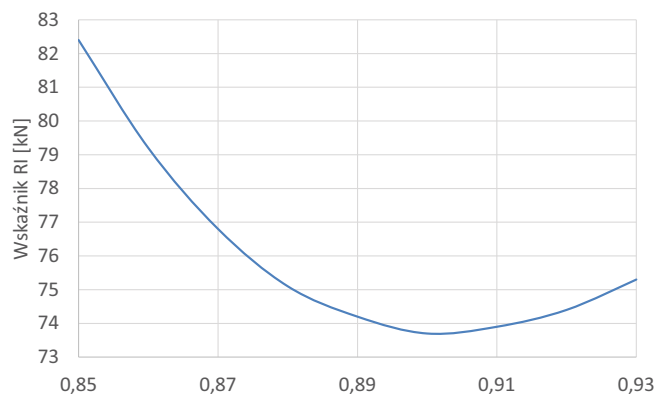


Fig. 6.  $RI$  vs.  $CWL$  in sample design task

## SUMMARY

The method and function presented in the article can be used to calculate the added wave resistance coefficient for bulk carriers having the following geometrical parameters:

- displacement  $D = 18\,500 - 56\,000$  t,
- length between perpendiculars  $L_{pp} = 132 - 210$  m,
- breadth  $B = 21 - 32,2$  m,
- draught  $d = 7,8 - 12$  m,
- waterplane area  $F_w = 2300 - 5600$  m<sup>2</sup>,
- waterplane coefficient  $CWL = 0,8 - 0,93$ ,

within a wide range of ship velocities  $V = 0 - 8$  m/s.

The parameters which are needed to calculate this function are basic parameters of the bulk carrier design, such as:

- waterplane area,
  - waterplane coefficient,
- and ship speed.

Within the linear theory of rolling, this function allows to calculate the mean added wave resistance for an arbitrary irregular head wave described by an arbitrary energy spectrum.

Thanks to that the developed function can have a wide range of applications, such as for instance:

- preliminary designing of bulk carriers: to take into account the added wave resistance in the resistance-propulsion characteristics,
- planning the navigation route: to work out speed characteristics of the bulk carriers with waves taken into account,
- calculating the weather factor in the energy efficiency design index, *EEDI*.

The article presents samples of practical use of the presented method to illustrate its applicability for calculating, for instance:

- the added wave resistance coefficient for a given encounter frequency,
  - the added wave resistance transfer function,
  - the statistical mean added wave resistance,
- and optimising the waterplane coefficient with respect to the added wave resistance at the preliminary bulk carrier design stage.

## BIBLIOGRAPHY

1. Abramowski, T.: Application of Artificial Intelligence Methods to Preliminary Design of Ships and Ship Performance Optimization, *Naval Engineers Journal* 125 (3), pp. 101-112, 2013.
2. Abramowski T.: Application of artificial neural networks to assessment of ship manoeuvrability qualities, *Polish Maritime Research*, 2008 (2), pp 15-21, 2018
3. Arribas F. Pe´rez: Some methods to obtain the added resistance of a ship advancing in waves, *Ocean Engineering* 34 (2007), pp. 946-955, 2007.
4. Bhattacharyya R.: *Dynamics of Marine Vehicles*, John Wiley & Sons Inc, 1978
5. Cepowski T.: Approximation of Added Resistance in Waves Based on Ro-Ro Ferry Main Dimensions and Wave Parameters, *Archives of Transport* 02/2012; 23(4), pp. 435-445, 2012
6. Cepowski T.: Determination of optimum Hull form for passenger car ferry with regard to its sea-keeping qualities and added resistance in waves, *Polish Maritime Research*, No 2(56), Vol 15, pp 3-11, 2008
7. Cepowski T.: Modelling of Added Wave Resistance on the basis of the Ship's Design Parameters, „Computer Systems Aided Science and Engineering Work in Transport, Mechanics and Electrical Engineering”, No. 121, pp. 39-46, Radom, 2008
8. Cepowski T.: On the modeling of car passenger ferryship design parameters with respect to selected sea-keeping qualities and added resistance in waves, *Polish Maritime Research*, No 3(61), Vol 16, pp 3-10, 2009
9. Chądzyński W.: “Elements of modern methodology of designing of floating objects (in Polish), *Prace Naukowe Politechniki Szczecińskiej*, Szczecin 2001
10. Dudziak J.: *The theory of the ship (in Polish)*, Fundacja Promocji Przemysłu Okrętowego i Gospodarki Morskiej, Gdansk 2008.
11. Faltinsen, O.M., Minsaas K.J., Liapis N., Skjrdal, S.: “Prediction of Resistance and Propulsion of a Ship in a Seaway”, *Proceedings of the 13th Symposium on Naval Hydrodynamics*, pp. 505-529, Tokyo 1980
12. Gerritsma J., Beukelman W.: *Analysis of the Resistance Increase in Waves of a Fast Cargo-ship*, *International Shipbuilding Progress*, No 18(217), 1972
13. Journe J.M.J.: *Verification and Validation of Ship Motions Program SEAWAY*, Report1213a, Delft University of Technology, Ship Hydromechanics Laboratory, The Netherlands, 2001
14. MATULJA D, SPORTELLI M., GUEDES SOARES C., PRPIĆ-ORŠIĆ J.: Estimation of Added Resistance of a Ship in Regular Waves, *Brodogradnja*, 62(2011) Vol. 3, pp 259-264
15. Nabergoj R., Jasna P.: A comparison of different methods for added resistance prediction, 22nd IWWWFB, Plitvice, Croatia 2007
16. SALVESEN, N.: “Added Resistance of Ships in Waves”, *Journal of Hydronautics*, 1978.

17. Szelangiewicz T.: Ship's Operational Effectiveness Factor as Criterion Cargo Ship Design Estimation, Marine Technology Transaction, Polish Academy of Sciences, Branch in Gdańsk, Vol. 11, 2000
18. Watson D.G.M: Practical Ship Design, Gulf Professional Publishing, 2002

#### **CONTACT WITH THE AUTHOR**

Tomasz Cepowski

Maritime University of Szczecin  
ul. Wały Chrobrego 1-2  
70-500 Szczecin

**POLAND**

# NUMERICAL SIMULATIONS OF HYDRODYNAMIC OPEN-WATER CHARACTERISTICS OF A SHIP PROPELLER

**Judyta Felicjancik**

CTO S.A. Ship Design and Research Centre, Gdansk

Environmental Doctoral Studies at Gdansk University of Technology, Faculty of Mechanical Engineering

**Sebastian Kowalczyk**

CTO S.A. Ship Design and Research Centre, Gdansk

**Karol Felicjancik**

**Krzysztof Kawecki**

Bota Technik Sp. z o.o. Limited Partnership

## ABSTRACT

*The paper presents the results of numerical simulations of ship propeller operation bearing the name of Propeller Open Water (POW) Tests. The object of tests was a sample ship propeller (PPTC1), the geometrical and kinematic data of which are available, along with the results of model tests, on the official page of the research centre involved in the measurements. The research aimed at verifying the correctness of results of numerical simulations performed in the model and real scale. The results of numerical analyses performed in the model scale were confronted with those measured in the experiment. Then, making use of dimensionless coefficients which characterise propeller's operation, the recorded model data were extrapolated to real conditions and compared with corresponding results of simulations. Both the numerical simulations and the experimental research were performed for the same propeller load states. The reported research is in line with other activities which aim at developing advanced numerical methods to support the process of ship propeller designing. .*

---

<sup>1</sup> Potsdam Propeller Test Case: <http://www.sva-potsdam.de/pptc-smp11-workshop/>

**Keywords:** CFD, model tests, POW Test, propeller, validation

## INTRODUCTION

Intensive development of computational fluid dynamics (CFD) methods allows nowadays to model the operation of a ship propeller in homogeneous velocity field in order to determine its hydrodynamic characteristics (similar to so-called propeller open water tests performed experimentally). The hydrodynamic open-water characteristics of a ship propeller have the form of dimensionless thrust coefficient  $K_T$  and torque coefficient  $K_Q$  as functions of the advance coefficient  $J$  for constant pitch ratio  $P/D$ . Determining ship propulsion characteristics, i.e. diagrams of propeller thrust, torque, and power as ship speed functions for constant propeller revolutions is essential for determining the propeller

operation point. Selecting an optimal advance speed for the given power passed to the propeller at its nominal revolutions results in more efficient fuel consumption. The hydrodynamic characteristics, applicable in propeller designing, are obtained from model tests which precisely maintain geometric similarity of the model and real propeller, as well as the similarity of water flow in the vicinity of the model and real propeller (referred to as kinematic similarity). These tests can have the form of open water propeller model tests or self-propelled ship model tests.

The use of advanced numerical methods, verified on the results of model tests, is a significant step towards full modelling of phenomena which accompany ship propeller operation in real conditions. It is noteworthy, however, that attempts to improve the level of accuracy of the performed

numerical simulations, for instance by modelling real and not simplified geometry of the propeller, or taking into account real cavitation phenomena, should always be followed by experimental verification of the obtained results.

The experimental results which are most frequently used to validate numerical methods are usually obtained from in-house tests, or those performed by other research centres and made available for international comparison tests. Based on the results of the in-house tests, a methodology of numerical analyses has been developed in the Ship Design and Research Centre (CTO SA) which allows to assess and predict cavitation on a ship propeller [12]. The developed methodology was verified on the results of cavitation which was experimentally measured on the propeller CP4691 in the CTO SA cavitation tunnel. The results of verification were presented at the international conference on advanced measurement techniques in Istanbul, Turkey [7]. The results of cavitation observation were complemented by analyses of hydroacoustic effects accompanying the modelled phenomenon. Finally, the results of numerical analyses and experimental measurements were compared. The result of the performed comparison was satisfying.

International comparison tests make it possible to compare results of in-house examination with those obtained in other research centres using different simulation codes and methodologies. This way was used to verify a valuable numerical method for ship propulsion analyses which was developed in CTO [3, 5]. The company Bota Technik sees considerable benefits coming from the use of this method, which manifest themselves, among other aspects, in increased efficiency and reliability of the ship propulsion design process. This method can be widely implemented and practically used by Bota Technik in realisation of design tasks, as well as in research and development activities.

The propeller used as the object of numerical and model examination has been designed to meet the needs of an international comparison test (benchmark test) and does not exist in real scale. The hydrodynamic characteristics of the sample propeller were generated as a result of standard tests performed in the model basin to validate numerical methods. The here examined propeller was designed in such a way as to allow the open water propeller to be tested within a wide velocity range of parameters of the approaching flow, including developed cavitation conditions. The experimental measurements were performed in the model basin and in the cavitation tunnel owned by the SVA Centre, Potsdam, Germany [2, 15].

In that experiment the propeller was tested in conditions corresponding to the tow test, with shaft immersion equal to 1.5 of propeller diameter D. In the resent research, to obtain open water propeller characteristics the simulation calculations were performed for the following values of the advance coefficient  $J$ : 0.6, 0.8, 1.0, 1.2 and 1.4. The range of analysis usually includes the design operation point, i.e. the parameter for which the propeller has been designed. In the

paper, the results of experimental and numerical examination of the propeller are shown in the form of dimensionless thrust and torque coefficients as functions of rotational speed  $n$  and diameter  $D$  of the propeller, and water density  $\rho$  (1-4) [6]:

The propeller thrust coefficient:

$$K_T = \frac{T}{\rho n^2 D^4} \quad (1)$$

The propeller torque coefficient:

$$K_Q = \frac{Q}{\rho n^2 D^5} \quad (2)$$

Speed (advance) coefficient:

$$J = \frac{V_A}{nD} \quad (3)$$

Propeller efficiency:

$$\eta_0 = \frac{J K_T}{2\pi K_Q} \quad (4)$$

where:  $T$  – thrust [N];  $Q$  – torque [Nm];  $V_A$  – advance speed [m s<sup>-1</sup>]

## DESCRIPTION OF THE EXAMINED OBJECT

The object of the analysis was a five-blade propeller identified as VP1304 (or PPTC), with the designed pitch coefficient  $P_{0.7}/D = 1.635$ . This is a right-handed adjustable pitch propeller with the diameter  $D = 0.25$ m in the model scale. The adjustment system affects the structure of propeller blades near the hub (a gap of 0.3 mm in width between the hub and the blade root), as well as the leading and trailing edges [1, 11]. The propeller geometry is schematically shown in Fig. 2. Geometric data of the propeller for real conditions were obtained by proper scaling. Moreover, the forecast of propeller operation in real conditions, used for comparison with the results of numerical calculations, was obtained as extrapolation of the model data. Such forecasting is a standard procedure, which bases on available results of model tests. The propeller diameter in the real scale, calculated using the scale coefficient, was equal to 3m. Water parameters (density, viscosity) corresponded to real values, characteristic for given basin conditions. Basic geometric data of the propeller are collated in Table 1.

Table 1. Basic data of propeller VP1304

	Symbol	Unit	Real scale	Model scale
No. of propeller model	-	-		VP1304
Type of propeller	-	-		CPP
Diameter	D	m	3	0.25
Design pitch coefficient for $r/R=0.7$	$P_{0.7}/D$	-		1.635
Expanded blade area ratio	$AE/A_0$	-		0.779

1 Ship propeller CP469 is a four-blade adjustable pitch propeller of the Polish training and research vessel „Nawigator XXI”.

	Symbol	Unit	Real scale	Model scale
Hub coefficient	$dh/D$	–	0.300	
Number of blades	$Z$	–	5	
Direction of rotation		–	Right-handed	
Scale coefficient	$\lambda$	–	1	12

## BOUNDARY CONDITIONS AND CALCULATION METHOD

The calculations which made the basis for hydrodynamic characteristics of the examined propeller in model and real scale were performed using the code STAR CCM+. The flow past the propeller was modelled using the unsteady flow model based on the Reynolds-Averaged Navier-Stokes (RANS) equations and the two-equation “SST k-omega” turbulence model. Flow modelling with the aid of RANS equations enables to obtain reliable results, at the same time preserving acceptable calculation times, due to the use of a simpler equation to close the basic system of Navier–Stokes equations. The applied turbulence model, recommended for the here examined type of flow, links together main advantages of basic k- $\epsilon$  and k- $\omega$  models, and introduces a term which limits overproduction of kinetic energy of turbulence in the areas with high pressure gradients. The k- $\epsilon$  model well models the turbulence in the free flow area and reveals low susceptibility of quantities describing the turbulence to inlet conditions. In turn, the k- $\omega$  model much better models the flow in the boundary layer, but is very susceptible to free-stream turbulence values. The applied combined model, transformed from the k- $\epsilon$  form to the equations for k and  $\omega$ , was complemented by introducing a SST (Shear Stress Transport) term which limits principal stresses in the flow [13].

The flow past the propeller VP1304 was modelled in a cylindrical domain having the following dimensions, expressed as multiples of propeller diameter D: 5D forward, 10D rearward, and 10D in diameter, see Fig.1. A homogeneous flow field was assumed at inlet. Table 2 collates basic data adopted as conditions for calculations in the both scales. The model scale reflects conditions of model propeller operation in the model basin, while the full scale corresponds to standard sea conditions. In both cases the calculation time step was assumed in such a way that it corresponded to the same fraction of full propeller revolution in both scales.

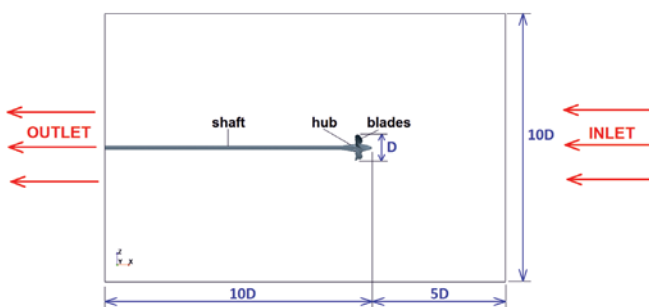


Fig. 1. Computational domain of the propeller VP1304

Table 2. Basic data assumed in calculations

Parameter	Unit	VP1304	
		Model scale	Real scale
Water density	$\text{kg m}^{-3}$	999.00	1025.87
Kinematic viscosity of water	$\text{m}^2 \text{s}^{-1}$	1.139E-6	1.188E-6
Propeller revolutions	$\text{s}^{-1}$	15.00	4.33
Propeller revolution per time step	°	3	3

The computational domain was discretised using the finite volume method (FVM), which consists in dividing the computational domain into a finite number of small elements bearing the name of control volumes and integrating the conservation equations over these elements. The method adapts to each type of grid and therefore is well applicable to the complex geometry of the examined propeller. The shape of the control volume can be arbitrary, which is a reason why this method is so popular and frequently used to solve fluid mechanics equations [8].

The calculations were performed on an unstructured polyhedral grid with the boundary layer surrounding the entire propeller (Fig. 2). Cell dimensions were adapted locally, based on the resultant values of  $Y^+$ , a parameter defining the way in which the equations are solved within the boundary layer [14]. As a result of domain discretisation, the grid consisting of over 5.5 million of finite volumes was obtained. Proper grid refinement on the propeller surface was needed to model properly the complicated geometry of propeller blades with sharp leading and trailing edges. Additional grid refinement in other space sections provided opportunities for better flow modelling near the propeller [4].

The calculation grid for the real scale cannot be generated via direct multiplication of node coordinates from the model scale by the scale coefficient. In general, surface elements on the outer walls of the propeller and volumetric elements of the major part of the computational domain can be scaled in this way, but direct scaling of dimensions of the cells composing the boundary layer is incorrect. The relative thickness of the boundary layer decreases with the increasing Reynolds number, i.e. is smaller for the real scale. Moreover, the boundary layer is related with the turbulence scales, which also change in proportion to the changing dimensions of the object. Proper modelling of flow phenomena requires adapting grid elements in the boundary layer to the nature of the flow, which in practice means decreasing the relative thickness of elements in the direction normal to the object's walls. The phenomena taking place in the boundary layer heavily affect the hydrodynamic drag of objects moving in the fluid, therefore their proper modelling is of primary importance for the performed analyses.

The propeller revolution was modelled using the model with steady reference frame (SRF), which simulated real propeller revolution in the domain, taking into account the grid motion. The water flow was in the direction of the X-axis.

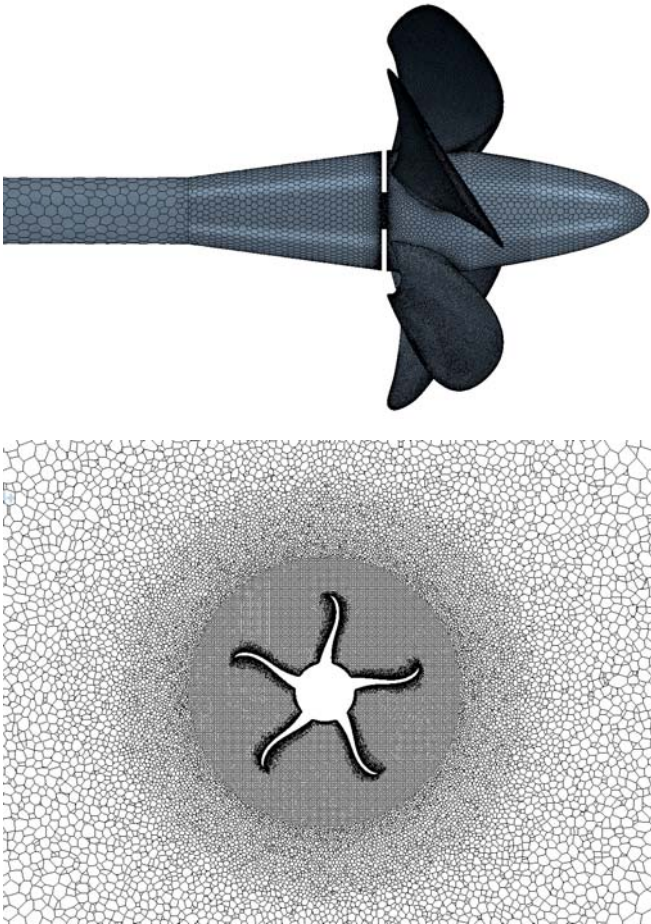


Fig. 2. Grid visualisation: a) on propeller, b) in propeller circle cross-section

## RESULTS AND DISCUSSION

The results of the numerical analyses, performed within a wide range of parameters, are collated in Tables 3-11, while the open water propeller characteristics are shown in diagrams in Fig. 3-5. Thrusts and torques were calculated only for propeller blades, and read after the forces have reached a proper convergence level. In each case (calculation point) the computing time was not the same.

Tables 3-5 collate numerical results (labelled as *CFD*) obtained from propeller calculations performed in the model scale. These results are compared with widely available experimental results (labelled as *EFD*) of examination of the same sample propeller. When the propeller load decreases (with the resultant increase of the advance coefficient  $J$ ), the difference between calculations and experiment increases, both for the thrust coefficient  $K_T$  and the torque coefficient  $10K_Q$ . As a consequence, the difference between the values of propeller efficiency  $\eta_O$  calculated and measured for the same load also increases. In Fig. 3 we can clearly see underestimation of operating parameters of the propeller for lower loads, for which the obtained coefficient values are becoming smaller. This is reflected in efficiency changes, as it depends on the both coefficients. The obtained values can also be affected by the quality of the modelled geometry. The numerical

analyses were performed using the available geometry with sharp trailing edges, which in fact, for technological reasons, have limited radii in the real propeller version used in model tests.

Table 3. Experimental results for model scale

$J$	EFD model scale		
	$K_{T,EFD}$	$10K_{Q,EFD}$	$\eta_{O,EFD}$
0.6	0.629	1.396	0.430
0.8	0.510	1.178	0.551
1.0	0.399	0.975	0.652
1.2	0.295	0.776	0.726
1.4	0.188	0.559	0.749

Table 4. Numerical results for model scale

$J$	CFD model scale		
	$K_{T,CFD}$	$10K_{Q,CFD}$	$\eta_{O,CFD}$
0.6	0.622	1.422	0.417
0.8	0.496	1.187	0.532
1.0	0.375	0.961	0.621
1.2	0.263	0.742	0.677
1.4	0.152	0.509	0.665

Table 5. Comparing experimental and numerical results for model scale

$J$	Difference (EFD mod-CFD mod)		
	$\Delta K_T$	$\Delta 10K_Q$	$\Delta \eta_O$
0.6	0.007	-0.026	0.013
0.8	0.014	-0.009	0.019
1.0	0.024	0.014	0.031
1.2	0.032	0.034	0.049
1.4	0.036	0.050	0.084

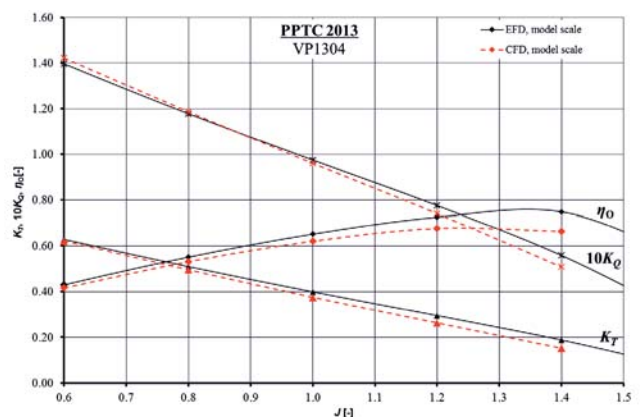


Fig. 3. Comparing experimental data and numerical results for model scale

Tables 6-8 collate numerical results (marked  $C_{FDS}$ ) obtained from propeller calculations performed in the real scale. These results are compared with widely available experimental

results (marked  $EFD_{\eta}$ ) of examination of the same sample propeller.

For lower propeller loads, mainly corresponding to the advance coefficient values  $J > 0.8$ , the difference between the calculated and measured values of the thrust coefficient  $K_T$  increases. Moreover, the calculated values move from the area of slight overestimation to the area of underestimated values. Nevertheless, the shape of the curve is very close to that expected within the analysed operation range. The curve of the torque coefficient  $10K_Q$  is more inclined, as compared to the reference curve. The advance coefficient  $J=1.05$  is the point of intersection of the both curves. From this point on, the numerical values are underestimated for lower propeller loads ( $J > 1.05$ ) and overestimated for higher loads ( $J < 1.05$ ). The values of propeller efficiency  $\eta_o$  are underestimated within the entire operating range, and the difference between the results of measurement and calculations increase with the decreasing load. In Fig. 4 the abovementioned relations between the numerical and experimental results are clearly visible.

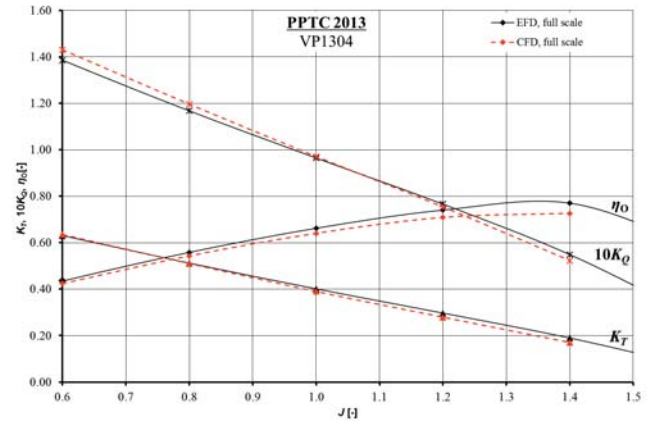


Fig. 4. Comparing experimental data and numerical results for real scale

Table 6. Experimental results for real scale

J	EFDS real scale		
	$K_T, EFD S$	$10K_Q, EFD S$	$\eta_o, EFD S$
0.6	0.631	1.386	0.435
0.8	0.512	1.168	0.558
1.0	0.401	0.965	0.662
1.2	0.297	0.766	0.740
1.4	0.190	0.549	0.770

Table 7. Numerical results for real scale

J	CFDS real scale		
	$K_T, CFD S$	$10K_Q, CFD S$	$\eta_o, CFD S$
0.6	0.636	1.430	0.424
0.8	0.511	1.196	0.544
1.0	0.390	0.970	0.640
1.2	0.280	0.753	0.709
1.4	0.170	0.522	0.726

Table 8. Comparing experimental and numerical results for real scale

J	Difference (EFD real-CFD real)		
	$\Delta K_T$	$\Delta 10K_Q$	$\Delta \eta_o$
0.6	0.005	0.044	-0.011
0.8	0.001	0.028	-0.014
1.0	-0.011	0.005	-0.022
1.2	-0.017	-0.013	-0.031
1.4	-0.020	-0.027	-0.044

Tables 9–11 collate differences between numerical and experimental results for the model and real scale. In experimental conditions, the difference is kept at a constant level for both the trust coefficient  $K_T$  and the torque coefficient  $10K_Q$ , which results from the fact that the results for the real scale were obtained from extrapolation of the model results. However, the propeller efficiency difference  $\Delta \eta_o$  increases with the decreasing propeller load. As for the numerical results, the differences between them are not kept precisely at the same level, but take similar values for both the thrust coefficient  $K_T$  and the torque coefficient  $10K_Q$ . The propeller efficiency difference  $\Delta \eta_o$  increases with the decreasing propeller load. It can be seen in Fig. 5 that despite similar trends in coefficient differences in both cases, the efficiency difference for the numerical case significantly increases with the increasing advance coefficient. This tendency is likely to be related with the scaling effect, as the extrapolation of model basin results ( $K_T$  and  $10K_Q$ ) is clearly kept at a constant level, while the efficiency  $\eta_o$  calculated from these quantities reveals a similar trend to that of the numerically obtained difference curve.

Table 9. Comparing experimental results for model and real scale

J	Difference (EFDS real-EFD mod)		
	$\Delta K_T$	$\Delta 10K_Q$	$\Delta \eta_o$
0.6	0.002	-0.010	0.005
0.8	0.002	-0.010	0.007
1.0	0.002	-0.010	0.010
1.2	0.002	-0.010	0.014
1.4	0.002	-0.010	0.021

Table 10. Comparing numerical results for model and real scale

J	Difference (CFDS real-CFD mod)		
	$\Delta K_T$	$\Delta 10K_Q$	$\Delta \eta_o$
0.6	0.014	0.009	0.007
0.8	0.015	0.009	0.011
1.0	0.015	0.010	0.019

J	Difference (CFDS real-CFD mod)		
	$\Delta K_T$	$\Delta 10K_Q$	$\Delta \eta_o$
1.2	0.017	0.012	0.032
1.4	0.019	0.014	0.062

Table 11. Comparing differences between numerical and experimental results for model and real scale

J	Difference (EFD - CFD)		
	$\Delta K_T$	$\Delta 10K_Q$	$\Delta \eta_o$
0.6	-0.012	0.001	-0.002
0.8	-0.013	0.001	-0.004
1.0	-0.013	-0.020	-0.009
1.2	-0.015	-0.022	-0.018
1.4	-0.017	-0.024	-0.041

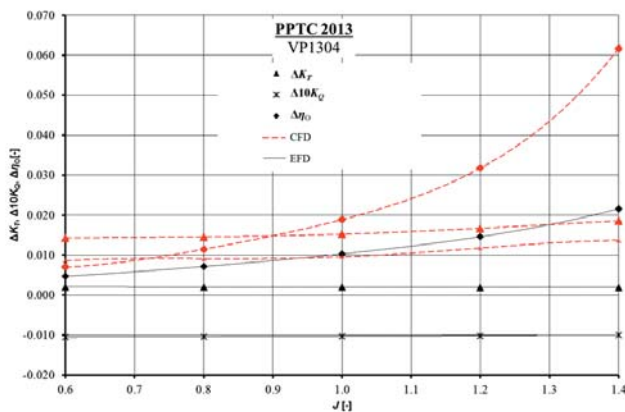


Fig. 5. Comparing differences between numerical and experimental results for model and real scale

## CONCLUSIONS

The results of numerical simulations of open water propeller operation, performed within the framework of international comparison workshops, enabled to verify the applied methods by comparing with the experimentally measured results. Public availability of the data on propeller geometry and its experimental examination provides opportunities for wide validation of numerical methods and comparing the quality of in-house achievements with the results obtained in other research centres. The results of numerical simulations performed in CTO SA reveal similar trends in the shapes of hydrodynamic characteristics of the examined propeller within the entire range of the advance coefficient. The differences between CFD and EFD results are small for higher values of the advance coefficient  $J$ . The highest discrepancy is observed in propeller efficiency results obtained for highest advance coefficient in the real scale. Although the general trend of the analysed differences is similar, the exact values differ much between each other. It is noteworthy, however, that the values for the real scale were obtained from extrapolation of the results of model

tests and not from measurements, which raises the question whether the observed differences reflect real nature of the simulated phenomena or are a consequence of the adopted extrapolation method.

The methodology of numerical simulations which was applied in CTO SA allows to obtain results, the quality of which is similar to those presented by other major research centres [9, 10, 11]. The developed method is similar to those quoted in the references and models the nature of the examined phenomena with the accuracy which is sufficiently high to recommend it for practical use.

Due to high convergence of the performed analyses, and the resultant high credibility of the obtained results, the use of the presented method by the design office of Bota Technik will considerably enhance their capacity in selection and design of ship propellers. The company Bota Technik will be able to offer the ship owner a properly selected propeller with its full characteristics. This ability will make a clear added value for the ship owner, and will allow the company to strengthen its competitiveness on the demanding market of ship propellers.

## BIBLIOGRAPHY

1. Barkmann U.: Potsdam Propeller Test Case (PPTC) - Open Water Tests with the Model Propeller VP1304. Report 3752, Schiffbau-Versuchsanstalt Potsdam, Germany 2011.
2. Barkmann U., Heinke H.J., Lubke L.: Potsdam Propeller Test Case (PPTC) - Test Case Description. Second International Symposium on Marine Propulsors, SMP'11, Workshop: Propeller performance, Hamburg, Germany 2011.
3. Bugalski T., Hoffmann P.: Numerical simulation of the interaction between ship hull and rotating propeller. Proceedings of a Workshop on Numerical Ship Hydrodynamics, Gothenburg 2010, pp. 441-446.
4. Bugalski T., Hoffmann P.: Numerical simulation of the self-propulsion model test. Second International Symposium on Marine Propulsors SMP'11, Hamburg, Germany 2011.
5. Bugalski T., Wawrzusiszyn M., Hoffmann P.: Numerical Simulations of the KCS - Resistance and Self-Propulsion. Proceedings of A Workshop on CFD in Ship Hydrodynamics, Vol. III, pp. 251-256, December 2-4, NMRI, Tokyo 2015.
6. Carlton J.: Marine Propellers and Propulsion, Elsevier, Amsterdam-Tokyo 2007.
7. Felicjancik J.: Propeller investigations by means of numerical simulation. The 4th International Conference on Advanced Model Measurement Technology for the Maritime Industry AMT'15, September 28-30, Istanbul, Turkey 2015.
8. Ferziger J.H., Perić M.: Computational Methods for Fluid

Dynamics. Springer, Berlin-Tokyo 2002.

9. Fujiyama K., Ho Kim Ch., Hitomi D.: Performance and Cavitation Evaluation of Marine Propeller using Numerical Simulations. Second International Symposium on Marine Propulsors, SMP'11, Hamburg, Germany 2011.
10. Gornicz T., Kulczyk J.: The Assessment of the Application of the CFD Package OpenFOAM to Simulating Flow around the Propeller. Marine Navigation and Safety of Sea Transportation: Maritime Transport & Shipping, 247, Poland 2007.
11. Klasson O.K., Huuva T.: Potsdam Propeller Test Case (PPTC). Second International Symposium on Marine Propulsors, SMP'11, Hamburg, Germany 2011.
12. Kowalczyk S., Felicjancik J.: Numerical and experimental propeller noise investigations. Ocean Engineering published by Elsevier (2016), vol. 120, pp. 108-115.
13. Menter F. R.: Two-Equation Eddy-Viscosity Turbulence Models for Engineering Applications. AIAA Journal (1994), Vol. 32, No 8, pp. 1598-1605.
14. Versteeg H.K., Malalasekera W.: An Introduction to Computational Fluid Dynamics the Finite Volume Method. Harlow, England 2007.
15. [http://www.sva-potsdam.de/pptc\\_ittc\\_switch.html](http://www.sva-potsdam.de/pptc_ittc_switch.html)

## CONTACT WITH THE AUTHOR

Judyta Felicjancik

*e-mail: judyta.felicjancik@cto.gda.pl*

Centrum Techniki Okrętowej S.A.  
Ship Design and Research Center  
Szczecińska 65 St.  
80-392 Gdańsk

**POLAND**

## CALM WATER PERFORMANCE OF HARD-CHINE VESSELS IN SEMI-PLANING AND PLANING REGIMES

Parviz Ghadimi <sup>1</sup>

Sasan Tavakoli <sup>1</sup>

Abbas Dashtimanesh <sup>2</sup>

<sup>1</sup> Amirkabir University of Technology, Islamic Republic of Iran

<sup>2</sup> Persian Gulf University, Islamic Republic of Iran

### ABSTRACT

*In the current paper, a mathematical model is developed for performance prediction of hard-chin boats which can be used in both semi-planing and planing regimes. The proposed model bases on the 2D+T theory and implements pressure distributions over the length of the hull in order to compute the forces. To determine the forces in the semi-planing range, a function is proposed for the non-dimensional length at which the transom effect appears. Three drag components, which are: frictional drag, induced drag, and spray drag, are considered in the computations performed using an iterative method to satisfy two equilibrium equations. The validity of the proposed method is verified by comparing the predicted trim angle and resistance against the available experimental data. Based on this comparison, it is observed that the proposed method reveals satisfying accuracy in both semi-planing and planing regimes. The method is then used to study variation of hydrodynamic and hydrostatic forces as the hull makes a transition from the semi-planing regime to the planing regime. In addition, different components of the resistance are analyzed.*

**Keywords:** hard-chine vessels, planing and semi-planing regimes, performance prediction, 2D+T theory

### NOMENCLATURE

B	Boat beam
c	Half-wetted beam of 2D section (m)
c	Time rate of half-wetted beam of 2D section (m/s)
c*	Lateral position reached by whisker spray (m)
CF	Frictional resistance coefficient
CΔ	Load Coefficient
Dp	Drag acting on pressure area (N)
Ds	Drag acting on spray area (N)
L	Lift force (N)
LC	Chine wetted length (m)
LK	Keel wetted length (m)
LM	Mean wetted length (m)
LCB	Longitudinal center of hydrostatic force (m)
LCHD	Longitudinal center of hydrodynamic force (m)
LCG	Longitudinal center of gravity (%L from transom)
FB2D	2D hydrostatic force (N/m)
FB	Hydrostatic force (N)
fHD2D	2D hydrodynamic force (N/m)
FHD	Hydrodynamic force (N)
FnB	Beam Froude Number
Gξζ	Body fixed coordinate

MB	Hydrostatic moment (N-m)
MHD	Hydrodynamic moment (N-m)
OXZ	Moving coordinate
p	Pressure (Pa)
R	Reduction function
Re	Reynolds Number
Sp	Pressure area (m <sup>2</sup> )
SS	Spray area (m <sup>2</sup> )
t	Time (s)
tCW	Chine wetting time (s)
tf	Final time of solution (s)
U	Vessel speed (m/s)
w	Water impact speed (m/s)
x	Distance of section from water intersection (m)
y	Lateral distance from wedge apex
α'	Non-dimensional position at which reductions appear
β	Deadrise angle (°)
Δ	Weight (N)
ρ	Water density (Kg/m <sup>3</sup> )
	Water impact flow potential
τ	Trim angle (deg)

## INTRODUCTION

Nowadays, hard-chine hulls are broadly used for recreational, sport, and military purposes. The presence of a chine in the transverse section of the hull results in flow separation from the chine and generation of the hydrodynamic force. This hydrodynamic force supports the boat weight and leads to the reduction of the wetted surface of the boat, thus dramatically diminishing the wave making resistance. All these together help the boat reach a high-speed. An important problem regarding the hydrodynamics of a hard-chine vessel is computation of its resistance and trim angle in steady motion. It can be solved through establishing the dynamic equilibrium. Overall, all earlier models focusing on the performance prediction in calm water have highlighted the planing regime. In the current paper, a model is introduced which predicts performance of the boat in both, the semi-planing and planing regimes.

The first model to predict the performance of a planing boat was presented by Savitsky (1964) who introduced some empirical relations for hydrodynamic and hydrostatic lift forces, as well as for the center of pressure of the hard-chine planing boat. This model was further developed three times by Savitsky. Firstly, Savitsky and Brown (1974) modified it to consider the effects of trim tabs and non-monohedral hull form. Later, Savitsky et al. (2007) presented new relations for considering the whisker spray drag in the initial model (1964). Finally, Savitsky (2012) widely studied a warped hull form by modifying his early model. Overall, the Savitsky method was not introduced to analyze the pre-planing regime and its use is only limited to the planing regime. Since the Savitsky method is empirical and the equations are valid for Froude numbers suitable in the planing regime, this method cannot be used for modeling both planing and semi-planing regimes. In order to analyze these two regimes simultaneously, some other options should be taken into account. It is noteworthy however, that some empirical methods for modeling hard-chine boats in semi-planing regimes are already known. Mercier and Savitsky (1973) presented empirical relations for determining the resistance of semi-planing hulls, in which they used curve-fitting. Some other research activities related to the prediction of dynamic equilibrium of planing hulls have been conducted with the emphasis on warped hull planing hulls ((Bertorello and Olivero (2007); Schachter et al. (2016)). In recent years, Radojicic et al. (2014a and 2014b) developed relations for the resistance of such a hull by applying artificial neural networks.

Computational fluid dynamics (CFD) schemes can be considered a good approach for determining the dynamic equilibrium of the planing hull and may provide adequate accuracy (Brizolla and Sera (2007)). Different researchers have achieved good accuracy in predicting the trim angle of the planing hull by using CFD (Brizzolara and Villa (2010); Garu et al. (2012); Mousavirad et al. (2015); Jiang et al. (2016)). However, it should be pointed out that while the accuracy of CFD solutions is good and reasonable, they are time consuming and cannot be easily used in the early stage

design. Therefore, mathematical methods are considered a good alternative and viable option.

On the other hand, the 2D+T theory and the water entry problem together have received huge attention from the researchers. Applying this theory can help solve different hydrodynamic problems, ranging from steady motion (Vorous (1996); Savander (1997); Zhao et al. (1997); Xu and Troesch (1997); Katayama et al. (2006); Brogolia and Iafrati (2010); Ghadimi et al. (2016a)) to unsteady motions in waves (Martin (1976a,b); Zarnick (1978,1979); Akers (1999); Garne and Rosen (2003); Sebastiani et al. (2008); Faltinsen and Sun (2011); Kanayoo et al. (2015) ; Haase (2015a); Ghadimi et al. (2016b, c)). Beyond this, in some of the recent research works, forces and moments acting on a planing hull exhibiting roll (Tavakoli et al. (2015); Ghadimi et al. (2016d)) and yawed motions (Tascon et al. (2009); Morabito et al. (2015)) have also been analyzed. The potential of the 2D+T theory for modeling different motions and conditions has been realized because of recent advances in studying the water entry problem. The initial point in this regards refers to the early research of von Karman (1929) who proposed using momentum variation of a wedge entering the water for finding the normal force acting on it. Later, such research workers as Wagner (1932) made attempts to modify the von Karman (1929) study. In the last two decades, different researchers have presented innovative approaches for compaction of forces in different conditions, with the emphasis on their applications for hydrodynamic modeling of planing hulls. For example, Korobkin (2013) mentioned that his work had been motivated by the 2D+T theory. Another example is the research by Tassin et al. (2014) who mentioned that their method had been developed in such a way that the hydrodynamic force acting on a planing hull is determined using the 2D+T theory. The works by Xu et al. (1999), Judge et al. (2004), Riccardi and Iafrati (2004), and Fairlie-Clarke and Tvietnes (2008) are other examples in this regard. In the recent years, Sun and Faltinsen (2012) determined the forces acting on a boat in a semi-planing range. On the other hand, Kim et al. (2013) predicted the performance of the round bilge boat in a semi-planing regime using the 2D+T theory.

In the current paper, the 2D+T theory is used to compute the performance of a hard chine boat in both semi-planing and planing regimes. The hydrodynamic forces are computed using the pressure distribution over the body. The boundary condition is implemented in each section in order to find the half wetted beam. The pressure is integrated and subsequently the hydrostatic pressure is taken into account. The performance of the boat is determined using two equilibrium equations. To consider the semi-planing regime in the computations, it is proposed to use a specific function for the longitudinal position, in which the transom effect appears. The validity of the proposed method is assessed by comparing the computed trim angle and resistance against the published experimental data. Also, a worked example is included as Appendix A, which explains in more detail particular solution steps to the analyzed problem.

# THEORETICAL APPROACH

## PROBLEM DEFINITION

It is assumed that a hard chine boat is moving forward with a speed  $U$  in steady condition and it has no oscillatory motion, as shown in Fig. 1. By assuming that the boat speed is categorized in both semi-planing and planing regimes, the boat is free to have a dynamic trim angle ( $\tau$ ) and rise up ( $Z_{CG}$ ). In this situation, the boat has the keel wetted length ( $L_k$ ) and the chine wetted length ( $L_c$ ), which can be observed in the top view of the boat.

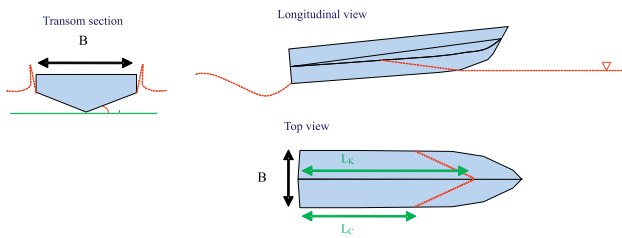


Fig. 1. Steady motion of a hard-chine boat in semi-planing and planing regimes.

## MOTION EQUATION

To establish the motion equation, two coordinate systems are considered. One of them is the body-fixed coordinate system ( $G\xi\zeta$ ) located at the center of gravity (CG). The  $\xi$ -axis is parallel to the base line and positive forward. The  $\zeta$ -axis is normal to the base line and positive downward. The second system ( $OXZ$ ) is a right-handed coordinate system moving with the forward speed of the boat and has no motion. The origin of this coordinate system is located at the intersection of the calm water surface by the normal line to the water passing through CG. The  $X$ -axis is parallel to the calm water surface and positive forward, while the  $Z$ -axis is normal to the calm water surface and positive downward.

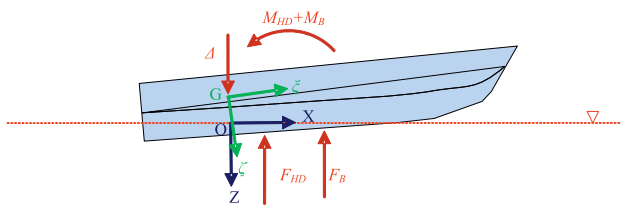


Fig. 2. Illustration of the coordinate systems and forces acting on the hard chin boat.

Forces and moments acting on the boat are shown in Fig. 2. They include the hydrodynamic force ( $F_{HD}$ ), the buoyancy force ( $F_B$ ), and their moments ( $M_{HD}$  and  $M_B$ ). After considering that the drag and thrust forces have no contribution in the motion equation, the motion equation in steady condition can be written as

$$\begin{aligned} \sum F_Z = 0 &\rightarrow W - F_{HD} - F_B = 0 \\ \sum M_G = 0 &\rightarrow M_{HD} + M_B = 0, \end{aligned} \quad (1)$$

where the first equation refers to the equilibrium in  $Z$  direction and the second equation indicates the equilibrium of the pitch moments about CG. To find the equilibrium condition, it is necessary to determine these forces. In the current paper they are determined using the 2D+T theory.

## 2D+T THEORY

It is assumed that the boat has no oscillatory motion and passes through a transverse plane, as illustrated in Fig. 3. The problem can be changed to a water entry problem with speed of  $w$  which can be found by

$$w = U \tan \tau, \quad (2)$$

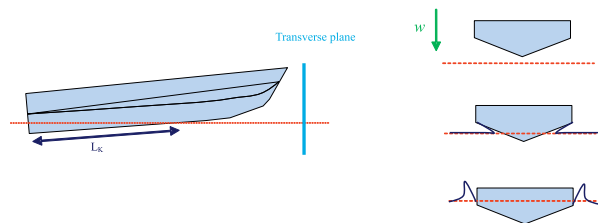


Fig. 3. Illustration of application of the 2D+T theory for solving the steady problem related to a hard chine boat in semi-planing and planing regimes.

The flow around the wedge sections can be solved through different approaches, making use of numerical methods (Zhao et al (1993); Maki et al. (2011); Ghadimi et al. (2012); Piro and Maki (2013); Ghadimi et al. (2013); Ghadimi et al. (2014a); Abraham et al. (2014); Farsi and Ghadimi (2014a and b); Facci et al. (2015 and 2016); Farsi and Ghadimi (2015); Shademani and Ghadimi (2016); Nguyen and Park (2016); Feizi Chekab et al. (2016)), and analytical methods (Mei et al. (1999); Yottu et al. (2007); Ghadimi et al. (2011); Tassin et al. (2014)). In the current paper, the analytical methods are utilized. By assuming that the fluid is perfect, the solution of the water entry problem can be written in the form:

$$\phi = w\sqrt{c^2 - y^2}, \quad (3)$$

where  $c$  is the transverse position of the spray root and  $y$  is the lateral distance from the apex, as displayed in Fig. 4.

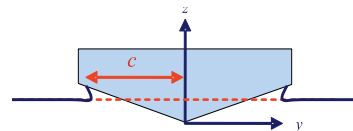


Fig. 4. Schematic of the wedge section entering the water.

Using the Bernoulli equation, the pressure acting on the section may be found as

$$p = \rho \left[ \frac{wcc}{\sqrt{c^2 - y^2}} - \frac{w^2}{2} \frac{y^2}{c^2 - y^2} \right]. \quad (4)$$

To determine the pressure, the values of  $c$  and  $\dot{c}$  are required. It is considered that the wedge experiences two phases, with dry chine or wet chine, as presented in Fig. 5. During the dry chine phase, these two parameters are found by

$$c = \frac{\pi}{2} \frac{wt}{\tan \beta}, \quad (5)$$

$$\dot{c} = \frac{\pi}{2} \frac{w}{\tan \beta}, \quad (6)$$

As the chines become wet, these two parameters are computed from the equations proposed by Algarin and Tascon (2014) as:

$$c = \sqrt{\left(\frac{b}{2}\right)^2 + \left[\frac{3}{2} \left[w \left(\frac{B}{2}\right)^2 (t - t_{CW})\right]\right]}, \quad (7)$$

$$\dot{c} = \frac{w^2}{2} \frac{\left(\frac{B}{2}\right)^2}{c \sqrt{c^2 - \left(\frac{B}{2}\right)^2}}, \quad (8)$$

where  $t_{CW}$  is the time spray root reaching the knuckles and can be found by

$$t_{CW} = \frac{\frac{B}{2} \tan \beta}{w}. \quad (9)$$



Fig 5. Illustration of phases in solving the steady problem.

It should be mentioned that Equations (7) and (8) are established by implementing the boundary condition at chines, as proposed by different researchers, for instance Korobkin and Malenica (2005).

The vertical hydrodynamic force ( $f_{HD}^{2D}$ ) acting on each section may be found by integrating the pressure over the wedge wall as follows:

$$f_{HD}^{2D} = \int p \cos \beta dy, \quad (10)$$

The 2D hydrostatic force ( $f_B^{2D}$ ) acts on the section which may be computed using the wetted area of each section. This force can be considered in the fully planing regime through the 2D+T theory (Sun and Faltinsen (2011); Akers (2014); Kanyoo et al. (2015); Haase et al. (2015)) and through empirical equations (Korovin Kroukovski et al. (1949); Savitsky et al.

(1964); Morabito (2010, 2014); Ghadimi et al. (2015b)), and also in the semi planing regime (Sun and Faltinsen (2012); Kim et al. (2013)). Before the chine is wetted, this force may be determined by

$$f_B^{2D} = \rho g c^2 \tan \beta, \quad (11)$$

while after chine wetting, it can be estimated by

$$f_B^{2D} = \rho g \left(\frac{B}{2}\right)^2 \tan \beta. \quad (12)$$

### THREE DIMENSIONAL FORCES

The three dimensional forces are computed by expanding 2D forces over the whole length of the vessel. The force due to hydrodynamic pressure is determined by

$$F_{HD} = \int_{L_K} R(\xi) f_{HD}^{2D} \cos \tau d\xi, \quad (13)$$

where  $R(\xi)$  is the transom reduction function, explained in Section 2.5. The pitching moment due to hydrodynamic pressure is obtained by

$$M_{HD} = F_{HD} \cdot LC_{HD}, \quad (14)$$

where  $LC_{HD}$  is the longitudinal position of the center of hydrodynamic force, determined by

$$LC_{HD} = \frac{\int_{L_K} R(\xi) f_{HD}^{2D} \xi d\xi}{\int_{L_K} R(\xi) f_{HD}^{2D} d\xi}. \quad (15)$$

The buoyancy force is determined by

$$F_B = \int_{L_K} R(\xi) f_B^{2D} d\xi, \quad (16)$$

and its pitching moment can be computed by

$$M_B = F_B \cdot LC_B, \quad (17)$$

where  $LC_B$  denotes the center of buoyancy force and can be determined by

$$LC_B = \frac{\int_{L_K} R(\xi) f_B^{2D} \xi d\xi}{\int_{L_K} R(\xi) f_B^{2D} d\xi}. \quad (18)$$

## TRANSOM REDUCTION

Equations (13) through (18) compose the transom reduction function. With the aid of this reduction function the forces can be predicted more accurately. The aim of using this function is to reduce the forces near the transom. In previous publications on the subject, Garme (2005) proposed a transom reduction function which can be used for 2D sections, while Morabito (2014) derived a new equation for the transom reduction function which may be used in longitudinal sections. Morabito (2015) has also emphasized the need for considering the transom reduction function when applying the 2D+T theory. It should be mentioned that in some classical works, a 3D dimensional correction factor has been used for correcting the integration of 2D force in such a way as to include transom effects. Examples of this type of correction can be found in the works of Mayo (1945), Milwitzky (1948), Schnitzer (1952), and Martin (1976a,b). Since the current research makes use of the 2D+T theory, it is preferred to use the transom reduction function proposed by Garme (2005), which can be written as

$$R(\xi) = \tanh \left[ \frac{2.5}{\alpha' B F n_B} (L_K - \xi) \right], \quad (19)$$

where  $\alpha'$  is the non-dimensional longitudinal position (from the transom) in which the reductions appears. Garme (2005) proposed that  $\alpha'$  be set to 0.34 for the planing range. Alternatively, Kim et al. (2013) proposed  $\alpha'$  to be equal to 0.6 in their research which deals with the semi-planing range. In the current paper, two new functions are proposed for  $\alpha'$ . After assuming that the hydrodynamic forces appear at  $F n_B = 1$ , two linear functions are proposed for  $\alpha'$ . The first function is proposed for the hydrostatic force and has the form:

$$\alpha' = \begin{cases} 0.34(F n_B - 1) & 1 < F n_B < 2 \\ 0.34 & F n_B > 2, \end{cases} \quad (20)$$

while the second function, proposed for the hydrodynamic force, is

$$\alpha' = \begin{cases} 1 - 0.66(F n_B - 1) & 1 < F n_B < 2 \\ 0.34 & F n_B > 2, \end{cases} \quad (21)$$

Variation of  $\alpha'$  as a function of the beam Froude number is displayed in Fig. 6.

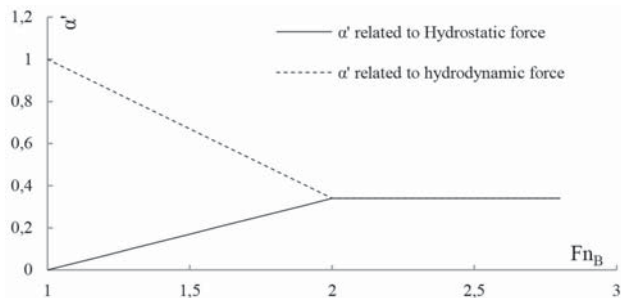


Fig 6.  $\alpha'$  as function of  $F n_B$ .

## RESISTANCE

The resistance of the boat is assumed to be a combination of frictional and hydrodynamic forces. The frictional resistance acts on both the pressure area, and the spray area. The frictional coefficient is computed from the ITTC 57 formula as

$$C_F = \frac{0.075}{(\log_{10} Re - 2)^2}. \quad (22)$$

Subsequently, the drag forces acting on the pressure area and the spray area can be computed, respectively, as

$$D_P = \frac{1}{2} \rho C_F U^2 S_P, \quad (23)$$

and

$$D_S = \frac{1}{2} \rho C_F U^2 S_S. \quad (24)$$

Here,  $S_p$  is the pressure area and may be computed by integrating the wetted length of each section as

$$S_p = \int c^* d\xi, \quad (25)$$

where

$$\begin{cases} c^* = c & t < t_{CW} \\ c^* = \frac{B}{2} & t > t_{CW}. \end{cases} \quad (26)$$

The drag force may also act on the spray area (Savitsky and Morabito (2011); Ghadimi et al. (2014b)). The spray area is computed using the method proposed by Savitsky et al. (2007). The resistance acting on the boat is determined by

$$R = \frac{D_P}{\cos \tau} + \frac{D_S}{\cos \tau} + F_{HD} \sin \tau \quad (27)$$

where the final term refers to the induced drag (drag due to the hydrodynamic force).

## CHINE WETTED LENGTH

The chine wetted length of the boat is determined using the relation

$$L_C = (t_F - t_{CW})U, \quad (28)$$

where  $t_F$  is the final time for solving the water entry problem, computed based on the keel wetted length. The mean wetted length of the boat is determined by

$$L_M = \frac{L_K + L_C}{2}. \quad (29)$$

## COMPUTATION PROCESS

In order to solve the steady motion of a hard-chine boat in both semi-planing and planning regimes, two systems of Equations (1) need to be satisfied. This is done using an iterative method. First, the trim angle ( $\tau$ ) and the keel wetted length ( $L_k$ ) are guessed and then the impact velocity is computed using Equation (2). Subsequently, the time duration is determined as

$$t_F = \frac{L_k \cos \tau}{U}. \quad (30)$$

The problem is solved from 0 to  $t_F$  and the hydrodynamic pressure is computed. Because of the utilization of the 2D+T theory, each solution time is converted to a longitudinal position by applying

$$\xi = -\left(L_k - \frac{vt}{\cos \tau}\right) + LCG. \quad (31)$$

At this stage, it is checked whether or not the heave equation is satisfied. If not, the keel wetted length should be modified and re-guessed. Subsequently, it is also checked whether or not the pitch equation is satisfied. If not, the trim angle should also be re-guessed. A schematic of the computational process is shown in Fig. 7. Also, to facilitate understating of the proposed method, a worked example of application of the proposed method and its successive steps are demonstrated in Appendix A.

## VALIDATION

The proposed method was validated by comparing the computed trim angle and resistance against the available experimental results. Accordingly, three steps were considered for assessing the accuracy of the method. To begin with, the planing hull series tested by Fridsma (1969) were considered, for which the trim angle and the resistance were computed. The obtained values of these parameters were compared against the experimental results in order to assess how accurately the proposed method can model these parameters for the prismatic planing hull series. In the second step, the USA coast Guard planing hull series was used as another reference for validating the obtained results. The experimental work dealing with the performance of a prismatic planing hull series was conducted by Metcalf et al. (2005). It can be considered a modern experimental effort. In addition, this planing hull series has different principal characteristics from those of the Fridsma series (1969). Finally, a planing hull with varied deadrise angle in its longitudinal direction was modeled. Positive validation of the proposed model through this step has made the precision in predicting calm water performance of a realistic (non-prismatic) hull form with the aid of the proposed model more convincing.

## FRIDSMAS SERIES OF PLANING HULLS

The Fridsma series has always been considered an important benchmark for validation purposes and several researchers, Akers (1999) for instance, have validated their results against the data reported by Fridsma (1969). Accordingly, the proposed method was also firstly validated on the results measured by Fridsma (1969). In the current paper, eight cases of the Fridsma series are considered. The cases were selected in such a way that they represent different load coefficients ( $C_{\Delta}$ ),  $L/B$ , deadrise angles, and LCG, intended for computation purposes. The principal characteristics of these cases are collated in Table 1.

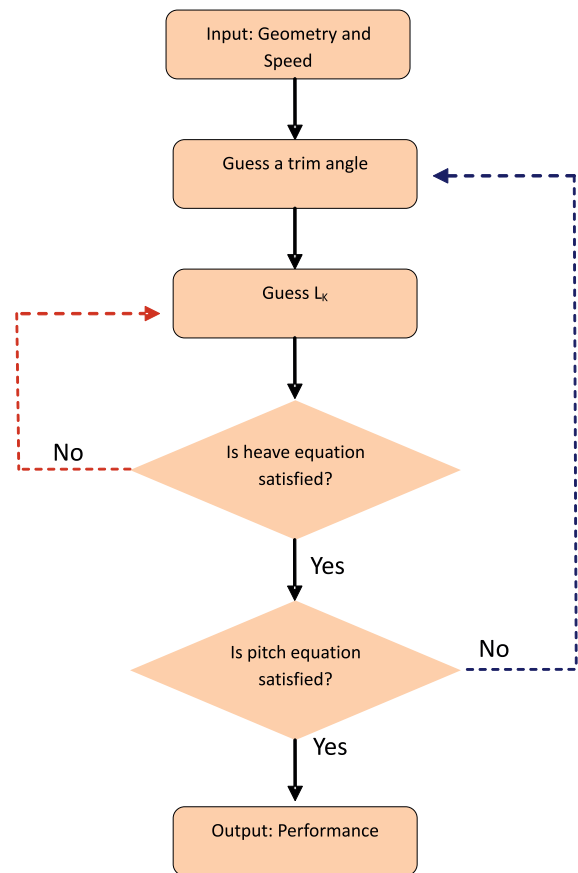


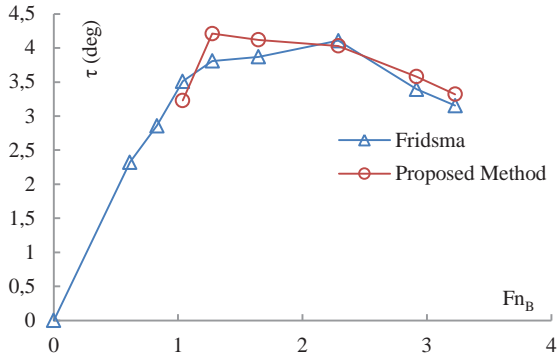
Fig. 7. The proposed algorithm for determining the performance of a hard-chine boat in semi-planing and planning regimes.

Table 1. Principal characteristics of Fridsma series planing hulls.

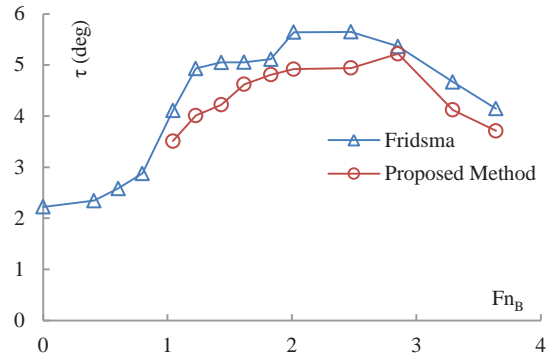
Case	1	2	3	4	5	6	7	8
$C_{\Delta} = \Delta / \rho g B^3$	0.304	0.608	0.608	0.304	0.912	0.608	0.304	0.912
Length / (m)	1.143	1.143	0.914	1.43	1.143	1.371	1.143	1.143
Beam / (m)	0.228	0.228	0.228	0.228	0.228	0.228	0.228	0.228
LCG / (%L from transom)	30	35	40	30	40	35	25	30
$\beta$	10	10	20	20	20	20	30	30

The predicted trim angles for the eight considered cases are displayed in Fig. 8. For each case, a plot of  $\tau$  vs.  $Fn_B$  is presented. The targeted computations were performed for  $Fn_B > 1$ , to help to assess the validity of the proposed method for determining the desired parameters for both semi-planing and planing regimes. Based on the plots related to Case 1, the proposed method has revealed good accuracy in predicting the trim. Relatively speaking, the predicted trend for the trim angle is similar to that observed in the experimental results. Good accuracy observed in this case shows that the proposed method can reliably predict the performance of a hard-chine vessel with the deadrise angle of 10 degrees and light load ( $C_{\Delta} = 0.304$ ) at  $Fn_B > 1$ . The trim angle predicted in Case 2 indicates that the precision of the current method is lower, as compared to Case 1 (This comparison is justified, as in both cases the deadrise angles are similar). The predicted trim angle at  $1 < Fn_B < 2.85$  is not as good as that in Case 1. Larger weight in Case 2 ( $C_{\Delta} = 0.608$ ) denotes that the weight increase of a hard-chine vessel may decrease the accuracy at  $Fn_B < 2.85$ . It is noteworthy that the reliability of the method increases dramatically when the beam Froude number exceeds 2.85. The plots in Cases 3 through 6 correspond to the hulls with the deadrise angle of 20 degrees. Each plot shows the accuracy of the method in one particular aspect. To begin with, Case 3 represents the hard-chine hull of  $L/B = 4$  and load coefficient 0.608. According to the plots related to this case, a relatively good accuracy in predicting the trim angle is observed. Also, the behavior of the predicted trim angle as a function of the Froude number is relatively similar to the trend observed in the experimental data. Good accuracy of trim angle estimation in Case 3 indicates that the proposed method may precisely determine the trim angle of a 20 degree hard-chine hull with small  $L/B$  ( $L/B = 4$ ) and moderate load ( $C_{\Delta} = 0.608$ ) at  $Fn_B > 1$ . Case 4 refers to the hard-chine boat with  $L/B = 5$  and light load ( $C_{\Delta} = 0.608$ ). Comparing the predicted results related to this case against the data measured by Fridsma (1969), it can be concluded that the proposed method reveals relatively good accuracy in predicting the trim at  $Fn_B > 2$ . At  $Fn_B = 1.33$ , the accuracy is worsened, but it cannot be characterized as poor. The measured trim angle at this beam Froude number is 3.85, while the predicted

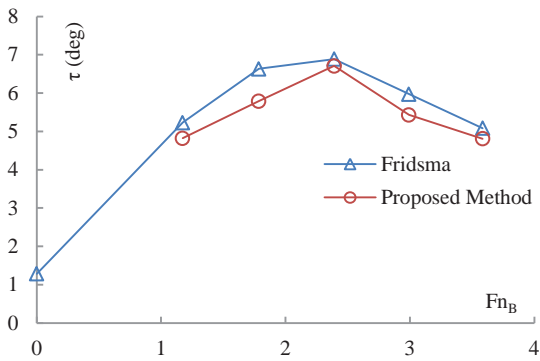
value is 3.21, which basically means that the absolute error is approximately equal to 15.9%. This error may be considered a reasonable accuracy for the semi-planing range. Case 5 refers to a 20-degree hard-chine hull with moderate  $L/B$  ( $L/B = 5$ ) and heavy load ( $C_{\Delta} = 0.912$ ). The results of this case show good accuracy in predicting the trim angle by the proposed method. It may be noted that the predicted trim angle for the deadrise angle of 20 degrees reveals relatively good accuracy at  $Fn_B > 1$  for both light-load ( $C_{\Delta} = 0.308$ , Case 4) and heavy-load conditions ( $C_{\Delta} = 0.912$ , Case 5), which is in some contrast with the results of the earlier discussed case of hard-chine hull with the deadrise angle of 10 degrees. Case 6 represents the 20-degree deadrise angle hull with large  $L/B$  ( $L/B = 6$ ) and light load ( $C_{\Delta} = 0.304$ ). Based on the plot presented for this case, it can be concluded that the accuracy in predicting the trim angle in this case is reasonably good. The trim angle for this case is underpredicted, but the error is not large for all investigated values of  $Fn_B$ . The maximum error for the trim angle in Case 6 occurs at  $Fn_B = 1.32$  and equals 10.8%. Ultimately, the accuracy of the proposed method in predicting the trim angle in Cases 7 and 8 is investigated. Both cases refer to the 30-degree hard-chine boat. In Case 7, the load is light ( $C_{\Delta} = 0.304$ ) and the LCG position is 25% of boat length from the transom. Case 8 deals with heavier load ( $C_{\Delta} = 0.304$ ) and the LCG position is 30% of boat length from the transom. For Case 7, the resulting plot is relatively similar to that showing the experimental results. Based on the plot in this case, the accuracy of the method in predicting the trim angle for this case is acceptable. As observed, the predicted results for all considered beam Froude numbers have approximately similar values to those recorded experimentally. This good accuracy is obvious at  $Fn_B > 1$  which shows that the proposed method can be effective in reducing hydrodynamic and hydrostatic forces near the transom in the semi-planing range. With regard to the computed trim angle in Case 8, reasonably good accuracy is observed. For this case, six different runs were performed with  $Fn_B$  ranging from 1 to 2. The obtained results testify to good accuracy of the proposed method in the semi-planing regime. The error for  $Fn_B = 1$  is slightly large, of about 24.3%, but it significantly decreases and approaches 7.04 percent at  $Fn_B = 1.43$ . There is also good accuracy for the case of  $Fn_B > 2$ .



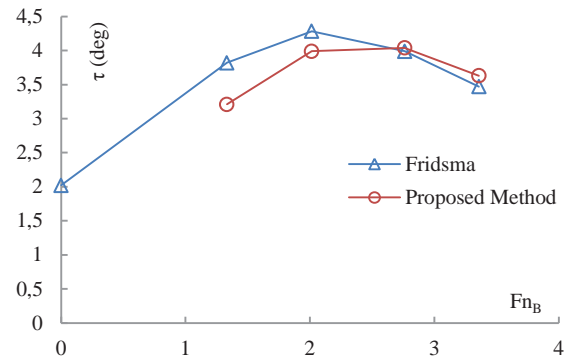
(a) Case 1



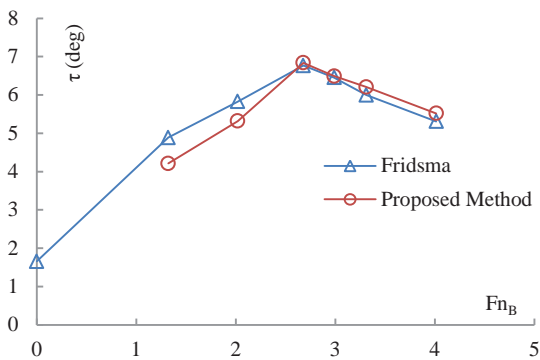
(b) Case 2



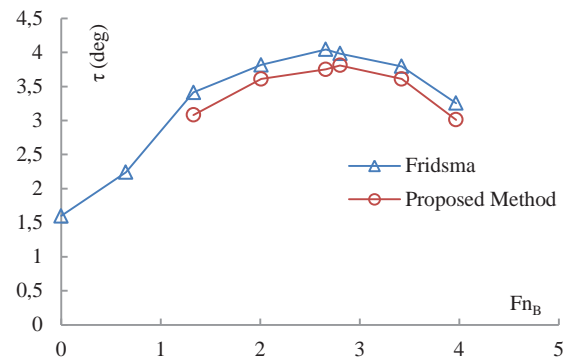
(c) Case 3



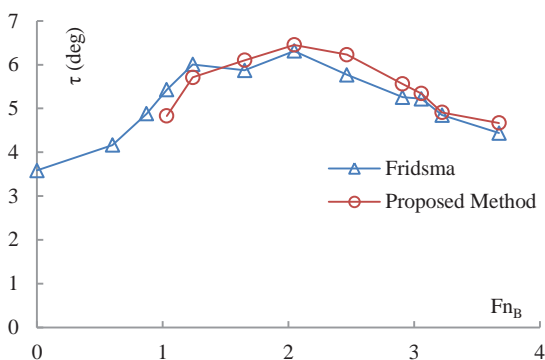
(d) Case 4



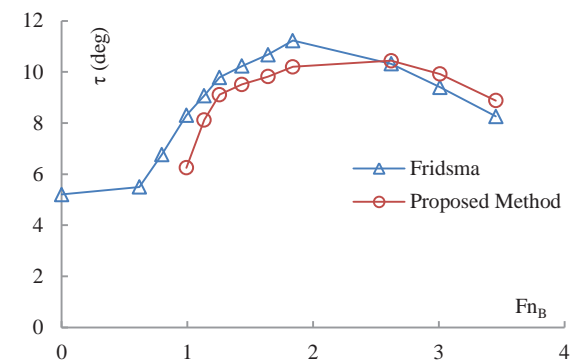
(e) Case 5



(f) Case 6



(g) Case 7

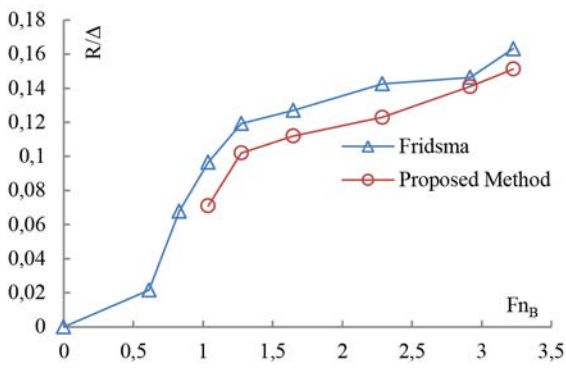


(i) Case 8

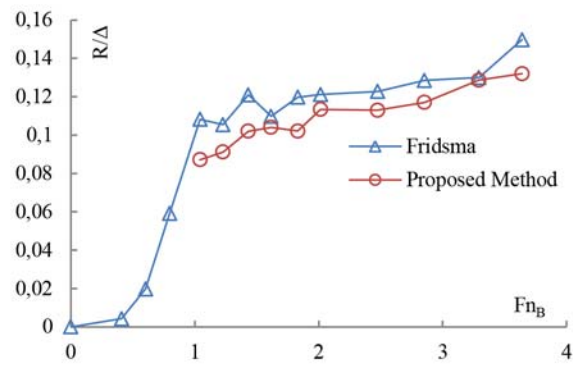
Fig. 8. Comparing the predicted trim angle with the results of experimental tests of Fridsma series planing hulls

The predicted resistance of Fridsma series planing hulls is shown in Fig. 9. Everywhere in the paper, the resistance is weight normalized and computed for all 8 cases shown in Table 1. First, the resistance in Case 1 was investigated. The plot produced for this case shows that the predicted resistance is not as accurate as the trim angle (see the corresponding plot in Fig. 8). At the lowest speed, identified by  $F_nB=1.03$ , the error is equal to about 26.2%. As the speed increases, the error decreases to become lower than 7.32% for  $F_nB=3.22$ . The resistance in Case 2 is predicted more accurately than in Case 1. The maximum error is observed at  $F_nB=1.04$ . The errors related to these two cases (Case 1 and 2) show that the current method reveals relatively good accuracy in predicting the resistance of hard-chine boats with the deadrise angle of 10 degrees. In addition, the resistance in Case 3 shows that the proposed method computes the resistance with high accuracy for  $F_nB>1$ . It is noteworthy that in this case, good accuracy in predicting the trim angle is also observed (see Fig. 8). Regarding the resistance in Case 4, a similar trend is observed to that in the experimental results. It can be pointed out that the non-dimensionalized resistance is slightly underpredicted in this case. However, the errors associated with this underprediction are not so significant and the mean value of the error for this case is 11.5%, which may be considered a reasonable error in predicting

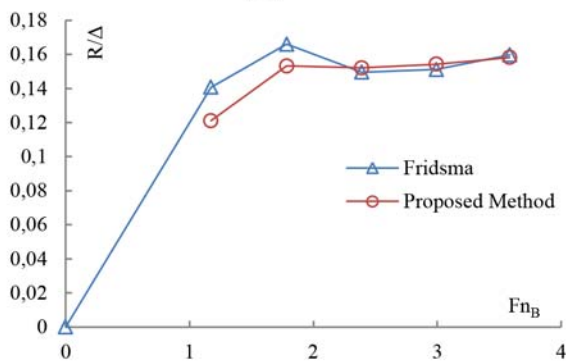
the resistance of hulls of this type in the pre-planing and planing regimes. The resistance predicted in Case 5 is not so accurate. According to the  $R/\Delta$  plot displayed for this case, the predicted resistance trend differs from that observed in the experimental results. For this case, the method exhibits some uncertainties. This fact can be due to heavy weight of the boat ( $C\Delta=0.912$ ) and possible iteration errors which may occur when determining the hydrodynamic force contribution and the wetted length. These errors can dramatically affect the predicted wetted surface, spray area, and subsequently the resistance. It should be noted that the trim angle in this case was predicted with good accuracy, as explained earlier. Furthermore, the resistance computed in Case 6 is in good agreement with the data reported by Fridsma (1969). Also, the predicted trend is approximately similar to that observed in the experimental plot. The predicted resistances in Cases 7 and 8, which deal with the hull of 30-degree deadrise angle, reveal good conformity with the experimental data. As observed, the resulting trends for  $R/\Delta$  vs.  $F_nB$  are similar to the plots presented by Fridsma (1969). It is noteworthy that for  $1<F_nB<2$  the resistance was predicted with relatively good accuracy, which indicates that the proposed method has good potential for predicting the hull resistance at the semi-planing range.



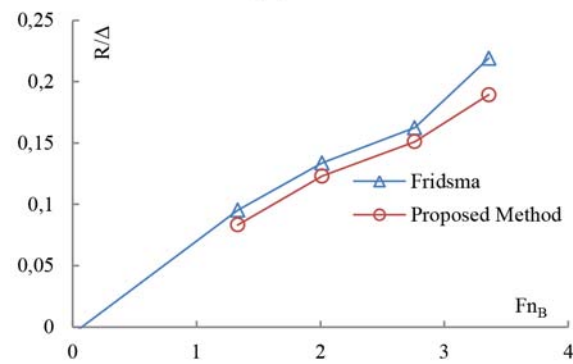
(a) Case 1



(b) Case 2

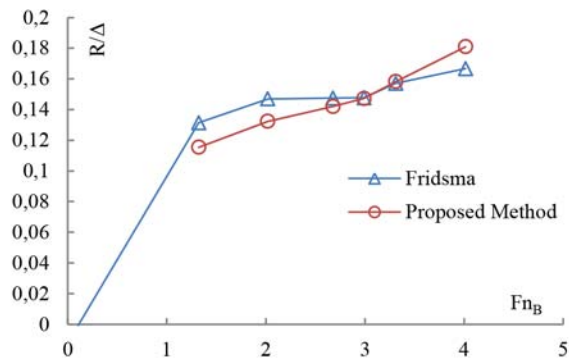


(c) Case 3

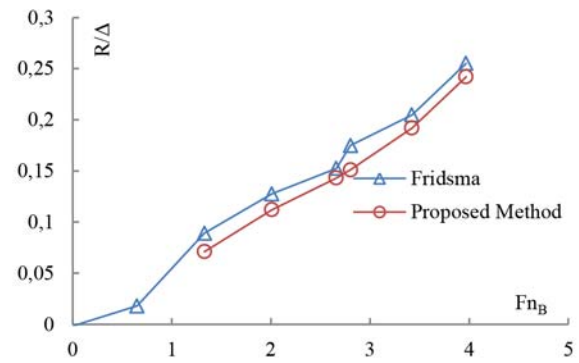


(d) Case 4

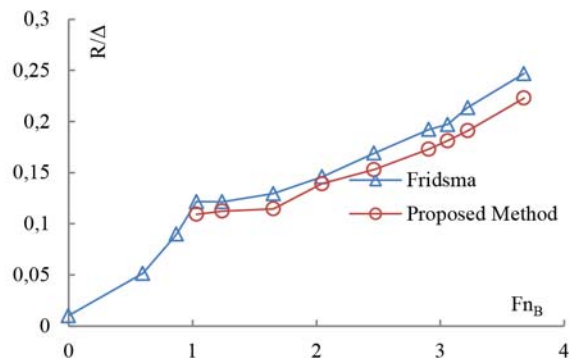
Fig. 9. Comparing the predicted resistance with the results of experimental tests of Fridsma series planing hulls.



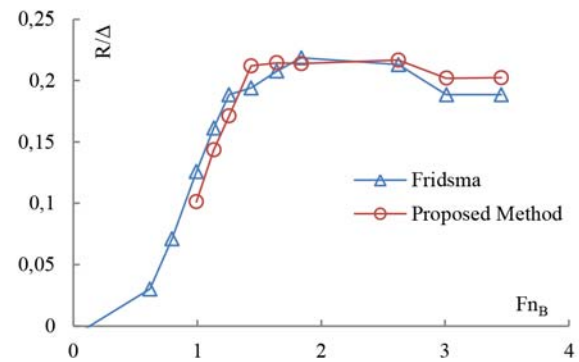
(e) Case 5



(f) Case 6



(g) Case 7



(i) Case 8

Fig. 9. Comparing the predicted resistance with the results of experimental tests of Fridsma series planing hulls.

## USA COAST GUARD SERIES

After examining the accuracy of the proposed method in performance (trim angle and resistance) prediction of Fridsma series planing hulls, another prismatic hull form was examined for validation purposes. This hull series bears the name of USA Coast Guard planing hull series, and includes four different hull forms. In the current paper, two of these hulls (Model 5629 and 5631) were examined. The performances of these hulls were experimentally reported by Metcalf et al. (2005). Here, the performance of each hull was analyzed for three different load coefficients and two different longitudinal CG positions. The principal hull characteristics and the considered validation cases are shown in Table 2. These cases were selected in such a way as to allow three different load conditions to be taken into account for each hull form.

Table 2. Principal characteristics of USA Coast Guard series planing hulls.

Case	5629-1	5629-2	5629-3	5631-1	5631-2	5631-3
$C_{\Delta} = \Delta / \rho g B^3$	0.303	0.381	0.491	0.421	0.530	0.683
Length / (m)	3.048	3.048	3.048	3.048	3.048	3.048
Beam / (m)	0.762	0.762	0.762	0.672	0.672	0.672
LCG / (%L from transom)	38	38	38	42	42	42
$\beta$	16.61	16.61	16.61	20	20	20

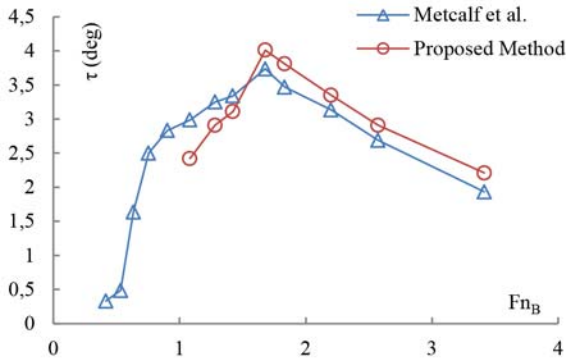
Figure 10 shows the predicted trim angle for the USA Coast Guard series planing hulls. The computations, accomplished at  $Fn_B > 1$ , provided opportunities for assessing the accuracy of

the proposed method in both the semi-planing and planing conditions. The plots related to Model 5629 (Fig. 10a, b and c) show that the proposed method accurately determines the trim angle for this hull form at different load conditions (including 0.303, 0.381 and 0.491). The maximum error for each load is observed at the speed categorized as the semi-planing range ( $1 < Fn_B < 2$ ). It should be noted that these errors are not significant and can be considered reasonable. In the case of load coefficient 0.303, the maximum error occurs at  $Fn_B = 1.08$  and approximately equals 18.9%. The errors dramatically decrease with the speed increase. The maximum error in predicting the trim angle in the case  $C_{\Delta} = 0.381$  is 13.4% and is observed at  $Fn_B = 1.03$ . In this case, the trim angle prediction error becomes smaller as  $Fn_B$  increases, which is a similar trend to that observed in the case  $C_{\Delta} = 0.303$ . Finally, the accuracy of the case with load coefficient of 0.491 is reasonably good, even at small beam Froude numbers (semi-planing regime). Overall, the observed general agreement between the trim angles predicted using the proposed method and the data reported by Metcalf et al. (2005) implies that the suggested method reveals reliable accuracy in predicting the trim angle of model 5629, which is a hard-chine hull with the deadrise angle of 16.61 degrees.

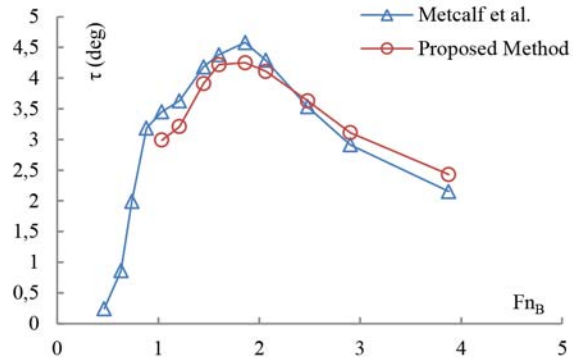
Another hull used to verify the validity of the current method is Model 5631. This hull was also studied at three different load conditions. The computed trim angle related to the first load condition of 0.421 is illustrated in Fig. 10d.

Relatively good accuracy is observed for this case, especially at  $Fn_B > 2$ . Although, at smaller beam Froude numbers ( $Fn_B < 2$ ) the accuracy is not so good, the errors seem reasonable. The maximum error is observed at  $Fn_B = 1.08$  and is approximately equal to 24.6%. Beyond this  $Fn_B$ , the error decreases and never becomes larger than 18.01%. The trim prediction accuracy for the load condition of 0.530 is good, as evidenced in

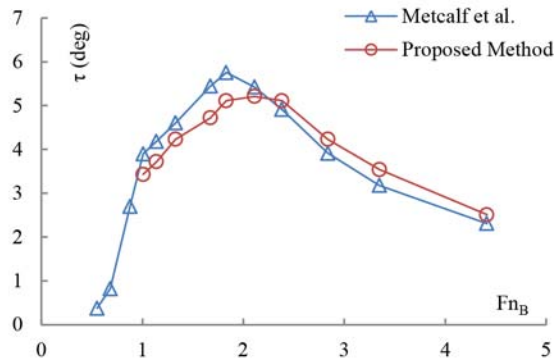
Fig. 10e. As observed, for all  $Fn_B$  values the predicted trim angles reveal good agreement with the experimental results. Figure 10f illustrates the computed trim angle for the case of  $C_{\Delta} = 0.683$ . The obtained plot (trim angle as a function of beam Froude number) behaves in relatively the same way as the experimental plot, which also corroborates reasonable accuracy of the proposed method.



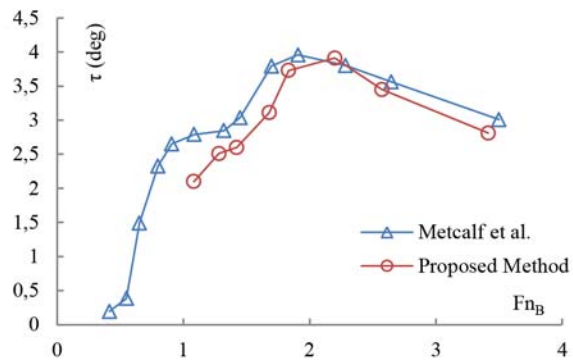
(a) Case 5629-1



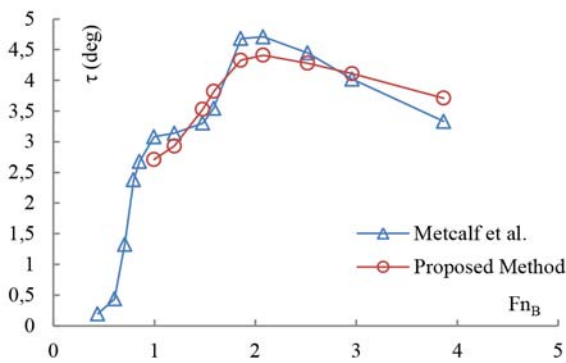
(b) Case 5629-2



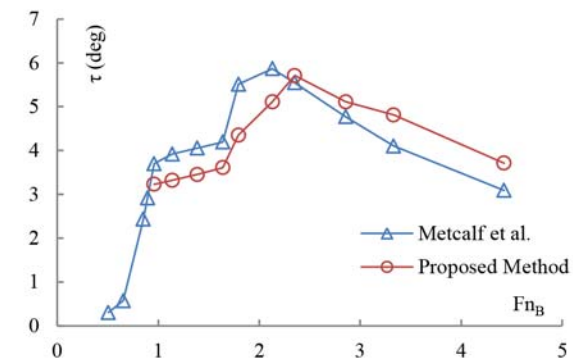
(c) Case 5629-3



(d) Case 5631-1



(e) Case 5631-2



(f) Case 6

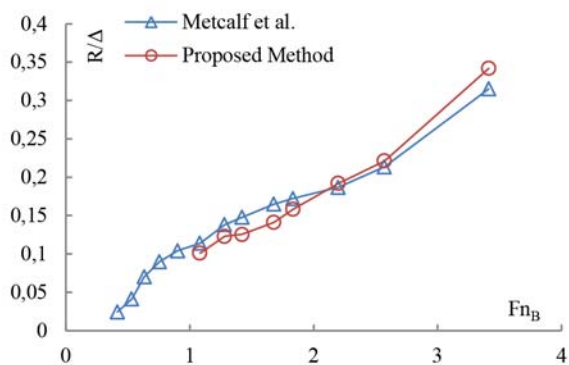
Fig. 10. Comparing the predicted trim angles with the experimental results by Metcalf et al. (2005).

The resistances computed for Models 5629 and 5631 are displayed in Fig. 11. First, the accuracy of the current method in predicting the resistance for Model 5629 is described. The plots referring to this model are presented in Fig. 11a, b and c for three different load coefficients (0.303, 0.381 and 0.491). As evident in the figure, the accuracy of the resistances calculated for load coefficients of 0.303 and 0.381 is reasonably good. The predicted  $R/\Delta$  vs.  $Fn_B$  trends are similar to those observed in the experimental data, and the computed values reveal very good conformity with the results of experimental measurements by Metcalf et al. (2005). At only one speed the accuracy is slightly worse, which is the largest  $Fn_B$  for both cases. Regarding the case with load coefficient of 0.303, the observed error at  $Fn_B=3.41$  is about 8.04%, while the error at  $Fn_B=3.87$  for the case with load of 0.381 is 8.75%. With

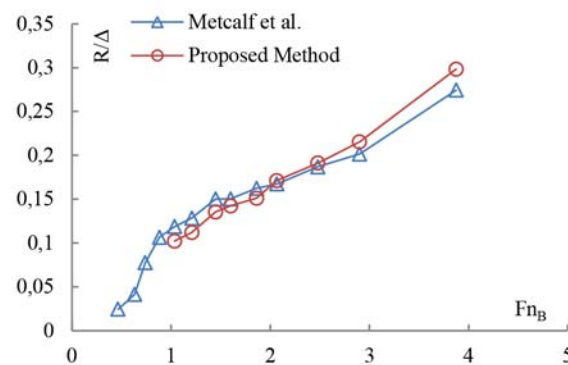
regards to the predicted resistance for Model 5629 with load coefficient of 0.491, it should be noted that the accuracy is not so good. In other words, the predicted resistances for this case are uncertain since the resulting trend differs from that observed in the experimental data.

The  $R/\Delta$  values calculated for Model 5631 are shown in Fig. 11d, e and f. It is noteworthy that for all three load conditions, the resistances were computed accurately. As observed, the predicted  $R/\Delta$  trends are similar to those observed in the experimental plots, which confirms good agreement between the predicted and experimental results.

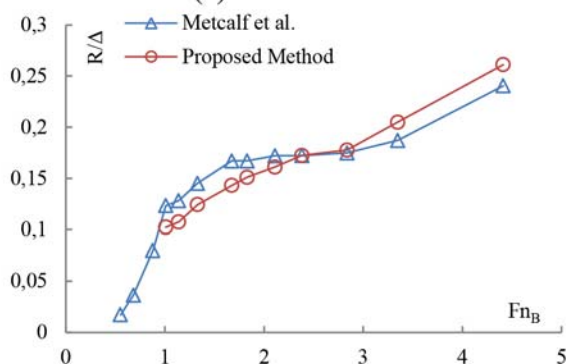
Overall, the observed good accuracy in resistance prediction for Models 5629 and 5631 indicates that the proposed method can reliably determine the resistances of prismatic hull forms at both planing and semi-planing ranges.



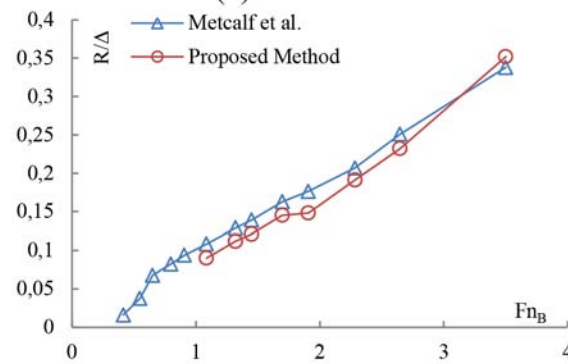
(a) Case 5629-1



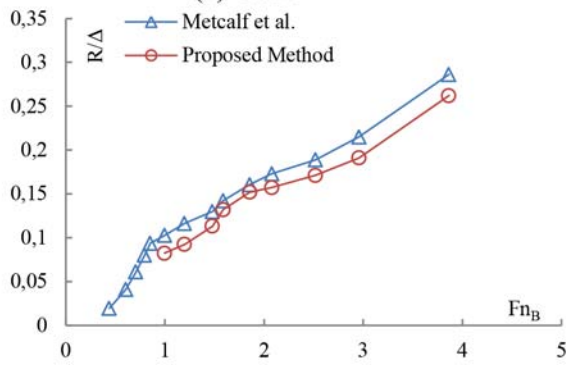
(b) Case 5629-2



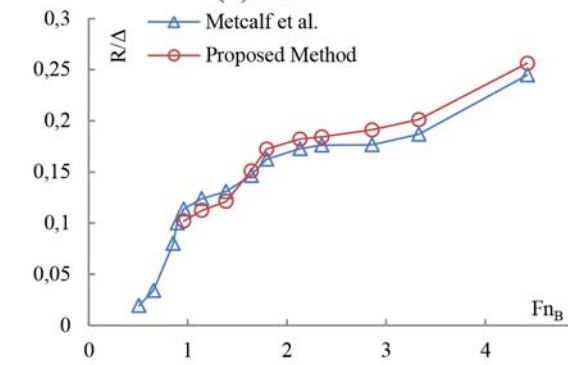
(c) Case 5629-3



(d) Case 5631-1



(e) Case 5631-2



(f) Case 5631-3

Fig. 11. Comparing the predicted resistances with the experimental results by Metcalf et al. (2005).

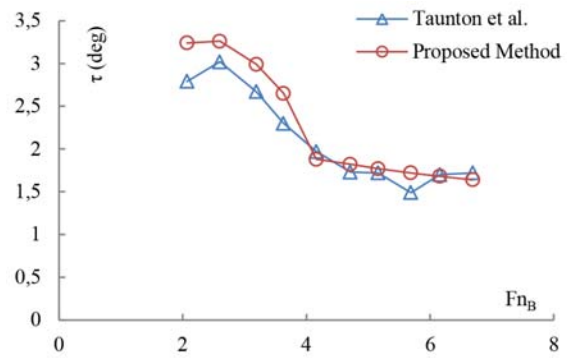
## MODEL C-SOUTHAMPTON

In addition to the two earlier examined planing hull series used for validation purposes, another planing hull series that has not a prismatic hull form was considered for further accuracy assessment of the proposed method. Validating the proposed method through the use of this hull series provides further confidence, as a more realistic hard-chine hull is mathematically modeled. That was why the planing hull series of Southampton was considered. From among all hulls existing in this series, Model C was only selected for assessing the potential of the proposed method. The trim angle reported for the other model in this series is very small (between 1 and 2 degrees) and cannot be determined using the proposed method. The principal dimension of Model C is shown in Table 3. It should be noted that this planing hull series was introduced by Taunton et al. (2010) and the performances of all hulls were measured in calm water.

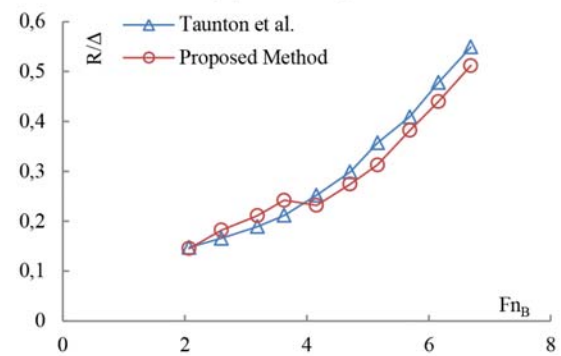
Table 3. Principal characteristics of Southampton Series Model C.

Case	Model C
$C_s = \Delta / \rho g B^3$	0.248
Length / (m)	2
Beam / (m)	0.46
LCG / (%L from transom)	33
$\beta$	22.5

Tauton et al. (2010) reported the performance of Model C at  $Fn_B > 2$  which means that this part of validation cannot support the semi-planing range for this hull form. Figure 12 shows the predicted trim angle and  $R/\Delta$ . With regard to the trim angle, it can be seen that the computed values are approximately similar to those recorded in the experiments, especially at  $Fn_B > 4$ . At small beam Froude numbers on this plot ( $2 < Fn_B < 3$ ), a relatively good agreement can be observed between the predicted trim angles and the measured data. In addition, the behavior of the  $\tau$  vs.  $Fn_B$  plot is approximately similar to the data reported by Tauton et al. (2005) at  $Fn_B > 3.63$ . Slight differences observed between the trends of these plots at smaller Froude numbers (ranging from  $Fn_B = 2.07$  to  $3.63$ ) can be due to the error associated with trim angle prediction for these Froude numbers. Over this range of Froude numbers, the maximum error occurs at the smallest Froude number  $Fn_B = 2.07$  and is approximately equal to 16.1%. The trend observed for this range of Froude numbers can be considered the same. The resistance computed using the proposed method is in reasonable agreement with the experimental values. However, the trends are not similar. At  $Fn_B = 3.63$ , a sudden resistance drop is observed, which is in contrast with the experimental plot. It is noteworthy that for this beam Froude number the trim angle also displays a sudden drop, see Fig. 12a. This trim angle drop results in high decrease of the predicted keel wetted length, which dominates the computations and leads to the resistance decrease. At larger  $Fn_B$ , the resistance trends are similar. The conformity between the experimentally recorded and numerically predicted trim angle values leads to a similar resistance trend for the beam Froude number  $Fn_B = 3.63$ .



(a) trim angle



(b) resistance

Fig. 12. Comparing the predicted trim angles and resistances with the experimental results by Taunton et al. (2010).

## RESULTS OF PARAMETRIC STUDIES

The results of the conducted parametric studies are presented in two different sections. In both sections, an attempt was made to identify variations of selected parameters when the fluid at the bottom of the boat starts producing the hydrodynamic force. First, the contributions of hydrodynamic and hydrostatic forces in weight supporting were examined. Subsequently, the resistance components were studied. The studies were performed for Cases 6 and 7 of the Fridsma series, since very good accuracy was earlier observed in performance prediction of these two hulls.

### CONTRIBUTION OF HYDRODYNAMIC AND HYDROSTATIC FORCES

Figure 13 shows percentage contribution of different forces at each beam Froude number. As evident in the figure, the contribution of the hydrodynamic force increases in both cases as the speed increases. The comparison between the results of these two hulls (Fig. 13a and b) implies that for Case 7, the hydrodynamic force contribution is larger at  $Fn_B < 2$ . This shows that for a hull with larger deadrise angle, larger hydrodynamic forces are needed to support the boat weight. A boat with larger deadrise angle has smaller hydrostatic force (because the submerged area of each section is smaller) and an additional hydrodynamic force is required.

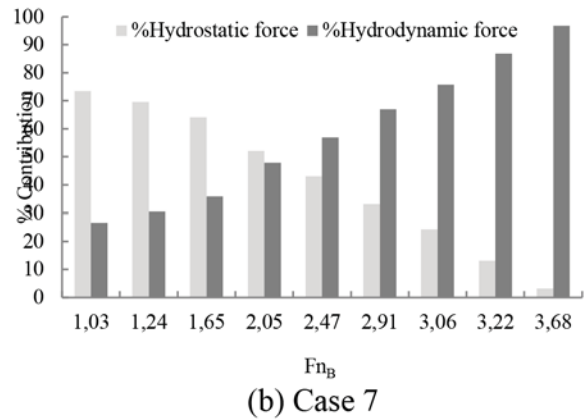
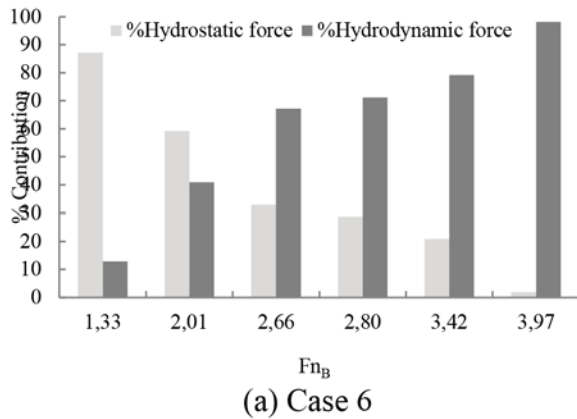


Fig. 13. Contribution of hydrodynamic and hydrostatic forces in supporting the boat weight.

### RESISTANCE COMPONENTS

The resistance components for the hard-chine boats in Cases 6 and 7 are illustrated in Fig. 14. The computed data show that the spray component is initially small, but as the speed increases this component becomes larger. This trend is observed in both cases. The frictional component in Case 6 increases dramatically with the increasing  $Fn_B$ , while in Case 7 only slight increase of this component is observed. This may be due to different trim angles of the boat (see Fig.

8). The trim angle in Case 7 is larger than that in Case 6, which leads to smaller wetted surface (because the hull needs a smaller surface to produce the hydrodynamic force) and, finally, to smaller frictional resistance. The generated plots also show that the induced resistance (the resistance due to hydrodynamic force) approaches a constant value for beam Froude numbers larger than 3 and has little variation beyond this range. The observed trend implies that this component becomes fixed when the hard-chine boat reaches a specific speed and its trim angle has little variation.

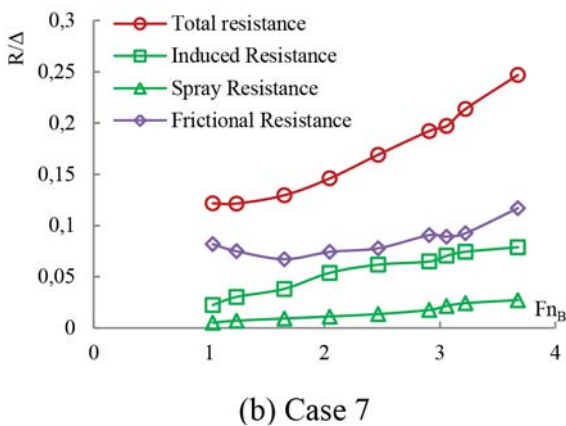
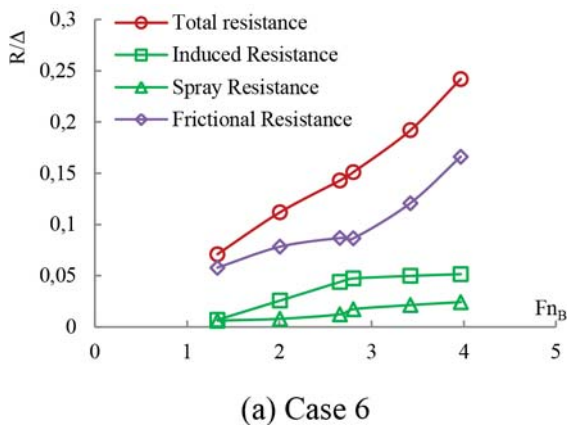


Fig. 14. Resistance components as  $Fn_B$  functions.

### 5. CONCLUSIONS

The paper presents a mathematical model to determine the performance of a hard chine boat in semi-planing and planing regimes. The model is based on the 2D+T theory and makes use of pressure distributions to determine the hydrodynamic forces. Transom effects are taken into account by using well-known empirical functions. Additionally, in the semi-planing regime, a special function is proposed to compute the non-dimensional length at which the transom effect begins. The trim angle and the keel wetted length of the boat are determined by satisfying the heave and pitch equations. This task is accomplished through an iterative process. Two guesses are taken into consideration with respect to the keel wetted length and the trim angle, and the final values are determined after a number of iterations.

The validity of the method was assessed using three different hull series. For each series, the trim angle and the resistance were computed and compared with the available experimental data. Two of these series represented prismatic boats, while the third series was a boat with variable deadrise angle in longitudinal direction. Overall, good accuracy has been observed in trim angle and resistance predictions, with similar trends between the computed results and experimental data.

The proposed method was also applied to study the variation of the hydrodynamic force as a function of the beam Froude number. It was demonstrated that the hydrodynamic component is very small at lower beam Froude numbers

(slightly larger than 1.0), and then significantly increases and dominates over the supporting force generated at the bottom. Moreover, different resistance components were analyzed. It is illustrated that the spray drag component increases with the increasing speed. It is also shown that the induced drag reaches a constant value.

The future work will extend the current method towards developing a model for maneuvering of hard-chine boats, where forward acceleration of the boat and motion in horizontal plane can be targeted. For this purpose, an attempt will be made to include the semi-planing range in the planned computation.

## REFERENCES

1. Abraham, J., Gorman, J., Reseghetti, F., et al., *Modeling and numerical simulation of the forces acting on a sphere during early-water entry*, Ocean Engineering, Vol. 76, 1-9, 2014.
2. Akers R.H.: *Dynamic Analysis of Planing Hulls in the Vertical Plane*, Proceedings of the Society of Naval Architects and Marine Engineers, New England Section, 1999.
3. Akers R.H.: 2014. *Advances in time-domain simulation of planing boats*. In: Proceedings of the Fourth Chesapeake Powerboat Symposium, Annapolis, MD, USA, 2014.
4. Algarin R., Tascon, O.: *Hydrodynamic Modeling of Planing Boats with Asymmetric and Steady Condition*, Proceedings of the 9th Conference on High Speed Marine Vehicles, Naples, Italy, 2011.
5. Algarin R., Tascon, O.: *Analysis of Dynamic Stability of Planing Craft on the Vertical Plane*, Ship Science and Technology, Vol. 8, No. 15, 2014.
6. Bertorello C, Olivero L.: *Hydrodynamic Resistance Assessment of non-mono-hedral planing hull forms based on Savitsky's methodology*, Australian Journal of Mechanical Engineering, Vol. 4, No. 2, 209-204, 2007.
7. Brizzolara S, Sera F. *Accuracy of CFD codes in the Prediction of planing surfaces hydrodynamic characteristics*. In: Proceedings of the 2nd International Conference on marine Research and Transportation, 2007.
8. Brizzolara S, Villa D., CFD simulation of planing hulls. In: Proceedings of the 7<sup>th</sup> International conference on High-Performance Marine Vehicles, Melbourne, Florida, USA, 2010.
9. Brogila R., Iafrafi A.: *Hydrodynamic of planing hulls in asymmetric conditions*. In: 28<sup>th</sup> Symposium on Naval Hydrodynamics Pasadena, California, 2010.
10. Facci, A.L., Panciroli, R., Ubertini, S., Porfiri, M.: *Assessment of PIV-based analysis of water entry problems through synthetic numerical datasets*, Journal of Fluids and Structures, Vol. 55, 484-500, 2015a.
11. Facci, A.L., Porfiri, M., Ubertini, S.: *Three-dimensional water entry of a solid body: A computational study*, Journal of Fluids and Structures, Vol. 66, 36-53, 2016.
12. Fairelie-Clarke, AC., Tvetnies T.: *Momentum and Gravity Effects During the Constant Velocity Water Entry of Wedge-Shaped Sections*, Ocean Engineering, Vol. 35, 2008.
13. Farsi, M., Ghadimi, P.: *Finding the best combination of numerical schemes for 2-D SPH simulation of wedge water entry for a wide range of deadrise angles*, International Journal of Naval Architecture and Ocean Engineering, Vol. 6, No. 3, 638-651, 2014a.
14. Farsi, M., Ghadimi, P., *Effect of flat deck on catamaran water entry through smoothed particle hydrodynamics*, Proceedings of the Institution of Mechanical Engineers Part M: Journal of Engineering for the Maritime Environment, Vol. 230, No. 2, 267-280, 2014b.
15. Farsi, M., Ghadimi, P.: *Simulation of 2D symmetry and asymmetry wedge water entry by smoothed particle hydrodynamics method*, Journal of the Brazilian Society of Mechanical Sciences and Engineering, Vol. 37, No. 3, 821-835, 2015.
16. Feizi Chekab, M.A., Ghadimi, P., Farsi, M.: *Investigation of three-dimensionality effects of aspect ratio on water impact of 3D objects using smoothed particle hydrodynamics method*, Journal of the Brazilian Society of Mechanical Sciences and Engineering, Vol. 38, No. 7, 1987-1997, 2016.
17. Fridsma G.: *A Systematic Study of the Rough-Water Performance of Planing Boats (PART I)*, Davidson Laboratory, Report No. 1275, 1969.
18. Garme K.: *Improved Time Domain Simulation of Planing Hulls in Waves by Correction of Near-Transom Lift*, International Journal of Shipbuilding Progress, Vol. 52, No. 3, 2005.
19. Garme K., Rosen A.: *Time domain simulations and full-scale trials on planing crafts in waves*, International Shipbuilding progress, Vol. 50, No. 3, 177-208, 2003.
20. Garo R., Datla R., Imas L.: *Numerical simulation of planing hull hydrodynamics*. In: Proceedings of the Third Chesapeake Powerboat Symposium, Annapolis, MD, USA, 2012.
21. Ghadimi, P., Saadatkhah, A., Dashtimanesh, A.: *Analytical solution of wedge water entry by using Schwartz-Christoffel conformal mapping*, International Journal of Modeling, Simulation, and Scientific Computing, Vol. 2, No. 3,

- 337-354, 2011.
22. Ghadimi P., Dashtimanesh A., Djeddi S.R.: *Study of water entry of circular cylinder by using analytical and numerical solutions*, Journal of Brazilian Society of Mechanical Sciences and Engineering, Vol. 34, No. 3, 225-232, 2012.
  23. Ghadimi, P., Feizi Chekab, M.A., Dashtimanesh, A.: *A numerical investigation of the water impact of an arbitrary bow section*, ISH Journal of Hydraulic Engineering, Vol. 19, No. 3, 186-195, 2013.
  24. Ghadimi, P., Feizi Chekab, M.A., Dashtimanesh, A.: *Numerical simulation of water entry of different arbitrary bow sections*, Journal of Naval Architecture and Marine Engineering, Vol. 11, No. 2, 117-129, 2014a.
  25. Ghadimi P., Tavakoli S., Dashtimanesh A., Pirooz A.: *Developing a computer program for detailed study of planing hull's spray based on Morabito's approach*. *Journal of Marine Science and Application*. Vol. 13, No. 4, 402-415. 2014b.
  26. Ghadimi P., Tavakoli S., Feizi Chakab M. A., Dashtimanesh A.: *Introducing a particular mathematical model for predicting the resistance and performance of prismatic planing hulls in calm water by means of total pressure distribution*, Journal of Naval Architecture and Marine Engineering, Vol. 12, No. 2, 73-94, 2015.
  27. Ghadimi P., Tavakoli S., Dashtimanesh A. Zamanian R.: *Steady performance prediction of a heeled planing boat in calm water using asymmetric 2D+T model*, Proceedings of the Institution of Mechanical Engineers, Part M: Journal of Engineering for the Maritime Environment, Published Online: 2016a. DOI: 10.1177/1475090216638680.
  28. Ghadimi P, Tavakoli S, Dashtimanesh A.: *Coupled heave and pitch motions of planing hulls at non-zero heel angle*. *Applied Ocean Research*, Vol. 59, 286-303, 2016b.
  29. Ghadimi P., Tavakoli S., Dashtimanesh A.: *An analytical procedure for time domain simulation of roll motion of the warped planing hulls*. Proceedings of the Institution of Mechanical Engineers, Part M: Journal of Engineering for the Maritime Environment, 230(4), 600-615, 2016c.
  30. Ghadimi P, Tavakoli S, Dashtimanesh A. A non-linear mathematical model for coupled heave, pitch and roll motions of a high-speed planing hull, *Journal of Engineering Mathematics*. Published Online, 2016d. 10.1007/s10665-016-9878-2.10.1007/s10665-016-9878-2.
  31. Haase H., Soproni J.P., Abdel-Maksoud M.: *Numerical analysis of a planing boat in head waves using 2D+T method*. *Ship Technology Research*, 62(3), 131-139, 2015.
  32. ITTC: *Report of Resistance Committee*, 8th International Towing Tank, Madrid, Spain, 1957.
  33. Conference, Venice, 2002.
  34. Jiang Y., Zou, J., Hu, A., Yang J.; *Analysis of tunnel hydrodynamic characteristics for planing trimaran by model test and numerical simulations*, *Ocean Engineering*, Vol. 13, 101-110, 2016.
  35. Judge C., Troesch A., Perlin M.: *Initial water Impact of a wedge at Vertical and Oblique Angles*, *Journal of Engineering Mathematics*, Vol. 48, 2004.
  36. Kanyoo P., Taunton D., Blake J.I.: *Development and optimization of mathematical model of high speed planing hulls*. In: *Proceedings of the 13<sup>th</sup> International Conference on Fast Sea Transportation (FAST 2015)*, DC, USA, 2015.
  37. Katayama T., Fujimoto M., Ikeda Y.: *A study in transverse stability loss of planing craft at super high forward speed*. In: *Proceedings of the 9<sup>th</sup> International Conference on Stability of Ships and Ocean Vehicles*, Rio de Janeiro, Brazil, 2006.
  38. Korobkin A.A.: *A linearized model of water exit*. *Journal of Fluid Mechanics*, 737, 368-386, 2013.
  39. Korobkin A.A., Melenica S.: *Modified Logvinovic model for hydrodynamic loads on asymmetric contours entering water*. In: *Proceedings of the 20<sup>th</sup> International Workshop on Water Waves and Floating Bodies*, Oslo, Norway, 2005.
  40. Krovin-Kroukovsky B.V., Savitsky D., William L.: *Wave contours in the wake of a 20° deadrise planing surface*. Davidson Laboratory, Report No. 337, 1949.
  41. Kim D.J., Rhee K.P., You Y.J.: *Theoretical Prediction of Running Attitudes of a Semi-Displacement Round Bilge Vessel at High Speed*, *Applied Ocean Research*, Vol. 42, 2013.
  42. Maki K.J., Lee D., Troesch AW., Vlahopoulos N.: *Hydroelastic impact of a wedge-shaped body*. *Ocean Engineering*, Vol. 38, 621-629.
  43. Martin M.: *Theoretical determination of porpoising instability of high-speed planing boat*. David Taylor Naval Ship Research and Development Center, Report No. 76-0068, 1976a.
  44. Martin M.: *Theoretical prediction of motion of high-speed planing boats in waves*. David Taylor Naval Ship Research and Development Center, Report No. 76-0069, 1976b.
  45. Mei X., Liu Y., *On the water impact of general two-dimensional sections*, *Applied Ocean Research*, Vol. 21, No. 1, 21-15, 1999.

46. Mercier J.A., Savitsky D.: *Resistance of Transom Shear Craft in the Pre-planing Range*, Davison Laboratory, Report No. 1667, Hoboken, NJ, USA, 1973.
47. Metcalf B.J., Faul L., Bumiller E., Slutsky, J.: *Resistance Tests of a Systematic Series of US Coast Guard of Planing Hulls*, NSWCCd-50-TR-2005/063, 2005.
48. Milwitzky B. 1948. A generalized theoretical and experimental investigation of the motions and hydrodynamic loads experienced by V-bottom seaplanes during step-landing impact. NACA TN 1516.
49. Morabito M.G.; *On the spray and bottom pressures of planing surfaces*, PhD Thesis, Stevens Institute of Technology, Hoboken, NJ, USA.
50. Morabito, M.G.; *Empirical Equations for Planing Hull Pressure Distributions*. Journal of Ship Research, Vol. 58, No. 3, 2014.
51. Morabito M.G.: *Prediction of Planing Hull Side Forces in Yaw Using Slender Body Oblique Impact Theory*, Ocean Engineering, Vol. 101, 2015.
52. Mousaviraad, S.M., Wang, Z., Stern, F.: *URANS studies of hydrodynamic performance and slamming loads on high-speed planing hulls in calm water and waves for deep and shallow conditions*, Applied Ocean Research, Vol. 51, 222-240, 2015.
53. Nguyen, V.-T., Park, W.-G.: *A free surface flow solver for complex three-dimensional water impact problems based on the VOF method*, International Journal for Numerical Methods in Fluids, Vol. 82, No. 1, 3-34, 2016.
54. Piro D.J., Maki K.J.: *Hydroelastic analysis of bodies that enter and exit water*, Journal of Fluids and Structures, Vol. 37, 134-150, 2013.
55. Riccardi G, Iafrati A.: *Water impact of an asymmetric floating wedge*. Journal of Engineering Mathematics, Vol. 49, 19-39, 2003.
56. Savitsky D.: *Hydrodynamic Design of Planing Hulls*, Marine Technology, Vol. 1, No. 1, 1964.
57. Savitsky D.; *The Effect of Bottom Warp on the Performance of Planing Hulls*, Proceedings of the third SNAME Chesapeake Powerboat Symposium, Annapolis, 2011.
58. Savitsky D., Brown W.: *Procedures for Hydrodynamic Evaluation of Planing Hulls in Smooth and Rough Water*, Marine Technology, Vol. 13, No. 4, 1978.
59. Savitsky D., Morabito M.: *Origin and characteristics of the spray patterns generated by planing hulls*, Journal of Ship Production, Vol. 27, No. 2, 63-83.
60. Savitsky D., DeLorme M. F., Datla R.; *Inclusion of Whisker Spray Drag in Performance Prediction Method for High-Speed Planing Hulls*, Marine Technology, Vol. 44, No. 1, 2007.
61. Savander BR.: *Planing hull steady hydrodynamics*. PhD Thesis. University of Michigan, Ann Arbor, Michigan, USA, 1997.
62. Sebastiani L., Bruzzone D., Gualeni P., et al.: *A practical method for the prediction of planing craft motions in regular and irregular waves*. In: Proceedings of the ASME 27<sup>th</sup> International Conference on Offshore Mechanics and Arctic Engineering, Estoril, Portugal, 2008.
63. Schachter RD, Riberio HJC.: *Dynamic equilibrium evaluation for planing hulls with arbitrary geometry and variable deadrise angles – The virtual prismatic hulls method*, Ocean Engineering, Vol. 115, 67-92, 2016.
64. Schnitzer E, 1952. Theory and procedure for determining loads and motions in chine-immersed hydrodynamic impacts. NACA TN 2813.
65. Shademani, R., Ghadimi, P.: *Estimation of water entry forces, spray parameters and secondary impact of fixed width wedges at extreme angles using finite element based finite volume and volume of fluid methods*, Brodogradnja, Vol. 67, No. 1, 101-124, 2016.
66. Sun H., Faltinsen O.M.: *Dynamic motions of planing vessels in head seas*. Journal of Marine Science and Technology, Vol. 16, 168-180, 2011.
67. Sun H., Faltinsen O.M.: *Hydrodynamic Forces on a Semi-Displacement Ship at High Speed*, Applied Ocean Research, Vol. 34, 2012.
68. Tascon O.D., Troesch A.W., Maki K.J.: *Numerical computation of hydrodynamic forces acting on a maneuvering planing hull via slender body theory-SBT and 2-D impact theory*. In: Proceedings of the 10<sup>th</sup> International Conference on Fast Sea Transportation (FAST 2009), Athens, Greece, 2009.
69. Tassin A., Korobkin AA., Cooker M.J.: *On analytical models of vertical water entry of symmetric body with separation and cavity initiation*. Applied Ocean Research, 48, 33-41, 2014.
70. Tavakoli S., Ghadimi P., Dashtimanesh A., Sahoo P.K.: *Determination of Hydrodynamic Coefficients Related to Roll Motion of High-Speed Planing Hulls*, Proceedings of the 13<sup>th</sup> International Conference on Fast Sea Transportation, DC, USA, 2015.

71. Radojčić D., Zgradić A., Kalajdžić M., Simić, A., *Resistance Prediction for Hard-Chine Hulls in the Pre-Planing Regime*, Polish Maritime Research, Vol. 21, 2014a.
72. Radojčić D., Morabito M.G., Simić A. P., Zgradić A.B.: Modeling with regression analysis and artificial neural networks the resistance and trim of series 50 experiments with V-bottom motor boats, *Journal of Ship Production and Design*, Vol. 30, No. 4, 153-174, 2014b.
73. von Karman T.: *The impact on Seaplane Floats During Landing*, NACA TN 321.
74. Vorus SW.: *A flat cylinder theory for vessel impact and steady planing*, J. Ship Research, Vol. 40, No. 2, 89-106, 1996.
75. Wagner H.: *Phenomena Associated with Impacts and Sliding on Liquid Surface*, NACA Translation of Uber Stoss- und Gleitvorgänge an der Oberfläche von Flüssigkeiten. Zeitschr. Angew. Math. Mech, Vol. 12, No. 4, 1932.
76. Xu L., Troesch A.W.; *A study on hydrodynamic of asymmetric planing surfaces*. In: Proceedings of the 5<sup>th</sup> International Conference on Fast Sea Transportation (FAST 99), Seattle, Washington, USA, 1999.
77. Xu L., Troesch A.W., Peterson R.: *Asymmetric hydrodynamic impact and dynamic response of vessels*. Journal of Offshore Mechanics and Arctic Engineering, Vol. 121, 83-89: 1999.
78. Yettou E.M., Derochers A., Champoux, Y.: *A new analytical model for pressure estimation of symmetrical water impact of a rigid wedge at variable velocities*, Journal of Fluids and Structures, Vol. 23, 502-522, 2007.
79. Zarnickh E.E.: *A nonlinear mathematical model of motions of a planing boat in regular waves*. David Taylor Naval Ship Research and Development Center, Report No. 78/032, 1978.
80. Zarnickh E.E.: *A nonlinear mathematical model of motions of a planing boat in irregular waves*. David Taylor Naval Ship Research and Development Center, Report No. SPD-0867-01, 1979.
81. Zhao R., Faltinsen O. M.: *Water entry of two-dimensional bodies*. Journal of Fluid Mechanics, Vol. 246, 593-612, 1993.
82. Zhao R., Faltinsen O. M., Haslum H.A.: *A simplified nonlinear analysis of a high-speed planing craft in calm water*. In: Proceedings of the 4<sup>th</sup> International Conference on Fast Sea Transportation (FAST 97), Sydney, Australia, 1997.

## APPENDIX A: A WORKED EXAMPLE

A particular case of US Coast Guard boat series (Case 5629-1) is hereby considered to move forward at a beam Froude Number of 2.2. The boat is first divided into  $n$  sections (here,  $n = 21$ ). The deadrise angle and the beam of each considered section are displayed in Table A. 1.

The initial trim angle (4.1 deg for this case) and the keel wetted length (0.5L for this case) are guessed. Subsequently, the 3D problem is changed to a 2D problem. From the intersection of the keel and calm water to the transom location,  $m$  sections are considered (here,  $m = 51$ ). The longitudinal distance of each section from the keel/calm water intersection is determined. Then, the half beam (column 2) of each section and its deadrise angles (column 3) are computed. The chine depth of each section is found using the formula  $\frac{B}{2} \tan \beta$  and the time of chine wetting of each section is then computed from Equation 9 (column 5). The corresponding solution time for each section is then determined using the formula  $x/\cos \tau)/U$  (column 6). Afterward, it is checked to see if the time  $t$  of each section is longer or shorter than the chine wetting time. In the latter condition the section experiences phase 1 (i.e. dry chine phase); otherwise it experiences phase 2 (i.e. wet chine phase). Later, depending on the phase, Equations (5) through (8) are utilized to find  $c$  and  $\dot{c}$  (columns 8 and 9).

Table A. 1. The deadrise angle and beam of each section.

Distance of section from transom (m)	Beam of section (m)	Deadrise angle of section (deg)
0	0.76	16.61
0.1524	0.76	16.61
0.3048	0.76	16.61
0.4572	0.76	16.61
0.6096	0.76	16.61
0.762	0.76	16.61
0.9144	0.76	16.61
1.0668	0.76	16.61
1.2192	0.76	16.61
1.3716	0.76	16.61
1.524	0.76	16.61
1.6764	0.76	16.61
1.8288	0.76	16.61
1.9812	0.76	16.61
2.1336	0.76	16.61
2.286	0.76	16.61
2.4384	0.76	16.61
2.5908	0.76	16.61
2.7432	0.76	16.61
2.8956	0.76	16.61
3.048	0.76	16.61

Table A. 2. Sectional characteristics after guessing the keel wetted length.

$x$ (m)	$B/2$ (m)	(deg)	$\frac{B}{2} \tan \beta$	$t_{cw}(s)$	$t$ (s)	Phase (1 or 2?)	$c$ (m)	$\dot{c}$ (m/s)
0	0.38	16.61	0.113355	0	0	1	0	0
0.03048	0.38	16.61	0.113355	0.167372	0.005054	1	0.011475	2.270389
0.06096	0.38	16.61	0.113355	0.167372	0.010109	1	0.022951	2.270389
0.09144	0.38	16.61	0.113355	0.167372	0.015163	1	0.034426	2.270389
0.12192	0.38	16.61	0.113355	0.167372	0.020217	1	0.045902	2.270389
0.1524	0.38	16.61	0.113355	0.167372	0.025272	1	0.057377	2.270389
0.18288	0.38	16.61	0.113355	0.167372	0.030326	1	0.068852	2.270389
0.21336	0.38	16.61	0.113355	0.167372	0.035381	1	0.080328	2.270389
0.24384	0.38	16.61	0.113355	0.167372	0.040435	1	0.091803	2.270389
0.27432	0.38	16.61	0.113355	0.167372	0.045489	1	0.103279	2.270389
0.3048	0.38	16.61	0.113355	0.167372	0.050544	1	0.114754	2.270389
0.33528	0.38	16.61	0.113355	0.167372	0.055598	1	0.126229	2.270389
0.36576	0.38	16.61	0.113355	0.167372	0.060652	1	0.137705	2.270389
0.39624	0.38	16.61	0.113355	0.167372	0.065707	1	0.14918	2.270389

0.42672	0.38	16.61	0.113355	0.167372	0.070761	1	0.160656	2.270389
0.4572	0.38	16.61	0.113355	0.167372	0.075816	1	0.172131	2.270389
0.48768	0.38	16.61	0.113355	0.167372	0.08087	1	0.183606	2.270389
0.51816	0.38	16.61	0.113355	0.167372	0.085924	1	0.195082	2.270389
0.54864	0.38	16.61	0.113355	0.167372	0.090979	1	0.206557	2.270389
0.57912	0.38	16.61	0.113355	0.167372	0.096033	1	0.218033	2.270389
0.6096	0.38	16.61	0.113355	0.167372	0.101087	1	0.229508	2.270389
0.64008	0.38	16.61	0.113355	0.167372	0.106142	1	0.240983	2.270389
0.67056	0.38	16.61	0.113355	0.167372	0.111196	1	0.252459	2.270389
0.70104	0.38	16.61	0.113355	0.167372	0.116251	1	0.263934	2.270389
0.73152	0.38	16.61	0.113355	0.167372	0.121305	1	0.27541	2.270389
0.762	0.38	16.61	0.113355	0.167372	0.126359	1	0.286885	2.270389
0.79248	0.38	16.61	0.113355	0.167372	0.131414	1	0.29836	2.270389
0.82296	0.38	16.61	0.113355	0.167372	0.136468	1	0.309836	2.270389
0.85344	0.38	16.61	0.113355	0.167372	0.141522	1	0.321311	2.270389
0.88392	0.38	16.61	0.113355	0.167372	0.146577	1	0.332787	2.270389
0.9144	0.38	16.61	0.113355	0.167372	0.151631	1	0.344262	2.270389
0.94488	0.38	16.61	0.113355	0.167372	0.156686	1	0.355737	2.270389
0.97536	0.38	16.61	0.113355	0.167372	0.16174	1	0.367213	2.270389
1.00584	0.38	16.61	0.113355	0.167372	0.166794	1	0.378688	2.270389
1.03632	0.38	16.61	0.113355	0.167372	0.171849	2	0.382988	1.702286
1.0668	0.38	16.61	0.113355	0.167372	0.176903	2	0.386488	1.142161
1.09728	0.38	16.61	0.113355	0.167372	0.181957	2	0.389188	0.951451
1.12776	0.38	16.61	0.113355	0.167372	0.187012	2	0.391488	0.844632
1.15824	0.38	16.61	0.113355	0.167372	0.192066	2	0.393588	0.771434
1.18872	0.38	16.61	0.113355	0.167372	0.197121	2	0.395488	0.718216
1.2192	0.38	16.61	0.113355	0.167372	0.202175	2	0.397388	0.673775
1.24968	0.38	16.61	0.113355	0.167372	0.207229	2	0.399088	0.639634
1.28016	0.38	16.61	0.113355	0.167372	0.212284	2	0.400688	0.611321
1.31064	0.38	16.61	0.113355	0.167372	0.217338	2	0.402288	0.586028
1.34112	0.38	16.61	0.113355	0.167372	0.222392	2	0.403788	0.564602
1.3716	0.38	16.61	0.113355	0.167372	0.227447	2	0.405288	0.545053
1.40208	0.38	16.61	0.113355	0.167372	0.232501	2	0.406688	0.528267
1.43256	0.38	16.61	0.113355	0.167372	0.237556	2	0.408088	0.512711
1.46304	0.38	16.61	0.113355	0.167372	0.24261	2	0.409388	0.499239
1.49352	0.38	16.61	0.113355	0.167372	0.247664	2	0.410688	0.486604
1.524	0.38	16.61	0.113355	0.167372	0.252719	2	0.411988	0.474719

The pressure distributions are computed in all sections using the Bernoulli equation (Equation (4)), after which the hydrodynamic force acting on each section is found. As an example, Fig. A. 1 shows the pressure distributions in four different sections: two for phase 1 and two for phase 2.

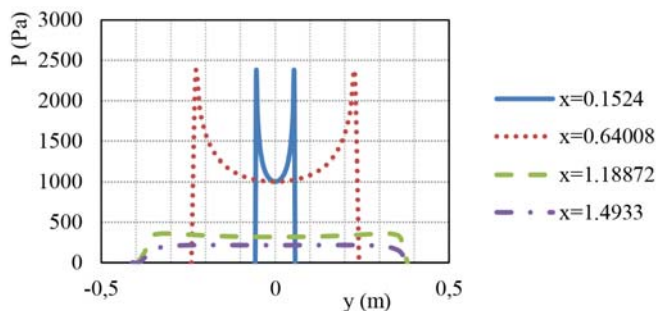


Fig. A. 1. Examples of computed pressure distributions in four different sections.

Using Equations (10) through (12), the hydrodynamic and hydrostatic forces acting on each section are computed (columns 2 and 3 in Table A. 3.). Then, the reduction magnitude in each section is computed using Equations (19) through (21) (column (4) in Table A. 3). This reduction is implemented to the sectional forces, and their values, after correction, are re-computed (columns (5) and (6) in Table A. 3). For better clarity, Fig. A. 2 shows the distributions of sectional forces in the longitudinal direction. The curves in this figure show the distributions before and after implementation of the reduction function.

Table A. 3. Sectional forces.

$x$ (m)	$f_B^{2D}$ (N/m) Without reduction	$f_{HD}^{2D}$ (N/m) Without reduction	R( $\xi$ )	$f_B^{2D}$ (N/m) With reduction	$f_{HD}^{2D}$ (N/m) With reduction
0	0	0	1	0	0
0.03048	0.160083	29.56091	0.999996	0.160083	29.56079
0.06096	0.640333	59.12181	0.999995	0.64033	59.1215
0.09144	1.44075	88.68272	0.999993	1.44074	88.6821
0.12192	2.561334	118.2436	0.999991	2.561311	118.2425
0.1524	4.002084	147.8045	0.999988	4.002037	147.8028
0.18288	5.763001	177.3654	0.999984	5.762912	177.3627
0.21336	7.844085	206.9263	0.99998	7.843926	206.9221
0.24384	10.24534	236.4872	0.999973	10.24506	236.481
0.27432	12.96675	266.0482	0.999965	12.9663	266.0389
0.3048	16.00834	295.6091	0.999955	16.00761	295.5957
0.33528	19.37009	325.17	0.999941	19.36894	325.1507
0.36576	23.052	354.7309	0.999923	23.05022	354.7034
0.39624	27.05409	384.2918	0.999899	27.05136	384.2529
0.42672	31.37634	413.8527	0.999868	31.3722	413.798
0.4572	36.01876	443.4136	0.999828	36.01255	443.3371
0.48768	40.98134	472.9745	0.999775	40.97211	472.8679
0.51816	46.26409	502.5354	0.999706	46.25047	502.3874
0.54864	51.86701	532.0963	0.999615	51.84706	531.8916
0.57912	57.7901	561.6572	0.999497	57.76105	561.375
0.6096	64.03335	591.2181	0.999343	63.99131	590.83
0.64008	70.59677	620.779	0.999142	70.53622	620.2466
0.67056	77.48035	650.3399	0.99888	77.39354	649.6113
0.70104	84.6841	679.9008	0.998536	84.56016	678.9057
0.73152	92.20802	709.4617	0.998088	92.03173	708.1054
0.762	100.0521	739.0226	0.997503	99.80226	737.1772
0.79248	108.2164	768.5836	0.996739	107.8634	766.0769
0.82296	116.7008	798.1445	0.995741	116.2037	794.7451
0.85344	125.5054	827.7054	0.994439	124.8074	823.1026
0.88392	134.6301	857.2663	0.992741	133.6528	851.0431
0.9144	144.075	886.8272	0.990526	142.7101	878.4253
0.94488	153.8401	916.3881	0.98764	151.9386	905.0613
0.97536	163.9254	945.949	0.983881	161.2831	930.7016
1.00584	174.3308	975.5099	0.978992	170.6685	955.0167
1.03632	185.0564	712.8405	0.972641	179.9934	693.3377
1.0668	196.1021	452.3537	0.964403	189.1216	436.2514

$x$ (m)	$f_B^{2D}$ (N/m) Without reduction	$f_{HD}^{2D}$ (N/m) Without reduction	R( $\xi$ )	$f_B^{2D}$ (N/m) With reduction	$f_{HD}^{2D}$ (N/m) With reduction
1.09728	207.468	364.6209	0.953744	197.8714	347.755
1.12776	219.1541	315.8852	0.939991	206.0028	296.9291
1.15824	231.1604	282.7139	0.92231	213.2015	260.7498
1.18872	243.4868	258.7345	0.89969	219.0625	232.7807
1.2192	256.1334	238.8104	0.870925	223.073	207.986
1.24968	269.1001	223.5712	0.834631	224.5992	186.5993
1.28016	282.3871	211.6077	0.78928	222.8824	167.0177
1.31064	295.9941	201.1609	0.7333	217.0525	147.5113
1.34112	309.9214	192.3461	0.665231	206.1693	127.9546
1.3716	324.1688	184.3318	0.583959	189.3012	107.6422
1.40208	338.7364	177.4726	0.489011	165.6457	86.78602
1.43256	353.6242	171.1347	0.380864	134.6826	65.17898
1.46304	368.8321	165.6608	0.261185	96.33339	43.2681
1.49352	384.3602	160.539	0.132899	51.08109	21.33548
1.524	400.2084	155.733	0	0	0

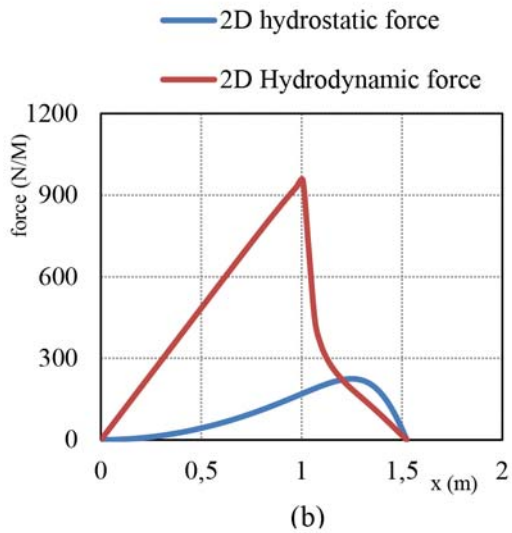
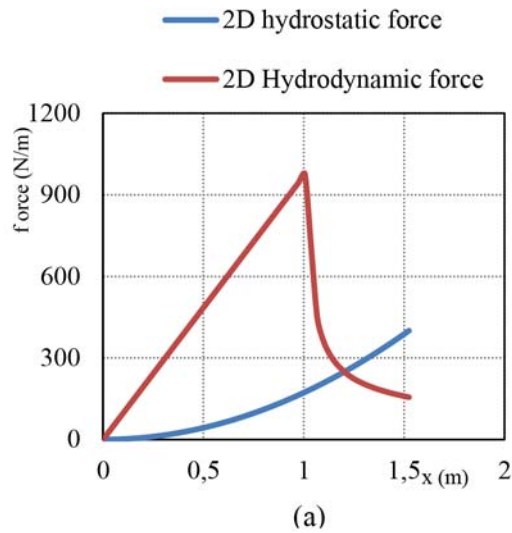


Fig. A. 2. Distribution of 2D sectional forces in longitudinal direction: without (a) and with (b) implementation of transom reduction.

The final three dimensional hydrodynamic and hydrostatic forces are subsequently found by integrating the sectional forces. Here, the trapezoidal integration method is used. It is shown that heave equation is satisfied ( $\Delta-L=0$ ) by checking the error for the heave force (Table A. 4.).

Table A. 4. Checking the heave force error for the guessed keel wetted length.

$F_{HD} = \int_{L_k} R(\xi) f_{HD}^{2D} \cos \tau d \xi, (N)$	606.0244
$F_b = \int_{L_k} R(\xi) f_b^{2D} d \xi, (N)$	149.8464
$L = F_b + F_{HD} (N)$	755.8708
$\varepsilon = \Delta - L (N)$	-592.1618

If the heave force error is negative the wetted length should be increased, if positive - it should be decreased. In the current example the keel wetted length is considered to increase by 0.2 m in each iteration. The results are shown in Table A. 5.

We can observe that after four iterations the error changes from negative to positive. Therefore, the correct keel wetted length is between 2.124 m and 2.324 m. Using mathematical computations, the keel wetted length for which the error approximately equals zero is found to be 2.246 m.

Table A. 5. Heave force error for different keel wetted lengths at  $\tau=4.1$ .

No. of iteration	1	2	3	4	5
LK(m)	1.524	1.724	1.924	2.124	2.324
$\varepsilon$ (m)	-592.162	-480.961	-358.071	-99.2996	63.23946

For the current wetted length, similar characteristics to those shown in Table A. 2 to A. 3 are calculated again. Then, the distance of each section from the CG is found as  $\xi = -(x - L_k + LCG)$  and the sectional moments due to 2D hydrodynamic and hydrostatic forces are determined, as displayed in Table A. 6.

Table A. 6. Sectional pitch moment.

$x(m)$	$\xi(m)$	$\int_{L_k} R(\xi) f_{HD}^{2D} \xi d \xi$	$\int_{L_k} R(\xi) f_b^{2D} \xi d \xi$
0	1.2648	0	0
0.04492	1.21988	45.43183	0.362588
0.08984	1.17496	86.94973	1.387879
0.13476	1.13004	124.5537	2.982162
0.17968	1.08512	158.2438	5.051727
0.2246	1.0402	188.0199	7.502864
0.26952	0.99528	213.8821	10.24186
0.31444	0.95036	235.8304	13.17501
0.35936	0.90544	253.8647	16.2086
0.40428	0.86052	267.9852	19.24893
0.4492	0.8156	278.1917	22.20227
0.49412	0.77068	284.4842	24.97492
0.53904	0.72576	286.8628	27.47317
0.58396	0.68084	285.3275	29.60331
0.62888	0.63592	279.8782	31.27162
0.6738	0.591	270.5149	32.3844
0.71872	0.54608	257.2377	32.84792
0.76364	0.50116	240.0465	32.56848
0.80856	0.45624	218.9412	31.45236
0.85348	0.41132	193.922	29.40586
0.8984	0.3664	164.9888	26.33526
0.94332	0.32148	132.1417	22.14687
0.98824	0.27656	95.38093	16.74702
1.03316	0.23164	42.45897	10.04207
1.07808	0.18672	3.986295	1.938486
1.123	0.1418	-11.3413	-7.65713
1.16792	0.09688	-21.9333	-18.8379
1.21284	0.05196	-30.3857	-31.6964
1.25776	0.00704	-37.4706	-46.3246
1.30268	-0.03788	-43.785	-62.8127
1.3476	-0.0828	-49.5471	-81.2486
1.39252	-0.12772	-54.6439	-101.716
1.43744	-0.17264	-59.4799	-124.292
1.48236	-0.21756	-63.8394	-149.043
1.52728	-0.26248	-67.9264	-176.013
1.5722	-0.3074	-71.777	-205.219
1.61712	-0.35232	-75.2482	-236.625
1.66204	-0.39724	-78.4912	-270.113

$x(m)$	$\xi (m)$	$\int_{L_k} R(\xi) f_{HD}^{2D} \xi d\xi$	$\int_{L_k} R(\xi) f_B^{2D} \xi d\xi$
1.70696	-0.44216	-81.3138	-305.433
1.75188	-0.48708	-83.7293	-342.126
1.7968	-0.532	-85.7825	-379.403
1.84172	-0.57692	-87.0684	-415.974
1.88664	-0.62184	-87.4731	-449.803
1.93156	-0.66676	-86.477	-477.786
1.97648	-0.71168	-83.5914	-495.41
2.0214	-0.7566	-78.2191	-496.486
2.06632	-0.80152	-69.8245	-473.243
2.11124	-0.84644	-57.7197	-417.153
2.15616	-0.89136	-41.6833	-320.824
2.20108	-0.93628	-22.0829	-180.785
2.246	-0.9812	0	0

The centers of hydrodynamic and hydrostatic pressure are computed using Equations (15) and (18). For the current condition ( $L_k=2.246$ ), it is shown that  $LC_{HD}=0.1944$  m and  $LC_B=-0.49$  m. Subsequently, it is checked whether or not the pitch equation is satisfied. The computed values are displayed in Table A. 7. An error associated with the pitch moment is calculated again. When this error is negative the trim angle should decrease; otherwise it should increase.

Table A. 7. Checking the pitch equation error.

$LC_{HD}$ (m)	-0.49
$LC_B$ (m)	0.1944
$M_B$ (N-m)	-260.697
$M_{HD}$ (N-m)	159.6667
$\varepsilon=M_{HD}-M_B$ (N-m)	-101.03

#### APPENDIX A.1: THE COMPUTED TRIM ANGLE AND ITS CORRELATION WITH EXPERIMENTAL DATA

For the initial trim angle of 4.1, the error associated with the pitch moment is equal to -101.03. Therefore, a new trim angle is guessed and the keel wetted length related to this trim angle is computed again (by producing similar tables to Table A. 2. through A. 5). Then, the error of satisfying the pitch equation by each guess is checked. As the sign of the error changes, the correct trim angle is to be between the last two guesses. At this stage, the trim angle is re-guessed by the 0.2 step size and the correct trim angle is found to be between 3.5 and 3.3, since the error changes sign when the trim is changed from 3.5 to 3.3 (Table A. 8). Using mathematical computations, the correct trim angle is estimated to be 3.352 and the keel wetted length is approximated to be 2.583. It should be noted that the trim angle measured by Metcalf et al. (2005) for this condition has been reported to be equal to about 3.13 degrees. Accordingly, the resultant error of 7.7% testifies to good accuracy of the proposed method.

Table A. 8. Errors for different trim angles.

No. Iteration	1	2	3	4	5
$\tau$ (deg)	4.1	3.9	3.7	3.5	3.3
$L_k$ (m)	2.246186	2.42528	2.411342	2.535468	2.610539
$\mathcal{E}$ (N-m)	-101.03	-49.784	-49.046	-13.1948	4.684451

#### CONTACT WITH THE AUTHOR

Parviz Ghadimi

*e-mail: pghadimi@aut.ac.ir*

Amirkabir University of Technology  
424 Hafez Ave.  
3314 Tehran

ISLAMIC REPUBLIC OF IRAN

# NUMERICAL PREDICTION OF WAVE PATTERNS DUE TO MOTION OF 3D BODIES BY KELVIN-HAVELOCK SOURCES

Hassan Ghassemi, Prof.

Isar Ghamari, Ph.D.

Arash Ashrafi, M.Sc.

AmirKabir University of Technology, Iran

## ABSTRACT

*This paper discusses the numerical evaluation of the hydrodynamic characteristics of submerged and surface piercing moving bodies. Generally, two main classes of potential methods are used for hydrodynamic characteristic analysis of steady moving bodies which are Rankine and Kelvin-Havelock singularity distribution. In this paper, the Kelvin-Havelock sources are used for simulating the moving bodies and then free surface wave patterns are obtained. Numerical evaluation of potential distribution of a Kelvin-Havelock source is completely presented and discussed. Numerical results are calculated and presented for a 2D cylinder, single source, two parallel moving source, sphere, ellipsoid and standard Wigley hull in different situation that show acceptable agreement with results of other literatures or experiments.*

**Keywords:** Free Surface Waves, Boundary Element Method (BEM), Kelvin-Havelock Source

## INTRODUCTION

A number of numerical methods for computing free-surface flows of ship forms are presented as robust and accurate on the basis of favorable comparisons between numerical predictions and experimental measurements. As a matter of fact, numerical predictions of free-surface flows about ship forms, including the steady-flow case of specific interest here, are notoriously unreliable, as is documented in Andrew et al. [1], Newman [3-4], Chen and Noblesse [4], Telste, and Noblesse [5], Hendrix and Noblesse [6]. Other trends of ship hydrodynamics including wave resistance in calm water were reviewed in Bulgarelli et al. [7]. On the other hand, some historical perspectives and reflections of ship waves were given by Tulin [8]. Compressive description on the ship resistance computations have been presented by Larrson and Baba [9]. Comparison of different approach for the ship resistance calculations carried out by Gatchell et al [10]. A 3D linear analysis of steady ship motion in deep water have presented in the Ph.D. dissertation [11]. Baar and Price also contain extensive comparisons of the authors own Kelvin-Havelock numerical predictions with experimental data [12].

A desingularized boundary integral method for fully nonlinear free-surface problems was described Cao et.al. [13]. An integral boundary element method (Rankine panel) to solve the flow around surface piercing hydrofoils and ships was presented by Hsin et.al. [14] as well as two iterative procedures for small and large Froude numbers were presented for fully submerged two dimensional hydrofoils under a free surface by Yasko et.al.[15]. Ghassemi et al. [16] and Ghassemi & Kohansal [17] have presented the nonlinear generated wave pattern due to three dimensional moving bodies. More detail formulae for 2D and 3D free surface flows due to moving disturbances have been presented by Tuck et al [18], Parau & Vanden-Broeck [19] and Uslu & Bal [20]. Javanmardi et al worked the prediction of wave patterns at large distances from a moving body in a confined channel [21]. In order to minimize the total resistance of a ship, an optimization of the hull shape investigated by Sun et al [22] and Zakerdoost et al [23]. The total resistance is assumed to be the sum of the wave resistance computed on the basis of the thin-ship theory and the frictional resistance. Smoothness of hull lines is proved with mathematical procedure, in which differentials of the hull lines functions are analyzed. The

wave-making resistance optimization, involving a genetic algorithm, uses Michell integral to calculate wave resistance. Recently, the computational results for KRISO Container Ship (KCS) are presented. CFD analyses are performed to simulate free surface flow around KCS by using RANS approach with success. Also, the complicated turbulent flow zone behind the ship is well simulated [24].

A major difficulty of the Kelvin-Havelock approach resides in the mathematical complexity of the corresponding Green function, often referred to as the Kelvin-Havelock source. Indeed, the complexity of the Kelvin-Havelock source and the simplicity of the Rankine source no doubt are major recommendations for using the Rankine-source approach. However, the Kelvin-Havelock source offers several important advantages compared with the Rankine source. In particular, the radiation condition that steady gravity waves do not exist ahead of a moving ship is automatically and exactly satisfied in the Kelvin-Havelock approach, whereas this radiation condition must be numerically simulated in the Rankine-source approach. Also, the infinite free surface must be truncated in some manner in Rankine source approach, whereas the infinite free surface is automatically reduced to a finite one in the Numann-Kelvin approach. The need for numerically simulation the radiation condition and for truncating the infinite free surface represents two basic difficulties of the Rankine-source approach. Another advantage of the Kelvin-Havelock source follows from the fact that it satisfies a linearized free surface boundary condition that provides a reasonable approximation to the exact free surface condition for many practical applications. In this case, there is no need for a free surface singularity distribution and the Kelvin-Havelock source can be used to obtain a simple approximate expression for the velocity potential of the flow about a ship that is defined explicitly in terms of the ship speed, size and shape.

In this paper, an efficient manner of evaluating Kelvin-Havelock source Green function are presented and then the procedure have been employed for submerged cylinder, sphere and ellipsoid and a Wigley hull. Wave pattern of the free surface are obtained and shown by the numerical method in qualitatively and quantitative. The validation of the present method is confirmed by showing good correlation with the available data.

## MATHEMATICAL FORMULATION OF THE PROBLEM

A three dimensional moving body at a constant velocity ( $U$ ) at or beneath the surface of a fluid of infinite depth is considered. The sketch of the body and flow are given in Fig. 1. The fluid is assumed to be inviscid, incompressible and the flow to be irrotational.

It was chosen a Cartesian frame of reference moving bodies and assumed that the flow is steady. The Cartesian coordinates ( $x, y, z$ ) is chosen with the  $z$ -axis directed vertically upwards and the  $x$ -axis in the opposite direction of the velocity ( $U$ ). The equation of the free surface is denoted by  $z = \eta(x, y)$ .

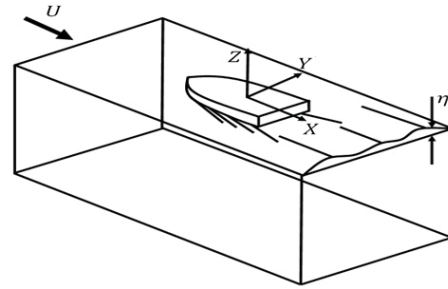


Fig. 1. Definition of coordinate system

Perturbation potential,  $\phi$ , and total potential,  $\Phi$ , should satisfy Laplace's equation in the fluid domain.

$$\nabla^2 \Phi = \nabla^2 \phi = 0 \quad (1)$$

Three boundary conditions on the free surface are given as follows:

### I) KINEMATIC BOUNDARY CONDITION ON THE BODY SURFACE:

The flow should be tangent to the wetted surface of the body:

$$\frac{\partial \phi}{\partial n} = -(U \hat{i}) \cdot \vec{n} = -U \cdot n_x \quad (2)$$

where  $\vec{n}$  is the unit normal vector to the wetted surface of the body, directed into the fluid domain.

### II) KINEMATIC FREE SURFACE CONDITION:

The fluid particles should follow the free surface,

$$\frac{DF(x, y, z)}{Dt} = 0 \quad \text{on } z = \eta(x, y) \quad (3)$$

where  $F(x, y, z) = z - \eta(x, y)$  and  $\eta$  is the free surface deformation.

### III) DYNAMIC FREE SURFACE CONDITION:

The pressure on the free surface should be equal to the atmospheric pressure ( $\rho_{atm}$ ). Applying Bernoulli's equation, the following equation can be obtained:

$$\frac{1}{2} [(\nabla \phi)^2 - U^2] + g\eta = 0 \quad \text{on } z = \eta(x, y) \quad (4)$$

where  $g$  is the gravitational acceleration.

If eq. (3) and eq. (4) are combined and linearized, then the following free surface condition can be derived:

$$\frac{\partial^2 \phi}{\partial x^2} + k_0 \frac{\partial \phi}{\partial z} = 0 \quad \text{on } z = 0 \quad (5)$$

Here,  $k_0 = \frac{g}{U^2}$  is the wave number.

#### IV) RADIATION CONDITION:

No upstream waves should occur. In order to prevent upstream waves, both the first- and second-order derivatives of perturbation potential with respect to  $x$  are forced to be equal to zero for the upstream region on the free surface.

$$\frac{\partial^2 \phi}{\partial x^2} = \frac{\partial \phi}{\partial x} = 0 \quad \text{as } x \rightarrow -\infty \quad (6)$$

#### V) INFINITE DEPTH CONDITION:

The perturbation potential should go to zero for infinite depth.

$$\lim_{z \rightarrow -\infty} \nabla \phi \rightarrow 0 \quad (7)$$

Finally after computing the potential distribution on free surface, the wave elevation is computed as follows:

$$\eta = -\frac{U}{g} \frac{\partial \phi}{\partial x} \quad (8)$$

### NUMERICAL SCHEME

Applying the integral representation for the potential function ( $p$ ), Green's second identity can be written as:

$$e\phi(p) = \iint_S \left[ \phi \frac{\partial G}{\partial n} - G \frac{\partial \phi}{\partial n} \right] dS \quad (9)$$

where  $e$  is a coefficient that its value depends on the position of the field point  $p$  in the fluid domain. If point  $p$  is placed on the boundary (body surface), then the coefficient  $e$  is replaced by 0.5. If point  $p$  is placed inside and outside of the body then the value of  $e$  is one and zero, respectively.

Also,  $G$  is the Green function of a Kelvin-Havelock source which it will be discussed hereafter. This Green function has 3 parts and we need to be able to solve it for a sample source and then use the solution for whole body. The Green function for a source in  $(x, y, z)$  which translates uniformly with speed  $U$  in infinite fluid and for an observation point in  $(x, y, z)$  is:

$$G(x, y, z; x_0, y_0, z_0) = S(X, Y, Z) + N(X, Y, Z) + W(X, Y, Z) \quad (10)$$

Term  $S$  (simple term) is defined as:

$$\begin{aligned} R &= \sqrt{(x - x_0)^2 + (y - y_0)^2 + (z - z_0)^2} \\ R' &= \sqrt{(x - x_0)^2 + (y - y_0)^2 + (z + z_0)^2} \end{aligned} \quad (11)$$

where:

$$\begin{aligned} R &= \sqrt{(x - x_0)^2 + (y - y_0)^2 + (z - z_0)^2} \\ R' &= \sqrt{(x - x_0)^2 + (y - y_0)^2 + (z + z_0)^2} \end{aligned} \quad (12)$$

And:

$$(X, Y, Z) = \frac{g}{U^2} (x - x_0, y - y_0, z + z_0) \quad (13)$$

Term  $N$  that is known as non-oscillatory near field term is defined as [19]:

$$N(X) = \frac{-2\nu}{\pi} \left\{ -\frac{1}{2\pi} \int_{-1}^1 \text{Im} \exp(A) E_1(A) dt \right\} \quad (14)$$

And:

$$A = \left[ Z(1 - t^2)^{\frac{1}{2}} + Yt + i|X| \right] (1 - t^2)^{\frac{1}{2}} \quad (15)$$

$E_1(A)$  is the well known exponential integral which can be expressed as:

$$E_1(A) = \int_0^{\infty} \frac{e^{-(t+A)}}{t+A} dt \quad (16)$$

Finally, the term  $W$  which is oscillatory far field term (or somewhere is known as wave term) represents the system of Kelvin waves trailing behind the singular point, as is indicated explicitly by the Heaviside unit step function and is expressed as:

$$\begin{aligned} W(X) &= (-4\nu)H(X) \int_{-\infty}^{+\infty} \text{Im} \left\{ \exp \left[ Z(1 + t^2) \right. \right. \\ &\quad \left. \left. + i(X + Yt)\sqrt{1 + t^2} \right] \right\} dt \end{aligned} \quad (17)$$

Numerical evaluation of the source potential thus involves three basic tasks corresponding to the evaluation of the simple singularity potential, the non-oscillatory near-field potential, and the wave potential. Two distinct numerical tasks must be considered for evaluating each of these potential parts. The first task is numerical evaluation of the main terms and their gradients, and the second is numerical integration of them over a flat triangle  $T$ .

#### I) SIMPLE TERM:

For evaluating the gradient of simple term it can be used the following relation:

$$\frac{\partial}{\partial n} \left( \frac{1}{R} \right) = \frac{\vec{R} \cdot \vec{n}}{|R|^3} \quad (18)$$

When the singular point is on the field element this term vanishes because it uses flat element and in  $R$  and  $n$  will be perpendicular to each other. For integrating this integrand over a flat element we can use simple Gauss method.

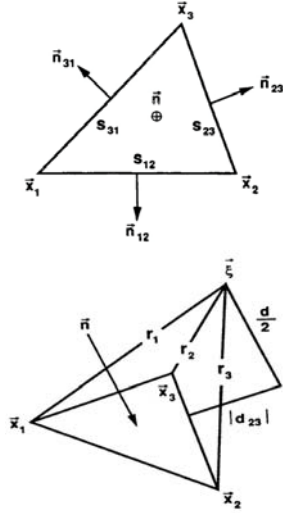


Fig. 2. Panel definition sketch

It is well known that the integration of simple term can be evaluated analytically. This integral over a flat triangular panel may be expressed in the form:

$$\iint_S \frac{1}{R} ds = d_{12} \ln \rho_{12} + d_{23} \ln \rho_{23} + d_{31} \ln \rho_{31} + d(\tan^{-1} t_{12} + \tan^{-1} t_{23} + \tan^{-1} t_{31}) \quad (19)$$

where the terms  $d_{ij}$ ,  $\rho_{ij}$ ,  $t_{ij}$  and  $d$  are now defined:

$$\rho_{ij} = \frac{r_{ij} - s_{ij}}{r_{ij} + s_{ij}} \quad (20)$$

that  $s_{ij}$  is the length of the side of the triangle  $T$  between the vertices  $\vec{x}_i$  and  $\vec{x}_j$ , as indicated in Fig. 2, and is defines as:

$$r_{ij} = r_i + r_j \quad (21)$$

where  $r_i$  representing the distance between the calculation point  $\vec{\xi}$  and the vertex  $\vec{x}_i$  of  $T$ , as shown in Fig. 2. The terms  $d_{ij}$  in equation (19) are defined as:

$$d_{ij} = [\vec{\xi} - (\vec{x}_i + \vec{x}_j)/2] \cdot \vec{n}_{ij} \quad (22)$$

And  $\vec{n}_{ij}$  is the unit vector in the plane of  $T$  normal to the side of  $T$  between the vertices  $\vec{x}_i$  and  $\vec{x}_j$  and pointing outside  $T$ , as indicated in Fig. 2. We then have:

$$n_{ij} = \vec{n} \times \frac{\vec{x}_j - \vec{x}_i}{s_{ij}} \quad (23)$$

where  $\vec{n}$  is the unit vector normal to  $T$  oriented as in Fig. 2; specifically, the vertices of the panel are numbered counterclockwise when the panel is viewed in the direction of the normal vector  $\vec{n}$ .

It can be verified that  $|d_{ij}|$  is the distance from the projection of the calculation point  $\vec{\xi}$  onto the plane of  $T$  to

the side of  $T$  between the vertices  $\vec{x}_j$  and  $\vec{x}_i$ , as shown in Fig. 2. The term  $d$  in eq. (19) is defined by:

$$d = 2|\vec{\xi} - \vec{x}_0| \cdot \vec{n} \quad (24)$$

Where  $\vec{x}_0$  is the centroid of  $T$  given by:

$$\vec{x}_0 = \frac{\vec{x}_1 + \vec{x}_2 + \vec{x}_3}{3} \quad (25)$$

It can be seen that  $d$  is equal to twice the distance between  $\vec{\xi}$  and the plane of  $T$ , as indicated in Fig. 2. Finally, the terms  $t_{ij}$  in (19) are defined as:

$$t_{ij} = \frac{2s_{ij}d_{ij}}{[r_{ij}(r_{ij} + d) - (s_{ij})^2]} \quad (26)$$

In the particular case when the calculation point  $\vec{\xi}$  is in the plane of the triangle  $T$ , we have  $d = 0$  and eq. (19) simplifies accordingly. If  $\vec{\xi}$  lies on one of the three sides of  $T$ , say on the side between the vertices  $\vec{x}_i$  and  $\vec{x}_j$ , we have and the contribution of the side  $ij$  in eq. (19) vanishes. If the calculation point  $\vec{\xi}$  is at one of the three vertices of  $T$ , say at  $\vec{x}_i$ , we have both  $d_{ij} = d_{ik} = 0$ , and the contributions of the two sides  $ij$  and  $ki$  in (19) vanish.

The foregoing exact analytic expressions for the simple term integral only need to be used for calculation points  $\vec{\xi}$  in the vicinity of the triangle  $T$ . Indeed, at large and intermediate distances from  $T$  the approximations can be computationally more efficient.

## II) OSCILLATORY NEAR FIELD TERM:

Calculating this term is considered in Newman [2] and Telste and Noblesse [5]. The latter study presents a computationally efficient method for evaluating the function  $N(X)$ , using table interpolation together with two term series representations for small and large values of  $R$ .

The function  $N(X)$  could be defined as the following alternative integrals:

$$N(X) = \frac{-2\nu}{\pi} \left\{ -\frac{1}{2\pi} \int_{-1}^1 \text{Im} \exp(A) E_1(A) dt \right\} = \frac{-2\nu}{\pi} \left\{ \frac{1}{2} \left[ 1 - \frac{Z}{R + |X|} \right] + \int_{-1}^1 \text{Im}[\exp(A) E_1(A) + \ln(A) + \gamma'] dt \right\} \quad (27)$$

Where  $E_1(A)$  is the exponential integration and was explained before and  $\gamma' = 0.577$  is Euler's constant. The calculation domain is  $-\infty \leq X, Y \leq \infty$  and  $-\infty \leq Z \leq 0$ .

The behavior of the function  $N(X)$  in the limits  $R \rightarrow \infty$  and  $R \rightarrow 0$  is given in Telste and Noblesse [5] as:

$$2N \sim \frac{1}{R} + \frac{C \left[ 1 - (1+C) \left( \frac{X}{R} \right)^2 \right]}{R^2}$$

as  $R \rightarrow \infty$  with  $C = 1/1 - \frac{Z}{R}$  (28)

And

$$2N \sim 1 - \frac{Z}{R + |X|} + \frac{|X|}{2} \ln[(R + |X|)/4]$$

$$+ \left( \frac{|X|}{4} \right) \left[ 2Y' - 1 - \frac{\left( \frac{1}{3} \right) (Y^2 - Z^2)}{(R + |X|)^2} \right]$$

$$- \frac{\left( \frac{Y}{3} \right) Y}{R + |X|} + \left( \frac{2Z}{3} \right) \left[ 1 - \frac{Z}{R + |X|} \right] \quad \text{as } R \rightarrow 0$$
 (29)

The transformation  $(X, Y, Z) \rightarrow (\rho, \alpha, \beta)$  defined below maps the semi-infinite space into the unit cube.

$$\rho = \frac{\sqrt{R}}{1 + \sqrt{R}}$$

$$\alpha = \frac{|X|}{|X| + \sqrt{Y^2 + Z^2}}$$

$$\beta = \frac{-Z}{\sqrt{Y^2 + Z^2}}$$
 (30)

The function  $N'(\rho, \alpha, \beta)$  is defined as  $N'(\rho, \alpha, \beta) = (1 + R)N(\rho, \alpha, \beta)$  and now we can use a simple and computationally efficient method for approximating the function  $N'$  consists in using table interpolation based on values of the function  $N'$  at equally-spaced values of the transformed coordinates  $\rho, \alpha, \beta$ . A simple and computationally efficient interpolation formula is linear interpolation in each of the three independent variables  $\rho, \alpha, \beta$ . More precisely, let the values of the function  $N'(\rho, \alpha, \beta)$  be given at equally spaced values:

$$\left( \rho_1 = 0, \rho_2, \dots, \rho_i, \rho_{i+1}, \dots, \rho_{N_\rho} = 1 \right)$$

$$\left( \alpha_1 = 0, \alpha_2, \dots, \alpha_i, \alpha_{i+1}, \dots, \alpha_{N_\alpha} = 1 \right)$$

$$\left( \beta_1 = 0, \beta_2, \dots, \beta_i, \beta_{i+1}, \dots, \beta_{N_\beta} = 1 \right)$$
 (31)

of the coordinates  $\rho, \alpha, \beta$  with

$$\Delta\rho = \rho_{i+1} - \rho_i = \frac{1}{N_\rho - 1} \quad \text{for } 1 \leq i \leq N_\rho - 1$$

$$\Delta\alpha = \alpha_{j+1} - \alpha_j = \frac{1}{N_\alpha - 1} \quad \text{for } 1 \leq j \leq N_\alpha - 1$$

$$\Delta\beta = \beta_{k+1} - \beta_k = \frac{1}{N_\beta - 1} \quad \text{for } 1 \leq k \leq N_\beta - 1$$
 (32)

The intervals,  $[p_i, p_{i+1}]$  and corresponding to any point  $(X, Y, Z)$  can be determined directly (that is, without performing a table search) from eq. (30) and the following formulas:

$$i = 1 + \text{Int}[\rho(N_\rho - 1)],$$

$$j = 1 + \text{Int}[\alpha(N_\alpha - 1)],$$

$$k = 1 + \text{Int}[\beta(N_\beta - 1)]$$
 (33)

where  $\text{Int}[x]$  is the largest integer less than or equal to  $x$ . Linear interpolation of the function  $N'(\rho, \alpha, \beta)$  is defined by:

$$N'(\rho, \alpha, \beta) = \gamma [\mu (vN'_{i+1,j+1,k+1} + \bar{v}N'_{i+1,j+1,k})$$

$$+ (1 - \mu)(vN'_{i+1,j,k+1} + \bar{v}N'_{i+1,j,k})]$$

$$+ (1 - \gamma) [\mu (vN'_{i,j+1,k+1} + \bar{v}N'_{i,j+1,k})$$

$$+ (1 - \mu)(vN'_{i,j,k+1} + \bar{v}N'_{i,j,k})]$$
 (34)

where,  $\mu, v$  and  $\bar{v}$  are given by:

$$\gamma = \rho(N_\rho - 1) - \text{Int}[\rho(N_\rho - 1)],$$

$$\mu = \alpha(N_\alpha - 1) - \text{Int}[\alpha(N_\alpha - 1)],$$

$$v = \beta(N_\beta - 1) - \text{Int}[\beta(N_\beta - 1)],$$

$$\bar{v} = 1 - v$$
 (35)

The non-oscillatory term  $N$  is now computed, and a seven-point Gauss method (which will be explained below) is used for integration on the triangular panels.

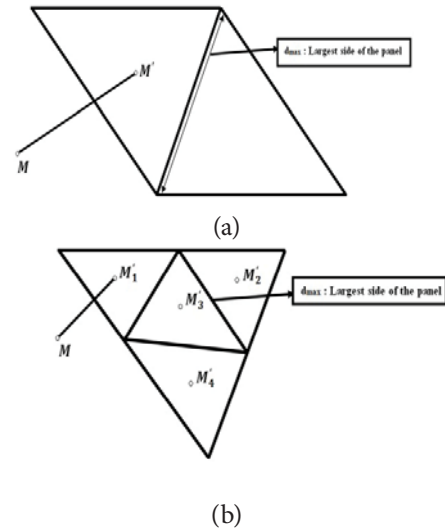


Fig.3. (a) Definition sketch for space integration. (b) Division of a triangular panel into four triangular panels

For integration of this non-oscillatory term over these triangular panels, the following criterion is defined:  $\rho_0 = \frac{MM'}{d_{max}}$ . Where  $M$  is the collocation point (field point) and  $M'$  is the center of gravity of the panel where  $N$  has to be integrated (Figure 3(a)), and  $d_{max}$  corresponds to the largest side of the panel. Three cases have been considered:

- If  $\rho_0 \geq 2$ , a seven-point Gauss integration method is performed over the triangular panel;
- If  $1 < \rho_0 < 2$ , the triangular panel is divided into four triangular panels following Figure 3(b); a seven-point Gauss integration method is then performed over the new panels;
- If  $\rho_0 \leq 1$  the triangular panel is also divided into four new triangular panels and new criteria on:  $\rho_{0i} = \frac{MM'_i}{d_{max_i}}$  for the four values of subscript  $i$  are applied;
- If  $\rho_0^i > 1$ , integration is done by the seven-point method;
- If  $\rho_0^i < 1$ , the panel is divided again into four new panels

and on each new panel integration is done by the seven-point method.

The seven-point rule of degree 5 is given by ([19]):

$$\iint_S N \cdot dS = \frac{A_T}{40} \left[ (9N_0) + \frac{(155 - \sqrt{15})(N'_1 + N'_2 + N'_3)}{30} + \frac{(155 + \sqrt{15})(N''_1 + N''_2 + N''_3)}{30} \right] \quad (36)$$

where  $N_0$ ,  $N'_i$  and  $N''_i$  represent the amount of function  $N$  between the field point and the points  $x_0$ ,  $x'_i$  and  $x''_i$  respectively of  $T$  defined as:

$$\begin{aligned} x_0 &= \frac{x_1 + x_2 + x_3}{3}, \\ \vec{x}'_i &= \frac{\vec{x}_0(6 - \sqrt{15})}{7} + \frac{\vec{x}_i(\sqrt{15} + 1)}{7}, \\ \vec{x}''_i &= \frac{\vec{x}_0(6 + \sqrt{15})}{7} - \frac{\vec{x}_i(\sqrt{15} - 1)}{7} \end{aligned} \quad (37)$$

### III) OSCILLATORY FAR FIELD TERM:

This term can be expanded as:

$$W(X) = (-4\nu)H(X) \int_{-\infty}^{+\infty} \text{Im} \left\{ \exp \left[ Z(1 + t^2) + i(X + Yt)\sqrt{1 + t^2} \right] \right\} dt \quad (38)$$

where  $\text{Im}$  denotes for the imaginary part. By defining the function  $H(X, t) = \exp[Zp^2 + i(X + Yt)p]$  with  $p = \sqrt{1 + t^2}$ . This term and its gradient can be written as:

$$\begin{aligned} W(X) &= H(X) \int_{-\infty}^{+\infty} \text{Im}\{H(X, t)\} dt, \\ W_X(X) &= \int_{-\infty}^{+\infty} \text{Re}[pH(X, t)] dt, \\ W_Y(X) &= \int_{-\infty}^{+\infty} \text{Re}[ptH(X, t)] dt, \\ W_Z(X) &= \int_{-\infty}^{+\infty} \text{Re}[p^2H(X, t)] dt \end{aligned} \quad (39)$$

Numerical integration of eq. (39) is troublesome due to the oscillatory behavior of the integrands increasing as  $Z$  decreases.

Boundary integration is performed analytically to compute the far-field velocity potential. The method has been developed in Hendrix and Noblesse [6] to compute symmetrical flows. Below it is provided formulas for evaluating the integrals on  $W$  and its gradient, which are obtained without taking into account any flow symmetry, and are therefore valid for lifting flows. In fact the 2 main objects that should be computed are:

$$\begin{aligned} I &= \iint_S W n_x ds = \int_{-\infty}^{\infty} dt \sum_{j=1}^{n_j} \iint_{S_j} \text{Im}\{H(X, t)\} ds \\ J_i &= \iint_{S_j} W n_i ds = \int_{-\infty}^{\infty} p \left[ (-n_{xj} - n_{yj}t) \text{Re} \iint_{S_j} H(X, t) ds + n_{zj} p \text{Im} \iint_{S_j} H(X, t) ds \right] dt \end{aligned} \quad (40)$$

The integral  $\iint_{S_j} H(X, t) ds$  (where  $H$  is given earlier) can be computed analytically, following Hendrix & Noblesse [6]. For a triangular panel  $j$  (with area  $\Delta S_j$ ) defined by its nodes  $X_1, X_2, X_3$  and for the flow observation point given by  $X$ , we obtain:

$$\iint_{S_j} H(X, t) ds = \iint_{S_j} \exp(A) ds = \frac{2\Delta S_j}{A_3 - A_2} \left[ \frac{\exp(A_3) - \exp(A_1)}{A_3 - A_1} - \frac{\exp(A_2) - \exp(A_1)}{A_2 - A_1} \right] \quad (41)$$

Where:  $A_k = Z_k p^2 + i(X_k + Yt)$

It must be kept in mind that this oscillatory part of Green's function is present only if and this condition must be taken into account in the computations

Thus, the previous integrals are single ones over  $t$ . For a given collocation point, only one integration on  $W$  has to be computed, integration over the total body area being performed analytically, instead of computing a single integral over  $t$  a number of times equal to the number of panels multiplied by the number of Gauss points on the panel in the method developed in the previous section. Concerning the integral over the gradient, for one collocation point, it has to be computed one integral over the panel area instead of as many integrals as the number of Gauss points. Numerical detail calculations of the all integrals presented in this paper can be found in [25-26].

## NUMERICAL RESULTS AND VALIDATION

### I. TWO-DIMENSIONAL CYLINDER EXPOSED TO A UNIFORM FLOW:

In this section, the results are presented for a 2D cylinder that are exposed to a uniform flow & then compare them with the exact solutions. ( $N$  is the number of elements that are applied for discretizing the boundary and  $R$  is the cylinder radius). In the tables 1 and 2 the value of velocity potential at nodal points for 10 and 20 elements and in constant and linear elements are shown.

Table 1. The values of velocity potential at given nodal points of a 2D cylinder-constant element  
(a: for (n=10) and b: for (n=20))  
(a)

x/a	Calculated	Analytic	Relative Error
0.904508	1.780076	1.809017	0.015998
0.559017	1.100148	1.118034	0.015998
5.55E-17	2.54E-11	1.11E-16	-----
-0.559020	-1.100150	-1.118030	0.015992
-0.904510	-1.780080	-1.809020	0.015998
-0.904510	-1.780080	-1.809020	0.015998
-0.559020	-1.100150	-1.118030	0.015992
-1.67E-16	2.54E-11	-3.33E-16	-----
0.559017	1.100148	1.118034	0.015998
0.904508	1.780076	1.809017	0.015998

(b)

x/a	Calculated	Analytic	Relative Error
0.975528	1.942999	1.951057	0.004130
0.880037	1.752805	1.760074	0.004130
0.698401	1.391034	1.396802	0.004129
0.448401	0.893099	0.896802	0.004129
0.154508	0.307741	0.309017	0.004129
-0.154510	-0.307740	-0.309020	0.004142
-0.448400	-0.893100	-0.896800	0.004126
-0.698400	-1.391030	-1.396800	0.004131
-0.880040	-1.752800	-1.760070	0.004131
-0.975530	-1.943000	-1.951060	0.004131
-0.975530	-1.943000	-1.951060	0.004131
-0.880040	-1.752800	-1.760070	0.004131
-0.698400	-1.391030	-1.396800	0.004131
-0.448400	-0.893100	-0.896800	0.004126
-0.154510	-0.307740	-0.309020	0.004142
0.154508	0.307741	0.309017	0.004129
0.448401	0.893099	0.896802	0.004129
0.698401	1.391034	1.396802	0.004129
0.880037	1.752805	1.760074	0.004130
0.975528	1.942999	1.951057	0.004130

Table 2. The values of velocity potential at given nodal points of a 2D cylinder-linear elements  
(a: for (n=10) and b: for (n=20))  
(a)

x/a	Calculated	Analytical	Relative Error
1.0000000000	2.0000000911	2.0000000000	0.0000000455
0.8090169944	1.6180340798	1.6180338987	0.0000001119
0.3090169944	0.6180340798	0.6180339887	0.0000001474
-0.3090169944	-0.6180338977	-0.6180339887	0.0000001472
-0.8090169944	-1.6180338977	-1.6180339887	0.0000000562
-1.0000000000	-1.9999999089	-2.0000000000	0.0000000455
-0.8090169944	-1.6180338977	-1.6180339887	0.0000000562
-0.3090169944	-0.6180338977	-0.6180339887	0.0000001472
0.3090169944	0.6180340798	0.6180339887	0.0000001474
0.8090169944	1.6180347980	1.6180339887	0.0000005002

(b)

x/a	Calculated	Analytical	Relative Error
1.0000000000	2.0000001392	2.0000000000	0.0000000696
0.9510565163	1.9021131718	1.9021130326	0.0000000732
0.8090169944	1.6180341279	1.6183398870	0.0001889338
0.5877852523	1.1755706438	1.1755705046	0.0000001184

x/a	Calculated	Analytical	Relative Error
0.3090169944	0.6180341279	0.6180339887	0.0000002252
0.0000000000	0.0000001392	0.0000000000	-----
-0.3090169944	-0.6180338496	-0.6180339887	0.0000002251
-0.5877852523	-1.1755703654	-1.1755705046	0.0000001184
-0.8090169944	-1.6180338496	-1.6180339887	0.0000000860
-0.9510565163	-1.9021128935	-1.9021130326	0.0000000731
-1.0000000000	-1.9999998609	-2.0000000000	0.0000000695
-0.9510565163	-1.9021128935	-1.9021130326	0.0000000731
-0.8090169944	-1.6180338496	-1.6180339887	0.0000000860
-0.5877852523	-1.1755703654	-1.1755705046	0.0000001184
-0.3090169944	-0.6180338496	-0.6180339887	0.0000002251
0.0000000000	0.0000001392	0.0000000000	-----
0.3090169944	0.6180341279	0.6180339887	0.0000002252
0.5877852523	1.1755706438	1.1755705046	0.0000001184
0.8090169944	1.6180341279	1.6183398870	0.0001889338
0.9510565163	1.9021131718	1.9021130326	0.0000000732

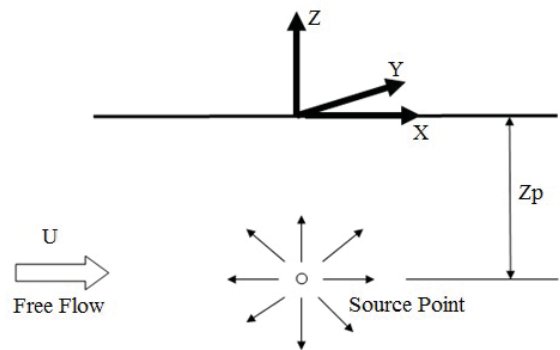


Fig. 4. Schematic of a moving submerged source

## II. MOTION OF A SUBMERGED SOURCE IN DEEP WATER:

The first step in evaluation and investigation of free surface waves is to test the accuracy of green function of the source which we want to use. So, in the first part the free surface waves due to motion of a submerged source is shown and is investigated which show a good agreement with other literature results. In figure 4 the schematic of the motion of a moving submerged source is shown.

In figure 5 wave pattern and contour of a submerged source in depth 2m and with velocity 1m/s is shown. The transverse and divergent waves are apparent in this pattern.

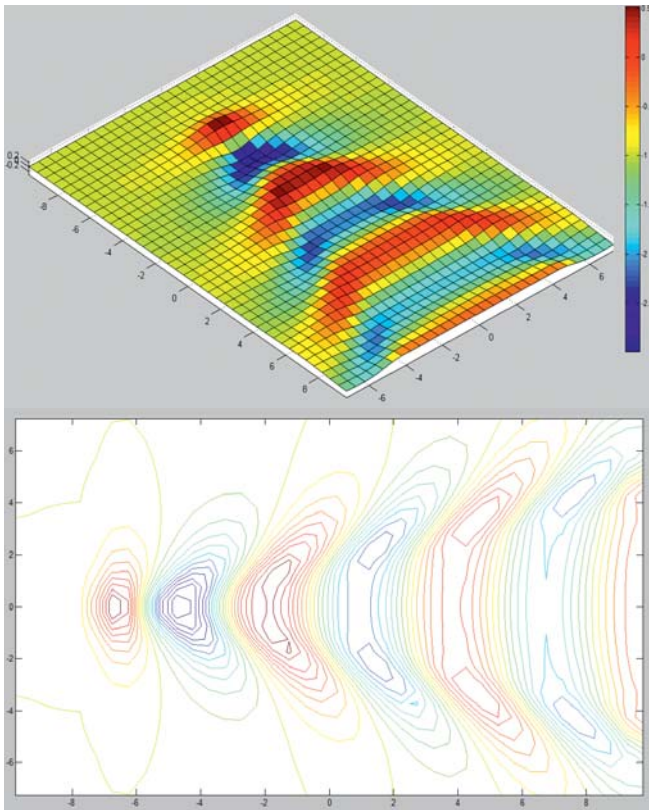
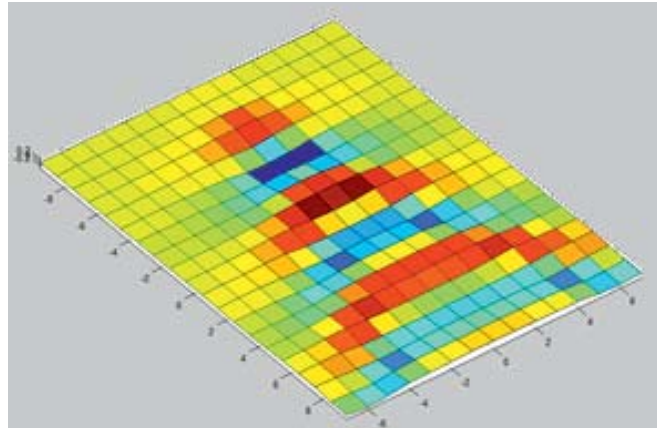
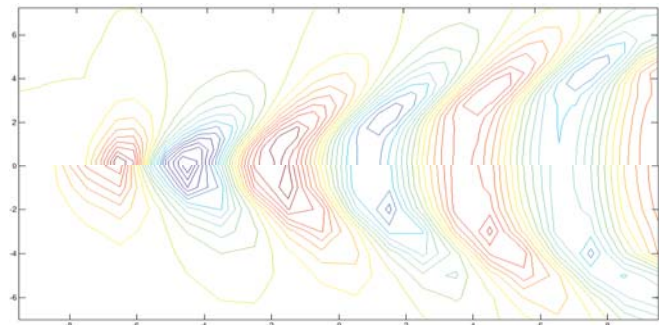


Fig. 5. Wave pattern and contour of a submerged source in depth 2m and with velocity 1m/s ( $Fn=0.22$ )



(b)

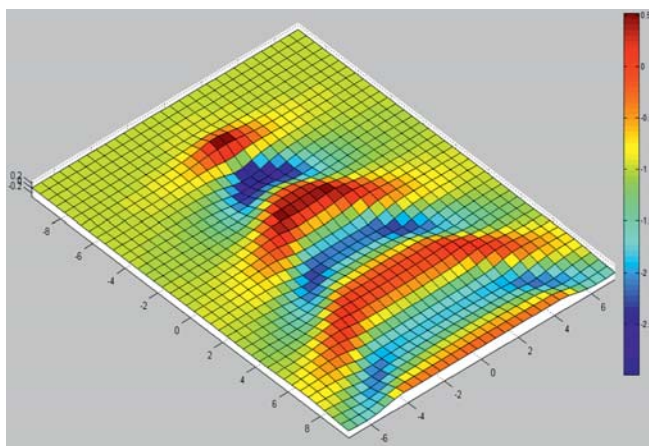


(c)

Fig. 6. Wave pattern of a source in  $Z=-2m$  and  $U=1m/s$  ( $Fn=0.22$ ), (with (a) 1200 and with (b) 300 free surface elements) and wave contour with 1200 element in upper part and 300 elements in lower part of (c)

In figure 6 the wave pattern and contour of previous situation with 300 and 1200 free surface elements are shown and as could be seen, both results are the same and this means that the results are independent of the number of elements.

In Figure 7 the wave profile in various transverse distances from source are shown and it could be seen that the wave amplitude decreases with increasing transverse distance from the source.



(a)

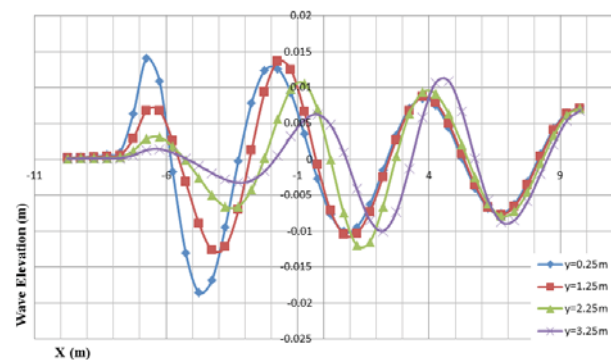


Fig. 7. Wave profile in various transverse distances from source

In figure 8 the wave pattern of 2 parallel moving source is shown and compared to the result of Parau, & Vanden [19].

The wave pattern changes with changing Froude number. In Figure 9, the wave patterns in different situation are shown. As shown in Figure 9 in low Froude numbers the transverse wave is dominant part of whole wave pattern but with increasing Froude number, the transverse waves are vanished and the divergent waves increase and in high Froude number, the wave pattern totally changes.

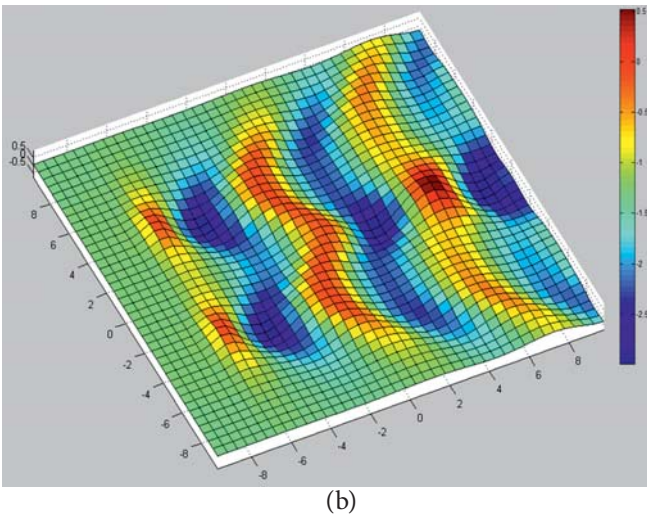
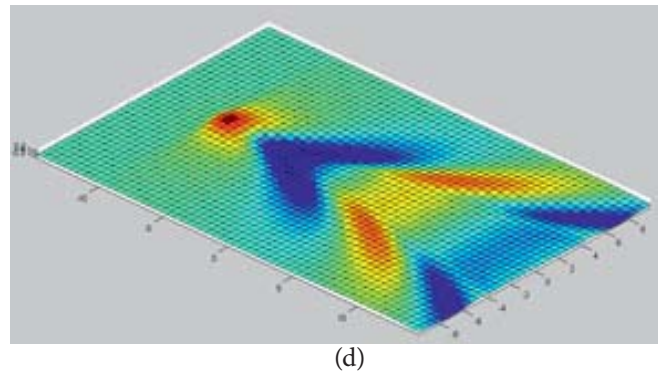
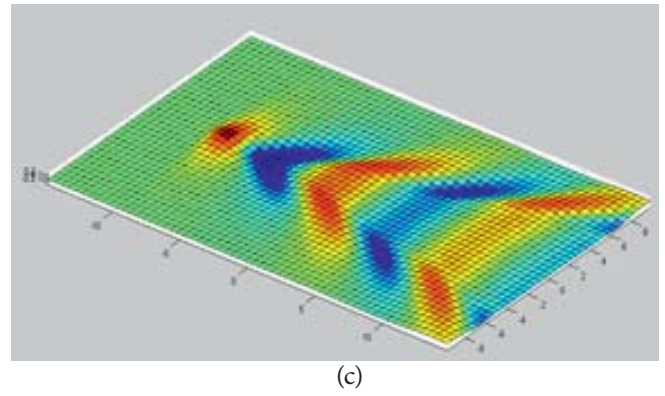
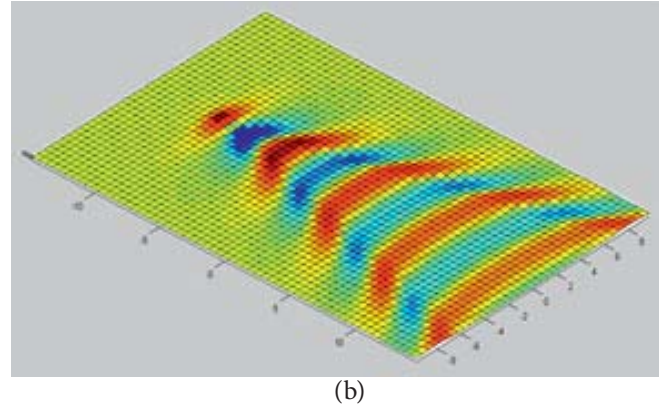
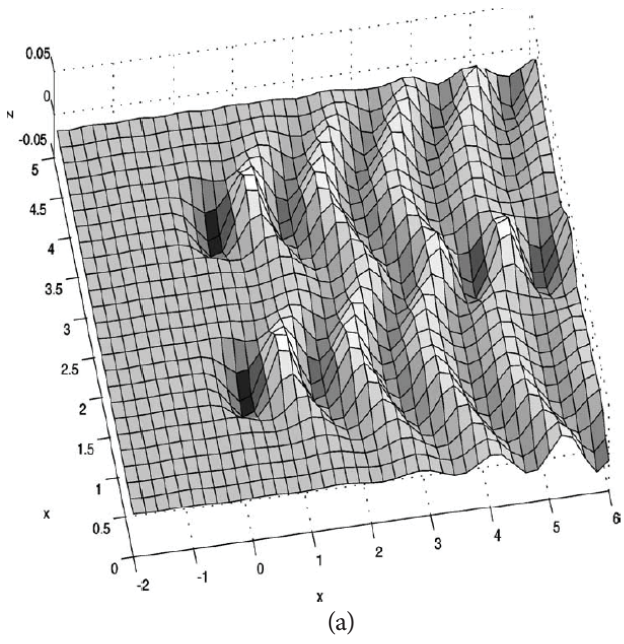


Fig. 8. Wave pattern of 2 moving source ( $F_n=0.4$ ). (a: from reference [19] and b: from the present method)

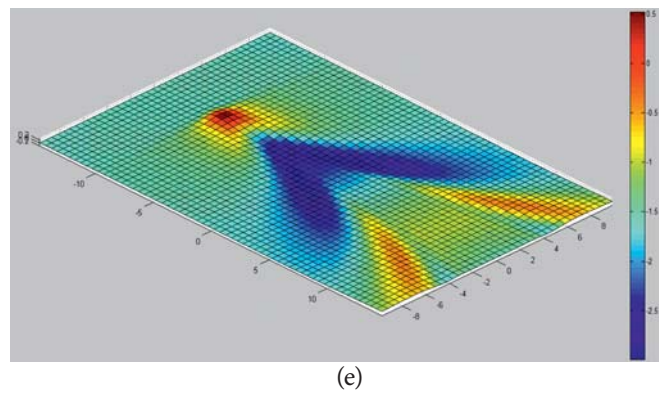
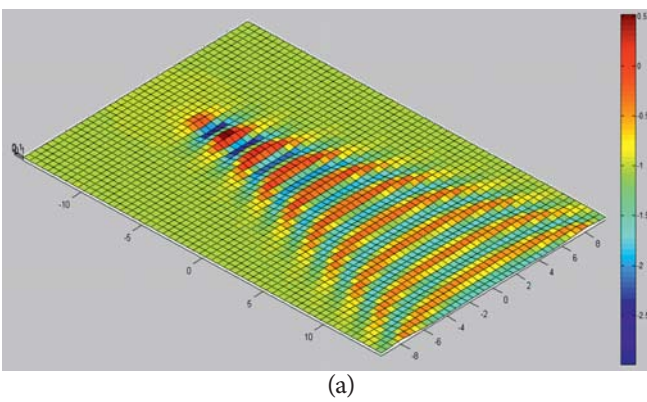


Fig. 9. Wave patterns of submerged source in  $Z=-3$  m with  $U=1, 2, 3, 4$  and  $4.5$  in A, B, C, D and E, respectively. ( $F_n=0.18, 0.36, 0.54, 0.72$  and  $0.8$ )

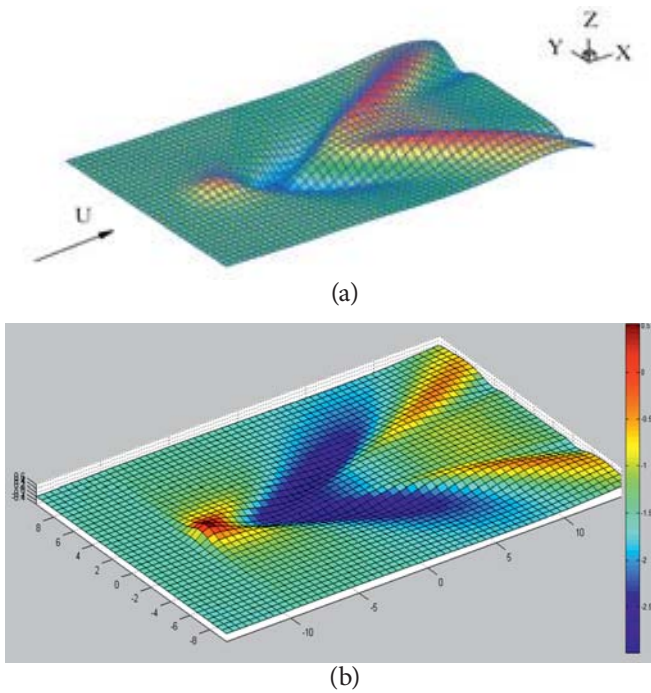


Fig. 10. Wave patterns of a submerged source in  $Z=-3$  m with  $U=4.5$  m/s ( $Fn=0.8$ ). (a: from reference [23] and b: from the present paper)

In Figure 10, the wave pattern in  $Fn=0.8$  is shown and compared to the results of Uslu & Bal [20].

### III. MOTION OF WIGLEY HULL AND SUBMERGED SPHERE AND ELLIPSOID IN DEEP WATER:

Figure 11 shows the wave pattern due to motion of a submerged sphere (with radius 1, in depth 2m and velocity 1 m/s).

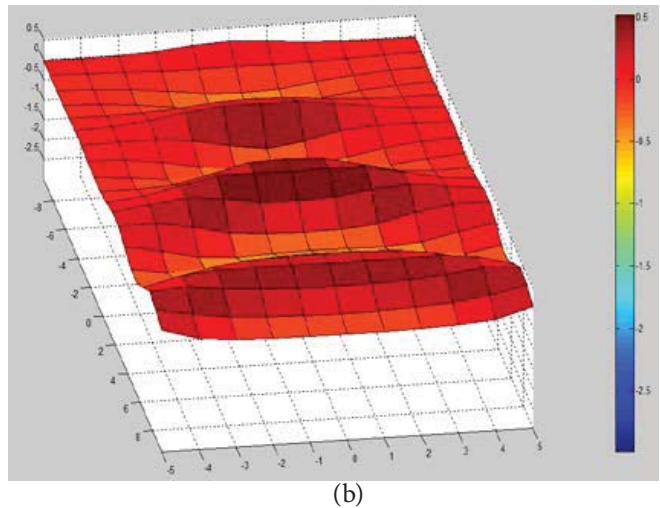


Fig. 11. Wave pattern of a submerged sphere in  $Z=-2$  m with  $U=1$  m/s, ( $Fn=0.22$ )

The effect of sphere velocity on the wave profile is shown in Figure 12, and it illustrates that wave amplitude increase with increasing velocity.

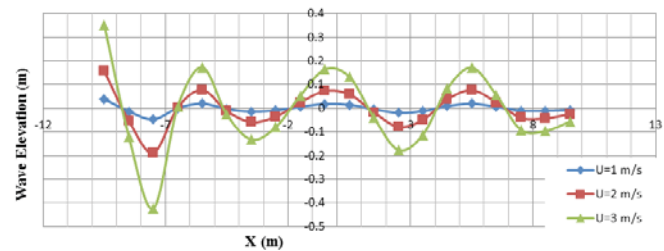
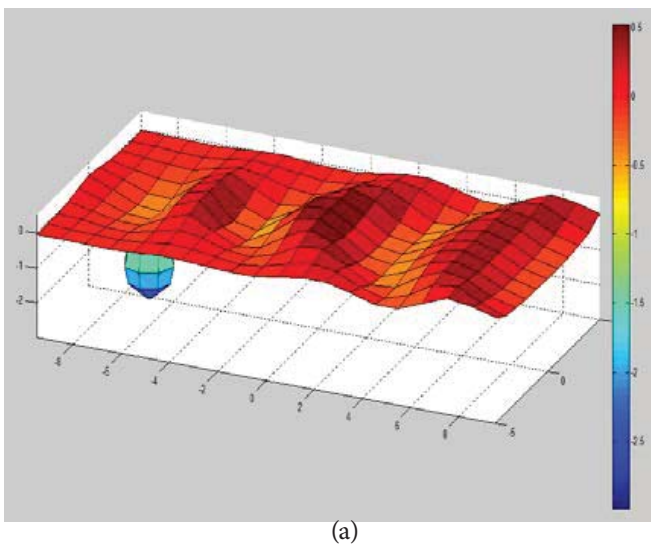


Fig. 12. Effect of sphere velocity on the wave profile

In Figure 13, the wave pattern of a submerged ellipsoid with large to small diameter ratio 4 in depth 2 m and velocity 3 m/s are shown.



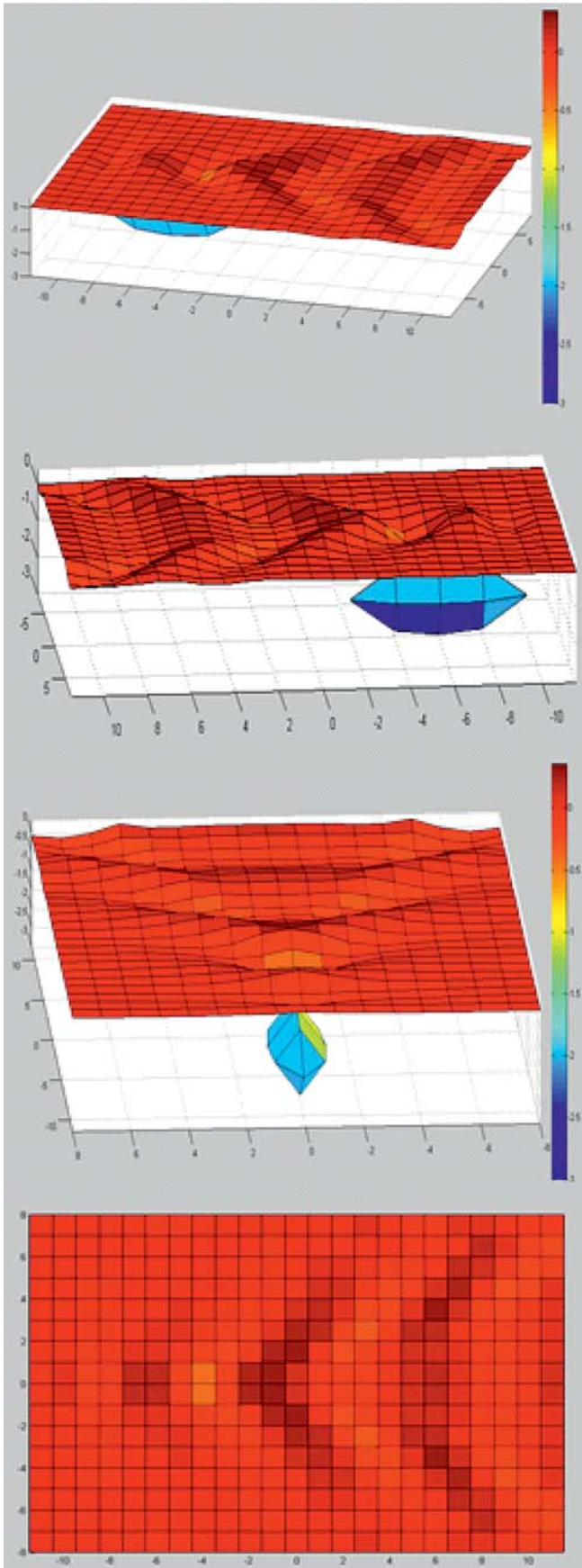


Fig. 13. Wave pattern of a submerged ellipsoid in  $Z=-2$  m with  $U=3$  m/s, ( $F_n=0.47$ )

Figure 14 shows the effect of submergence depth over the wave profile. It depicts that with increasing submergence depth, the wave amplitude decrease and as could be seen from  $Z=-6$  m, approximately it doesn't create any wave on free surface. It means that in depth of 6 meter and below, we can analyze the motion of this ellipsoid without considering the free surface effect and we can use just term for green function.

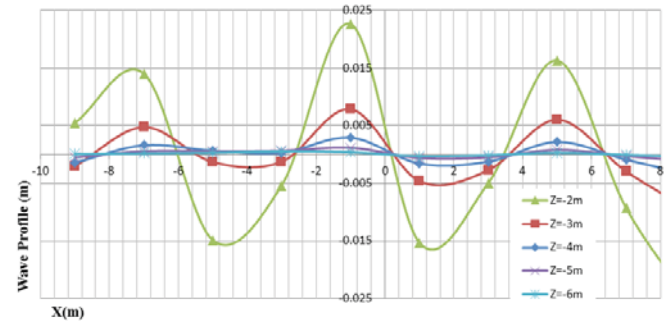


Fig. 14. Wave profile of a submerged ellipsoid in various depths with  $U=1$  m/s

A Wigley hull is recognized with its body equation which is  $y = \pm \frac{B}{z} \left[ 1 - \left( \frac{z}{T} \right)^2 \right] \left[ 1 - \left( \frac{x}{0.5L} \right)^2 \right]$  where  $B$  is hull beam,  $L$  is body length and  $T$  is draft. In figure 15, the wave pattern of a Wigley hull with ratios  $L/B=4$ ,  $B/T=1$  and  $U=2.5$  m/s is shown.

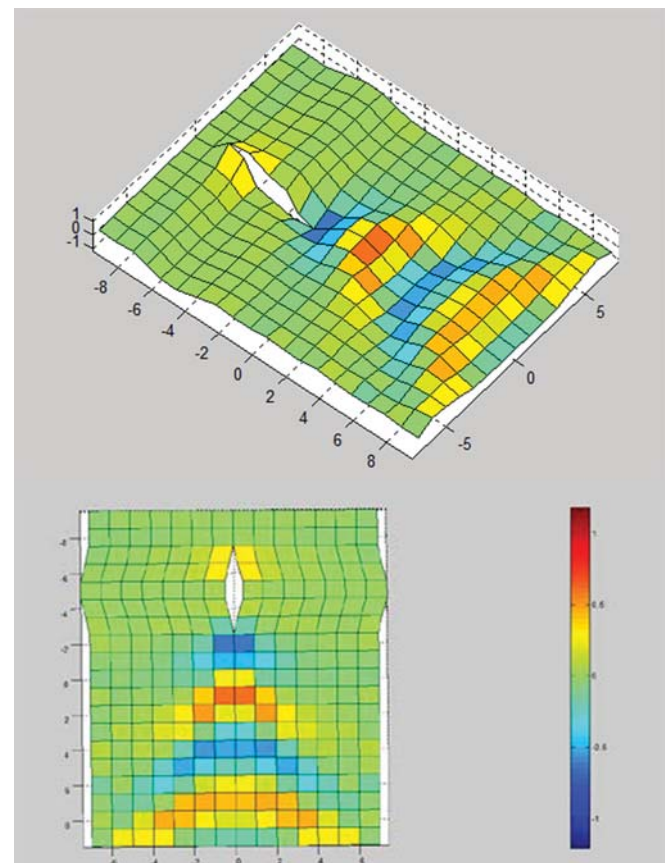


Fig. 15. Wave pattern of a Wigley hull with  $U=2.5$  m/s

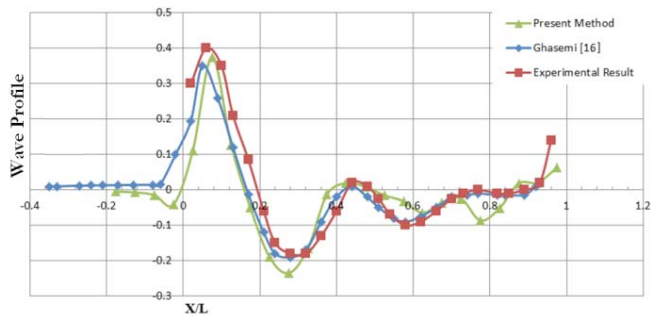


Fig. 16. Wave profile of a Wigley hull  $U=2.5$  m/s ( $Fn=0.25$ )

The wave profile of a Wigley hull with ratios  $L/B=10$ ,  $B/T=1.6$  and  $U=2.5$  m/s is shown in Figure 16, and compared to experimental data and results of by Ghassemi et al. [16], that shows good agreement between them.

## CONCLUSIONS

In this paper, the numerical evaluation of the hydrodynamic characteristics of submerged and surface piercing moving bodies are presented. In results for 2D cylinder, more accuracy of linear elements in comparison of constant elements is apparent. For example the relative error of constant elements are in order of whereas in linear elements are in order of , although it also depends on the number of elements. Then in 3D bodies, the results obtained by a potential-based panel method to calculate free surface waves induced by submerged or surface-piercing bodies have been presented. This method uses the distribution of Kelvin-Havelock sources for modeling the body and this method enabling the flow to be calculated without any discretization of the free surface leading to automatic satisfaction of the radiation and linearized free-surface boundary conditions. Computations of the oscillating and non-oscillating terms of Green's function are performed by accurate methods.

This method gives suitable solution and the agreement between the results of experimental measurements and the present numerical method is satisfactory and indicates the robustness and practical worthiness of the proposed method. Since the used code was written in MATLAB software, the running process took much time so the elements didn't selected too much on the body surface and this is the main reason for the little deviation from experimental and literature results.

Final practical application of this method can be found the relation between of the wave length and body speed, like this formula  $\lambda = 2\pi V^2/g$ . For example; if any submerged body is moving under free surface generating wave, we can measure the wave length and find the body's speed.

Further works must be devoted to the precision of the boundary integrals for source and field points close to the free surface, particularly when the Froude number increases. Finally, it seems to be interesting to develop in the future a second-order method for calculating the nonlinear free surface problem with high accuracy.

## REFERENCES

1. Andrew, R. N., Baar, J. J. M. and Price, W.G. "Prediction of ship wave-making resistance and other steady flow parameters using Neumann-Kelvin theory", Proc., Royal Institution of Naval Architects, 1987.
2. Newman, J. N., "Evaluation of the wave-resistance Green function, Part 1-the double integral", Journal of Ship Research, 31(2), 1987a, pp.79-90.
3. Newman, J. N., "Evaluation of the wave-resistance Green function, Part 2-the single integral on the centerplane", Journal of Ship Research, 31(3), 1987b, pp.145-150.
4. Chen, C. Y. and Noblesse, F., "Comparison between theoretical predictions of wave resistance and experimental data for the Wigley hull". Journal of Ship Research, 27, 4, 1983, pp.215-226.
5. Telste, J. G. and Noblesse, F., "The non-oscillatory near-field in the Green function for steady flow about a ship", Proceeding 17th Symposium of Naval Hydrodynamics, The Hague, 1988, 39-52.
6. Hendrix, D. and Noblesse, F., "Recipes for computing the steady free surface flow due to a source distribution", Journal of Ship Research, 36(4), 1992, pp.346-359.
7. Bulgarelli, U. P., Lugni, C. and Landrini, M., "Numerical Modeling of Free Surface Flows in Ship Hydrodynamics", International Journal for Numerical Methods in Fluids, 43, 2003, pp.465-481.
8. Tulin, M. P., "Reminiscences and Reflections: Ship Waves, 1950-2000". Journal of Ship Research, 49, 2005, pp.238- 246.
9. Larrson, L. and Baba, E., "Ship Resistance and Flow Computations". Advances in Marine Hydrodynamics, Computational Mechanics Publications, 1996; 1-76.
10. Gatchell, S., Hafermann, D., Jensen, G., Marzi, J. and Vogt, M., "Wave resistance computations-a comparison of different approaches", Proceedings of the 23rd Symposium on Naval Hydrodynamics, Val de Reuil, France, 2001.
11. Baar, J. J. M. "A three-dimensional linear analysis of steady ship motion in deep water". Ph.D. Dissertation, Brunel University, U.K., 1986.
12. Baar, J. J. M. and Price, W.G. "Evaluation of the wavelike disturbance in the Kelvin wave source potential", Journal of Ship Research., 32(1), 1988, pp44-53.
13. Cao, Y., Schultz, W. W. and Beck, R. F. "Three-dimensional desingularized boundary integral methods for potential

- problems”, *International Journal of Numerical Methods in Fluids*, 12, 1991, pp785–803.
14. Hsin, C. Y. and Chou, S. K., “Applications of a hybrid boundary element method to the analysis of free surface flow around lifting and non-lifting bodies”, *Proceeding of the 22nd Symposium on Naval Hydrodynamics*, Washington D.C., U.S.A., 1998.
  15. Yasko, M., “Boundary element method for a hydrofoil near the free surface”. *Engineering Analysis with Boundary Elements*, 21, 1998, pp.191–194.
  16. Ghassemi, H., Kohansal, A. and Ghamari, I., (2009) “Nonlinear free surface flows due to the lifting and non-lifting moving bodies” May, 2009, *Proceeding of the 16th International Conference of the ISME*, Tehran, Iran.
  17. Ghassemi H. and Kohansal A. R., “Wave Generated by the NACA4412 Hydrofoil near Free Surface”, *Journal of Applied Fluid Mechanics*, Vol. 6, No. 1, pp. 1-6, 2013.
  18. Tuck, E., Scullen, D. and Lazauskas, L., “Wave patterns and minimum wave resistance for high-speed vessels” *International 24th Symposium on Naval Hydrodynamics*, Fukuoka, Japan, 2002.
  19. Parau, E., and Vanden-Broeck, J. M., “Nonlinear two- and three-dimensional free surface flows due to moving disturbances”, *European Journal of Mechanics B/Fluids* 21, 2002, pp.643–656.
  20. Uslu, Y. and Bal, S., “Numerical prediction of wave drag of 2-d and 3-d bodies under or on a free surface” *Turkish Journal Engineering Environment Science*, 32, 2008, pp.177-188.
  21. Javanmardi, M., Binns, J. R., Renilson, M.R. and Thomas, G., “The prediction of wave patterns at large distances from a moving body in a confined channel”, *18th Australasian Fluid Mechanics Conf. Launceston, Australia, December 2012*.
  22. Sun, J., Lv, X., Liu, W., Ning, H. and Chen, X., “Research on a method of hull form design based on wave-making resistance optimization”, *Polish Maritime Research*, 19(3), 2012, pp16-25.
  23. Zakerdoost, H., Ghassemi H. and Ghiasi M., “Ship hull form optimization by evolutionary algorithm in order to diminish the drag”, *Journal Marine Science Applied* (2013) 12: 170-179.
  24. Ozdemir, Y. H., Cosgun, T., Dogrul, A. and Barlas, B. “A numerical application to predict the resistance and wave pattern of KRISO container ship”, *Brodogradnja*, 67(2), 2016.
  25. Paris, F. and Canas J., “Boundary element method: fundamental and applications”, *Oxford University Press*, 1997.
  26. Ghassemi, H. and Bakhtiari, M., “Boundary element method”, *Amirkabir University of Technology Publication*, 2016.

#### CONTACT WITH THE AUTHORS

Hassan Ghassemi

*e-mail: gasemi@aut.ac.ir*

Faculty of Maritime Engineering AmirKabir University  
of Technology  
Hafez Ave., Tehran

**IRAN**

Isar Ghamari

*e-mail: isar.ghamari@ntnu.no*

Department of Marine Technology Norwegian  
University of Science and Technology (NTNU) Trondheim,

**NORWAY**

Arash Ashrafi

*e-mail: arashonline65@aut.ac.ir*

Faculty of Maritime Engineering AmirKabir University  
of Technology  
Hafez Ave., Tehran

**IRAN**

# OPTIMAL DESIGN AND NUMERICAL SIMULATION ON FISH-LIKE FLEXIBLE HYDROFOIL PROPELLER

Gang Xue<sup>1)</sup>, Ph. D,  
Yan Jun Liu<sup>1)</sup>, Prof., PH. D,  
Muqun Zhang<sup>1)</sup>, Master  
Wei Zhang<sup>1)</sup>, Ph. D,  
Jian Zhang<sup>1)</sup>, Ph. D,  
Huaqing Luo<sup>1)</sup>, Master  
Rui Jia<sup>1)</sup>, Master

<sup>1)</sup> Key Laboratory of High Efficiency and Clean Mechanical Manufacture, Ministry of Education, School of Mechanical Engineering, Shandong University, Ji'nan, China

## ABSTRACT

*Hydrofoil is widely used in underwater vehicle for the excellent hydrodynamic characteristics. Currently, researches are mostly about the rigid hydrofoil while the flexible hydrofoil, like the caudal fin, has not been studied adequately. In this paper, the fish was regarded as the bionic object. Then the kinematics model to describe the fish swimming was put forward. A fin-peduncle propulsion mechanism was designed based on the kinematics model to achieve the similar sine curve swimming model. The propulsion mechanism was optimized by Matlab to reduce the deviation between the output curve of the fin-peduncle propulsion mechanism and the ideal motion trajectory. Moreover, the motion phase angles among flexible articulations are optimized to reduce fluid resistance and improve propulsive efficiency. Finally, the fish-like hydrofoil oscillation is simulated by fluid-solid coupling method based on the Fluent. It was shown that the optimized flexible fish-like oscillation could generate the motion that follows the similar law of sine. The propulsive efficiency of oscillating hydrofoil propeller is much higher than that of the screw propeller, and the flexible oscillation has higher propulsive efficiency than the rigid oscillation without obvious fluid resistance increase.*

**Keywords:** -bionics; flexible hydrofoil; phase angle; hydrodynamic coefficient

## INTRODUCTION

Autonomous Underwater Vehicle (AUV) is an important device for marine operations, which has been used as an important tool for submarine pipeline laying, subsea equipment maintenance, etc. The marine organisms have benefited the natural evolution for millions of years. It will do a lot favor to introduce bionics into the study of AUV. Fish could swim in high speed and good maneuverability under water. It is observed that the dolphin could swim in 3 times to 7 times of the body length per second and the turning radius can be 23% to 30% of the body length [1]. In 1994, MIT developed the world's first fish-like robot, Robo Tuna, whose maximum speed was 2m/s [2]. After that, more attentions have been attracted on the fish-like robot. The PF-300 with two motors controlling the fish-like body collaboratively was designed by Japanese researchers [3]. Harbin Engineering

University developed a fish-like robot to imitate the atlantic bluefin tuna with a three-link tail [4]. Du Ruxu developed a cable-driven robot fish, whose body was flexible and the propulsion efficiency could reach 65% [5]. Beihang University developed a series of fish-like robots, SPC, which can swim as long as 70.2km [6].

Besides, a number of numerical studies on the hydrodynamic characteristics of oscillating hydrofoil have been performed. The slender-body theory was put forward for the deformable body to describe the conditions in which fish will benefit higher Froude propulsion efficiency [7]. The numerical simulation method on the three-dimensional flexible fish model was employed to study the hydrodynamic characteristics of swimming motion [8]. Lagrangian coherent structures (LCS) defined by the ridges of the finite-time Lyapunov exponent (FTLE) was utilized in this study to elucidate the time-dependent turbulent flows around a Clark-Y hydrofoil [9].

Compared with the screw propeller, the fish-like flexible oscillating hydrofoil propeller has higher propulsive efficiency and better maneuverability. In this research, the fin-peduncle propulsion mechanism was designed and optimized to simulate the fish swimming. Besides, the phase angles among flexible articulations are optimized to reduce fluid resistance and improve propulsive efficiency. Finally, the fish-like hydrofoil oscillation is simulated by fluid-solid coupling method based on the Fluent.

## PROPULSION MECHANISM

### KINEMATICS MODEL

According to the observation of fish swimming, an equation to describe the centerline trajectory of the swimming fish body was put forward [10].

$$h(x_n, t) = H(0.21 - 0.66x_n + 1.1x_n^2 + 0.35x_n^8) \sin(2\pi ft) \quad (1)$$

where  $x_n$  is the ratio of the body coordinate value (marked as  $x$ ) and the body length (marked as  $L$ ),  $t$  is the movement time,  $h(x_n, t)$  is the oscillation amplitude of the body,  $H$  is the maximum oscillation amplitude at the end of the caudal peduncle,  $f$  is the oscillating frequency of the caudal peduncle.

After studying the oscillating movements of the fish body, Wang simplified the kinematics model [11]. Supposing that the maximum oscillation amplitude of the fish head is one tenth of the body length and the oscillation amplitude of the barycenter is zero, the simplified equation for the centerline trajectory of the fish body can be described as:

$$h(x_n, t) = H(0.1 - 1.3x_n + 2.2x_n^2) \sin(2\pi ft) \quad (2)$$

The centerline trajectories of the fish body at different moment are shown in Fig. 1.

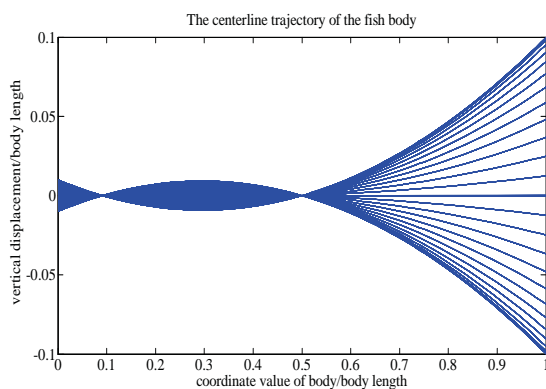


Fig. 1 The centerline trajectories of the fish body

The kinematics equation at the end of the tail can be described as:

$$h(t) = H \sin(2\pi ft) \quad (3)$$

The pitching movement of the caudal fin lags behind its plunging movement, which can be described as:

$$\theta(t) = \theta_{max} \sin(2\pi ft + \varphi) \quad (4)$$

where  $\theta_{max}$  is the maximum oscillation angle, and  $\varphi$  is the phase angle between the plunging movement and the pitching movement.

The swimming speed of the fish can be marked as  $v$  and the length of the caudal fin can be marked as  $l$ . The kinetic coordinate system for caudal fin can be established, as shown in Fig. 2.

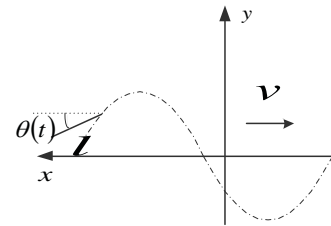


Fig. 2 The kinetic coordinate system for caudal fin

In Fig. 2, the full line is the caudal fin and the dotted line is the plunging movement trajectory of the caudal fin.

The coordinate value for the movement of the caudal fin at any time in the kinetic coordinate can be described as:

$$x = vt - l \cos[\theta_{max} \sin(2\pi ft + \varphi)] \quad (5)$$

$$y = H \sin(2\pi ft) - l \sin[\theta_{max} \sin(2\pi ft + \varphi)] \quad (6)$$

### MECHANISM DESIGN

The propulsion mechanism for the fish-like flexible oscillating hydrofoil propeller was designed based on the kinematics model. The mechanism sketch is shown in Fig. 3.

As shown in Fig. 3, member AB, rotating around A, is driven by the servo motor. The rotation is transformed into the sinusoidal reciprocating motion of member CD, which is connected with member AB by prismatic joint and revolute joint. Member CD and member EF are connected to member DE by revolute joints. Member EF is fixed to member FG. Member CD will drive member DE, member EF, and member FG to achieve the sinusoidal movement output. An actuator is fixed at the end of member FG to control the caudal fin swinging lagged behind member FG in certain phase angle independently.

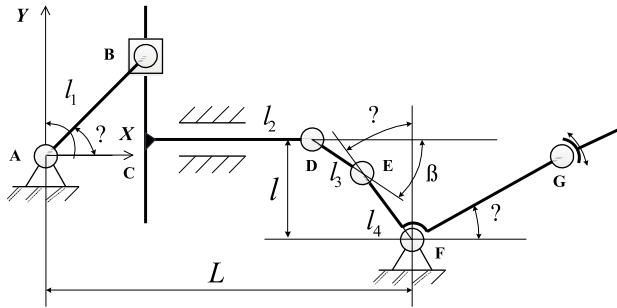


Fig. 3 The mechanism sketch of the propulsion mechanism

In Fig. 3, a coordinate system is established where the origin is point A. Point F is fixed on the coordinate. As the position relations shown in Fig. 3, some formulas can be deduced as:

$$l_3 \sin \beta + l_4 \cos \alpha = l \quad (7)$$

$$x_C = l_1 \cos \theta \quad (8)$$

$$x_D = l_1 \cos \theta + l_2 \quad (9)$$

$$x_E = l_1 \cos \theta + l_2 + l_3 \cos \beta \quad (10)$$

$$x_F = l_1 \cos \theta + l_2 + l_3 \cos \beta + l_4 \sin \alpha \quad (11)$$

$$l_1 \cos \theta + l_2 + \sqrt{l_3^2 - (l - l_4 \cos \alpha)^2} + l_4 \sin \alpha = L \quad (12)$$

where  $x_C$ ,  $x_D$ ,  $x_E$ , and  $x_F$  are the coordinate values of C, D, E, and F.  $l_1$ ,  $l_2$ ,  $l_3$ , and  $l_4$  are the length of member AB, member CD, member DE, and member EF.  $l$  is the distance between point D and point F in Y direction.  $L$  is the distance between point A and point F in X direction.  $\alpha$ ,  $\beta$ , and  $\theta$  are the angles as shown in Fig. 3.

The propeller model was designed based on the mechanism sketch, as shown in Fig. 4.

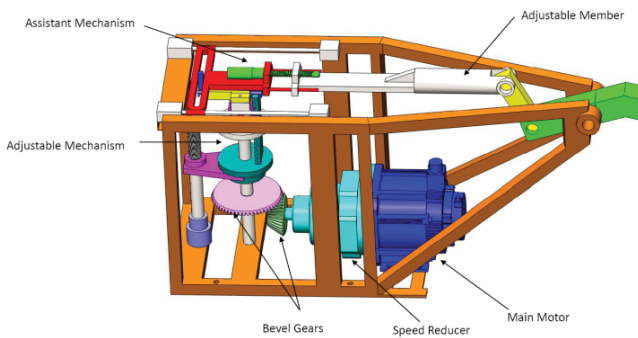


Fig. 4 The propeller model

The length of the adjustable member can be changed. If the adjustable member is shortened, the balanced position for the plunging movement of caudal peduncle will move up, and if the adjustable member is lengthened, it will move down. So the swimming direction of the fish-like robot will be controlled by the adjustment of the adjustable member length.

## OPTIMIZATION BASED ON MATLAB

The length of the mechanism members affect the plunging movement of caudal peduncle, which increases the difficulty of the propulsion mechanism design. At present, the most used method for the mechanism design with the given motion law or the motion trajectory is the function approximation method [12]. However, it is very complicated for the multivariable mechanism optimization. Matlab contains a variety of optimization toolbox, which can be applied in the design optimization of the mechanism to improve the efficiency and accuracy of the calculation.

The propulsion mechanism can be simplified as Fig. 5 shown.

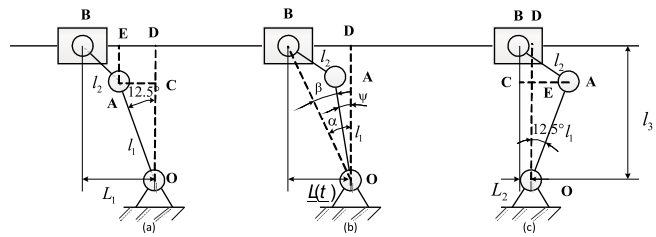


Fig. 5 Mechanism Moment Position

The left limit position is shown in position (a), the right limit position is shown in position (c), and position (b) shows any moment position of the movement. The block B goes the sinusoidal reciprocating motion.

The oscillating frequency of the plunging movement is about 2.1Hz and the range of that is about 25° according to the observation. It means the oscillating range of member OA is about 12.5°. The length of member OA (marked as  $l_1$ ), the length of member AB (marked as  $l_2$ ), the vertical height between point B and point O (marked as  $l_3$ ), and the movement stroke of block B (marked as  $L$ ) are the main parameters to affect the final output of the mechanism.  $l_1$ ,  $l_2$ , and  $l_3$  are the design variables and the follow equation can be established as:

$$x = [l_1; l_2; l_3]^T \quad (13)$$

As shown in Fig. 5(b), the horizontal distance between point B and point O can be described by  $L(t)$ , as:

$$L(t) = 0.5L \cos 4\pi t + \frac{L_1 + L_2}{2} \quad (14)$$

where  $t$  is the movement time,  $L_1$  and  $L_2$  are the

horizontal distance of the left limit position and the right position between point B and point O.

As shown in Fig. 5(a) and Fig. 5 (c),  $L_1$  and  $L_2$  can be described as:

$$L_1 = \sqrt{l_2^2 - (l_3 - l_1 \cos 12.5^\circ)^2} + l_1 \sin 12.5^\circ \quad (15)$$

$$L_2 = \sqrt{l_2^2 - (l_3 - l_1 \cos 12.5^\circ)^2} - l_1 \sin 12.5^\circ \quad (16)$$

The ideal oscillating law of member OA can be described by  $\Psi$ , as:

$$\Psi = 12.5^\circ \sin 4\pi t \quad (17)$$

To minimize the square of the difference between the mechanism output angle and the ideal output angle, the target function can be described as:

$$F(x) = \sum_{t=0}^{0.25} [\Psi(x) - \Psi]^2 \quad (18)$$

where  $\Psi(x)$  is the oscillating angle of member OA, which can be described as:

$$\Psi(x) = \alpha(t) - \beta(t) \quad (19)$$

where  $\alpha(t)$  and  $\beta(t)$  can be calculated from  $\triangle OBD$  and  $\triangle OAB$  as:

$$\alpha(t) = \arccos\left[\frac{l_3}{\sqrt{l_3^2 + L^2(t)}}\right] \quad (20)$$

$$\beta(t) = \arccos\left\{\frac{l_1^2 + [l_3^2 + L^2(t)] - l_2^2}{2l_1\sqrt{l_3^2 + L^2(t)}}\right\} \quad (21)$$

The swimming resistance is little with the streamlined shape. It is shown that the swimming resistance will reduce 75% with the slender ratio of the fish body being 4.5 under the bionics theory. In this research, the length of the fish-like robot body was set as 0.9m, so the widest of the body is no more than 0.2m. Besides, in order to make the robot swim autonomously, the swimming parameters should be variable according to different conditions, so the movement stroke of block B cannot be too small.

To achieve the good transmission of the mechanism, the minimum transmission angle should be larger than  $40^\circ$ . The two limit positions of the movement are shown in Fig. 6. The transmission angle at the limit position should be larger than  $40^\circ$ , which will make sure the good transmission at any time of the movement.

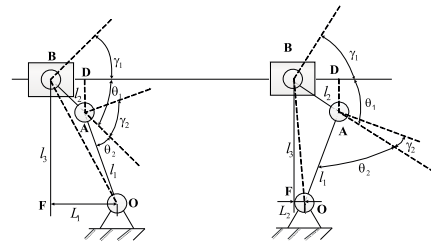


Fig. 6 The transmission angle at the limit position  $\theta_1$

In Fig. 6, the constraint conditions of the pressure angle at the limit position can be obtained from  $\triangle ADB$ , as:

$$\frac{l_3 - l_1 \cos 12.5^\circ}{l_2} \leq \sin 50^\circ \quad (22)$$

In Fig. 6, the constraint conditions of the pressure angle  $\theta_2$  at the limit position can be obtained from  $\triangle OAB$ , as:

$$\frac{L_1^2 + l_3^2 - l_1^2 - l_2^2}{2l_1 l_2} \geq \cos 50^\circ \quad (23)$$

$$\frac{L_2^2 + l_3^2 - l_1^2 - l_2^2}{2l_1 l_2} \geq \cos 50^\circ \quad (24)$$

The optimization of rod mechanism is simple nonlinear programming problem, and the fmincon function in Matlab toolbox is available. Therefore, the target function was calculated every 0.02s and all the results were accumulated to a sum. According to the optimization, the optimal design variables of the solution are  $x = [143.605; 62.196; 187.8459]^T$ , which means  $l_1 = 143.605\text{mm}$ ,  $l_2 = 62.196\text{mm}$ , and  $l_3 = 187.8459\text{mm}$ . The lengths are set as  $l_1 = 144\text{mm}$ ,  $l_2 = 62\text{mm}$ , and  $l_3 = 188\text{mm}$  for manufacturing and the output angle of the mechanism is compared with the ideal output angle, as shown in Fig. 7.

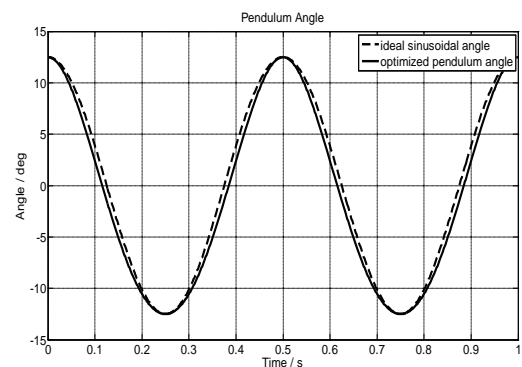


Fig. 7 The output angle of the mechanism and the ideal output angle

In Fig. 7, the dotted line is the ideal outputs angle and the solid line is the actual output angle of the designed mechanism. It comes to the conclusion that the actual output angle amplitude of the designed propulsion mechanism is  $12.5^\circ$  and changes follow the similar law of sine, which is similar to the ideal output angle.

## STUDY OF PHASE ANGLE

The forces on the caudal fin were analyzed, as shown in Figure 8.

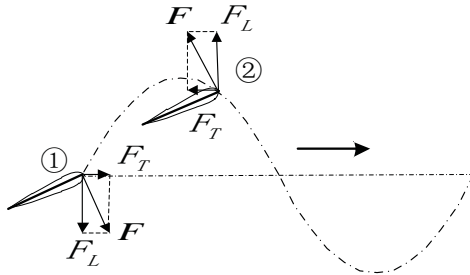


Fig. 8 Analysis of the forces on caudal fin

In Fig. 8,  $F_T$  is the thrust force, which goes along the forward direction at position ①, and it is positive. The caudal fin moves down with the caudal peduncle at position ②, and the force direction is perpendicular to the caudal fin upward. The thrust force goes along the reverse-forward direction, which is negative.

As the observation of the fish swimming, the relation between the swimming velocity and the oscillating frequency is linear. Besides, the oscillation amplitude of the caudal peduncle is essentially unchanged during the swimming process. The biologists point out that the amplitude of the caudal peduncle oscillation is about 0.17 to 0.25 times of the body length. Therefore, the movement parameters of the fish-like robot are as follows:

Swimming speed:  $v = L \text{ m/s}$  ;

Maximum oscillation range of the caudal fin:  $H = 0.1L \text{ m}$  ;

Frequency of the oscillation:  $f = 2 \text{ Hz}$  ;

Maximum oscillation angel range of the caudal fin:  
 $\theta_{max} = 30^\circ$  .

The phase differences between the pitching movement of caudal fin and the plunging movement of caudal peduncle are set as  $60^\circ$ ,  $90^\circ$  and  $120^\circ$  for the kinematics simulation. The oscillation of the caudal fin and the motion trajectory of the swing shaft are shown in Fig. 9 to Fig. 11

As the phase difference is  $60^\circ$ , the caudal fin produces more negative force than positive force, and it is the same as the phase difference is  $120^\circ$ . When the phase difference is  $90^\circ$ , the caudal fin produces positive thrust all the period. So it is considered that the phase difference between the caudal fin plunging movement and pitching movement controls the attack angle of the caudal fin movement, and  $90^\circ$  is the best phase angel.

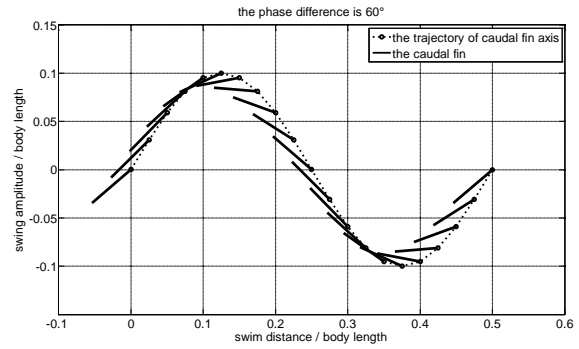


Fig. 9 The phase difference is  $60^\circ$

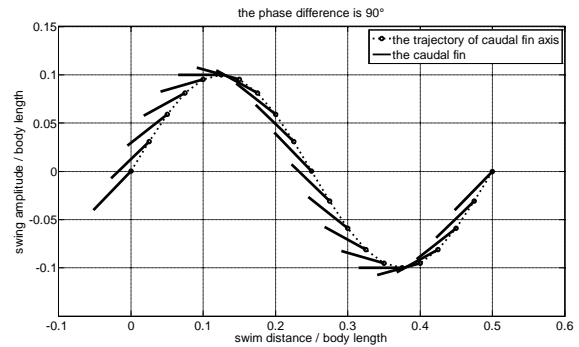


Fig. 10 The phase difference is  $90^\circ$

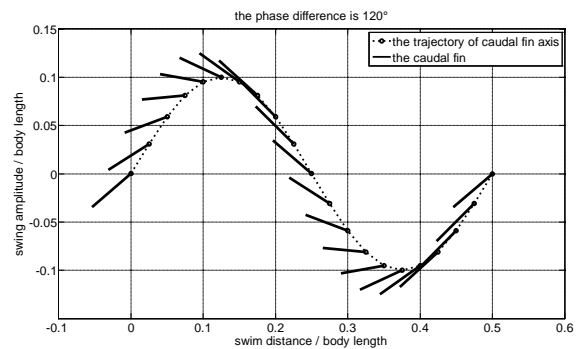


Fig. 11 The phase difference is  $135^\circ$

## HYDRODYNAMIC COEFFICIENTS ANALYSIS

The hydrodynamic coefficients can be defined as:

$$c_d = \frac{F_d}{\frac{1}{2} \rho C_0 v^2} \quad (25)$$

$$c_l = \frac{F_l}{\frac{1}{2} \rho C_0 v^2} \quad (26)$$

$$c_m = \frac{M}{\frac{1}{2} \rho C_0^2 v^2} \quad (27)$$

where  $c_d$  is drag coefficient,  $c_l$  is lateral force coefficient,  $c_m$  is moment coefficient,  $F_d$  is drag produced by flexible oscillating hydrofoil,  $F_l$  is lateral force produced by flexible oscillating hydrofoil,  $M$  is oscillation moment around the head of the fish body produced by flexible oscillating hydrofoil,  $\rho$  is fluid density,  $C_0$  is chord length of the hydrofoil,  $v$  is flow velocity of the fluid.

The SIMPLE Method (Semi-implicit Method for Pressure-Linked Equations) was used to solve the pressure-velocity coupling equations, and the UDF (User Defined Function) was used to achieve the flexible oscillation in the commercial software Fluent. In the simulation, the oscillation frequency of the fish body and the caudal fin is 2Hz, the hydrofoil is the airfoil of NACA0014, the chord length of fish body is 200mm, the chord length of caudal fin is 60mm, and the oscillating scope of caudal fin is  $\pm 45^\circ$ .

In the kinematics model,  $H$  is the maximum lateral oscillation amplitude at the end of the fish body, which could express different flexibilities in different values. The flexibility is better with larger lateral oscillation amplitude. If  $H$  is zero, the fish body is rigid without any oscillation, but the caudal fin will oscillate as usual.

The hydrodynamic characteristics of flexible oscillating hydrofoil were analyzed in the still water under the condition that the fish oscillated in situ. To use the commercial software Fluent, a minor water flow velocity should be available. The flow velocity was set as 0.01m/s to avoid distinct influence on the flow field.

The curves of the drag coefficient and the lateral force coefficient of fish body in a period in the still water with different oscillation amplitude are shown in Fig. 12.

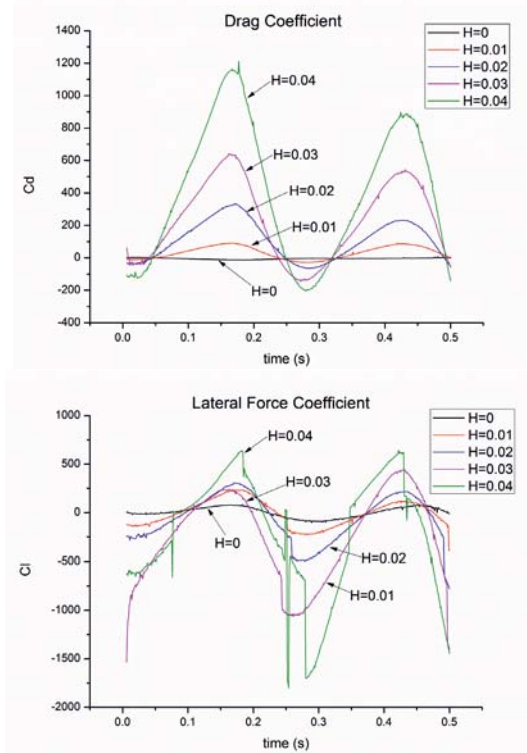


Fig. 12 Drag coefficient curves and lateral force coefficient curves of fish body in the still water

The drag coefficient curves indicate that the drag coefficient approximates a straight line when the fish body doesn't oscillate ( $H = 0$ ), which means the fish body produce no thrust force. The amplitude of the drag coefficient increases with the flexible oscillating amplitude of the fish body getting larger. There are two peak values in a fish body oscillation period and the drag coefficient variation period is half of the fish body oscillation period. The maximum values appear at the 1/4 period and 3/4 period of the fish body oscillation, which means the fish body produces the maximum thrust at these two moments. The integration value during the whole period is positive, which indicates that the fish could go forward with the fish body oscillation in the still water.

As shown in the lateral force coefficient curves, the amplitude and fluctuation of the lateral force increase with the flexibility getting better, and the lateral force generated by the oscillation is unstable. At the 1/2 period of the oscillation, the immense change occurs because the fish body oscillates from one side of the center line to another side. The lateral force consumes the energy generated by the oscillation and increases the swimming instability.

The curves of the drag coefficient and the lateral force coefficient of caudal fin during an oscillation period in the still water with different oscillation amplitude are shown in Fig. 13.

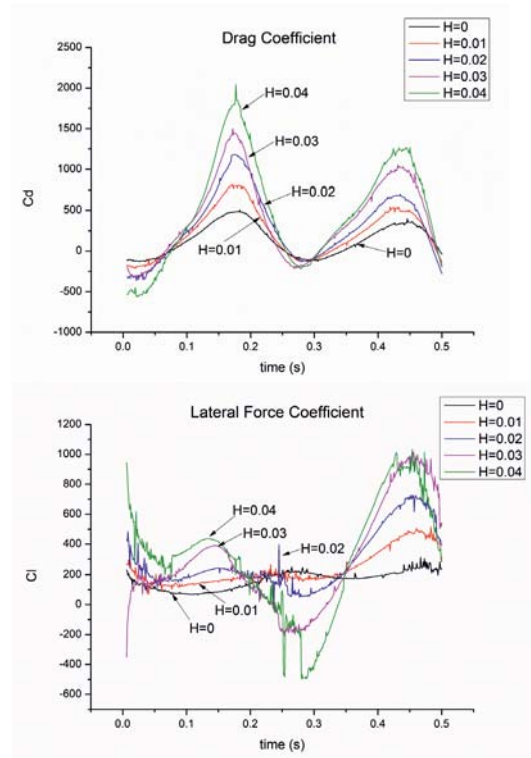


Fig. 13 Drag coefficient curves and lateral force coefficient curves of caudal fin in the still water

As shown in drag coefficient curves, the change trend of the drag coefficient produced by the caudal fin oscillation is same as that of the fish body oscillation. The amplitude of the caudal fin drag coefficient increases with the flexibility and

the oscillation amplitude of the fish body getting larger. The comparison between the drag coefficient curves of fish body and caudal fin shows that the drag coefficient value of the caudal fin is bigger, which means that the wake field generated by the fish body oscillation promotes the drag coefficient produced by the caudal fin compared with the oscillation without wake field. The drag coefficient values are almost positive in the whole period, which means the oscillation of the caudal fin has evident effects on the propulsion.

As shown in lateral force coefficient curves, the lateral force generated by the caudal fin oscillation increases with the flexibility and oscillation amplitude of the fish body getting larger under the same angle oscillation amplitude of the caudal fin, which indicates that more energy generated by the caudal fin oscillation is consumed. Most of the lateral force coefficient values are positive and the integration during an oscillation period is not equal to zero, which indicates that the caudal fin oscillation would accumulate to unidirectional force and go against the swimming. Accordingly, the unidirectional force should be reduced with the actuator controlling the amplitude and phase of the caudal fin oscillation in the fish-like robot development.

## CONCLUSION

In this research, the kinematics model for the fish-like robot movement was established and the propulsion mechanism was designed based on the model. The length of members in the propulsion mechanism was optimized by the function *fmincon* in Matlab. The motion curves of the fin-peduncle propulsion mechanism are proven to be similar with that of the ideal motion.

The phase difference between the pitching movement of caudal fin and the plunging movement of caudal peduncle was studied. When the phase angle is 90°, the propulsion mechanism would produce thrust in the whole motion period without any resistance. Meanwhile, the advantage of the articulatory fin-peduncle mechanism is obvious compared with the single oscillating caudal fin.

According to the curves of the hydrodynamic coefficients, the variation period of the drag coefficient and lateral force coefficient is half of the fish body oscillation period, and the variation period of the moment coefficient is as same as the fish body oscillation period. In the still water, the larger the flexible oscillation amplitude is, the bigger the lateral force integration value in a period is, and more energy is consumed.

## CONFLICT OF INTEREST

The authors declared that they have no conflicts of interest to this work.

## ACKNOWLEDGEMENTS

The research was supported by the front and emerging discipline team oriented project of Shandong University “marine resources and utilization of key scientific research”

(project number 2014QY006) and “The Fundamental Research Funds of Shandong University” (2016JC035), hereby thanks.

## BIBLIOGRAPHY

1. Nagai, M. (2002). Thinking fluid dynamics with dolphins. US: IOS Press.
2. Triantafyllou, M. S., and Triantafyllou, G. S. (1995). An efficient swimming machine. *Scientific American*, 272(3): 64-70.
3. Koichi, H., Tadanori, T., and Kenkichi, T., 2000, “Study on turning performance of a fish robot,” First International Symposium on Aqua Bio-Mechanisms, pp. 287-292.
4. Cheng, W., 2004, “Research on Simulation and Control Technology for Bionic Underwater Vehicle,” Ph.D. thesis, Harbin Engineering University, Harbin, China.
5. Du, R. X., Li, Z., Kamal, Y. T., Pablo, V. A., 2015, “Robot Fish,” New York: Springer Tracts in Mechanical Engineering.
6. Liang, J. H., Zhang, W. F., Wen, L., Wang, T. M., Liu, and Y. J. (2010). Propulsion and Maneuvering Performances of Two-Joint Biorobotic Autonomous Underwater Vehicle SPC-III. *Robot*, 32(6):726-731.
7. Lighthill, M. J. (1960), Note on the swimming of slender fish, *Journal of Fluid Mechanics*, Vol.9: 305-317.
8. Leroyer, A., Visonneau, M.(2005), Numerical methods for RANSE simulations of a self-propelled fish-like body, *Journal of Fluids and Structures*, Vol.20, No.7: 975-991.
9. Zhao, Y., Wang G. Y., Huang, B., Wu, Q., Wang, F. F. (2015), Lagrangian-Based Investigation of Unsteady Vertex Structure Near Trailing Edge of a Hydrofoil, *Transactions of Beijing Institute of Technology*, Vol.35, No.7: 666-670.
10. Romaneko, E. V. (2002). Fish and dolphin swimming. Bulgaria: Pensoft Publishers.
11. Wang, L., Yu, J. Z., Hu, Y. H., Fan, R. F., Huo, J. Y., and Xie, G. M. (2006). Mechanism design and motion control of robotic dolphin. *Acta Scientiarum Naturalium Universitatis Pekinensis*, 42(3): 294-301.
12. Wang, W. J. (2006). Optimal design of planar linkage based on Matlab optimization toolbox. *Light Industry Machinery*, 24(4): 76

## **CONTACT WITH THE AUTHORS**

Yanjun Liu Prof.

*e-mail: lyj111ky@163.com*

Key Laboratory of High Efficiency  
and Clean Mechanical Manufacture  
Ministry of Education  
School of Mechanical Engineering  
Shandong University, Ji'nan

**CHINA**

## OPERATION EVALUATION METHOD FOR MARINE TURBINE COMBUSTION ENGINES IN TERMS OF ENERGETICS

Marek Dzida, Prof.

Jerzy Girtler, Prof.

Gdansk University of Technology, Poland

### ABSTRACT

*An evaluation proposal (quantitative determination) of any combustion turbine engine operation has been presented, wherein the impact energy occurs at a given time due to Energy conversion. The fact has been taken into account that in this type of internal combustion engines the energy conversion occurs first in the combustion chambers and in the spaces between the blade of the turbine engine. It was assumed that in the combustion chambers occurs a conversion of chemical energy contained in the fuel-air mixture to the internal energy of the produced exhaust gases. This form of energy conversion has been called heat. It was also assumed that in the spaces between the blades of the rotor turbine, a replacement occurs of part of the internal energy of the exhaust gas, which is their thermal energy into kinetic energy conversion of its rotation. This form of energy conversion has been called the work. Operation of the combustion engine has been thus interpreted as a transmission of power receivers in a predetermined time when there the processing and transfer in the form (means) of work and heat occurs. Valuing the operation of this type of internal combustion engines, proposed by the authors of this article, is to determine their operation using physical size, which has a numerical value and a unit of measurement called joule-second [joule x second]. Operation of the combustion turbine engine resulting in the performance of the turbine rotor work has been presented, taking into account the fact that the impeller shaft is connected to the receiver, which may be a generator (in the case of one-shaft engine) or a propeller of the ship (in the case of two or three shaft engine).*

**Keywords:** work, Hamilton work, Maupertius work, energy, turbine combustion engine

### INTRODUCTION

Many publications regard the issue of marine diesel engines with piston ignition. This work is interpreted as the work conversion in the form of heat and energy work  $E$  of the engine and the transmission to the receiver at a given time  $t$  [3, 17, 18, 19]. The action interpreted this way of this type of engine (in evaluative terms) is determined by a physical quantity that has a possible to determine numerical value and unit of measure called joule-second [joule  $\times$  second]. One can consider the operation of marine turbine combustion engines in a similar way.

Such an interpretation of the operation of marine diesel engines, both piston and turbine is the result of the method

of analogy, enabling the transfer of insights from one object of research (empirical system) to another. The inspiration for the considerations made in this article on the effects of these internal combustion engines have been proposed by P.L. Maupretius and W.R. Hamilton for the operation of mechanical system. They proposed that the operation of such systems should be considered as a physical quantity that describes the change in mechanical energy over time. As a result, classical physics is known to act as an interpretation result of the energy changes in time, expressed as a product of energy and time, which makes the unit of measurement of the activity a joule-second [22, 24]. The authors assumed that the same effect may be considered for internal combustion engines with the difference that the concept of energy is

generalized as it is understood in thermodynamics. Therefore, it is assumed that the energy ( $E$ ) is a scalar characterizing the state of the internal combustion engine, both the piston and also the turbine. Energy, as the property of these engines, like and thermodynamic system, can be disclosed only if it is transformed in a way (form) of heat and / or work. For this reason, it is assumed that the heat and work execution are possible. In these engine types one can distinguish in addition to mechanical energy, e.g. Linear motion of the piston (combustion piston engines) or rotation (with the rotor of the turbine and the compressor turbine engine), such types of energy as chemical energy of fuel or air or a mixture of air-fuel internal energy of exhaust gas, thermal energy, radiant energy emitted into the environment during operation of the engine, etc. As a result, it was concluded that it would be interesting to take the problem of valuation of work of a turbine combustion engine, for example, the engine used for ship propulsion.

### FORMULATION OF THE PROBLEM OF VALUATING THE PERFORMANCE OF A TURBINE COMBUSTION ENGINE

The basis to make a consideration of the determination of the work of marine turbine combustion engines, as well as operation of marine piston engines for main ship propulsion [2, 3, 5, 6, 7, 8], were the works of W. R. Hamilton and P. L. Maupertius [22, 24]. The Hamilton work ( $D_H$ ) refers to the work of mechanical system, which causes the simultaneous change of kinematic and potential Energy, whilst the Maupertius work ( $D_M$ ) refers to a change only of the kinetic energy of the mechanical system.

Hamilton work considered in classical mechanics when dealing with equations of motion of a mechanical system (system of material points), is expressed by formula [10, 22, 24]:

$$D_H = \int_{t_1}^{t_2} E_H dt, \quad E_H = E_k - E_p \quad (1)$$

where:

$E_H$  – energy, so called Lagrange function (lagrangian),  
 $E_k$  – kinetic energy,  $E_p$  – potential energy.

A similar analytical for has the Maupertius work, which is expressed as follows [10, 22]:

$$D_M = \int_{t_1}^{t_2} 2E_k dt \quad (2)$$

In physics, the operation is interpreted as the value which is the size of the multiplication of the momentum and the displacement of the body [22]. Such action can be expressed by the formula:

$$D_p = \int_{t_1}^{t_2} p s dt = \int_{t_1}^{t_2} m v s dt = \int_{t_1}^{t_2} m a s dt = \int_{t_1}^{t_2} F s dt \quad (3)$$

where:

$p$  – momentum,  $s$  – distance,  $m$  – mass,  $v$  – speed,  
 $a$  – acceleration,  $F$  – force,  $t$  – time

The action specified by equation (3) may be important in maritime transport. It can be characterized by the energy demand needed to overcome the difficulties of stopping of a ship in motion, appearing on the collision course with other ships. From the considerations referenced in publication [21], a cargo ship (for example) travelling at a speed of 16w (~30km/h) will be stopped after 5000m, when breaking does not use the main engine of the ship and 950m when the main ship engine is used. Formula (3) allows to ascertain, how much value of the energy ( $E$ ) is needed for the ship to do the work ( $L$ ) on at a certain way for it to stop and avoid collision with another ship or hydraulic structures located on the course of the ship, which should be stopped.

In quantum mechanics, the equivalent operation is the Planck constant ( $h$ ), which specifies the ratio of energies of a time quanta of electromagnetic radiation ( $E_\nu$ ) of the frequency  $\nu$ . Thus a source of radiation that may be represented by the following formula [10, 12]:

$$h = \frac{E_\nu}{\nu} \quad (4)$$

A characteristic feature of such activities is that they are physical quantities of the unit measurement, which is *joule-second* [Js]. The same effect can be interpreted in a turbine combustion engine, that is, as the conversion in it and transfer of Energy by this engine while taking into account the time.

Operation of each turbine combustion engine may be considered in deterministic and probabilistic terms. In the deterministic approach, where the energy  $E$  does not change within the time interval  $[0, t]$ , the action ( $D$ ) of such an engine can be expressed as the following formula [11]:

$$D = Et \quad (5)$$

For a case when the energy ( $E$ ) depends on the time ( $t$ ), the action  $D = D(t)$  must be determined from the relationship:

$$D(t) = \int_0^t E(\tau) d\tau \quad (6)$$

where:

$E(t)$  – energy converted during the operation of the engine at time  $t$ ,

$[0, \tau]$  – time interval during which the engine is operational.

During the operation of the engine, Energy is disclosed at the time of its transformation, which takes two forms of work or heat. Therefore, the effect of turbine combustion engine interpreted according to the formula (6) can also be expressed as formulas, in which the under-integral functions are work ( $L$ ) and heat ( $Q$ ) [9]:

$$D_L(t) = \int_0^t L(\tau) d\tau \quad D_Q(t) = \int_0^t Q(\tau) d\tau \quad (7)$$

where:

$DL(t)$  – action connected with work in time  $t$ ,

$DQ(t)$  – action connected with heat transfer in time  $t$ ,

$[0, t]$  – engine operation time interval,

$t$  – time of engine operation, which is an independent variable.

Consideration of the operation of turbine combustion engines in this perspective seems useful because consideration of values of power of the engine based on the analysis and assessment of just how energy transfer, which is the work ( $L$ ) does not give full knowledge about its suitability for the job (work is a form of energy conversion). This insight gives an overall view of the processed energy ( $E$ ) and time ( $t$ ) of its processing, which is the size  $D(t) = E(t) \times t$ , which can be called (in the valuating sense) the operation of this type of engine. Such an understanding of turbine combustion engine includes information about how long is or can energy  $E$  be processed. If we limit the analysis of the Energy conversion only to work ( $L$ ), as a method (form) of energy conversion than taking into account the work period one can determine that the engine operation which then should be defined as  $D_L(t) = L(t) \times t$ . So understood engine operation includes information on how long work  $L$  is or may be performed. It is also an important information as the one that contains the power ( $N$ ) of the engine, which can be determined by knowing the work  $L$  and time  $t$  of its conduct. As it is known, power contains information on how quickly the work ( $L$ ) can be done.

The interpretation of the operation of the turbine combustion engine proposed by the authors of this article has the advantage that the descriptive evaluation of the action of these engines, e.g. good, not best, disturbing etc. may be replaced by the evaluation resulting from the comparison of their performance with the benchmark of using numbers from the unit of measurements which are joule-seconds.

$D_M \geq D_W$  In the presented aspect, the working of a turbine combustion engine may be considered as [3, 9, 10, 11]:

- a) Action required ( $D_W$ ), that is, one which is necessary for the job by the turbine combustion engine being the making of the required useful work ( $L_{e(W)}$ ) demanded by the receiver, e.g. generator or ship driving propeller,
  - b) Action possible ( $D_M$ ), that is, one which can be achieved by a turbine combustion engine that can perform only useful work, which is feasible at his given technical condition.
- For this reason, work can be referred to as useful possible work ( $L_{e(M)}$ ).

Therefore, it can be assumed that each turbine combustion engine is capable of suitability (fit for the job), if:

$$D_M \geq D_W \quad (8)$$

In the opposite case, when  $D_W \geq D_M$  one should assume, that the turbine combustion engine is in the state of unfitness, as it is unfit for the job.

### PROPOSAL TO DETERMINE THE PERFORMANCE OF THE TURBINE COMBUSTION ENGINE

Turbine combustion engines with different functional structure can be installed in the power units of ships [14]. In recent years, turbine combustion engines with high energy efficiency have appeared. The company *General Electric* manufactures combustion turbine of type LMS 100 with

a capacity of 100 MW, of which thermal efficiency reaches 46% [25]. However, these engines, apart from their energy, must have high reliability, which can be determined using well-known theory of reliability indicators of reliability. However, these indicators refer only to time of proper operation. Taking into consideration additional relationship (8), the reliability of a turbine combustion engine can also be applied to the values resulting from the Energy equation (6) and (7). In the following discussion an example of two shaft turbine combustion engine will be presented with a heat regenerator, consisting (for example) of the following four main devices (as part of reliability) [1, 4, 14]: compressor, combustor, turbine of combustion exhaust gas and power turbine (fig. 1).

When considering the operation of this type of engine, one can additionally consider essential equipment necessary for the smooth operation of said engine as the air filter and the heat regenerator. Such a system diagram of said machine including the air filter and the heat regenerator has been presented in Figure 2 [1, 4, 14].

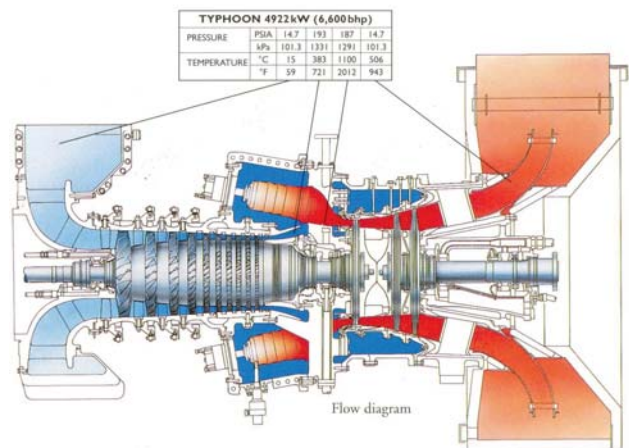


Fig. 1. Cross-section of a sample double-shaft turbine combustion engine, which elements of reliability such as compressor, combustion chamber, turbine of exhaust gas and drive turbine can be distinguished [23].

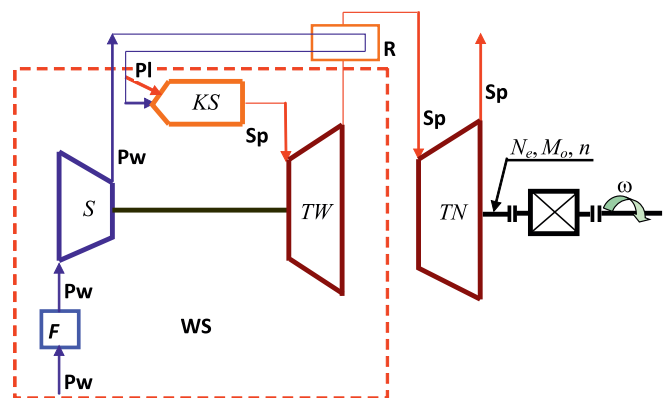


Fig. 2. Functional structure of a double shaft turbine combustion engine: F - air filter, S - compressor, KS - combustion chamber, R - regenerative heat conveyor, TW - turbine of exhaust gas, WS - exhaust gas generator, TN - drive turbine, Pl - fuel, Pw - air, Sp - fumes,  $N_e$  - power output,  $M_o$  - average torque,  $n$  - rotation speed,  $\omega$  - angular velocity.

From literature, one can ascertain, that in the case of

turbine combustion engines [1, 14, 21, 25, 23], as in the case of compression ignition engines [5, 15, 16, 20, 21], conversion of chemical energy (contained in the air-fuel mixture generated in the combustion chambers) into thermal energy (heat) and the mechanical energy of the rotor of the turbine combustion engine allows the power output  $N_e$ . This power must be generated by the time  $t$  required to perform the task by the engine. This means, that to complete the task at this time useful work  $L_e = N_e \times t$  must be performed by any suitable turbine combustion engine. Execution of this work is the result of production of torque ( $M_o$ ) possible to measure (e.g. as a result of impulsive or optical torque meters) at a certain rotation speed ( $n$ ) of each turbine combustion engine. Therefore, the operation of the turbine combustion engine interpreted as energy conversion leading to the performing of useful work  $L_e$  for time  $t$  can be expressed as the relationship:

$$D_{L_e} = \int_0^t L_e(\tau) d\tau = 2\pi \int_0^t n(\tau) M_o(\tau) \tau d\tau \quad (9)$$

where:

$L_e$  – useful work,  $t$  – time of operation of the turbine combustion engine,  $n$  – rotation speed of the turbine propeller,  $M_o$  – average torque measured at the engine shaft.

Due to the fact that the useful work of the turbine combustion engine can be expressed by formula [14]

$$L_e = N_e \cdot t = \dot{m}_{pow} b_j W \eta_k \eta_i \eta_m t \quad (10)$$

the operation of such an engine can be presented using the relationship (9) as:

$$D_{L_e} = \int_0^t L_e(\tau) d\tau = \int_0^t \dot{m}_{pow} b_j W \eta_k \eta_i \eta_m t d\tau \quad (11)$$

but,  $b_j = \frac{\dot{m}_{pal}}{\dot{m}_{pow}}$ ,  $b_j W = q_{pal}$ ,

where:

$L_e$  = useful work,  $t$  – time of operation of the turbine combustion engine,  $\dot{m}_{pow}$  – air mass stream,  $\dot{m}_{pal}$  – fuel mass stream,  $b_j$  – unit fuel requirement (fuel requirement for one unit of air),  $W$  – calorific value of the fuel,  $\eta_k$  – the efficiency of the combustion chamber,  $\eta_i$  – the efficiency of the internal circuit,  $\eta_m$  – mechanical efficiency of the turbine combustion engine,  $q_{pal}$  – heat unit contained in the fuel.

During the operation of each turbine combustion engine its condition deteriorates. This is due to the fact that the combustion of the fuel in the work areas of the engine combustion chambers and the flow generated by the exhaust turbine vane through the spaces causes the thermal and mechanical load, the most thus loaded systems is the turbine blades. Also the compressor blades of the turbine exhaust gas get contaminated (fig. 2), on which salt particles form the air get deposited. Additionally, the load of both mechanical and thermal turbine combustion engine bearings and aging of

lubricating oil causes significant increase in the consumption of these tribological over time. Considerable difficulty of ensuring the proper operation of any turbine combustion engine occurs with the appearance of instability and volatility temperature and exhaust gas pressure in the combustion chamber of such an engine. It makes possible action ( $D_M$ ) of the engine decrease over time of its life. Therefore it may happen that the engine performance required ( $D_W$ ) for the job  $Z$  in time  $t_z$  necessary to accomplish this task may be greater than the potential (i.e.  $D_W > D_M$ ). This situation, in accordance with formula (10) and (11) was illustrated in fig. 3.

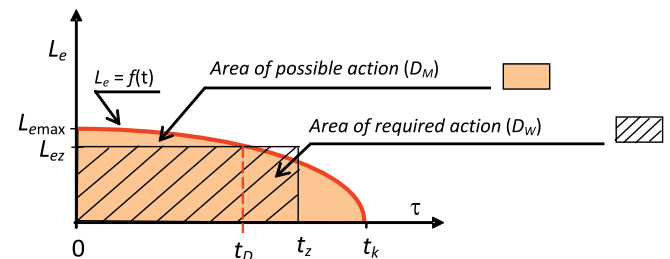


Fig. 3. Example case interpretation, where  $D_w < D_M$ ;  $D_w$  – action required,  $D_M$  – action possible,  $t_D$  – operation time of the engine, after which the  $D_w = D_M$ ,  $t_z$  – time needed to complete the task,  $t_k$  – critical time, after the expiry of which the engine cannot operate,  $t$  – operation time

Decreasing function of useful work ( $L_e$ ) during operation time ( $\tau$ ) is (fig. 3) due to decrease in the total engine efficiency  $\eta_e = \eta_k \times \eta_i \times \eta_m$  due to engine wear. It's obvious, because the turbine combustion engine, as any thermodynamic system, according to the second law of thermodynamics loses over time its arrangements as a result of rising energy dissipation, resulting in an increase in its entropy. In view of the rising time energy dissipation decreases the function  $\eta_e = f(\tau)$ , which is a consequence of the decrease in operating  $L_e(\tau)$ , which was incorporated in formulas (9) and (11). The reduction of the work at constant heat taken to the engine ( $Q_d = Q_{pal} = idem$ ), results from the following relationship [1]:

$$L_{e(k)}(\tau) = \eta_{e(k)}(\tau) \cdot Q_{pal} = \eta_{e(k)}(\tau) \cdot \dot{m}_{pow(k)}(\tau) \cdot b_{j\{k\}}(\tau) \cdot W$$

where:

$k = 1, 2, 3, \dots$  indexes corresponding to the respective moments  $t: \tau_1, \tau_2, \tau_3, \dots$ , for which inequalities  $\eta_{e(1)} > \eta_{e(2)} > \eta_{e(3)} \dots$  occur, and where  $\tau_1 < \tau_2 < \tau_3 < \dots$ , and this leads to uneven  $L_{e(1)} > L_{e(2)} > L_{e(3)} \dots$

The field of possible action ( $D_M$ ) illustrated in fig. 3 can be calculated from the formula

$$P_M = D_M = \int_0^t f(t) dt \quad (12)$$

Whereas the field of action required ( $D_W$ ) can be calculated from the formula

$$P_W = D_W = L_{ez} \cdot t_z \quad (13)$$

A comparison of formulas (12) and (13) shows that

$D_w < D_M$ , which means that the turbine combustion engine is not fit for such task Z, which may be implemented when the engine will do the work  $L_{ez}$  during time  $t_z$ .

The graphical interpretation of the action shown in fig. 3. shows that after time  $t_D$  of engine operation, the engine cannot complete the task Z. On the other hand, this engine can perform all the tasks that the time to do the job  $L_{ez}$  will be less than the time  $t_D$ , or at most equal to that time.

## COMMENTS AND CONCLUSIONS

Operation of the internal combustion engine has been interpreted as providing the Energy required at a given time, which can be expressed in the form of a physical quantity with a unit of measure called *joule-second*.

The proposed interpretation of the operation of turbine combustion engines is the first such attempt, outlined in general. It needs to be clarified, which will not be easy because of the need for detailed identification of all types of energy that are converted during operation of the engine, and so (fig. 2) in the compressor, combustion chamber, regenerative heat conveyor, turbine of exhaust gas and drive turbine. It, that the characteristics of the propeller of the ship which is the receiver of energy supplied by the turbine combustion engine should also be taken into account.

Certainly the presented considerations about the operation of turbine combustion engines have cognitive advantages, but it is difficult now to understand of how much scientific importance they are. In turn, the utilitarian qualities are difficult to assess because of a problem with the implementation of the relevant empirical research.

Similarly, one can examine the effects of other marine equipment and even devices used in other types of transports, e.g. in road transport.

## LITERATURE

- Dzida M.: Identyfikacja przyczyn niestacjonarności oraz niestabilności temperatury i ciśnienia gazów za komorą spalania turbiny gazowej. Monografie 16. Wydawnictwo Politechniki Gdańskiej, Gdańsk 2000.
- Girtler J.: Possibility of valuation of operation of marine diesel engines. Journal of POLISH CIMAC, Vol 4, No 1, 2009.
- Girtler J.: Energy-based aspect of operation of diesel engine. COMBUSTION ENGINES No 2/2009 (137).
- Girtler J.: Semi-Markov reliability model of gas turbine combustion engines. Proceedings of the Second International Scientific Symposium COMPOWER'2000. Politechnika Gdańska, Gdańsk 2000, s.133-140.
- Girtler J.: A method for evaluating theoretical and real operation of diesel engines in energy conversion formulation taking into account their operating indices. Polish Maritime Research. - Vol. 18, No. 3(70), 2011, s. 31-36.
- Girtler J.: Possibility of defining theoretical operation for diesel engines in energy terms. Combustion Engines (Silniki Spalinowe), 2011, nr 3, s. 1-9[pdf].
- Girtler J.: Valuation method for operation of crankshaft-piston assembly in combustion engines in energy approach. Journal of POLISH CIMAC. - Vol. 6, no. 1 (2011), s. 89-98.
- Girtler J.: The method for determining the theoretical operation of ship diesel engines in terms of energy and assessment of the real operation of such engines, including indicators of their performance. Journal of POLISH CIMAC. - Vol. 6, no. 1 (2011), s. 79-88.
- Girtler J.: Energetyczny aspekt diagnostyki maszyn. Diagnostyka. Nr 1(45), 2008, s.149-156.
- Girtler J.: Quantitative interpretation of energy-based systems and index of their reliability. Journal of Polish CIMAC. Vol 3, nr 1, 2008, s.87-94.
- Girtler J.: Conception of valuation of combustion engine operation. Journal of KONES Powertrain and Transport. Vol. 15, nr 2, 2008, s. 89-96.
- Gribbin J.: In Search of Schrödinger's Cat Quantum Physics Reality. Wyd. polskie: W poszukiwaniu kota Schrödingera. Zysk i S-ka Wydawnictwo s.c. Poznań 1 997.
- Helwitt P.G.: Fizyka wokół nas. PWN, Warszawa 2001.
- Kowalski A.: Okrętowe turbozespoły spalinowe. WM, Gdańsk 1983.
- Piotrowski I., Witkowski K.: Okrętowe silniki spalinowe. Wyd. TRADEMAR, Gdynia 1996.
- Piotrkowski I., Witkowski K.: Eksploatacja okrętowych silników spalinowych. AM, Gdynia 2002.
- Roślanowski J.: Identification of ships propulsion engine operation by means of dimensional analysis. Journal of POLISH CIMAC, Vol. 4, No 1, 2009.
- Rudnicki J.: Loads of ship main diesel engine in the aspect of practical assessment of its operation. Journal of POLISH CIMAC, Vol. 3, No 1, 2008.
- Rudnicki J.: On making into account value of operational applied to ship main propulsion engine as an example. Journal of POLISH CIMAC, Vol. 4, No 1, 2009.
- Wajand J.A., Wajand Jan T.: Tłokowe silniki spalinowe średnio- i szybkoobrotowe. WNT, Warszawa 2000.

21. Wojnowski W.: Okrętowe siłownie spalinowe. Część I. Wyd. Akademia Marynarki Wojennej, Gdynia 1998.
22. Encyklopedia fizyki współczesnej. Praca zbiorowa. Redakcja Nauk Matematyczno-Fizycznych i Techniki Zespołu Encyklopedii i Słowników PWN. PWN, Warszawa 1983.
23. Informator European Gas Turbine Limited. England. Publication No 108/1997.
24. Leksykon naukowo-techniczny z suplementem. Praca zbiorowa. Zespół redaktorów Działu Słownictwa Technicznego WNT. WNT, Warszawa 1989.
25. McNeely M.: GE's LMS 100, a „Game Changer”. New gas turbine combines frame and aero technology, achieves 46% efficiency. Diesel & Gas Turbine. Worldwide. January-February 2004, pp.38, 40, 42 and 43.

## CONTACT WITH THE AUTHOR

Marek Dzida

*e-mail: dzida@pg.gda.pl*

Jerzy Girtler

*e-mail: jgirtl@pg.gda.pl*

Gdańsk University of Technology  
FACULTY OF OCEAN ENGINEERING AND SHIP  
TECHNOLOGY  
11/12 Narutowicza St.  
80 - 233 Gdańsk

**POLAND**

## 3-D SIMULATION OF VERTICAL-AXIAL TIDAL CURRENT TURBINE

Zhang Zhiyang,

Ma Yong,

Jiang Jin,

Liu Weixing,

Ma Qingwei,

Shipbuilding Engineering Collage, Harbin Engineering University, Heilongjiang, Harbin, China

### ABSTRACT

*Vertical-axial tidal current turbine is the key for the energy converter, which has the advantages of simple structure, adaptability to flow and uncomplex convection device. It has become the hot point for research and application recently. At present, the study on the hydrodynamic performance of vertical-axial tidal current turbine is almost on 2-D numerical simulation, without the consideration of 3-D effect. CFD (Computational Fluid Dynamics) method and blade optimal control technique are used to improve accuracy in the prediction of tidal current turbine hydrodynamic performance. Numerical simulation of vertical-axial tidal current turbine is validated. Fixed and variable deflection angle turbine are comparatively studied to analysis the influence of 3-D effect and the character of fluid field and pressure field. The method, put the plate on the end of blade, of reduce the energy loss caused by 3-D effect is proposed. The 3-D CFD numerical model of vertical-axial tidal current turbine hydrodynamic performance in this study may provide theoretical, methodical and technical reference for the optimal design of turbine.*

**Keywords:** Tidal current energy, vertical-axial turbine, hydrodynamic performance, CFD, numerical simulation, 3-D effect

### INTRODUCTION

Tidal current energy becomes an alternative of fossil petroleum as it is renewable and greatly reserved across the world [8] [15] [4]. The key equipment to extract tidal current energy is the tidal turbine. Vertical-axial turbine has simple structure and small draft, adapts to various flow directions, rarely faces cavitation problems, therefore it becomes the hot spot in recent research for its many advantages [22] [23]. The purpose of vertical-axial turbine study is to optimize the design, improving the prediction of hydrodynamic performance. Such prediction is based on experimental and theoretical methods. The problem in the experimental prediction is the long period and high cost. Comparatively, theoretical prediction is effective and

economic. Hitherto three main theoretical methods are widely used in engineering practice. The first is based on the law of momentum, the second is based on vortex theory, the third is based on CFD for viscous flow [6] [3] [5]. As the rapid development of computer science, CFD methods becomes more and more effective and economic [9] [13] [7] [19] [10] [12]. To accomplish the prediction in a realistic, accurate, and fast way, many researchers have applied dynamical boundary model [2], turbulence model [1] [20] [17], unsteady rotation method, free surface effect, and many other approaches. In 2008 Sun studied the dynamical boundary problem of H-type turbine using slipping mesh method [18]. Yeung et al used STAR-CD to simulate k- $\epsilon$  turbulence model to study cycloid-type vertical-axial turbine [14]. In 2010, a refined UDF control slipping mesh method was applied on cycloid-type turbine by

Luo et al [16, 21, 24]. In 2011, Li studied further in the accuracy and reliability in such CFD simulation, proposing a method to calculate dynamical model under unsteady rotation. This method gave a possibility to simulate freely variable deflection angle turbine[25].

Until now the understanding of the validation of 2-D and 3-D simulation, the mechanism of different performance between 2-D and 3-D simulation, and how to reduce the energy loss caused by 3-D effect is not sufficient. These unknown aspects are key factors in improvement of efficiency. In this study we used CFD method to examine the validation of simulation, establish techniques of vertical-axial turbine simulation, and improve the accuracy of prediction. 2-D and 3-D simulation are validated and comparatively studied. Along with blade optimal control techniques, fixed and variable deflection angle turbine is simulated in 3-D to analysis the influence of 3-D effect and the character of fluid field and pressure field. A method to reduce the energy loss caused by 3-D effect is proposed as a reference for turbine design and optimization

## ANALYSIS OF FLUID DYNAMICS

### ANALYSIS OF FLUID DYNAMICS

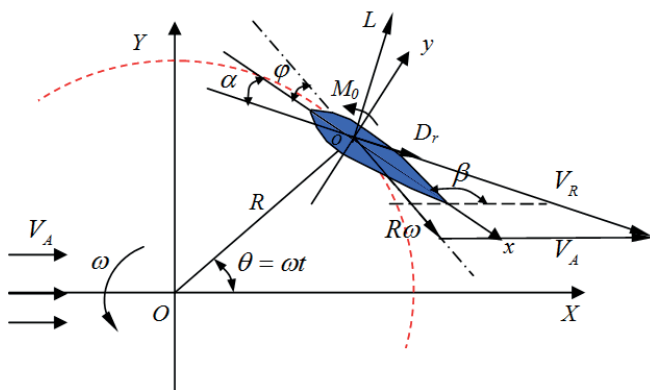


Fig. 1. Coordinate system and forces on the blades

The cross section of the vertical-axial turbine blade is shown as Fig. 1. The blades are uniformly arranged along the circle. The flow velocity is  $V_A$ , driving the turbine to rotate with angular velocity  $\omega$ , converting kinematic of the flow to electric power. Here we assume the turbine rotates counter-clockwise and  $\omega$  is constant. Global coordinate OXYZ is established, the center of the main shaft is located at the original point. The flow is along the X direction. A local coordinate oxyz is attached on any blade. Its self-rotating center is at o the origin. The arc line is parallel to x coordinate, pointing from the end of the blade to the front.  $\theta$  is location angle,  $\varphi$  is the deflection angle of the blade.

The relative velocity  $\vec{V}_R$  of blade and flow satisfies

$$\vec{V}_R = \vec{\omega} \times R + \vec{V}_A \quad (1)$$

$\vec{V}_R$  can be computed by

$$V_R = \sqrt{V_A^2 + (R\omega)^2 + 2R\omega \cdot V_A \sin \theta} \quad (2)$$

The hydrodynamic attack angle  $\alpha$  is the angle between  $V_R$  and x-axis, it is positive when counterclockwise, negative when clockwise.

$$\tan \alpha = \frac{V_A \cos(\theta + \varphi) - R\omega \sin \varphi}{V_A \sin(\theta + \varphi) + R\omega \cos \varphi} \quad (3)$$

As shown in Fig.1, the force acted on a single blade by the flow is resolved into lift force  $L$ , damping force  $D_r$ , and the momentum  $M_o$  to o. We can resolve the force on a blade into to resultant parts,  $f_x$  along the arc and  $f_y$  perpendicular to the arc, the point of action is o.

$$\vec{f} = (f_x, f_y) = (D_r, L) \begin{pmatrix} -\cos \alpha & \sin \alpha \\ \sin \alpha & \cos \alpha \end{pmatrix} \quad (4)$$

Another way is to resolve the force on normal and tangent directions,

$$\vec{f}' = (f_n, f_t) = (D_r, L) \begin{pmatrix} -\cos(\alpha + \varphi) & \sin(\alpha + \varphi) \\ \sin(\alpha + \varphi) & \cos(\alpha + \varphi) \end{pmatrix} \quad (5)$$

The momentum of a single blade to the turbine is

$$q = f_t R + M_o = R[L \sin(\alpha + \varphi) - D_r \cos(\alpha + \varphi)] + M_o \quad (6)$$

The above discussion is all about instantaneous quantity of a single blade. When the turbine rotates steadily, the forces on the blade and main shaft are periodic. Assume the number of blades is  $Z$ , in a period, the average momentum  $\bar{Q}$  and average power  $\bar{P}$  are

$$\bar{Q} = \frac{Z}{2\pi} \int_{-\pi/2}^{3\pi/2} q(\theta) d\theta \quad (7)$$

$$\bar{P} = \frac{Z}{2\pi} \int_{-\pi/2}^{3\pi/2} q(\theta) \omega d\theta \quad (8)$$

Here we define the dimensionless coefficients

$$\lambda = \frac{R\omega}{V_A}, \quad Re = \frac{\rho V_A C}{\mu}, \quad \sigma = \frac{ZC}{2\pi R}, \quad \bar{C} = \frac{C}{R},$$

$$C_p = \frac{P}{0.5 \rho V_A^3 D b} = f(\rho, \mu, V_A, \omega, R, b, Z, C, C_1, \varphi),$$

$$\bar{C}_1 = \frac{C_1}{C}, \quad \delta = \frac{b}{C}$$

Where  $\lambda$  is the ratio of blade velocity and flow velocity,  $R_e$  is Reynold number,  $\sigma$  is blade denseness, the ratio of sum of arc lengths and orbit circumference,  $\bar{C}$  is the ratio of blade arc and diameter,  $\bar{C}_1$  is the ratio of the distance from the shaft to the tip and the chord length,  $\delta$  is the aspect ratio,  $C_p$  is the efficient coefficient,  $\mu$  is the viscosity of the fluid,  $R$  is the radius of the turbine,  $D$  is its diameter,  $b$  is the span of the blade, and  $P$  is the power of the turbine.

### CONTROL OF DEFLECTION ANGLE

When computing hydrodynamic performance of the turbine, equations 9 and 10 are used to control blade motion[11]. Equations 9 and 10 shows the relation between speed ratio and denseness of  $a$  and  $b$ . If the location of blade small shaft (0.3 C) and flow velocity (1 m/s) are determined, the values of  $a$  and  $b$  can be obtained by merely given speed ratio and denseness of the turbine, and therefore obtain the curve of deflection angle. Hence for any turbine model (if the blade type, location of small shaft and flow velocity do not change), the change of deflection angle relating to a specific speed ratio can be obtained.

$$a = \frac{p_1 + p_2 \ln(x) + p_3 \ln^2(x) + p_4 \ln^3(x) + p_5 y + p_6 y^2}{1 + p_7 \ln(x) + p_8 \ln^2(x) + p_9 \ln^3(x) + p_{10} y + p_{11} y^2} \quad (9)$$

$$b = \frac{q_1 + q_2 \ln(x) + q_3 \ln^2(x) + q_4 y + p_5 y^2 + p_6 y^3}{1 + q_7 \ln(x) + q_8 \ln^2(x) + q_9 \ln^3(x) + q_{10} y} \quad (10)$$

Where  $x$  is the speed ratio,  $y$  is the denseness,  $p_1$  to  $p_{11}$  and  $q_1$  to  $q_{10}$  are given in Table 1.

Tab. 1. Coefficients

$p_1$	2.408E+14	$q_1$	35.55
$p_2$	-1.025E+15	$q_2$	-115.35
$p_3$	3.520E+15	$q_3$	72.91
$p_4$	-1.360E+15	$q_4$	131.03
$p_5$	6.706E+14	$q_5$	-320.38
$p_6$	-1.125E+16	$q_6$	-241.51
$p_7$	-4.332E+13	$q_7$	-2.77
$p_8$	9.200E+13	$q_8$	0.54
$p_9$	1.028E+14	$q_9$	1.50
$p_{10}$	1.512E+14	$q_{10}$	1.66
$p_{11}$	-9.267E+14		

## COMPUTING CONFIGURATION AND MESHING

In this study the numerical simulation is mainly based on ANSYS CFX, the entire calculation region is divided into blade region, rotation region, and outflow region. Blade region includes a small region containing the blade, using a cylinder to enclose the blade and making the mesh denser around the blade. Rotation region contains the whole turbine using another cylinder. Outflow region is the entire flow region outside the turbine. Slip mesh is applied to connect the three regions to guarantee the computing accuracy. The meshes of the model are all structural mesh, with refinement around the blade tip. Instantaneous simulation is used, the turbine turns  $3^\circ$  in each time step. The inflow is set uniform and the outflow and surrounding boundary is set open boundary condition. The absolute pressure is 1atm. No-slip condition is used on the blade surface, and turbulence model is chosen as SST model. The mesh of outflow region is shown in Fig.2, blade region in Fig.3, and rotation region in Fig. 4. The meshing details of the blade surroundings are shown in Fig.5, the refinement of blade tip in Fig.6.

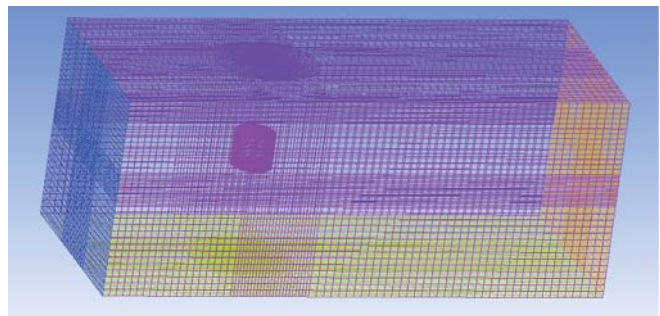


Fig.2. Flow region

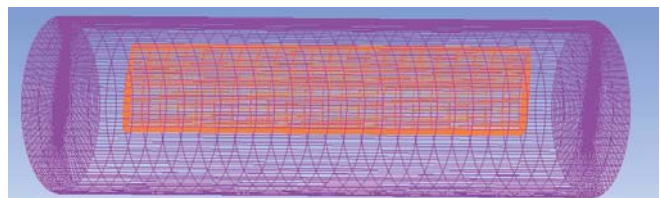


Fig.3. Blade region

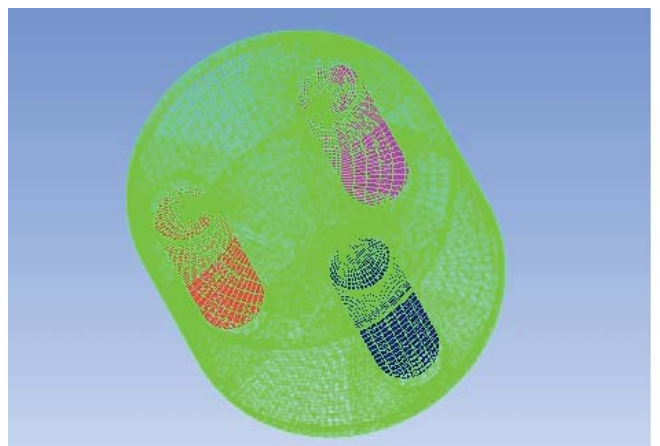


Fig. 4. Rotation region

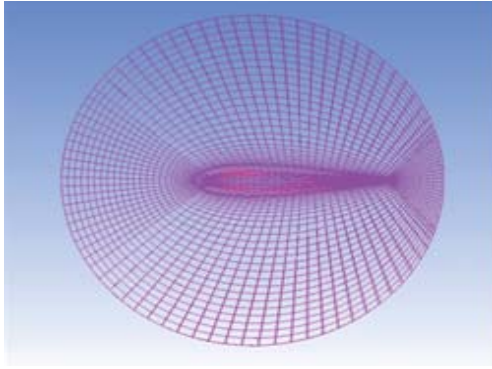


Fig.5. Mesh refinement around the blade

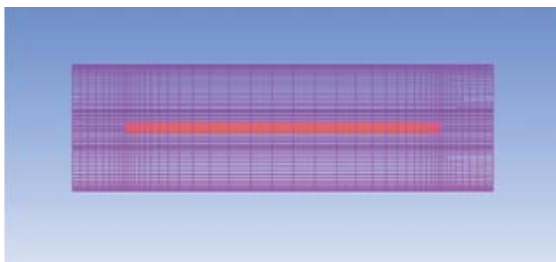


Fig.6. Mesh refinement at blade tip

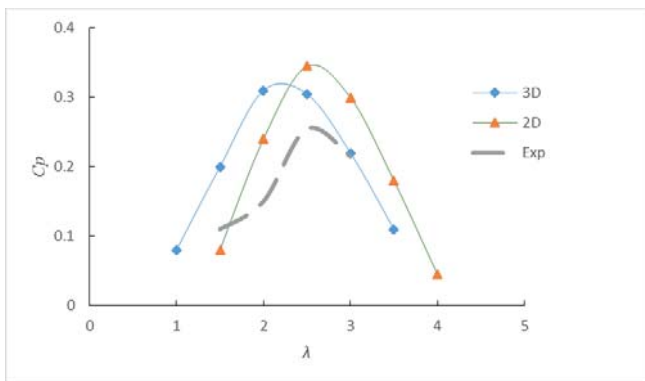


Fig.7. Result of numerical simulation

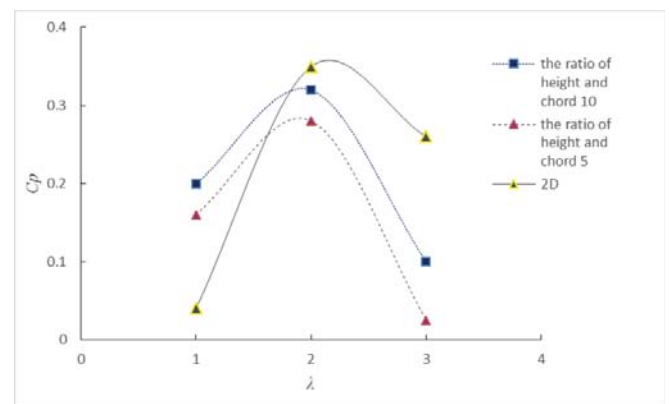


Fig.8. Simulation result of fixed deflection angle turbine

## SIMULATION RESULTS AND ANALYSIS

This section investigates the validity of 3-D numerical simulation, influence of 3-D effect and the reduction of 3-D effect, fixed and variable deflection angle turbine are computed, 2-D and 3-D simulation are compared, the case with vortex elimination plate is also simulated.

## VALIDATION OF 3-D SIMULATION

Validation of 3-D simulation is demonstrated using NACA0018 blade. The number of blades is 3, the arc length of blades is 0.1524m, arc length to radius ratio is 0.3. As shown in Fig.7, there is difference between the results of numerical method and experiment, where in 2-D simulation the changing trends of these results are the same, but the numerical result is much higher than the experimental result. This is due to the infinite length of the blade in 2-D simulation when 3-D effect is neglected. But when 3-D effect is under concern, the numerical result is close to the experimental result.

## SIMULATION OF FIXED AND VARIABLE DEFLECTION ANGLE TURBINE

### (1) Fixed deflection angle turbine simulation

The difference between 2-D and 3-D simulation is the span of foil. In 2-D simulation the span of foil is regarded as infinite, while in 3-D simulation it is a determined value. At the top and bottom ends of the blade there is large flow division, many vortices are generated and cause energy lose. Here we choose turbine modes of aspect ratio values 5 and 10 respectively to perform 3-D simulation, then compare with the result of 2-D turbine models. The results are shown in Fig.8.

As shown in Fig.8, when the speed ratio is large, the efficiency is higher in 2-D simulation, which is coincide with the analysis in the last section and interprets that 3-D effect can reduce the turbine efficiency. When the speed ratio is small, 3-D efficiency is much higher than 2-D efficiency, which contradicts the former analysis and needs further discussion. From the comparison between the models with aspect ratios 5 and 10, we find that higher efficiency occurs at larger aspect ratio, indicating that the increase of aspect ratio shall reduce 3-D effect, therefore increasing the aspect ratio can be used to reduce 3-D effect.

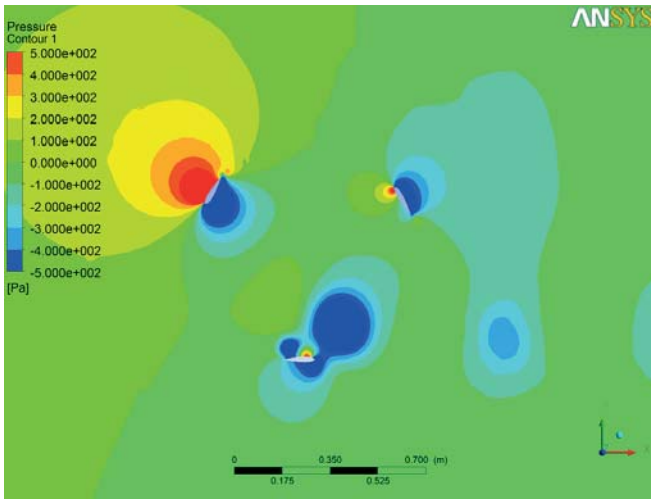


Fig. 9. 2-D simulation pressure nephogram at  $\lambda=1$

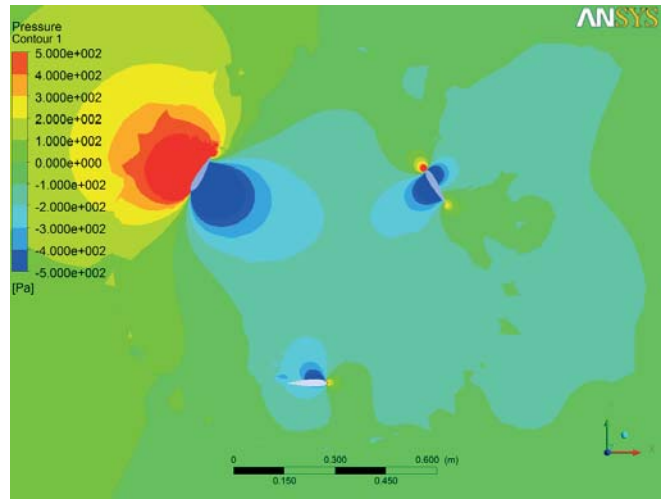


Fig. 12. 3-D simulation pressure nephogram at  $\lambda=2$

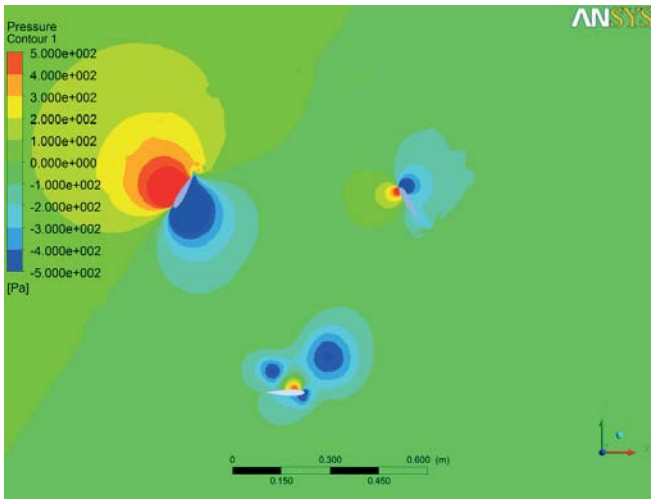


Fig. 10. 3-D simulation pressure nephogram at  $\lambda=1$

Large error occurs in 3-D simulation when the speed ratio is small. Fig. 9 10 11 12 are pressure nephograms of the flow field in 2-D and 3-D simulations respectively. The turbine is at the same place. We find that the pressure around the blade is lower in 2-D simulation, particularly for the blade of location angle  $30^\circ$ , the whole back of this blade is in low pressure region. But in 3-D simulation only a small part is in low pressure region. Pressure drop on the blade back is often caused by over large attack angle, which leads to flow separation. We can conclude that higher efficiency occurs in 3-D simulation because when flow separation seldom happen, the computing result of lift is larger, therefore the efficiency is larger.

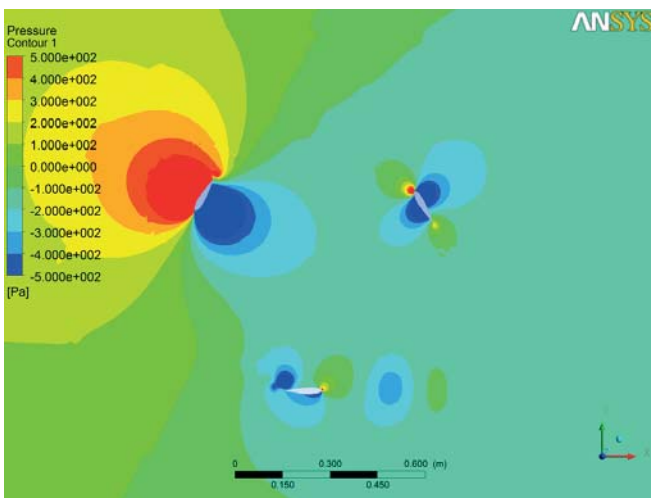


Fig. 11. 2-D simulation pressure nephogram at  $\lambda=2$

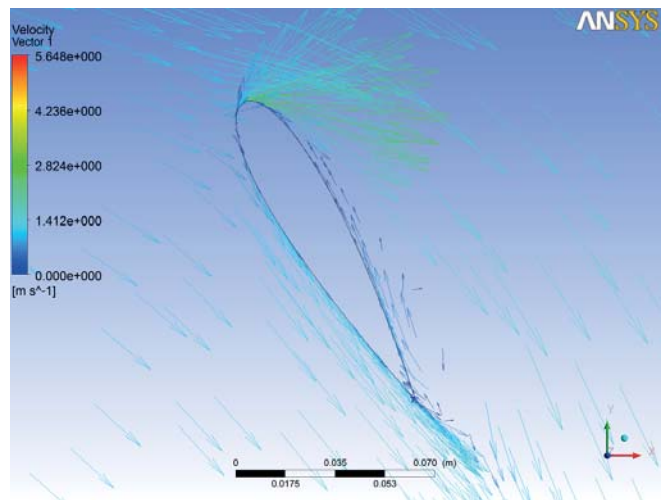


Fig. 13. 2-D velocity vectors at  $\lambda=1$

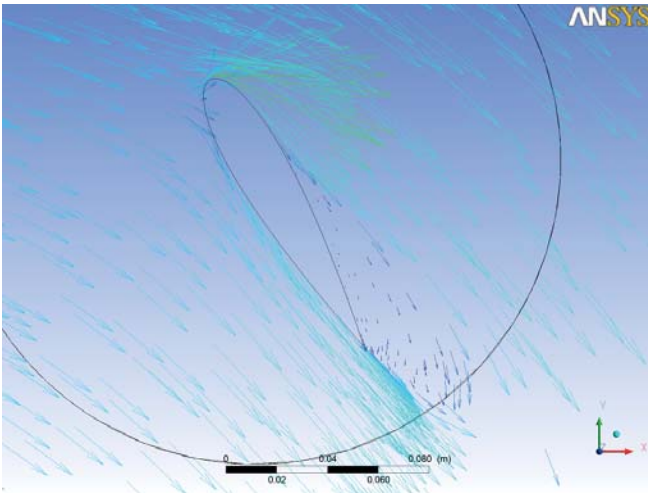


Fig. 14. 3-D velocity vectors at  $\lambda=1$

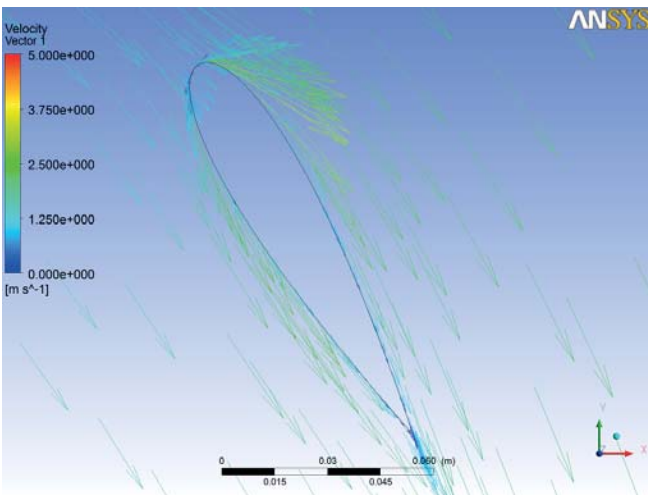


Fig. 15. 2-D velocity vectors at  $\lambda=2$

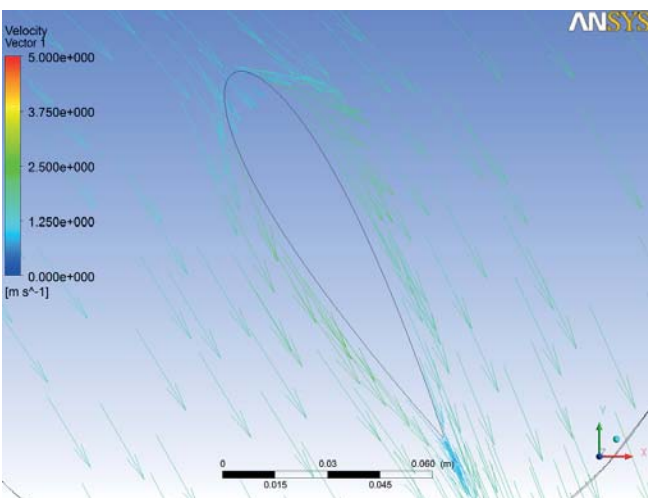


Fig. 16. 3-D velocity vectors at  $\lambda=2$

When the location of blade is  $30^\circ$ , backflow occurs. In Fig.5.8 backflow occurs only at the root of the blade, this indicates that in 3-D simulation flow separation seldom happens, the same result as in the above section.

Fig.13 to Fig.16 are pressure nephograms and velocity vectors in 2-D and 3-D simulation. No big difference can be found between the two.

The range of attack angle of the blades is wide when the speed ratio is small, the blades often stall under this situation, making the results in 3-D simulation slightly higher, on the other hand, 2-D result is better, therefore 2-D simulation should be employed under small speed ratio. When under medium speed ratio, the range of attack angle becomes narrow, 3-D simulation considers 3-D effect and reflect real physical properties of the model, therefore is more accurate

## (2) Variable deflection angle turbine simulation

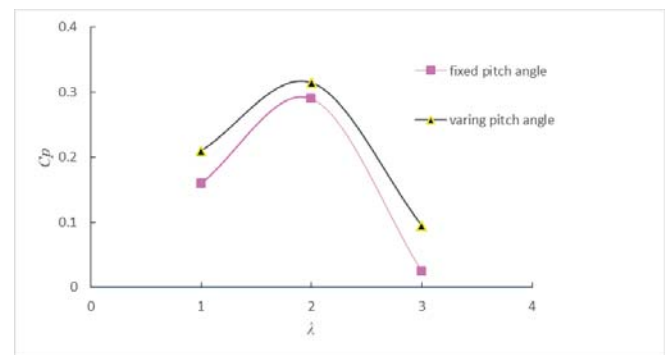


Fig. 17. Comparison of efficiency between fixed and variable deflection angle turbine

The control methods of dynamic mesh in 3-D and 2-D simulations are same, but in 3-D simulation the mesh number is much larger, the computing time is longer. To study the hydrodynamic performance of the variable deflection angle turbine, we compare it with a fixed deflection angle turbine (Fig.17). A model of span of foil equals to 5 is used.

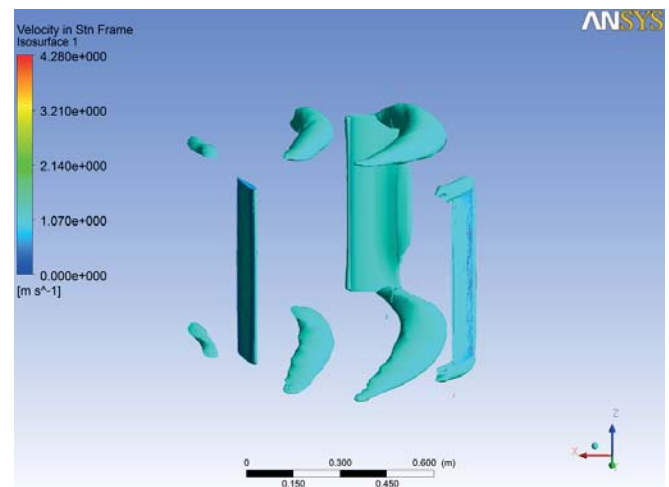


Fig.18 Tip vortices of fixed deflection angle blade at  $\lambda=2$

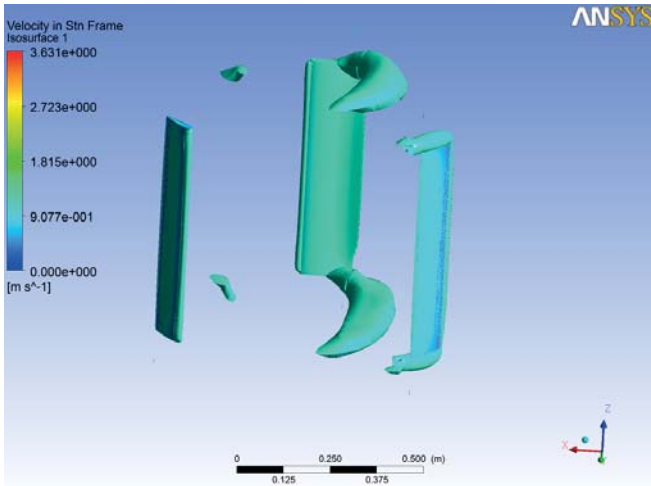


Fig.19. Tip vortices of variable deflection angle blade at  $\lambda=2$

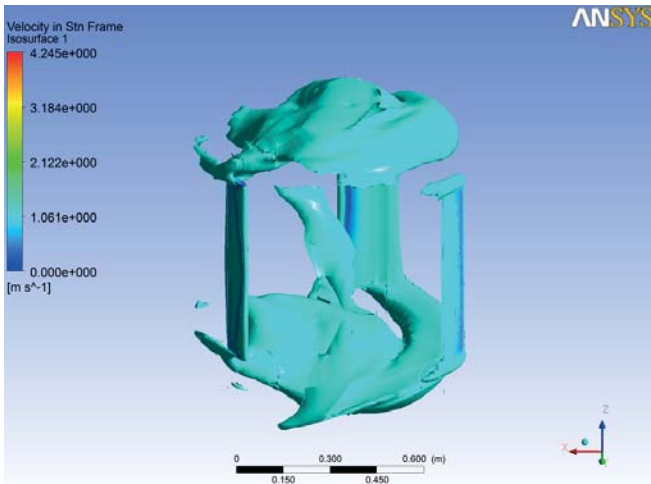


Fig.20. Tip vortices of fixed deflection angle blade at  $\lambda=3$

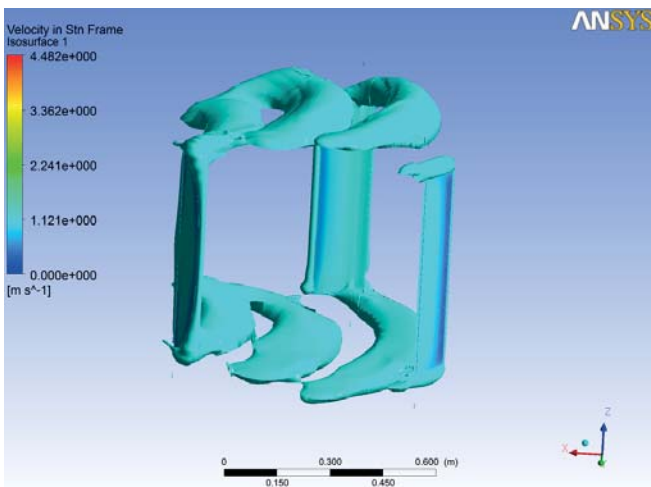


Fig.21. Tip vortices of variable deflection angle blade at  $\lambda=3$

From Fig.18 to Fig.21, vortices occurs in the wake of the two blade ends, causing energy lose, and this is the greatest difference between 3-D and 2-D simulation, since water flows with different velocities on the top and bottom surfaces of the blade, a pressure difference occurs and push water at the end of blade from high-pressure region to low pressure region, vortices therefore are generated. Else we find that under the same speed ratio, variable deflection angle turbine generate more vortices than its fixed counterpart. This is also the reason that variable deflection angle turbine is more effective. When speed ratio is increased, the vortices become stronger.

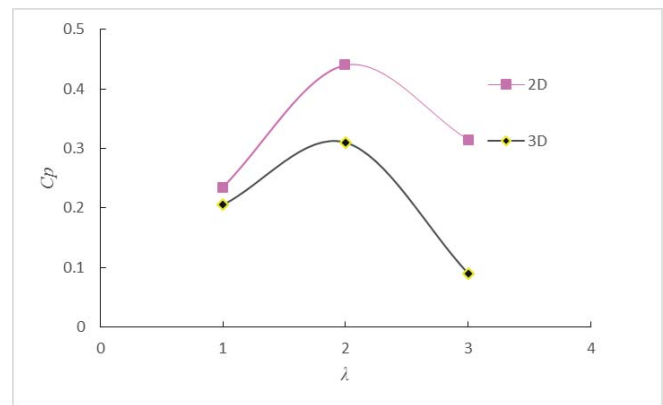


Fig. 22. Comparison of efficiency between 2-D and 3-D variable deflection angle turbine

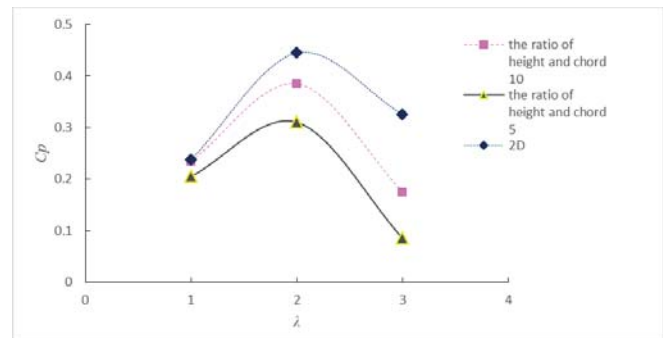


Fig. 23 Influence of aspect ratio

We find that 2-D simulation of variable deflection angle turbine is more effective than that in 3-D simulation, the difference between the two becomes larger as the speed ratio grows. We know that the difference between 2-D and 3-D simulation is the span of foil, and therefore concludes that the influence of aspect ratio becomes larger as the speed ratio becomes larger, this may because as the speed ratio increases, the relative velocity between blade and water becomes larger, more and stronger vortices occurs and take away more energy.

### STUDY OF 3-D EFFECT

3-D effect of vertical-axial turbine is mainly caused by aspect ratio. For variable deflection angle turbine with aspect

ratio 5 and 10, the compare result of efficiency is shown in Fig.22. From Fig.23 we see that as the aspect ratio increases, the turbine efficiency under each speed ratio raises, but it is lower in 3-D simulation than in 2-D simulation in all cases. Therefore as the aspect ratio increases, 3-D effect becomes weak, and if the aspect ratio increases continually, the efficiency curve of 3-D simulation shall approach asymptotically to that of 2-D simulation. In the figure we also find that as the speed ratio increases, the difference between the three curves becomes larger and larger, this is because the increase of speed ratio reinforces the influence of 3-D effect. If we intend to reduce 3-D effect we should take the following two methods: (1) make the aspect ratio large, (2) make the speed ratio small.

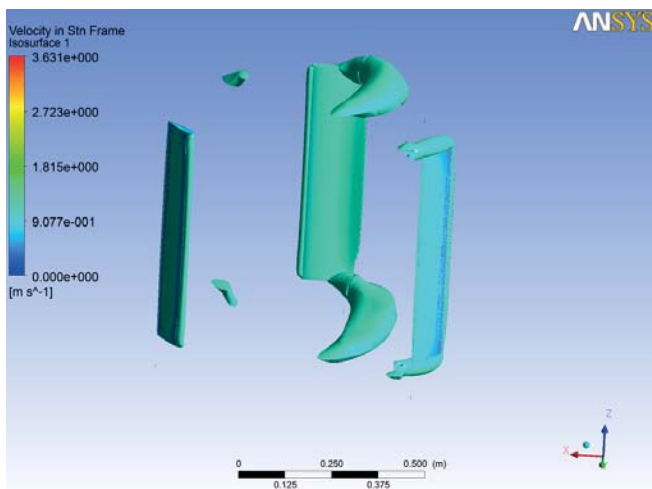


Fig. 24. Vortices at  $\lambda=2$  and aspect ratio 5

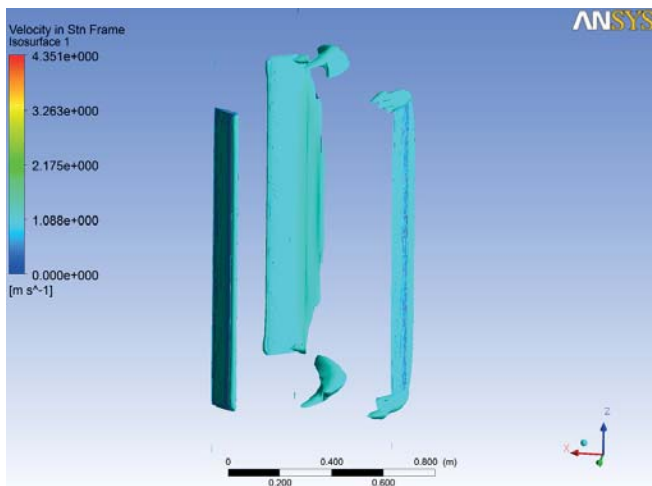


Fig. 25. Vortices at  $\lambda=2$  and aspect ratio 10

Fig.24 to Fig.27 depict vortices at the blade ends under different aspect ratios. We find that the change of aspect ratio do not influence the vortices much, but when the aspect ratio is large, the total turbine efficiency raises, but the energy lose caused by vortices keep its value, therefore make small effect on the turbine.

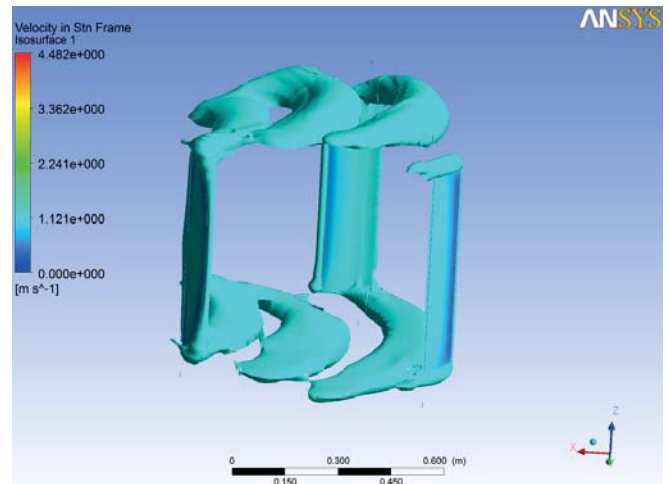


Fig. 26. Vortices at  $\lambda=3$  and aspect ratio 5

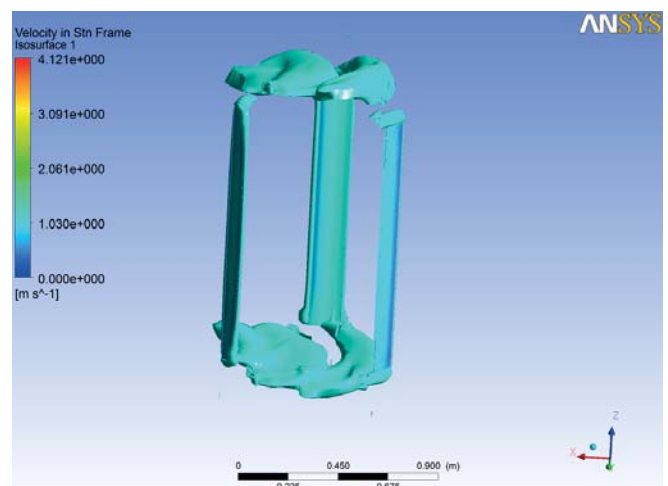


Fig. 27. Vortices at  $\lambda=3$  and aspect ratio 10

### METHOD TO REDUCE ENERGY LOSE CAUSED BY 3-D EFFECT

The vortices at the blade ends cause energy lose. To reduce such lose we can add a plate at the blade ends, which can restrain the generation of vortices. We use CFX software to simulate its performance to test its effect. The model of blade is chosen as NACA0018, the mesh is shown in Fig.28 and Fig.29.

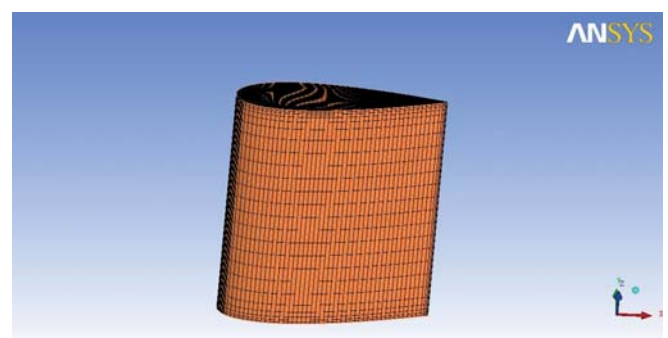


Fig. 28. Blade without plate

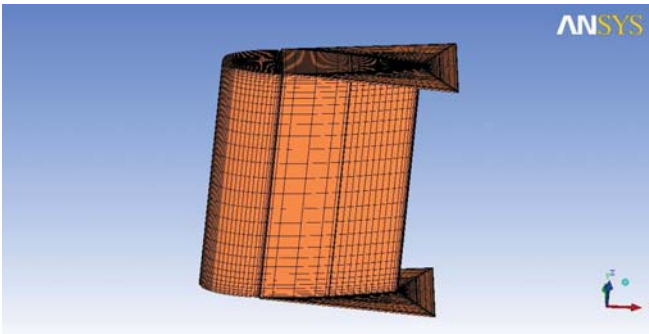


Fig. 29. Blade with plate

Let the inflow velocity be 3 m/s, using CFX software to simulate the lift coefficient and momentum coefficient of the two kinds of blades with different attack angles. The details are shown in the following figure.

We find from Fig.30 to Fig.32 that when the blades are added plates, its lift coefficient and drag coefficient both have an increase of 10 %, but the drag coefficient is far less than the lift coefficient, therefore the overall performance of the turbine has a considerable reinforcement. As the vertical –axial turbine is lift type turbine, its hydrodynamic performance will be prompted after installing a plate with a 10 % increase of efficiency.

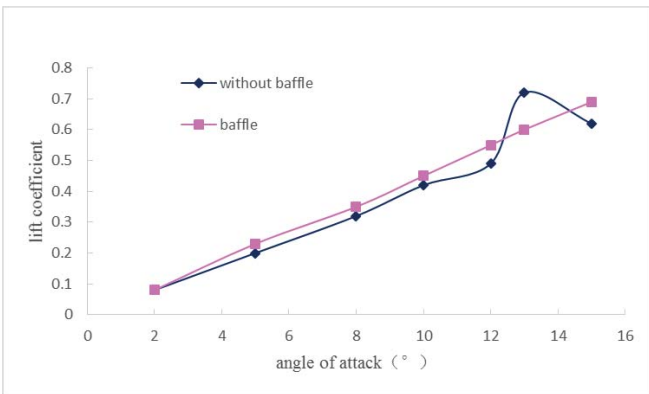


Fig. 30. Comparison of lift coefficient

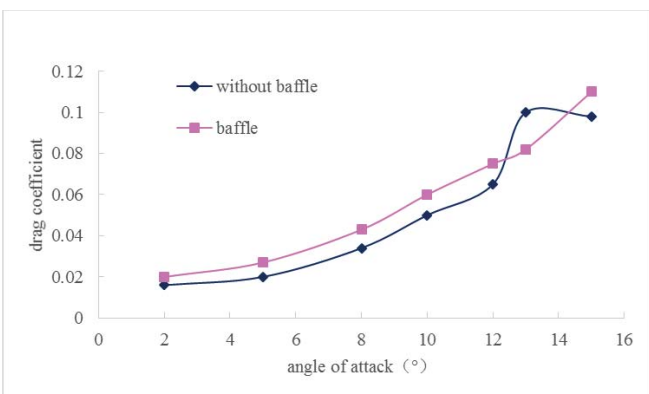


Fig. 31. Comparison of drag coefficient

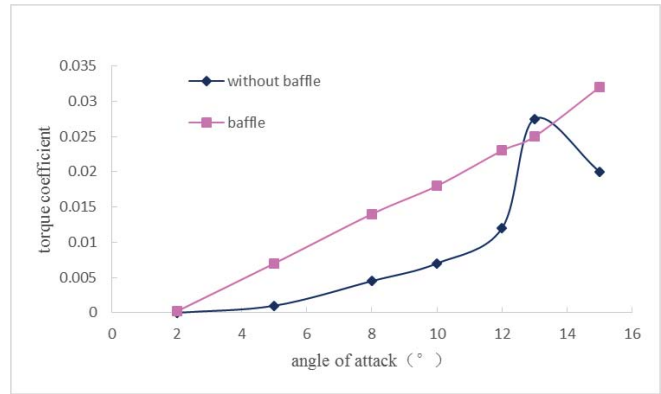


Fig. 32. Comparison of blade momentum

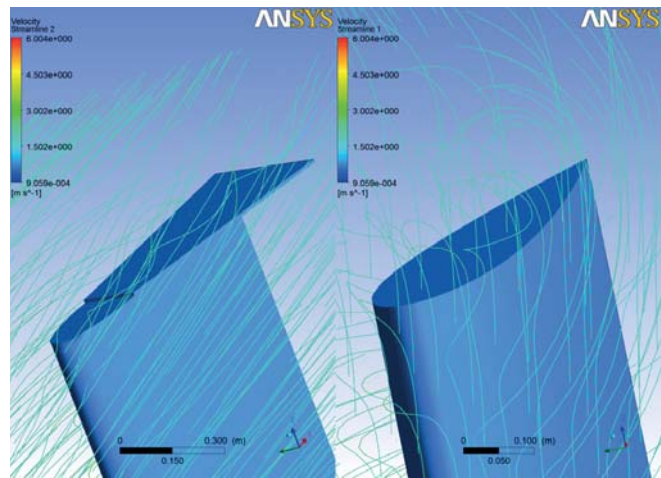


Fig. 33. Comparison of stream line at blade tip with attach angle equals to 15°

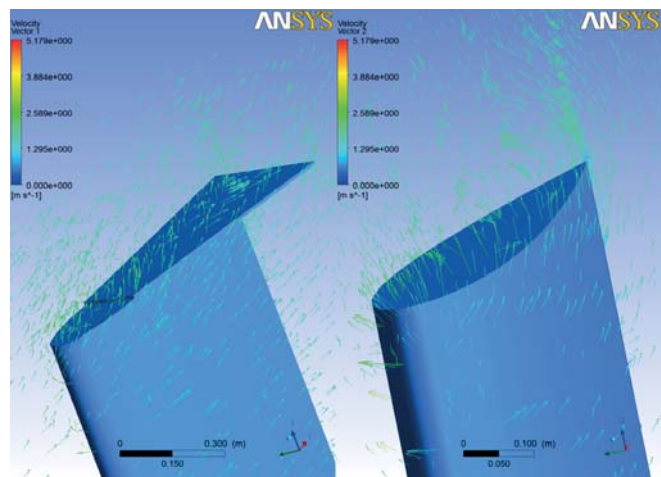


Fig. 34. Comparison of velocity vector at blade tip with attach angle equals to 15°

In Fig.33 (streamline) and Fig.34 (velocity vector), the plates at the ends of the blade can effectively prevent the vortices from being generated, reduce energy lose and enhance its performance.

## CONCLUSION

(1) When the speed ratio is large, 3-D simulation is more accurate than 2-D simulation, but under small speed ratio flow separation is much easy to happen, making the results of hydrodynamic performance computation inaccurate.

(2) The energy lose caused by energy lose generated by vortices at the ends of blades is the main reason of difference between 3-D simulation results and 2-D simulation results. Such 3-D effect increases as the speed ratio increases and decreases as the aspect ratio increases. As the aspect ratio becomes very large, 3-D simulation results is close to 2-D results.

(3) Adjusting deflection angle to control the range of attack angle is an effective way to improve the turbine efficiency by 5 % in the method proposed in this paper.

(4) Adding a plate at the ends of blade can effectively reduce the generation of wake vortices and therefore weaken the 3-D effect, the efficieney increases by about 10 %.

## ACKNOWLEDGEMENT

This work was supported by National Natural Science Foundation of China (No.51309069, 11572094), the Special Funded of Innovational Talents of Science and Technology in Harbin (No.RC2014QN001008), the China Postdoctoral Science Foundation (No.2014M561334,2015T80330), the Heilongjiang Postdoctoral Science Foundation (No. LBH-Z14060).

## REFERENCES

1. F L Ponta, P M Jacovkis. A vortex model for Darrieus turbine using finite element techniques. *Renewable Energy*, 2001, 24:1-18.
2. G Beer, I Smith, C Duenser. *The Boundary Element Method with Programming: For Engineers and Scientists*, Springer-Verlag, New York, 2008.
3. Guerri, O., Sakout, A. and Bouhadeh, K., Simulations of the Fluid Flow around a rotating Vertical Axis Wind Turbine, *Wind Engineering*, 2007, 31(3):149-163
4. H F Hassan, A El-Shafie, O A Karim. Tidal current turbines glance at the past and look into future prospects in Malaysia. *Renewable and Sustainable Energy Reviews*, 2012 16: 5707-17
5. Hamada, K., Smithb, T., Durrani, N., Qind, N. and Howell, R., Unsteady Flow Simulation and Dynamic Stall around Vertical Axis Wind Turbine Blades, AIAA Aerospace Sciences Meeting and Exhibit, Reno, Nevada, 7-10 January 2008.
6. Horiuchi, K., Ushiyama, I., and Seki, K., Straight Wing Vertical Axis Wind Turbine: A Flow Analysis, *Wind Engineering*, May 2005, 29(3):243-252
7. H Versteeg, W Malalasekera. *An Introduction to Computational Fluid Dynamics: The Finite Volume Method*, Prentice-Hall, Upper Saddle River, NJ, 2007.
8. I G Bryden, S J Couch, A Owen et al. Tidal current resource assessment. *Proceedings of the Institution of Mechanical Engineering Part A Journal of Power and Energy*, 2007 221(2): 125-135
9. J C Tannehill, D A Anderson, R H Pletcher. *Computational Fluid Mechanics and Heat Transfer*, 2d ed., Taylor and Francis, Bristol, PA, 1997.
10. J D Anderson, Jr. *Fundamentals of Aerodynamics*, 4th ed., McGraw-Hill, New York, 2007.
11. J. Jiang, Analysis of vertical-axial turbine hydrodynamic performance and application and development of optimal design [D], Harbin: Ph.D. thesis in Harbin Engineering University, 2012.
12. J N Newman, *Marine Hydrodynamics*, M.I.T. Press, Cambridge, MA, 1977.
13. J Tu, G H Yeoh, C Liu. *Computational Fluid Dynamics: A Practical Approach*, Butterworth-Heinemann, New York, 2007.
14. Koukina, E., Kanner, S., and Yeung, R. W., "Actuation of Wind-Loading Torque on Vertical Axis Turbines at Model Scale", *Proceedings, Oceans'15, Marine Technology Society/IEEE*, Paper 141206-002, Genoa, Italy, May18-21,2015
15. L S Blunden, A S Bahaj. Tidal energy resource assessment for tidal stream generators. *Proceedings of the Institution of Mechanical Engineering Part A Journal of Power and Energy*, 2007 221(2): 137-146
16. L Zhang, Q J Luo, R G Han, Deflection angle optimization of vertical axis tidal current turbine. *Journal of Harbin Institute of Technology*, 2011 43 (sup1): pp. 281-285.
17. M.S.U.K. Fernando and V.J. Modi. A Numerical Analysis of the Unsteady Flow Past a Savonius Wind Turbine. *J. Wind Engineering & Industrial Aerodynamics*. October 1989,32(3),303-327P
18. Sun Ke, Numerical simulation of H type vertical-axial turbine and deflector, HEU Ph.D. thesis, 2008: pp. 44-51
19. T Cebeci. *Computational Fluid Dynamics for engineers*. Springer-Verlag, New York, 2005.

20. Y Li. Development of a Procedure for Predicting the Power Output from a Tidal Current Turbine Farm, PhD thesis, University of British Columbia, Vancouver, B.C., Canada, 2008
21. M Tomera. Dynamic positioning system for a ship on harbour manoeuvring with different observers. Experimental results. Polish Maritime Research. SEP 2014, 21(3): 13-24.
22. Y Li, S M Calisal. Modeling of twin-turbine systems with vertical axis tidal current turbines: Polish Maritime Research, 2010 37: 627-637
23. Y Li, S M Calisal. Modeling of twin-turbine systems with vertical axis tidal current turbines: Part II—torque fluctuation. Ocean Engineering, 2011 38: 550-558
24. V V Klemas, Coastal and Environmental Remote Sensing from Unmanned Aerial Vehicles: An Overview. Journal of Coastal Research. SEP 2015, 31(5): 1260-1267.
25. Z C Li, L Zhang, K Sun, X W Zhang, Numerical simulation of vertical axis tidal current turbine. ACTA ENERGY SOLARS SINICA, 2011 32 (9): pp. 1321-1326.

## CONTACT WITH THE AUTHOR

Ma Yong

Shipbuilding Engineering Collage  
Harbin Engineering University  
Heilongjiang, Harbin, 150001

**CHINA**

# THE HARDWARE IMPLEMENTATION OF DEMONSTRATOR AIR INDEPENDENT ELECTRIC SUPPLY SYSTEM BASED ON PEM FUEL CELL

Grzeczka G., PhD

Szymak P., PhD

Institute of Electrical Engineering and Automatics

Polish Naval Academy, Poland

## ABSTRACT

*The paper presents results of the research project whose the main goal was to build a technology demonstrator of an electric supply system based on the PEM fuel cell. The electric supply system is dedicated to operation on a board of a submarine during emergency situations. The underwater conditions influence on a specific architecture of supply subsystems of the PEM fuel cell system. In this case the fuel cell stack is supplied by both clean hydrogen and clean oxygen stored in pressurized tanks. The hydrogen has to be delivered in a closed loop, while the oxygen can be delivered in a closed or an open loop. In the technology demonstrator, the supply of the fuel cell stack by the hydrogen in the closed loop and the oxygen in the open loop with a precise control of its flow were used.*

*In the paper, a hardware and a software structures of the technology demonstrator are presented. Then, selected results of the PEM fuel cell system operation are included. The results of the research show precise control of the oxygen and a response of the system on rapid changes of an electric load responding to the loads working during an emergency situation on a board of a submarine. Mainly, results of the real fuel cell system operation are presented. The results of numerical research can be found in several publications of the authors included in the bibliography of the paper.*

**Keywords:** PEM fuel cell system, Air Independent System, control of oxygen

## INTRODUCTION

More often, hydrogen fuel cells are used to supply different devices and vehicles both for civilian and military applications. One of the more popular hydrogen fuel cells used in mobile applications are low-temperature PEM (Proton Exchange Membrane) fuel cells. This technology is also used with success in underwater mobile platforms. Nowadays, there are constructions of submarines and unmanned underwater vehicles using PEM stacks to generate an electric energy needed for their working. The most mature examples of underwater platform with PEM fuel cells are German submarine class 214 [4] and Japan AUV (Autonomous Underwater Vehicle) Urashima [16]. Another interesting examples of using fuel cell in marine application are AUV Hugin [5] with alkaline aluminium hydrogen peroxide semi fuel cell and AUV Clipper [6] using magnesium fuel and oxygen from the sea. The main reason for using the fuel cell

technology in mobile applications, especially in underwater vehicles, is currently the highest achievable energy density. Having such an energy source can be especially useful in the emergency situation on board of a submarine. Surviving underwater on board of the submarine during its failure until the rescue units approach and help is only possible when the crew has access to power supply of life support systems and communications.

Mentioned above benefits justify using PEM fuel cells additionally to technologically advanced chemical batteries currently used on submarines or unmanned underwater vehicles [7]. The hybrid combination of these two energy sources should provide a masked operation with mentioned above possibility of surviving underwater in case of emergency situations.

The use of hydrogen to power mobile platforms is currently very carefully examined solution in terms of both the marine [17] and land or air.

This paper presents selected results of carried out research whose the main objective was to build technology demonstrator to achieve knowledge and experience allowing to develop the essential requirements for this type of equipment in the submarine environment. In the next sections, following stages of the project are described.

The project was carried out in the following stages:

- 1) Measurement on board of a submarine,
- 2) Designing mathematical model of the fuel cell system,
- 3) Building the technology demonstrator of the fuel cell system,
- 4) Experimental research.

The project was finished by making recommendations for future research and/or purchase of this kind of power system on board of a submarine.

## MEASUREMENT ON BOARD OF SUBMARINE

The demand for electrical energy, and thus the use of individual electrical consumers on board of a submarine is dictated by the exploitation state, which she is at the moment. Exploitation states of the ship depend only on the nature of the tasks performed by her. Despite diversity and variability of conditions in which these tasks are performed, there are four exploitation states, which can be considered in terms of the use of emergency supply: moving the ship to the area of operation, operating a ship in the area of operation, the ship lying at the bottom in the area of operation and the ship lying at the bottom – the failure of the submarine.

During the measurements on board of a submarine, identification of following processes was carried out: processes of generating, converting and transmission of electric energy on board of the selected submarine not only in a failure state, but also during all exploitation states of the ship. Below, there are presented results of measurements of low energy demand exploitation states, that are especially significant for discussed subject. The first state is lying on the seabed, Tab.1. The main electric motor is stopped but in a stand-by mode. The manoeuvring desktop is supplied. The commander may decide to turn off additional devices in case of the task or tactical situation that requires long lasting lying on the seabed and complete silence on the ship.

Tab. 1. Demand for energy in the state "lying on the seabed".

Type of power supply	Current A	Power kW
156 - 220 DC	35,58	6,76
115 V 60 Hz	34,8	4,00
110 V DC	0,25	0,03
115 V 400 Hz	29,98	3,45
24 V DC	5,00	0,12
220 V 60 Hz	3,00	0,66
<b>TOTAL</b>	<b>108,61</b>	<b>15,01</b>

While lying on the seabed the energy demand is seven times lower than in a low speed movement. The use of the fuel cells in that state, allows to stay for a long period of time in the

submerged state without necessity of energy replenishment.

The failure of a submarine, lying on the seabed is very important hypothetical state, in which the submarine can be after a failure, collision with a submerged object and falling to the bottom. From the survival point of view, and in consequence the crew rescue of the damaged submarine, providing sufficient amount of energy is essential for successful rescue action. Power consumption in this state is limited to the minimum, Tab. 2. But it is totally dependent on the right operation of the devices after the event which led the submarine to the state of lying on the seabed.

Tab. 2. Demand for energy in the state "failure of a submarine".

Type of power supply	Current A	Power kW
156 - 220 DC	21,00	3,99
115 V 60 Hz	14,00	1,61
110 V DC		
115 V 400 Hz		
24 V DC	3,60	0,09
220 V 60 Hz		
<b>TOTAL</b>	<b>38,60</b>	<b>5,69</b>

In the considered state, there are presented the power demand of the devices, which should be powered on, regarding their operational ability and energy supply.

Relating to the actual trends of rescue mission for the crew of the damaged submarine, the crew should survive on the submarine even two weeks. That is possible by having adequate amounts of means of sustaining life on the submarine and emergency electric energy sources.

It was found that the levels of demand for electric energy for both failure state and the ship lying at the bottom in the area of operation are of the same order.

The results of this research helped to determine the power requirements for designed system and indicated the possibilities of using emergency power supply based on PEM fuel cells for operation in two mentioned above exploitation states of the submarine.

## MATHEMATICAL MODEL OF FUEL CELL SYSTEM

In parallel with the measurement described in the previous section, a mathematical model of the emergency power system based on PEM fuel cells C was designed. In the Fig. 1, block diagram of the emergency power systems based on PEM fuel cells is presented. While in the Fig. 2, schematic diagram of the system is shown.

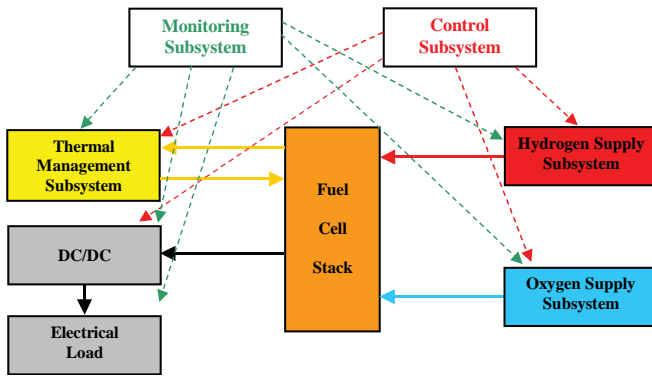


Fig. 1. Block diagram of emergency power supply system based on hydrogen fuel cell

The main result of this stage is the mathematical description of the fuel cell system operation in the form of differential equations and matrix equations of state implemented in Simulink environment (Fig. 2). All the subsystems (Fig. 1) are illustrated by different colors. Elements of the control subsystem are integrated with other subsystems, especially blocks named 'PID'.

In the designed power supply system (Fig. 2) the mathematical model of fuel cell stack with following features was used:

- 1) an analytical,
- 2) control-oriented,
- 3) steady-state,
- 4) isothermal,
- 5) cell-averaged.

The model of the fuel cell stack includes:

- 1) model of overall fuel cell stack voltage,
- 2) cathode and anode flow models,
- 3) membrane hydration model.

The mathematical description of the model used in the research is described in more details in [2][3][13]. The model of the fuel cell stack is mainly destined for control purposes. There are also alternative models of fuel cell stacks included in literature which are focused on other features and destined for other purposes, e.g. 3D model of gasses flows [10], model of polymeric super ionic membranes for fuel cell [1], another approach to control of the fuel cell systems [11], etc.

For graphical user interface with fuel cell model (Fig. 2) Matlab window, illustrated in the Fig. 3, was designed.

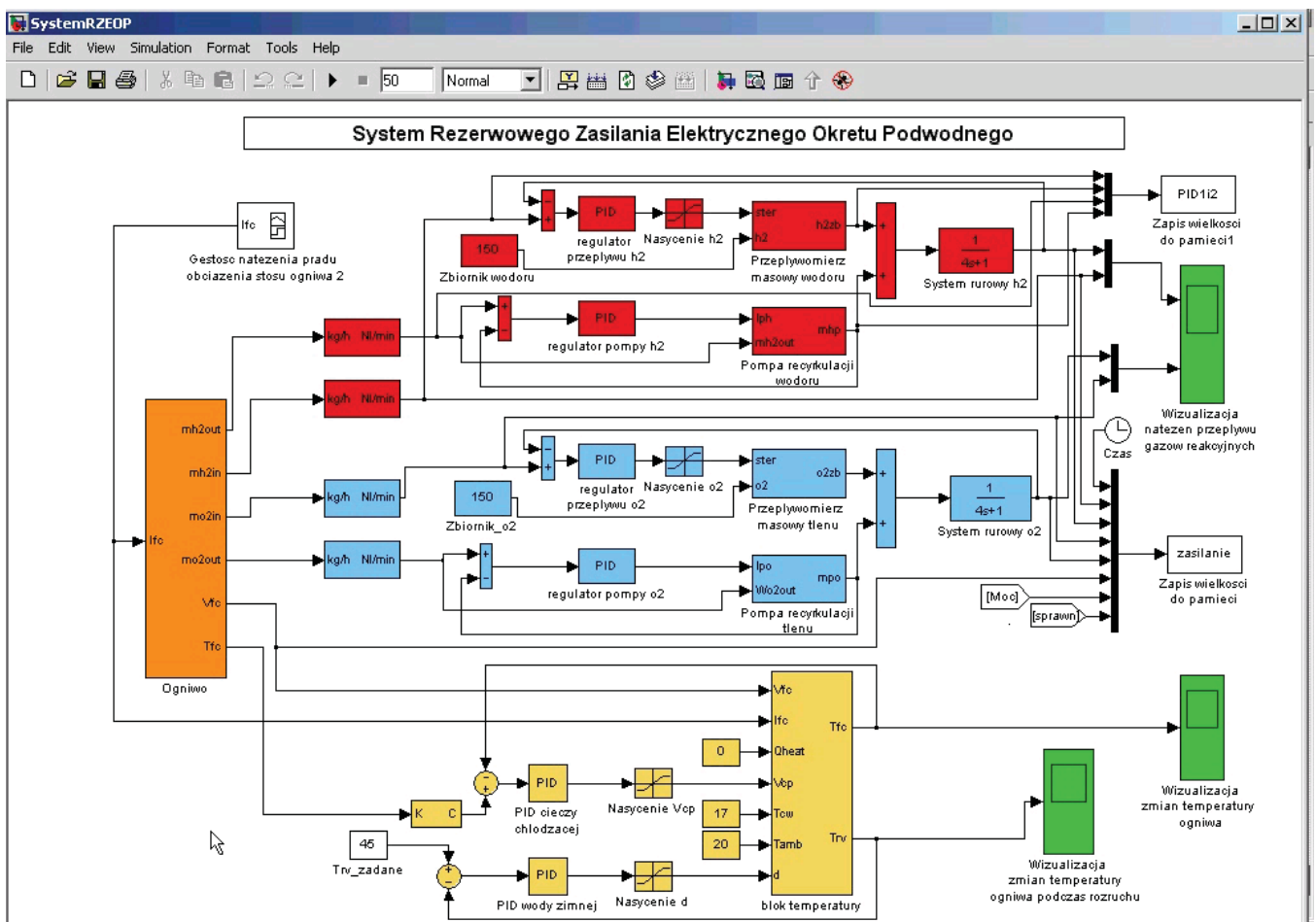


Fig. 2 Implementation of the PEM fuel cells model in Simulink environment (orange blocks: fuel cell stack, red blocks: hydrogen supply subsystem, blue blocks: oxygen supply subsystem, yellow blocks: thermal management subsystem, green blocks: monitoring subsystem)

The window allows the control and visualization of the all important operating parameters of the fuel cell stack.

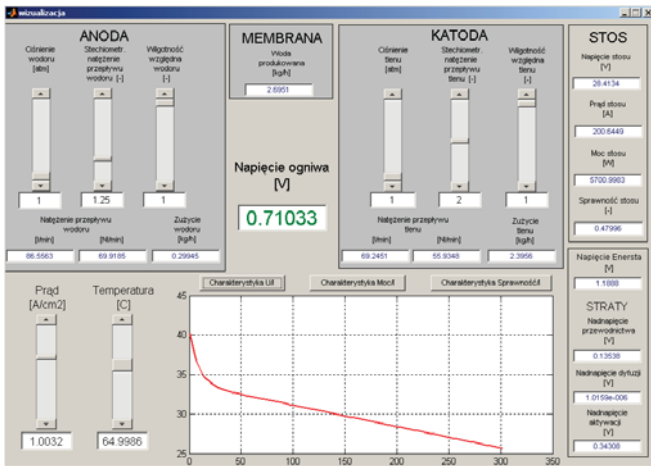


Fig. 3 Visualization of PEM fuel cells parameters in Matlab

The parameters of the model of the fuel cell stack was tuned based on experimental data obtained from the Nedstack company – the manufacturer of 6 kW stack used in the technology demonstrator (described in more details in the next section). The stack modelling was carried out in cooperation with Stanisław Hożyń [8].

Based on a comparison of characteristics obtained from the model and the real 6 kW stack [3], it can be concluded that the mathematical model parameters were chosen correctly and implemented simulator properly represents the behavior of the fuel cell stack in steady state. Correctly validated model allowed examine the impact of significant parameters (temperature of the stack, pressure and relative humidity of the reaction gases) on the operation of the fuel cell stack [13][15]. Moreover, it allowed determine the best parameters of its control subsystem [12][14]. At the end, results of numerical research enabled to determine assumptions for building technology demonstrator of emergency power supply system of submarine based on hydrogen fuel cell.

## TECHNOLOGY DEMONSTRATOR OF FUEL CELL SYSTEM

In the next stage, the real technology demonstrator was built. The main purposes of the demonstrator are:

- 1) the demonstration of possibility of using the PEM fuel cells technology for emergency supply of the submarine, especially at the time of failure,
- 2) the verification of possibility of using the PEM fuel cells as an alternative source of electric energy on board of a submarine.

In future research the demonstrator can be:

- 1) an element of the laboratory stand for testing different methods of hydrogen storage,
- 2) a basis for the training of crews of future submarine with hybrid propulsion consisting of, among others, the fuel cell system.

Finally, the entire system was built in the Laboratory of Electric Drives in Polish Naval Academy (Fig. 4). The demonstrator was named as “Air Independent Electric Supply System” AIESS.



Fig. 4. Technology demonstrator of Air Independent Electric Supply System in Laboratory of Electric Drives

The AIESS consists of:

- 1) PEM fuel cell system with nominal power 6 kW based on P8 stack from Nedstack Company, Arnhem, Netherlands,
- 2) DC/DC converter stabilizing voltage at level 220 V, connected in parallel with supercapacitors,
- 3) the electric load consisting of: an electric motor, a lighting set and a heating,
- 4) installations and pressured tanks of oxygen, hydrogen and nitrogen.

The PEM fuel cell system is controlled by S7-300 PLC. The controller is connected with a touch panel and PC through MPI protocol. The touch panel performs Human Machine Interface, whereas PC visualizes operation and registers parameters of the system. In the Fig. 5, application CVM (Cell Voltage Measure) installed on PC is presented.

The main window of application CVM is divided into the following panels (from top to down):

- 1) the buttons panel for connecting or disconnecting the PLC application and call the configuration window,
- 2) the voltage panel showing the voltages on each fuel cell in the form of a bar graph and the minimum, maximum and average value of overall stack voltage,
- 3) the current state system panel showing the real-time operational status of the system components on its schematic diagram with the display of the main parameters of the AIESS.

The whole registered and visualized parameters are archived in a \*.text file. It allows to make analyses of the system operation off-line and examine long-lasting processes, e.g. process of membrane deterioration.

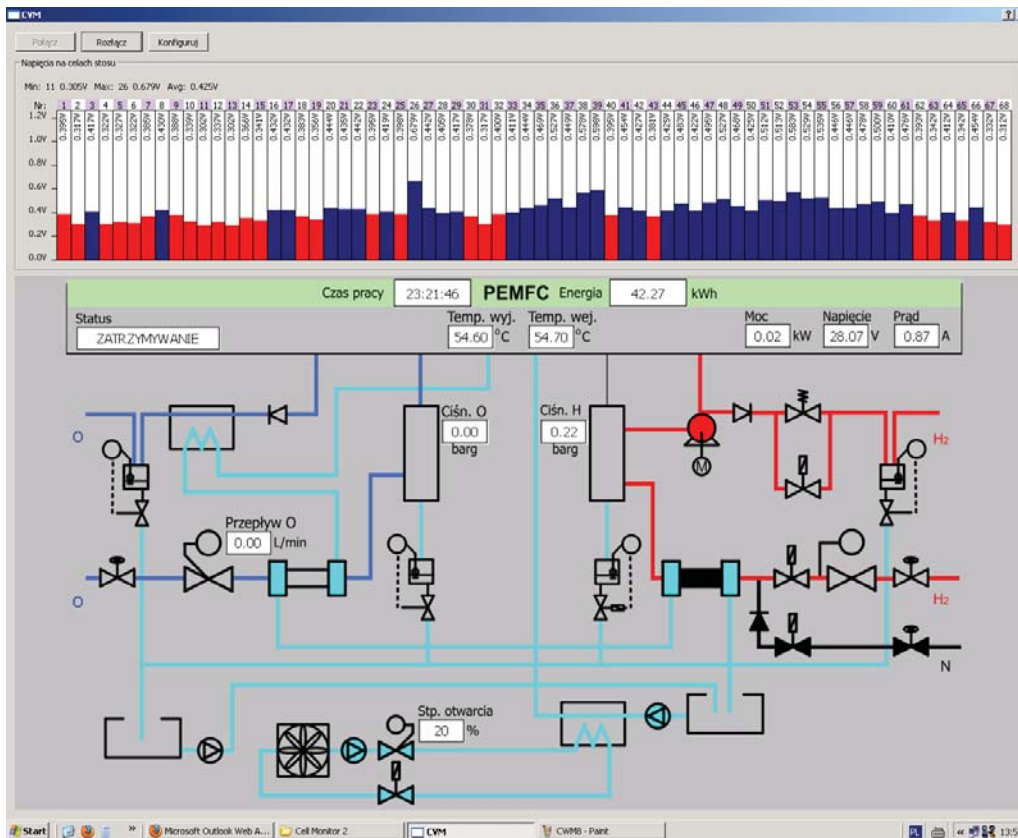


Fig. 5. Application CVM for visualization and registration of parameters of the AIESS

Parameters of the elements of the AIESS included in the reactant gasses supply subsystems, thermal management subsystem, control subsystem, etc. were selected based on the results of simulation studies using the designed mathematical model of the system. Moreover, experiences gathered during collaboration with the companies: Nedstack from The Netherlands and Apisystems Gdańsk and Linde Gas Polska from Poland were used to achieve final version of the AIESS.

It should be underlined that the demonstrator consists of two main parts: the emergency power system creating the proper technology demonstrator and the laboratory stand for its testing. The stand is used for real-time visualization and archivisation of the fuel cell stack operation and the operation of subsystems providing the reaction gasses: hydrogen and oxygen with humidification of the reactant gasses and cooling subsystem.

## EXPERIMENTAL RESEARCH

Experimental studies were carried out in two stages:

- 1) simulation research based on the mathematical model of the fuel cell system,
- 2) measurement of parameters of fuel cell system called AIESS.

The first stage of the study was carried out using analytical and control-oriented, isothermal and cell-averaged model of the fuel cell stack operating in a steady state. This model

was implemented in Matlab / Simulink environment and then its parameters were tuned to the fuel cell stack from Nedstack company (Arnhem, Netherlands). Details of the research are contained in [3][12][13][14][15].

The second stage of the study was carried out in three phases. In the first phase, the measurement of polarization characteristics of P8 Nedstack PEM fuel cells was carried out. The stack was supplied by clean oxygen. Then, measurement of oxygen excess, appearing at open architecture of oxygen supply subsystem was performed. At the end of the studies, influence of changes of an electrical load on the work of AIESS was examined.

## MEASUREMENT OF POLARIZATION CHARACTERISTICS OF THE FUEL CELL STACK P8

In the first part of the study, measurement of the polarization characteristics of the fuel cell stack P8 was made in the conditions of the stack supply by pure hydrogen and oxygen. Nedstack company – the manufacturer of the stack provided only the polarization characteristics of the stack in the conditions of the stack supplied by pure hydrogen and air (Fig. 6).

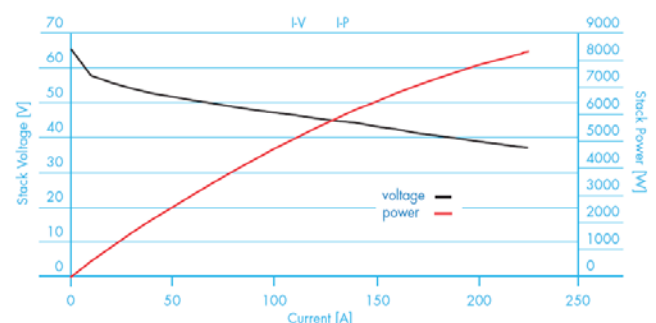


Fig. 6. The polarization characteristics of the fuel cell stack P8 supplied by pure hydrogen and oxygen from the surrounding air (www.nedstack.com)

During the research the stack was supplied by pure hydrogen and oxygen. The course of the measured polarization characteristics of the fuel cell stack P8 (supplied by pure oxygen) is presented in Fig. 7.

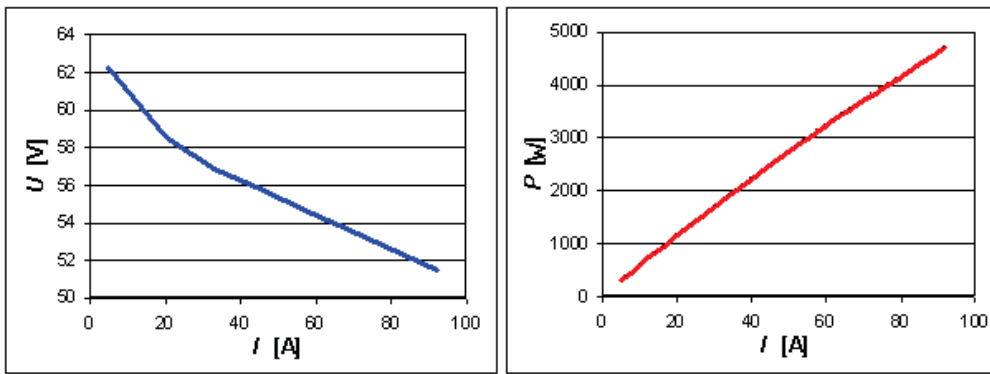


Fig. 7. Polarization characteristics  $U(I)$  i  $P(I)$  of the fuel cell stack P8 (supplied by pure oxygen)

Comparing the obtained characteristics (Fig. 7 and 8) with the characteristics specified by the manufacturer (Fig. 6), it can be seen a similar course of these characteristics. An important advantage in the case of supplying the stack by pure oxygen compared to the supplying by air is increase of produced power at the output of approx. 10% (for operating point 100 A we achieved increase of 7.7%). Observed growth of the output power confirmed the numerical results carried out in the previous stage of the study [3][13].

The figure below (Fig. 8) shows the course of the polarization characteristic  $P(I)$  in two different temperatures of the fuel cell stack operation: 308,15°K and 331,15°K. As it can be seen (Fig. 8), the higher operating temperature of the fuel cell stack results in a greater efficiency, that is for the same current, the output power is higher. The deviation of the both characteristics increases with the increase of a current load. This is important for the operation of AIESS, that is the system can deliver large currents after reaching operating temperature of the stack 333,15°K  $\pm$ 2°K. It is the temperature range recommended by the manufacturer of the fuel cell – the Nedstack company.

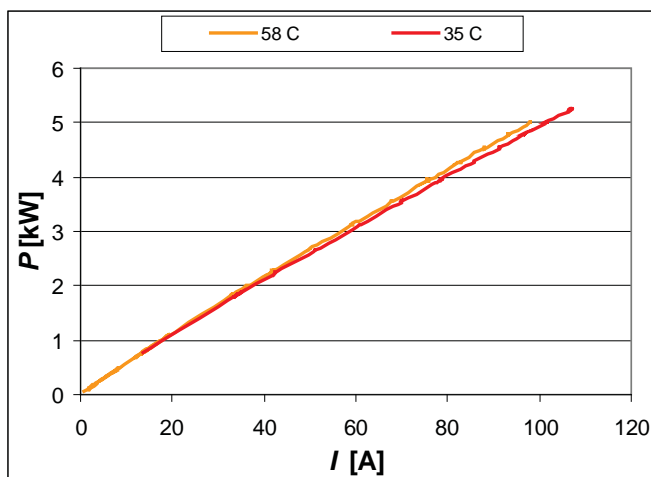


Fig. 8. The polarization characteristics  $P(I)$  of the fuel cell stack P8 supplied by pure oxygen for the operating temperature: 308,15°K i 331,15°K

The temperature has significant importance for the

intensity of electro-catalysis process of hydrogen on platinum, that is the higher the temperature, the higher the intensity. Upper limit of the operating temperature range due to the fact that at higher temperatures reduces the relative humidity of the reaction gas, and water in PEM fuel cell is used for the transport of hydrogen protons through the ion-conductive

membrane. Therefore, the temperature range recommended by the manufacturer is a kind of a compromise, aimed at finding the best operating conditions of a specific type of PEM fuel cells.

### MEASUREMENT OF THE OXYGEN EXCESS AT THE OUTLET OF THE STACK

As it was mentioned earlier, in this fuel cell system, oxygen supply subsystem was designed and built in an original way, that is the subsystem is without recirculation of oxygen. Such a process of delivering oxygen to the stack requires precise control of the oxygen so that oxygen excess on the output is not too large, that is it could be consumed by the crews.

The measurement of the oxygen excess was preceded by tuning PID settings of oxygen flow implemented in the controller Bronkhorst F-201. As a result of this process, a smooth course of the volumetric flow rate of oxygen at the inlet of the fuel cell was achieved, as shown in Fig. 9. In this figure flow rate is represented in percentages scale, where 100% corresponds to the flow of 65 Nl/min. Presented in this figure oxygen flow corresponds to a fairly significant step change of a load current: from 6 A to 57 A and from 57 A to 92 A, which corresponds to the following changes in output power: from 0.37 kW to 3.08 kW and from 3.08 kW to 4.73 kW (Fig. 10). The observed initial power 0.37 kW is due to the fact that the devices, e.g. pumps are powered directly from the fuel cell system, when it started working.

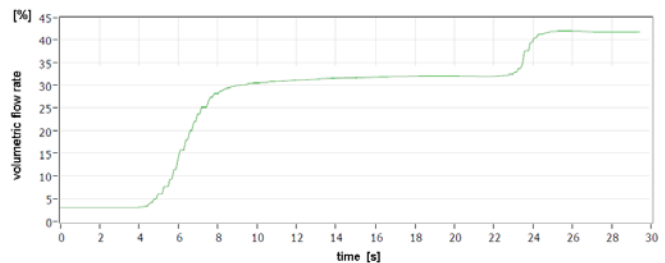


Fig. 9. The course of volumetric flow rate of oxygen at the inlet of the fuel cell stack for a given step change in load current from 6 A to 57 A and then to 92 A

As can be seen from Fig. 9, the smooth flow of oxygen corresponds to step changes of current and voltage with a single overshoot equal to 5 A and 2 V (Fig. 10). The resulting overvoltage approx. 2 V, corresponds to the voltage drop at the

single cell equal to 0.05 V (assuming a uniform distribution on all cells of the fuel stack). This voltage drop is not dangerous for stack operation and potential damage of any cell.

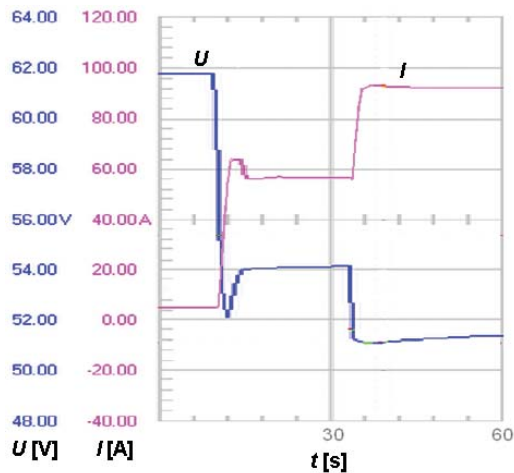


Fig. 10. The course of current and voltage at the output of the fuel cell system for a given step change in load current of 6 A to 57 A and then to 92 A (measured by Fluke)

In the Fig. 11, the course of the volumetric flow rate of oxygen excess at the output of the fuel cell stack for the mentioned above step changes of load current is shown. As it can be seen from the graph, the oxygen excess is up to 2.5%, which corresponds to a flow rate equal to 1.62 Nl/min. This oxygen excess is consumed by 5-6 people being in a rest state (it is assumed that the resting human body consumes from 0.25 to 0.35 Nl/min of pure oxygen). Assuming that the AIESS will be used on board a submarine, where the crew consists of 20 people or more, it can be concluded that the observed excess oxygen does not endanger the health and lives of the crew.

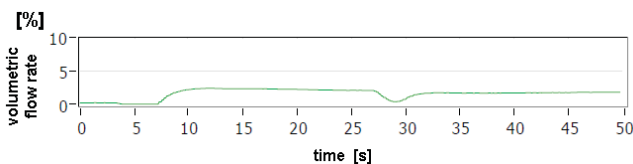


Fig. 11. The course of volumetric flow rate of oxygen excess at the outlet of the fuel cell stack for a given step change of load current from 6 A to 57 A and then to 92 A

A higher flow rate than 2.5% can be observed at the time of reducing the current load. In this case, the following pulse of oxygen flow rate was observed: with the amplitude of up to 7.4% (4.8 Nl/min) and the duration approx. 5 sec. Registered oxygen flow rates during decrease of the current load also do not pose a threat to the health and life of crew, even if there were continuous.

## THE INFLUENCE OF THE LOAD ON THE WORK OF THE FUEL CELL SYSTEM

In the next phase, the impact of changes of the electrical load (changing continuously, and then jumping) on the AIESS was examined. Many tests of the PEM fuel cell stack were

performed, e.g. PEM fuel cells during “heating up” process and then working in the recommended operating temperature range  $333,15^{\circ}\text{K} \pm 2^{\circ}\text{K}$ , for the given discrete and for continuous load changes, etc. The all results are included in the report on the grant [3]. In the next part of the paper, the time courses of main parameters for the regime with step changes of the load are presented. This regime requires a rapid response system on large changes of an electrical load.

The results of the test for the step increments of an electrical load are presented in Fig. 12 to 16. These step changes simulate the behavior of electrical devices during the state of emergency situation on board of submarine. In the laboratory test, these devices are emergency lighting, electric motor coupled to a generator (ventilation system on board of submarine) and electric heating.

In the Fig. 12, the course of voltage DC/DC converter can be observed. Voltage variations are within the scope  $\pm 1\text{V}$ . This reflects the good work of the DC/DC converter.

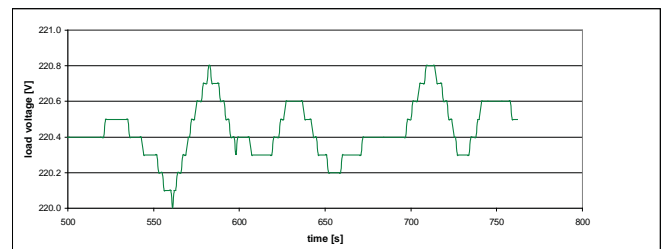


Fig. 12. Stabilization of the load voltage during the test

The changes of the load current described previously correspond to comparable change of current and voltage of the fuel cell (Fig. 13). Only start-up of the electric motor in 516 s and in 619 s of the experiment correspond to the pulse increases of the fuel cell current. These pulse increases have short time of duration and result in overvoltage of approx. 10 V. For the fuel cell stack consisting of 68 cells, it gives an average of 0.14 V voltage drop on a single cell. This poses no threat of damage of the fuel cell stack.

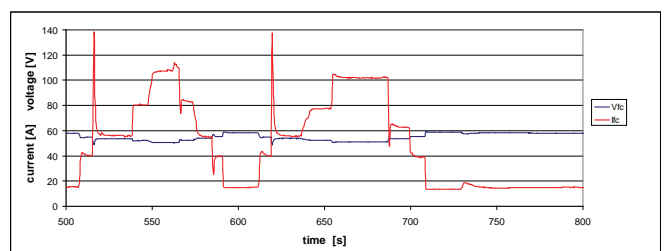


Fig. 13. The course of voltage and current of the fuel cell stack during the test

Described earlier changes of load correspond to small changes of the hydrogen pressure and oxygen (Fig. 14). Small hydrogen pressure changes indicate properly adopted control of hydrogen pressure at the inlet of the stack and the gas pump in the recirculation circuit. Appearing periodically „peaks” of hydrogen pressure waveform are results of the purges of the anode compartment of the stack. The purging is performed cyclically and it is needed for removal of water from anode

compartment.

The course of the oxygen pressure is closely related to the course of the oxygen flow rate (Fig. 15), which in turn results from the generated power on the load. It was assumed for the technology demonstrator of the fuel cell system that the oxygen flow rate is proportional to the current drawn by the load. The proportionality factor was chosen so that the required power was delivered to the load and the minimum oxygen excess was at the output of the stack.

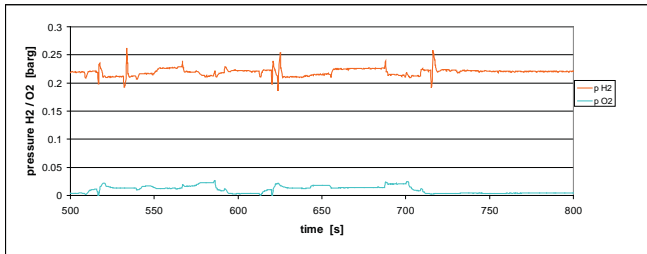


Fig. 14. The course of pressure changes of hydrogen and oxygen during the test

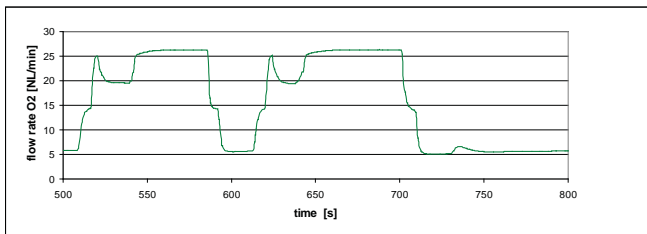


Fig. 15. The course of the oxygen flow rate changes during the test

In the Fig. 16, the changes of temperature at the input and output of the stack are presented. It can be seen that during the increase of the current load, the temperature at the outlet of the fuel cell stack also increases. This is due to the fact that in proportion to the power generated by the fuel cell stack, the losses in the form of heat also increase. Based on the course of the temperature at the stack input, it can also be seen that the heat is effectively transferred into the secondary cooling circuit. Therefore, changes of temperature resulting from the changes of an electrical load is less at the input than at the output of the stack. This demonstrates the proper operation of the cooling system and indicate properly selected heat exchangers and control of the flow of cooling liquid.

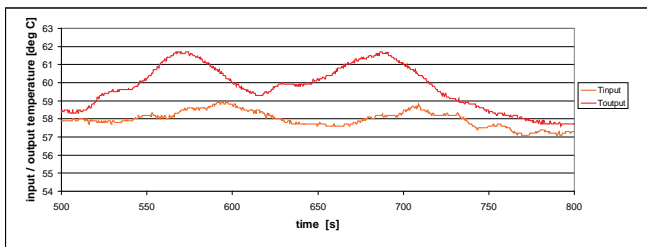


Fig. 16. The course of changes of cooling water temperature at the inlet and at outlet of the fuel cell stack during the test

## SUMMARY

As a final effect of the project, hardware technology demonstrator of emergency power supply system of submarine using a hydrogen fuel cell was built. The parameters of the system meet the requirements regarding the backup power source.

In addition, based on equipment of Laboratory of Electric Drives in Polish Naval Academy the stand for testing the demonstrator was designed and built. Based on the stand many tests were performed that enabled the verification of the simulation model and verification of the design assumptions.

Developed power supply system based on PEM fuel cell adapted to work in the conditions without air correctly responds to changes of a current load and the well stabilizes voltage supplying electric loads, simulating electrical devices during the state of emergency situation on board of submarine.

Performed hydrogen supply subsystem with gas recirculation in a closed-loop enables rapid response of PEM fuel cell stack on changes the electrical load.

The proposed oxygen supply subsystem open due to the reduction in the number of its components, is one of the simplest solutions, and thus potentially the most reliable solution. Registered flow of oxygen excess (appearing at the output of the fuel cell stack) do not pose a threat to life or health of the crew of the submarine. The entire oxygen supply subsystem properly (without threat of the fuel cell stack damage or destruction) responds to the changes of the current load.

The promising result of the project are the hardware facilities and the research team able to carry out further work related to PEM fuel cells technology, especially including the production and storage of hydrogen and optimization of hydrogen cell technology for marine conditions.

## ACKNOWLEDGMENT

For developing the initial concept of using fuel cells for submarines and to initiate research on the fuel cells [3] we thank Professor Zbigniew Korczewski, former Dean of the Faculty of Mechanical and Electrical Engineering in Polish Naval Academy, where the project was implemented.

For professional assistance and cooperation we thank the Director of the Institute of Exploitation of Ship Engine Room Cdr Dr. Tomasz Lus as well as employees of companies Nedstack (Netherlands), Apisystems Gdańsk and Linde Gas Poland (Gdynia branch).

Special thanks to Members of scientific and technical team from the Naval Academy, who worked on the Air-Independent Electrical Supply System.

## BIBLIOGRAPHY

1. Bujło P.: *Polymeric super ionic membranes for fuel cell PEMFC*, in Polish, PhD thesis, Wrocław University of Technology, Wrocław 2006.

2. Gasser F.: *An analytical, control-oriented state space model for a PEM fuel cell system*, PhD thesis, Ecole Polytechnique Federale de Lausanne, Lausanne 2006.
3. Grzeczka G., Szymak P.: *Grant Report on Air Independent Electric Supply System based on PEM Fuel Cell*, in Polish, Main Library Archive, Polish Naval Academy, Gdynia, Poland, 2010.
4. Hammerschmidt A. E.: *Fuel Cell Propulsion of Submarines*, Advanced Naval Propulsion Symposium 2006, October 30 - 31, 2006, Arlington, VA, USA.
5. Hasvold Ø., Johansen K. H., and Vestgaard K.: *The alkaline aluminum hydrogen peroxide semi-fuel cell for the HUGIN 3000 autonomous underwater vehicle*, Proceedings of the 2002 Workshop on Autonomous Underwater Vehicles, San Antonio, 2002, USA, pp. 89-94.
6. Hasvold Ø., Lian T., Haakaas E., Størkersen N., Perelman O., and Cordier S.: *CLIPPER: A long-range, autonomous underwater vehicle using magnesium fuel and oxygen from the sea*, Journal of Power Sources, Vol. 136, 2004, pp. 232-239.
7. Hasvold Ø. and Størkersen N.: *Electrochemical power sources for unmanned underwater vehicles used in deep sea survey operations*, Journal of Power Sources, Vol. 96, 2001, pp. 252-258.
8. Hożyń S., Żak B.: *Fuzzy Control of Reactant Supply System in PEM Fuel Cell*, Trans Tech Publications, Solid State Phenomena, 2012, Vol. 180, pp. 11-19.
9. Korczewski Z., Szac P.: *Technical Conditions of Using Fuel Cells for Reserve Electric Supply of Kobben Submarine*, in Polish, Scientific Journal SYMSO 2006, pp. 65 - 72.
10. Nguyen P.T.: *A Three-Dimensional Computational Model of PEM Fuel Cell with Serpentine Gas Channels*, University of Western Ontario, 2001.
11. Pukrushpan J., Stefanopoulou A., Peng H.: *Control of Fuel Cell Power Systems*, Advances in Industrial Control, Springer, London 2004.
12. Szymak P., Grzeczka G.: *Control of Oxygen Flow in Air Independent PEM Fuel Cell System*, Conference Proceedings of 5<sup>th</sup> Hydrogen & Energy Symposium, Stoos 2011.
13. Szymak P.: *Mathematical model of PEM fuel cell stack supplied with clean oxygen and hydrogen*, in Polish, Institute of Logistics and Storage, Logistyka, No 3, 2009, pp. 78-85.
14. Szymak P.: *Control of Thermal Management Subsystem of PEM Fuel Cell Stack*, HARD Publishing Company, Polish Journal of Environmental Studies, Vol.18, No.4B, 2009, pp. 187-190
15. Szymak P.: *Influence of working temperature of PEM fuel cell on its power and efficiency*, Institute of Logistics and Storage, Logistyka, No 6, 2009, pp. 254-261.
16. Yamamoto I., Aoki T., Tsukioka S., Yoshida H., Hyakudome T., Sawa T., Ishibashi S., Yokoyama K., Maeda T., et al.: *Fuel Cell System of AUV 'Urashima'*, Conference Proceedings of IEEE Oceans/Techno-ocean, 2004.
17. Żółtowski B., Żółtowski M.: *A hydrogenic electrolyzer for fuels*, Polish Maritime Research, No. 4(84) Vol 21, 2014, pp.79-89.

#### CONTACT WITH THE AUTHOR

Grzegorz Grzeczka

e-mail: [g.grzeczka@amw.gdynia.pl](mailto:g.grzeczka@amw.gdynia.pl)

Polish Naval Academy  
Śmidowicza Street 69  
81-127 Gdynia

**POLAND**

## ON POWER STREAM IN MOTOR OR DRIVE SYSTEM

Zygmunt Paszota, Prof.

Gdansk University of Technology, Poland

### ABSTRACT

*In a motor or a drive system the quantity of power increases in the direction opposite to the direction of power flow. Energy losses and energy efficiency of a motor or drive system must be presented as functions of physical quantities independent of losses. Such quantities are speed and load. But the picture of power stream in a motor or drive system is presented in the literature in the form of traditional Sankey diagram of power decrease in the direction of power flow. The paper refers to Matthew H. Sankey's diagram in his paper „The Thermal Efficiency of Steam Engines” of 1898. Presented is also a diagram of power increase in the direction opposite to the direction of power flow. The diagram, replacing the Sankey's diagram, opens a new prospect for research into power of energy losses and efficiency of motors and drive systems.*

**Keywords:** motors, drive systems, energy losses, energy efficiency, Sankey diagram, new research field

### INTRODUCTION

Energy losses and energy efficiency of a motor or drive system should be presented as dependent on the physical quantities independent of the losses. Such independent quantities are speed and load of the motor shaft required by the machine or device driven by the motor. The momentary speed and load decide on the momentary motor useful power and, in a different way, on the kinds and momentary quantities of the losses. However, the energy losses and energy efficiency of motors are determined by researchers and manufacturers as dependent on physical quantities which depend on the losses. For instance, the energy efficiency of motors used in hydrostatic drive are presented as dependent on the flow intensity of motor feeding liquid and on the decrease of pressure in the motor. A reason of such situation is the traditional, commonly accepted and used, but unfortunately erroneous picture of power stream in the motors and drive systems, presented in the literature by means of the Sankey diagram of power decrease in the direction of power flow [2, 3].

### DRIVE INVESTIGATIONS CARRIED OUT BY MATTHEW H. SANKEY

Matthew H. Sankey was an Irish mechanical engineer and captain in the Corps of Royal Engineers where he did research into increase of energy efficiency of steam engines. He was a member of the British Institution of Civil Engineers. His extensive paper *The Thermal Efficiency of Steam Engines* where he presented diagrams of power flow in a drive system, was published in the „Minutes of Proceedings of the Institution of Civil Engineers” in 1898. In 1899, Journal of the American Society of Naval Engineers, under the title *The Thermal Efficiency of Steam Engines*, concluded: „One of the most important engineering papers published in recent years was the report of the committee appointed by the Institution of Civil Engineers to consider and report to the council upon the subject of the definition of a standard or standards of thermal efficiency for steam engines. We print the main portion below as given in the Proceedings of the above society” [1].

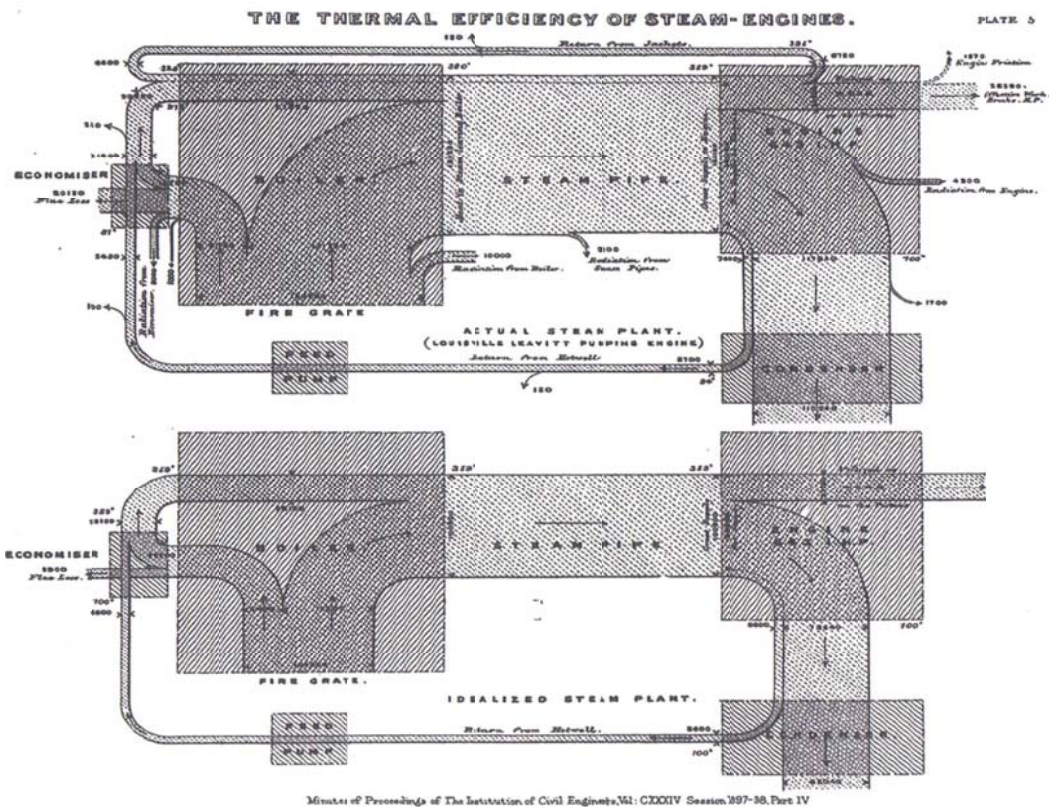


Fig. 1. Diagrams of power decrease in steam plant (actual and idealized) investigated by Sankey, presented in [1]

In his paper, Sankey presented two diagrams of power flow in the investigated, actual and idealized, steam plants. The diagrams are shown in Fig.1.

Sankey writes about the diagrams:

„The boiler, the engine, the condenser and air pump, the feed pump and economizer, are indicated by rectangles upon the diagram. The flow of heat is shown as a stream, the width of which gives the amount of heat entering and leaving each part of the plant per unit of time; the losses are shown by the many waste branches of the stream. Special attention is called to the one (unfortunately small) branch which represents the work done upon the pistons of the engine”.

In the case of smaller power losses which occur in the idealized steam plant, Sankey shows slight increase of useful power of the engine and also decrease of power consumed by the engine (in steam pipe) and decrease of power consumed by the boiler. In effect, the energy efficiency of steam plant is increased.

From the power flow diagrams in Fig. 1 and from the above quoted Sankey’s comment, it may be concluded that power losses are treated as wasted branches of the main stream and weakening that stream and also that „the work (per unit of time) done upon the pistons of the engine” results from power consumed by the system and powers of losses in the system.

The diagram of power stream in a drive system, adopted by Sankey, is probably an effect of his concentration on the decrease of the main stream of power in the direction of power flow due to energy losses in the system, wasted and abstracted outwards.

It can be noticed in Sankey diagrams of Fig. 1, that the quantity of energy losses in a drive system changes depending on the system quality even when the system useful power practically does not change.

Therefore it may be assumed that, depending on whether we deal with an actual or an idealized system, with the same physical quantities describing the drive system useful power (e.g. the same motor shaft speed and load), the consumed input power will change with the power of energy losses.

It may also be assumed that the quantity of input power consumed by the system will be determined by the required output useful power and powers of energy losses in the system, related to its quality.

However, with the Sankey diagram one cannot present energy losses in a drive system as dependent on physical quantities deciding on the system output useful power, present the input consumed power as dependent on the output useful power or describe mathematically the system power of energy losses and energy efficiency as dependent on the motor speed and load in the system.

Maybe, Sankey in his considerations did not feel a need to describe mathematically the relations of energy losses in a motor or drive system or the relations of energy efficiency to the physical quantities deciding on them.

A simplified diagram of power stream in a motor or drive system, referring to the Sankey diagram, has the form presented in Fig. 2.

In accordance with Fig. 2 the motor (drive system) useful (output) power  $P_u$  results from a difference of the consumed

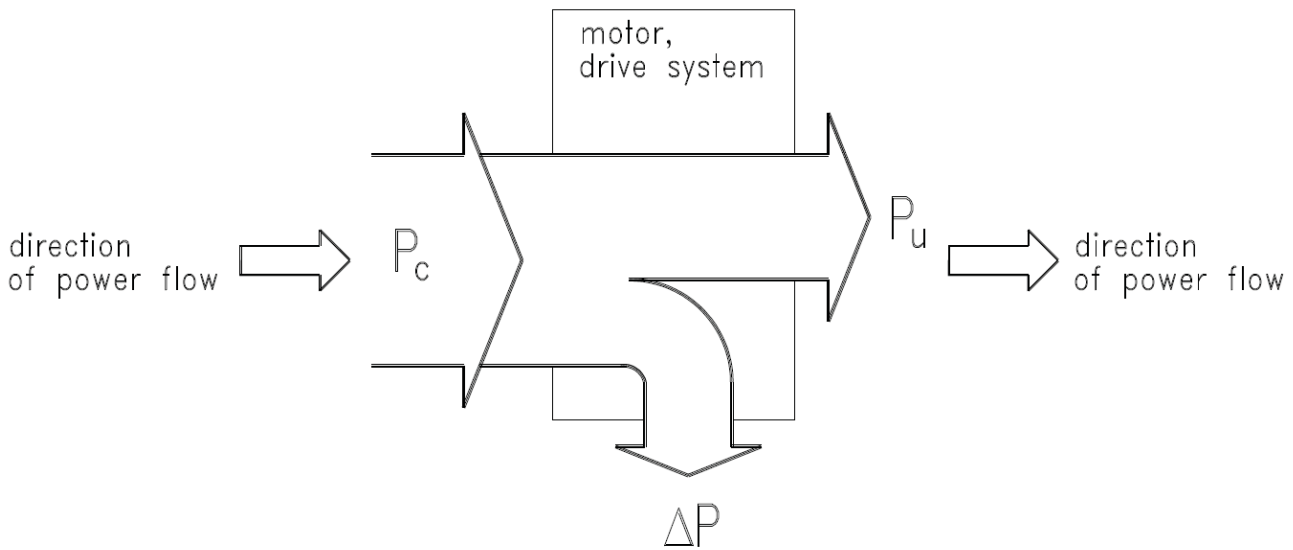


Fig. 2. Simplified diagram of decrease of power in motor or drive system in the direction of power flow, referring to Sankey diagram in Fig. 1  
 $P_c$  - the consumed (input) power expressed in [W],  $P_u$  - the useful (output) power [W],  $\Delta P$  - the power of losses [W].

(input) power  $P_c$  and power of losses,  $\Delta P$ :

$$P_u = P_c - \Delta P. \quad (1)$$

A consequence of (1) is connection between the power of energy losses,  $\Delta P$ , and the consumed power  $P_c$ , and description of the motor or drive system energy efficiency  $\eta$  in the form:

$$\eta = \frac{P_u}{P_c} = \frac{P_c - \Delta P}{P_c} = 1 - \frac{\Delta P}{P_c}. \quad (2)$$

Formula (2), related to the power decrease diagram in Fig. 2, describing the energy efficiency  $\eta$ , allows only to determine the effectiveness of the use of the consumed power  $P_c$  in a motor or drive system.

The Sankey diagram and the resulting formulae (1) and (2) do not fully describe the physical phenomena occurring in a drive system.

The energy losses, e.g. mechanical, volumetric, pressure losses in a motor or drive system, are abstracted outwards in the form of heat. However the different losses depend on the physical quantities deciding directly about them. Simultaneously power of the losses enforces an increase of power stream at the inlet to the system element where they occur in order to overcome them. The useful power of a drive system must result from the power required from the system by a machine or device driven by it.

The diagram of power stream in a motor or drive system should show the physical quantities directly or indirectly deciding on the values of individual losses. Mathematical descriptions of the losses should allow to formulate descriptions of the resulting energy efficiencies. The product of individual efficiencies decides of the energy efficiency of elements and, in effect, of the drive system overall efficiency. However the

Sankey diagram does not give such possibility.

### DIAGRAM OF POWER INCREASE OPPOSITE TO THE DIRECTION OF POWER FLOW

Evaluation of the energy behaviour of different kinds and sizes of motor or drive systems requires their energy efficiencies to be described and compared as dependent on the motor shaft or piston rod speed coefficient  $\overline{\omega}_M$  and load coefficient  $\overline{M}_M$  changing in its operation field ( $0 \leq \overline{\omega}_M < \overline{\omega}_{Mmax}$ ,  $0 \leq \overline{M}_M < \overline{M}_{Mmax}$ , respectively). Maximum values of the speed coefficient  $\overline{\omega}_{Mmax}$  and load coefficient  $\overline{M}_{Mmax}$  result from the drive system maximum capacity and the losses, and they outline the operating field limits. Fig. 3 presents the motor operating field in a drive system.

The current angular speed  $\omega_M$  (rotational speed  $n_M$ ) required from a rotational hydraulic motor or the linear speed  $v_M$  required from a linear hydraulic motor (hydraulic cylinder), operating in a hydrostatic drive system, are replaced, in mathematical models of the energy losses and energy efficiency, by the motor speed non-dimensional coefficient  $\overline{\omega}_M$ :

$$\overline{\omega}_M = \frac{\omega_M}{\omega_{Mt}} = \frac{n_M}{n_{Mt}} = \frac{\omega_M q_{Mt}}{2\pi Q_{Pt}} = \frac{n_M q_{Mt}}{Q_{Pt}}, \quad (3)$$

or

$$\overline{\omega}_M = \frac{v_M}{v_{Mt}} = \frac{v_M S_M}{Q_{Pt}}. \quad (4)$$

The rotational motor theoretical angular speed  $\omega_{Mt}$  (rotational speed  $n_{Mt}$ ) is treated as a constant reference value for the motor current angular speed  $\omega_M$  (rotational speed  $n_M$ ). The value  $\omega_{Mt}$  ( $n_{Mt}$ ) results from the quotient of the theoretical pump capacity  $Q_{Pt}$  and the theoretical motor absorbing capacity  $q_{Mt}$

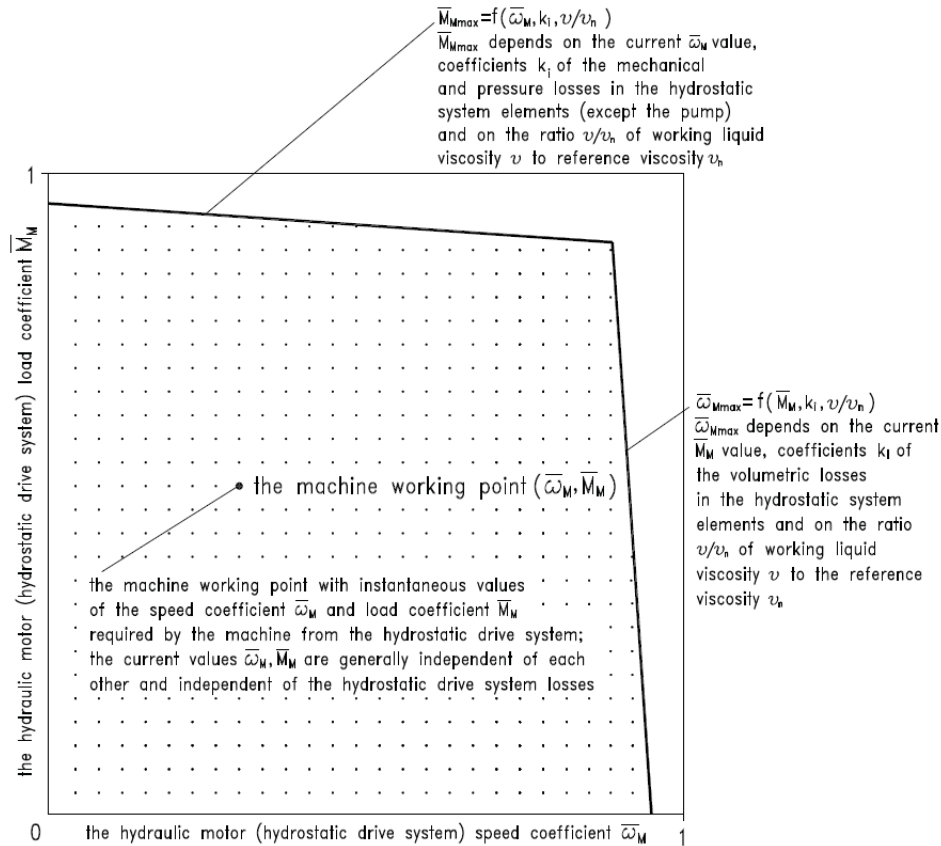


Fig. 3. The range of the motor speed coefficient  $\bar{\omega}_M$  and load coefficient  $\bar{M}_M$  ( $0 \leq \bar{\omega}_M < \bar{\omega}_{Mmax}$ ,  $0 \leq \bar{M}_M < \bar{M}_{Mmax}$ , respectively) in a hydrostatic drive system [2]

per one shaft revolution.

The linear motor theoretical speed  $v_{Mt}$  is treated as a constant reference value for the motor current speed  $v_M$ . The value  $v_{Mt}$  results from the quotient of the theoretical pump capacity  $Q_{Pt}$  and the motor piston area  $S_M$ .

The current torque  $M_M$  required from a rotational motor or the current force  $F_M$  required from a linear motor, operating in a hydrostatic drive system, are replaced by the motor load non-dimensional coefficient  $\bar{M}_M$ :

$$\bar{M}_M = \frac{M_M}{M_{Mt}} = \frac{2\pi M_M}{q_{Mt} p_n}, \quad (5)$$

or

$$\bar{M}_M = \frac{F_M}{F_{Mt}} = \frac{F_M}{S_M p_n}. \quad (6)$$

The rotational motor theoretical torque  $M_{Mt}$  is treated as a constant reference value for the motor current torque  $M_M$ . The value  $M_{Mt}$  results from the product of the system nominal pressure  $p_n$  (in the pump outlet conduit) and the motor theoretical absorbing capacity  $q_{Mt}$  per one shaft revolution.

The linear motor theoretical force  $F_{Mt}$  is treated as a constant reference value for the motor current force  $F_M$ . The value  $F_{Mt}$  results from the product of system nominal pressure  $p_n$  and the motor piston area  $S_M$ .

A simplified diagram of power stream, showing an impact of the useful power  $P_u$ , i.e. an impact of speed and load of shaft

or piston rod, on the power  $\Delta P$  of energy losses in motor or drive system, and in effect on the increase of power in the direction opposite to the direction of power flow and on the consumed power  $P_c$ , is presented in Fig. 4.

In a motor or drive system, the quantity of power increases in order to overcome the power of energy losses, in the direction opposite to the direction of power flow.

The useful (output) power  $P_u$  of motor or drive system operating in the ( $0 \leq \bar{\omega}_M < \bar{\omega}_{Mmax}$ ,  $0 \leq \bar{M}_M < \bar{M}_{Mmax}$ ) field, is independent of the losses power  $\Delta P$  in the motor or drive system, and it results from momentary values of the speed coefficient  $\bar{\omega}_M$  and load coefficient  $\bar{M}_M$  required by the driven device:

$$P_u = f(\bar{\omega}_M, \bar{M}_M). \quad (7)$$

The losses power  $\Delta P$  of in the motor or drive system depends on the system structure and quality of its components and, in a different way, on momentary values of the motor speed coefficient  $\bar{\omega}_M$  and load coefficient  $\bar{M}_M$  changing in the ( $0 \leq \bar{\omega}_M < \bar{\omega}_{Mmax}$ ,  $0 \leq \bar{M}_M < \bar{M}_{Mmax}$ ) range, respectively:

$$\Delta P = f(\bar{\omega}_M, \bar{M}_M). \quad (8)$$

The consumed (input) power  $P_c$  of motor or drive system results from the sum of the useful power  $P_u$  and losses power

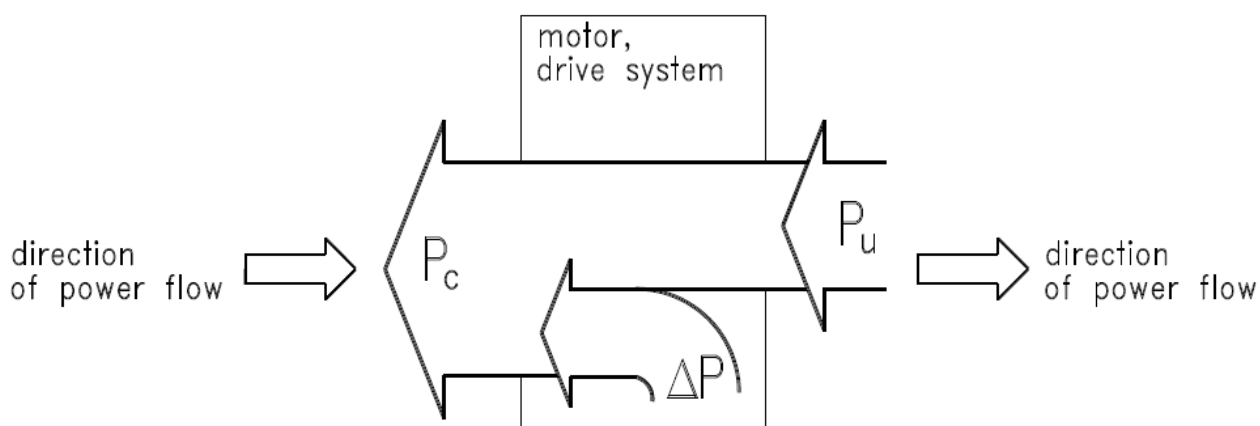


Fig. 4. Simplified diagram of the increase of power in motor or drive system opposite to the direction of power flow, replacing the Sankey diagram presented in Fig.1

$\Delta P$  of:

$$P_c = P_u + \Delta P = f(\bar{\omega}_M, \bar{M}_M). \quad (9)$$

A consequence of (8) and (9) is description of the motor or drive system energy efficiency  $\eta$  as dependent on  $\bar{\omega}_M$  and  $\bar{M}_M$ :

$$\eta = \frac{P_u}{P_c} = \frac{P_u}{P_u + \Delta P} = \frac{1}{1 + \frac{\Delta P}{P_u}} = f(\bar{\omega}_M, \bar{M}_M). \quad (10)$$

Formula (10) describing the energy efficiency  $\eta$ , in comparison with formula (2), allows not only to determine the effectiveness of the use of the power  $P_c$  consumed in the motor or drive system, but also to describe mathematically the dependence of the momentary value of the useful power  $P_u$ , losses power  $\Delta P$  and, in effect, the consumed power  $P_c$  and momentary value of the energy efficiency  $\eta$  on the speed coefficient  $\bar{\omega}_M$  and load coefficient  $\bar{M}_M$  of the motor shaft or piston rod.

In the hydrostatic drive [4], energy investigations of pump and hydraulic motor as independent machines consist in determination of the pressure coefficients  $k_i$ , volumetric and mechanical losses. The coefficients  $k_i$  are used in mathematical descriptions of the relations of individual losses to the physical quantities directly deciding on them. The pressure, volumetric, mechanical and overall energy efficiency characteristics of the machines in question are determined in parallel with evaluation of the overall efficiency of a hydrostatic system where they are used. Knowledge of the values of the coefficients  $k_i$  of losses in elements of hydrostatic system allows to obtain, by using a numerical method, the pump efficiencies:  $\eta_{p_p}$ ,  $\eta_{p_v}$ ,  $\eta_{p_m}$  and  $\eta_p$ , hydraulic motor efficiencies:  $\eta_{M_p}$ ,  $\eta_{M_v}$ ,  $\eta_{M_m}$  and  $\eta_M$ , conduit efficiency  $\eta_c$ , throttling control assembly (if it is used) structural efficiency  $\eta_{st}$  and the hydrostatic drive system overall efficiency  $\eta$  in function of  $\bar{\omega}_M$  and  $\bar{M}_M$ , in the hydraulic motor (hydrostatic system) operating field ( $0 \leq$

$\bar{\omega}_M < \bar{\omega}_{M_{max}}$ ,  $0 \leq \bar{M}_M < \bar{M}_{M_{max}}$ ) and at a selected value of the ratio  $\nu/\nu_n$  of the hydraulic oil viscosity  $\nu$  and the reference viscosity  $\nu_n$ . The proposed method is precise by definition and simple in use. It simplifies the laboratory investigation of pumps, hydraulic motors and hydrostatic drive systems. It allows to seek for energy - saving structures of hydrostatic drive system.

## CONCLUSION

From the diagrams of power decrease in a steam plant investigated by Sankey and from the Sankey's comment it may be concluded that power losses are treated as wasted branches of the main stream and weakening that stream and also that „work (per unit of time) done upon the pistons of the engine” results from power consumed by the system and powers of losses in the system. The diagram of power stream in the drive system, adopted by Sankey, was probably an effect of his concentration on the decrease of main power stream in the direction of power flow, caused by energy losses in the system, which are wasted and abstracted outwards.

However, referring to Sankey diagrams for an actual and idealized steam plant it can be noted that the level of energy losses in a drive system changes depending on the system quality even when the system useful power remains practically unchanged.

Therefore it may be concluded that, depending on whether we consider an actual or idealized system, the input consumed power, with the same physical quantities describing the drive system useful output power (e.g. the same motor shaft speed and load), will change as dependent upon the power of energy losses in the system.

Also, it may be concluded that the input power consumed by system will be decided by output useful power and powers of energy losses related to the system quality.

However, using the Sankey diagram, one can not present

the drive system energy losses as dependent on the physical quantities deciding on the system output useful power, present the relation of the input consumed power to the output useful power or describe mathematically the powers of energy losses and system energy efficiency as dependent upon the speed and load of motor in the system.

Description of the motor or drive system energy efficiency  $\eta$ , obtained from the Sankey diagram, allows only to determine the effectiveness of the use of consumed power.

The Sankey diagram does not describe in full the physical phenomena occurring in a drive system.

In a motor or drive system, the quantity of power increases in order to overcome the power of energy losses, in the direction opposite to the direction of power flow.

The useful (output) power of a motor or drive system working in the operating field ( $0 \leq \bar{\omega}_M < \bar{\omega}_{Mmax}$ ,  $0 \leq \bar{M}_M < \bar{M}_{Mmax}$ ), is independent of the powers of losses in the motor or drive system and results from the momentary values of the speed coefficient  $\bar{\omega}_M$  and load coefficient  $\bar{M}_M$  required by the driven device.

Power of energy losses in a motor or drive system depends on the system structure and quality of its elements and, in a different way, on the momentary values of the motor speed coefficient  $\bar{\omega}_M$  and load coefficient  $\bar{M}_M$  changing in the ( $0 \leq \bar{\omega}_M < \bar{\omega}_{Mmax}$ ,  $0 \leq \bar{M}_M < \bar{M}_{Mmax}$ ) range, respectively.

The proposed formula (10), describing the energy efficiency  $\eta$ , allows not only to determine the effectiveness of the use of power consumed in a motor or drive system, but also to describe mathematically the relations of momentary value of useful power, power of losses and, in effect, consumed power and momentary value of energy efficiency to the motor shaft (or piston rod) speed coefficient  $\bar{\omega}_M$  and load coefficient  $\bar{M}_M$  changing in the ( $0 \leq \bar{\omega}_M < \bar{\omega}_{Mmax}$ ,  $0 \leq \bar{M}_M < \bar{M}_{Mmax}$ ) range, respectively.

The proposed diagram of power increase opposite to the direction of power flow in a motor or drive system, replacing the Sankey diagram, opens a new prospect for research into power of energy losses and efficiency of motors and drive systems.

Reference [4] presents a proper and complete view of the energy losses and energy efficiency of a hydrostatic drive system. It is an example to be followed in other types of drive. It allows to compare objectively the energy efficiencies of different drives.

## BIBLIOGRAPHY

1. Sankey M. H.: *The Thermal Efficiency of Steam Engines*. „Minutes of Proceedings of the Institution of Civil Engineers”. CXXXIV (1897 - 1898, Part IV). Reprint in Journal of the American Society of Naval Engineers. Vol. XI.NO.4. November, 1899. pp. 949 ÷975. ( Retrieved from University of Michigan)
2. Paszota Z.: *Losses and energy efficiency of drive motors and systems. Replacement of the Sankey diagram of power decrease in the direction of power flow by a diagram of power*

*increase opposite to the direction of power flow opens a new perspective of research of drive motors and systems*. Polish Maritime Research 1/2013

3. Feature/Eastern Europe: *Driving a new perspective. Professor Zygmunt Paszota, faculty of ocean engineering and ship technology, Gdansk University of Technology, Poland, explains a new approach to the Sankey Diagram for drive motors*. The Naval Architect, May 2013, pp. 72 ÷ 76,
4. Paszota Z.: *Energy losses in hydrostatic drive. Drive investigation method compatible with diagram of power increase opposite to the direction of power flow*. LAP LAMBERT Academic Publishing, 2016

## CONTACT WITH THE AUTOR

Zygmunt Paszota

*e – mail: zpaszota@pg.gda.pl*

Gdansk University of Technology  
11/12 Narutowicza St.  
80-233 Gdansk  
Poland

**POLAND**

## FERROMAGNETIC FLOW OF VISCOUS FLUID IN A SLOT BETWEEN FIXED SURFACES OF REVOLUTION

Sawicki Jerzy, Assoc. Prof. UTP

University of Technology and Life Sciences in Bydgoszcz, Poland

### ABSTRACT

*In this paper the steady laminar flow of viscous incompressible ferromagnetic fluid is considered in a slot between fixed surfaces of revolution having a common axis of symmetry. The boundary layer ferromagnetic equations for axial symmetry are expressed in terms of the intrinsic curvilinear orthogonal coordinate system  $x, \theta, y$ . The method of perturbation is used to solve the boundary layer equations. As a result, the formulae defining such parameters of the flow as the velocity components  $v_x, v_y$ , and the pressure, were obtained.*

**Keywords:** laminar flow, incompressible ferromagnetic fluid, method of perturbation

### INTRODUCTION

Magnetic fluids are a group of materials with properties hardly ever encountered in nature [9, 15]. A combination of fluid and ferromagnetic material makes, without external magnetic field, magnetic fluids not to show magnetization and, reversely, the magnetic fluid, when subjected to external magnetic field, changes its properties [3, 8, 10]. Depending on the concentration of ferromagnetic particles, the magnetic fluid behaves like Newton fluid or non-Newton fluid [10].

Nowadays there are many different applications of magnetic fluids in engineering, e.g., in slide bearings, clutches, brakes, seals, electrohydraulic servomotors, linear and rotary mufflers, etc [1, 9, 11, 13].

Modeling of laminar flow of viscous fluids going through slots between movable and non-movable rotating surfaces exposed to magnetic field still plays a significant role in engineering [6, 7, 12, 14, 16]. With that in mind, it is important for the studies in this field to be performed both in terms of theory and possible practical applications [2, 4, 5].

The purpose of this study is to analyze the theory of the impact of magnetic field and the flow inertia on the ferromagnetic fluid flow in a slot between fixed surfaces of revolution.

### BASIC EQUATIONS

The motion of the ferromagnetic fluid in the slot, as shown in Fig. 1, is laminar and isothermal.

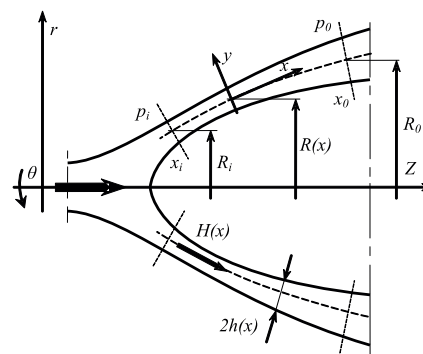


Fig. 1. Ferromagnetic fluid flow area

The flow takes place in the external, steady and heterogeneous magnetic field. However, it has been assumed that the ferromagnetic fluid is electrically non-conductive and the vectors of magnetic field strength and magnetization, respectively, are parallel to each other. The surfaces are

described with the function which denotes the radius of the median between the fixed surfaces, together with the function which denotes the distance of each surface from the median, measured along the normal to the median.

According to the principles of mass momentum conservation, the equations of motion are [3]:

The continuity equation:

$$\nabla V = 0 \quad (1)$$

The momentum equation:

$$\rho(\mathbf{V}\nabla)\mathbf{V} = -\nabla p + \mu\Delta\mathbf{V} + \mu_0(\mathbf{M}\nabla)\mathbf{H} \quad (2)$$

where:  $\mathbf{V}$ ,  $\mathbf{M}$ ,  $\mathbf{H}$ ,  $p$ ,  $\rho$ ,  $\mu$ ,  $\mu_0$  – are: the velocity vector of fluid flow, the vector magnetization vector of the magnetic field, pressure, density, dynamic viscosity, and magnetic permeability of vacuum.

Eqs (1) and (2), to be completed, require some additional equations describing the magnetic field, i.e. the magnetostatic equations of:

$$\nabla \times \mathbf{H} = 0 \quad (3)$$

$$\nabla \mathbf{B} = 0 \quad (4)$$

$$\mathbf{B} = \mu_0(\mathbf{H} + \mathbf{M}) \quad (5)$$

The equations for motion are assumed to describe the general case of the flow in the curvilinear coordinates system [14, 16]. If the asymptotic transformations have been made, the equations can be reduced to a simpler form:

$$\frac{1}{R} \frac{\partial(Rv_x)}{\partial x} + \frac{\partial v_y}{\partial y} = 0 \quad (6)$$

$$\rho \left( v_x \frac{\partial v_x}{\partial x} + v_z \frac{\partial v_x}{\partial y} \right) = -\frac{\partial p}{\partial x} + \mu \frac{\partial^2 v_x}{\partial y^2} + \mu_0 M_x \frac{\partial H_x}{\partial x} \quad (7)$$

$$\frac{\partial p}{\partial y} = 0 \quad (8)$$

where:  $v_x, v_\theta, v_y, p, M_x, H_x$  – respectively: velocity components, pressure, component of magnetization, component of magnetic field.

Thus, from equation (8) we have:

$$p = p(x) \quad (9)$$

The boundary conditions for velocity components are:

$$v_x(x, \mp h) = 0, \quad v_y(x, \mp h) = 0, \quad (10)$$

Moreover, the inlet and outlet pressure under slot conditions can take the form of:

for

$$p = p_i \quad \text{for} \quad x = x_i \quad (11)$$

for

$$p = p_o \quad \text{for} \quad x = x_o$$

where:  $x_i$  – denotes the inlet coordinate,  $x_o$  – the outlet coordinate.

## SOLUTION OF THE EQUATIONS OF MOTION

Introducing the following dimensionless quantities:

$$\tilde{x} = \frac{x}{R_o}, \quad \tilde{y} = \frac{y}{h_o}, \quad \tilde{R} = \frac{R}{R_o}, \quad (12)$$

$$\tilde{v}_x = \frac{v_x}{v_o}, \quad \tilde{v}_y = \frac{v_y R_o}{v_o h_o}, \quad \tilde{p} = \frac{p h_o}{\mu v_o R_o}$$

We can present the equations of motion (6) (8) in the form:

$$\frac{1}{\tilde{R}} \frac{\partial(\tilde{\rho} R \tilde{v}_x)}{\partial \tilde{x}} + \frac{\partial(\tilde{\rho} \tilde{v}_y)}{\partial \tilde{y}} = 0 \quad (13)$$

$$\lambda \left( \tilde{v}_x \frac{\partial \tilde{v}_x}{\partial \tilde{x}} + \tilde{v}_y \frac{\partial \tilde{v}_x}{\partial \tilde{y}} \right) = -\frac{\partial \tilde{p}}{\partial \tilde{x}} + \frac{\partial^2 \tilde{v}_x}{\partial \tilde{y}^2} + RF \tilde{M}_x \frac{\partial \tilde{H}_x}{\partial \tilde{x}} \quad (14)$$

$$0 = -\frac{\partial \tilde{p}}{\partial \tilde{y}} \quad (15)$$

where:

$$RF = \frac{\mu_0 M_o H_o h_o^2}{\mu v_o R_o}, \quad \tilde{H}_x = \frac{H_x}{H_o}, \quad \tilde{M}_x = \frac{M_x}{M_o},$$

$$\lambda = Re \frac{h_o}{R_o}, \quad Re = \frac{2\rho v_o h_o}{\mu}$$

The quantities marked with subscript 'zero' are average values within the discussed flow domain;  $\lambda$  – the modified Reynolds number which satisfied the condition:

$$\lambda < 1 \quad (16)$$

From Eq.(13) and (15) one can see that in the motion of ferromagnetic fluid, if condition (16) is satisfied, is a small parameter in Eq. (14).

Thus, the solution can be sought to in the form of power series with respect to  $\lambda$  [16]:

$$\tilde{v}_x = \sum_{i=0}^{\infty} \lambda^i \tilde{v}_x^i, \quad \tilde{v}_y = \sum_{i=0}^{\infty} \lambda^i \tilde{v}_y^i,$$

$$\tilde{p} = \sum_{i=0}^{\infty} \lambda^i \tilde{p}^i \quad (17)$$

Introducing the series (17) into Eq. (13) and (14), after necessary transformations, the terms referring to the same power of dimensional form  $\lambda$ , if we restrict ourselves to the linear approximation and return to the previous one, we receive the following equations:

$$\frac{1}{R} \frac{\partial(Rv_x^0)}{\partial x} + \frac{\partial v_y^0}{\partial y} = 0 \quad (18)$$

$$0 = -\frac{\partial p^0}{\partial x} + \mu \frac{\partial^2 v_x^0}{\partial y^2} + \mu_0 M_x \frac{\partial H_x}{\partial x} \quad (19)$$

$$\frac{1}{R} \frac{\partial(Rv_x^1)}{\partial x} + \frac{\partial v_y^1}{\partial y} = 0 \quad (20)$$

$$\rho \left[ v_x^0 \frac{\partial v_x^0}{\partial x} + v_y^0 \frac{\partial v_x^0}{\partial y} \right] = -\frac{\partial p^1}{\partial x} + \mu \frac{\partial^2 v_x^1}{\partial y^2} + \mu_0 M_x \frac{\partial H_x}{\partial x} \quad (21)$$

The boundary conditions, according to Eq.(10) and (11), take the form of [16]:  
for

$$v_x^0 = v_x^1 = v_y^0 = v_y^1 = 0 \quad \text{for } y = \mp h \quad (22)$$

for

$$p^0 = p_i \quad p^1 = 0 \quad \text{for } x = x_i \quad (23)$$

$$p^0 = p_0 \quad p^1 = 0 \quad \text{for } x = x_0$$

Integrating Eq. (18) and (21) and making the boundary conditions (22) and (23) to be valid, we have:

$$v_x^0 = \frac{1}{2\mu R h^3} \frac{p_i - p_0 - B_i + B_0}{A_i - A_0} (y^2 - h^2) \quad (24)$$

$$v_y^0 = \frac{h'}{2\mu R h^4} \frac{p_i - p_0 - B_i + B_0}{A_i - A_0} (h^2 y - y^3) \quad (25)$$

$$p^0 = B(x) + \frac{[A(x) - A_0](p_i - B_i) - [A(x) - A_i](p_0 - B_0)}{A_i - A_0} \quad (26)$$

$$v_x^1 = \frac{\rho \left( \frac{p_i - p_0 - B_i + B_0}{A_i - A_0} \right)^2 (R h)'}{840 \mu^3 R^3 h^7} (35 h^2 y^4 - 7 y^6 + 5 h^6 - 33 h^4 y^2) \quad (27)$$

$$v_y^1 = \frac{\rho \left( \frac{p_i - p_0 - B_i + B_0}{A_i - A_0} \right)^2}{840 \mu^3 h^7} \left\{ \left[ \frac{(R h)'}{R^2 h^7} \right] (y^7 - 7 h^2 y^5 - 5 h^6 y + 11 h^4 y^3) + \frac{(R h)'}{R^2 h^7} (44 h^3 y^3 - 14 h y^5 - 30 h^5 y) \right\} \quad (28)$$

$$p^1 = D(x) - \frac{[A(x) - A_0] D_i - [A(x) - A_i] D_0}{A_i - A_0} \quad (29)$$

where:

$$R' = \frac{dR}{dx}, \quad h' = \frac{dh}{dx},$$

$$A(x) = \int \frac{dx}{R(x)h^3}, \quad A_i = A(x_i), \quad A_0 = A(x_0)$$

$$B(x) = \frac{\mu_0 M_0 H_0 R_0}{R}, \quad B_i = B(x_i), \quad B_0 = B(x_0)$$

The complete solution of the ferromagnetic fluid flow problem inside a slot between curvilinear surfaces is made up of the sum of partial solutions.

### FERROMAGNETIC FLUID FLOW BETWEEN FIXED CONICAL SURFACES

After introducing the functions used for describing the flow area geometry (Fig. 2) in Eq. (24) through (29):

$$R(x) = x \sin(\alpha), \quad R_i = x_i \sin(\alpha),$$

$$R_0 = x_0 \sin(\alpha), \quad R' = \sin(\alpha)$$

and introducing the dimensionless quantities:

$$\xi = \frac{x}{R_0}, \quad \eta = \frac{y}{h}, \quad \bar{R}' = 1,$$

$$\bar{v}_x = \frac{v_x}{v_{xmax}^0}, \quad \bar{v}_y = \frac{v_y}{v_{xmax}^0} \frac{R_0}{h}, \quad v_{xmax}^0 = \frac{p_0 h^2 (\bar{p}_i - 1)}{2x \mu R_0 (a_0 - a_i)}$$

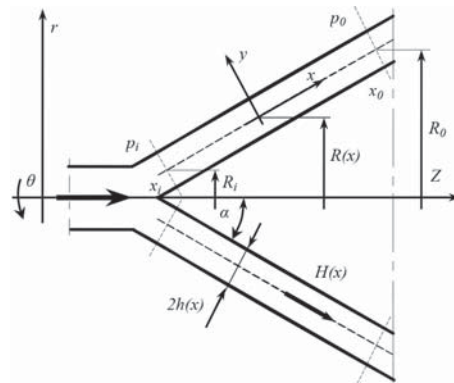


Fig. 2. Conical slot geometry

we get the following dimensionless formulas representing the velocity and pressure field in the slot:

$$\bar{v}_x^0 = \left( 1 - \frac{\bar{B}_i - \bar{B}_0}{\bar{p}_i - 1} \right) (1 - \eta^2), \quad (30)$$

$$\bar{v}_y^0 = 0, \quad (31)$$

$$\bar{p}^0 = \bar{B}(x) + \frac{[a(x) - a_0](\bar{p}_i - \bar{B}_i) - [a(x) - a_i](1 - \bar{B}_0)}{a_i - a_0}, \quad (32)$$

$$\bar{v}_x^1 = -\frac{1}{420\xi^2} \Lambda c \frac{a_i - a_0}{\bar{p}_i - 1} \frac{[\bar{p}_i - 1 - \bar{B}_i + \bar{B}_0]^2}{a_i - a_0} (5 - 7\eta^6 + 35\eta^4 - 33\eta^2) \quad (33)$$

$$\bar{v}_y^1 = \frac{1}{240\xi^3} \Lambda c \frac{a_i - a_0}{\bar{p}_i - 1} [\bar{p}_i - 1 - \bar{B}_i + \bar{B}_0]^2 (\eta^7 - 7\eta^5 + 11\eta^3 - 5\eta) \quad (34)$$

$$\bar{p}^1 = \bar{D}(x) - \frac{[a(x) - a_0] \bar{D}_i - [a(x) - a_i] \bar{D}_0}{a_i - a_0} \quad (35)$$

where:

$$a(x) = \ln(\xi), \quad a_i = a(\xi_i), \quad a_0 = a(\xi_0),$$

$$\bar{B}(x) = \frac{RF}{\xi}, \quad \bar{B}_i = \bar{B}(\xi_i), \quad \bar{B}_0 = \bar{B}(\xi_0),$$

$$RF = \frac{\mu_0 M_0 H_0}{p_0},$$

$$\bar{D}(x) = -\frac{3}{35} \Lambda c \frac{(\bar{p}_i - 1 - \bar{B}_i + \bar{B}_0)^2}{\xi^2}, \quad \bar{D}_i = \bar{D}(\xi_i),$$

$$\bar{D}_0 = \bar{D}(\xi_0), \quad \Lambda c = \frac{\rho p_0 h^4}{\mu^2 R_0^2 (a_i - a_0)^2}.$$

The above given formulas have been illustrated in Fig 3 Fig 6.

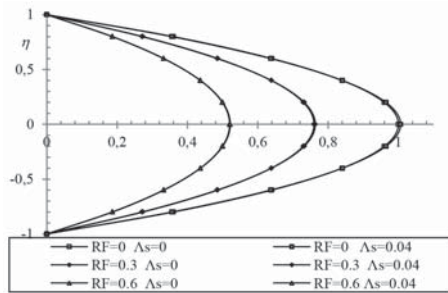


Fig. 3. Effect of the magnetic pressure number RF and longitudinal inertia forces on the velocity profile  $\bar{v}_x$  and  $\bar{v}_x^0$ , ( $\xi_i = 0,2$ ,  $\xi_0 = 0,6$ ,  $\bar{p}_i = 5$ .)

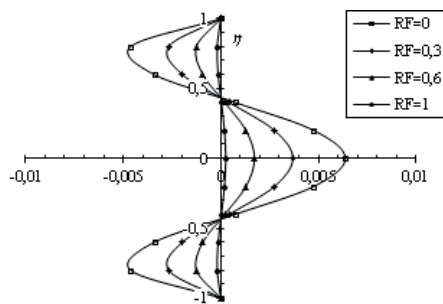


Fig. 4. Effect of the magnetic pressure number RF and longitudinal inertia forces on the velocity profile  $\bar{v}_x^1$ , ( $\xi_i = 0,2$ ,  $\xi_0 = 0,6$ ,  $\bar{p}_i = 5$ ,  $\Lambda c = 0,04$ )

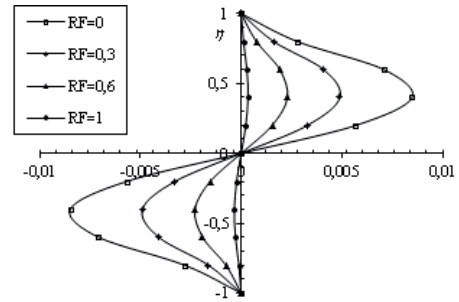


Fig. 5. Effect of the magnetic pressure number RF and longitudinal inertia forces on the velocity profile  $\bar{v}_y^1$ , ( $\xi_i = 0,2$ ,  $\xi_0 = 0,6$ ,  $\bar{p}_i = 6$ ,  $\Lambda c = 0,04$ ),

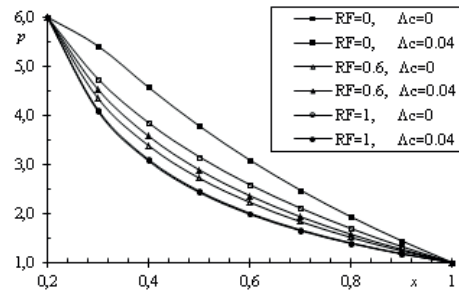


Fig. 6. Effect of the magnetic pressure number RF and dimensionless parameter corresponding to the effect of longitudinal inertia forces on the pressure  $\bar{p}$  ( $\xi_i = 0,2$ ,  $\xi_0 = 1$ ,  $\bar{p}_i = 6$ )

## FERROMAGNETIC FLUID FLOW BETWEEN FIXED SPHERICAL SURFACES

The parameters used to describe the flow area geometry can be written as follows (Fig. 7):

$$R(x) = R_k \sin(\varphi), \quad R_i = R_k \sin(\varphi_i),$$

$$R_0 = R_k \sin(\varphi_0),$$

$$R' = \cos(\varphi), \quad \varphi = \frac{x}{R_k}.$$

After introducing the functions used for describing the geometry of the flow area (Fig. 7) in Eq. (24) through (29) and providing the dimensionless quantities:

$$\eta = \frac{y}{h}, \quad \bar{R} = \frac{R(x)}{R_0}, \quad \bar{R}' = \cos(\varphi)$$

$$\bar{v}_x = \frac{v_x}{v_{xmax}^0}, \quad \bar{v}_y = \frac{v_y}{v_{xmax}^0} \frac{R_k \sin(\varphi_0)}{h}, \quad v_{xmax}^0 = \frac{p_0 h^2 (\bar{p}_i - 1)}{2\mu \sin(\varphi) (a_0 - a_i) R_0}$$

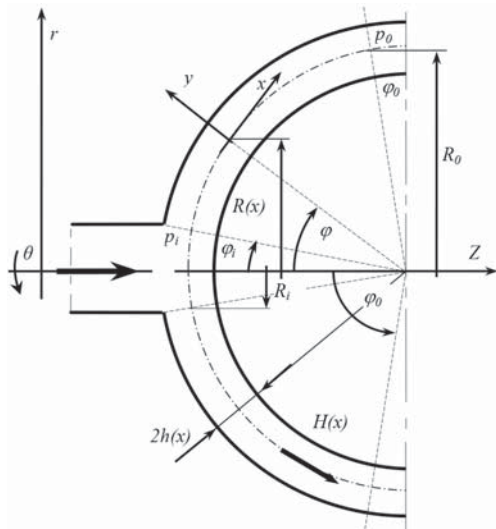


Fig. 7. Spherical slot geometry

we obtain the formulas representing the motion of the ferromagnetic fluid inside the slot between the fixed spherical surfaces:

$$\bar{v}_x^0 = \left(1 - \frac{\bar{B}_i - \bar{B}_0}{\bar{p}_i - 1}\right) (1 - \eta^2), \quad (36)$$

$$\bar{v}_y^0 = 0 \quad (37)$$

$$\bar{p}^0 = \bar{B}(x) + \frac{[a(x) - a_0](\bar{p}_i - \bar{B}_i) - [a(x) - a_i](1 - \bar{B}_0)}{a_i - a_0}, \quad (38)$$

$$\bar{v}_x^1 = -\frac{1}{420} \Lambda_s \frac{a_i - a_0}{\bar{p}_i - 1} \frac{[\bar{p}_i - 1 - \bar{B}_i + \bar{B}_0]^2 \cos(\varphi)}{a_i - a_0 \sin^2(\varphi)} (5 - 7\eta^6 + 35\eta^4 - 33\eta^2) \quad (39)$$

$$\bar{v}_y^1 = \frac{1}{240 \sin^3(\varphi)} \Lambda_s \frac{a_i - a_0}{\bar{p}_i - 1} [\bar{p}_i - 1 - \bar{B}_i + \bar{B}_0]^2 \frac{1 + \cos^2(\varphi)}{3} (\eta^7 - 7\eta^5 + 11\eta^3 - 5\eta) \quad (40)$$

$$\bar{p}^1 = \bar{D}(x) - \frac{[a(x) - a_0]\bar{D}_i - [a(x) - a_i]\bar{D}_0}{a_i - a_0} \quad (41)$$

where:

$$a(\varphi) = \ln \left| \tan \left( \frac{\varphi}{2} \right) \right|, \quad a_i = a(\varphi_i), \quad a_0 = a(\varphi_0),$$

$$\bar{B}(\varphi) = \frac{RF}{\sin(\varphi)}, \quad \bar{B}_i = \bar{B}(\varphi_i), \quad \bar{B}_0 = \bar{B}(\varphi_0),$$

$$RF = \frac{\mu_0 M_0 H_0}{p_0},$$

$$\bar{D}(x) = -\frac{3}{35} \Lambda_s \frac{(\bar{p}_i - 1 - \bar{B}_i + \bar{B}_0)^2}{\sin^2(\varphi)},$$

$$\bar{D}_i = \bar{D}(\varphi_i), \quad \bar{D}_0 = \bar{D}(\varphi_0), \quad \Lambda_s = \frac{\rho p_0 h^4}{\mu^2 R_0^2 (a_i - a_0)^2}.$$

Since diagrams of the ferromagnetic fluid flow velocity distribution along the slot between the fixed spherical surfaces show no substantial differences from the ferrofluid flow velocity distribution in the slot between the fixed conical surfaces, only the formulas for pressure profiles are illustrated in the diagram (Fig. 8).

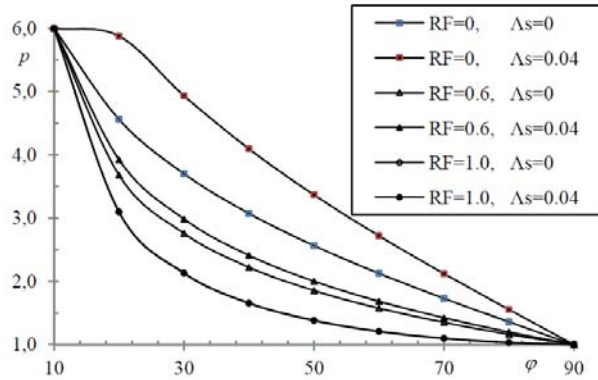


Fig. 8. Effect of the magnetic pressure number RF and dimensionless parameter corresponding to the effect of longitudinal inertia forces on the pressure  $\bar{p}$  ( $\varphi_i = 10^\circ$ ,  $\varphi_0 = 90^\circ$ ,  $\bar{p}_i = 6$ )

## DISCUSSION OF THE RESULTS

With the diagram and equations describing the components of the field of velocity and pressure, it is possible to formulate the following conclusions:

**For longitudinal velocity  $v_x$**  (Fig. 3):

- the main profile of velocity  $v_x$  is a parabolic profile identical to traditional Poisseuille flow profile caused by a steady gradient of pressure (constant pressure difference) characteristic for the so-called Reynolds approximation;
- the so-called secondary profile symmetric to the slot symmetry axis formed due to the occurrence of the flow inertia effects, overlaps the main velocity profile  $v_x$  (Fig. 4).

**For transverse velocity  $v_y$**  (Fig. 5):

- distribution of transverse velocity  $v_y$  is the result of inertia effects occurring in the flow,
- an increase in the magnetic field strength expressed with an increase in the value of magnetic pressure number  $R$  results in decreasing the longitudinal and transverse velocity components.

**For pressure** (Fig. 6 and Fig. 8):

- inertia effects ( $\Lambda_{L_c}, \Lambda_{L_s} > 0$ ) cause a minimum pressure increase along the slot,
- an increase in the magnetic field strength expressed with an increase in the value of magnetic pressure number, causes a pressure drop along the slot.

The flow through slots with curvilinear profiles is less susceptible to inertia effects.

## BIBLIOGRAPHY

1. Bednarek S.: Ferromagnetic fluids - materials with unusual properties and their applications, 2009, Foton, Institute of Physics, Jagiellonian University, spring 104
2. Buhler L.: Magneto hydrodynamic flow in ferromagnetic pipes, Forschungszentrum Karlsruhe GmbH, 2002
3. Ezekiel F.D.: Ferrolubricants: 1975, New Application, Mechanical Engineering, 2
4. Huang W., Wang X.: Ferrofluids lubrication: a status report, 2015, Lubrication Science, 02
5. Lemarquand V. , Lemarquand G.: Ferrofluid seals, ,New Tribological Ways, 2011, 04.
6. McAlister K. W., Rice W.: Throughflows between rotating surfaces of revolution, having similarity solutions, J. Appl. Mech. Trans. ASME, Series E, 1970, 37, 4
7. McAlister K.W., Rice W.: Flows between stationary surfaces of revolution, having similarity solutions, J. Appl. Mech. Trans. ASME, Series E, 1972, 39, 2
8. Muc A., Barski M.: Magnetorheological fluids and their practical applications, Technical magazine, Cracow University of Technology , 2007, Z1-M
9. Nada G.S., Osman T.A.: Journal bearings lubricated by magnetic fluids with couple stresses, Tribology Letters, 2007, 27, 3
10. Neuringer J.L., Rosenzweig R.E.: Ferrohydrodynamics, Phys. Fluids, 1964, 7, 12
11. Ravaut R., Lemarquand G., Lemarquand V.: Mechanical properties of ferrofluids applications: Centering effect and capacity of a seal, Tribology International , 2010, 01.
12. Reinhardt E., Lund W.J. : The influence of fluid inertia on the dynamic properties of journal bearings, J. Lubric. Technol., Trans. ASME, Series F , 1975,, 97, 2
13. Safar Z.S., Nada G.S., Osman T.A.: Static and dynamic characteristic of magnetized journal bearing lubricated with ferrofluids, Tribology International , 2001, 02
14. Sawicki J.: Magneto hydrodynamic flow of viscous fluid in a slot between curvilinear surfaces of revolution, Engineering Transactions, PAN-IPPT, 1996, 44 ,1
15. Szliomis M.I.: Magnitnyye zhidkosti ( in Russian), Usp., Fiz. Nauk, 1974, 112, 3
16. Walicki E. , Sawicki J., Ziejewski M.: Inertia effect in magnetic throughflow fluid in a slot between fixed surfaces of revolution, Mec. Applique, 1978, 23, 6.

## CONTACT WITH THE AUTHOR

Sawicki Jerzy, Assoc. Prof. UTP

*e-mail: jerzy.sawicki@utp.edu.pl*

University of Science and Technology in Bydgoszcz  
Faculty of Mechanical Engineering  
Department of Applied Mechanics  
Al. Prof. S. Kaliskiego 7  
85-796 Bydgoszcz

**POLAND**

# A METHOD FOR DETERMINING THE USABILITY POTENTIAL OF SHIP STEAM BOILERS

Łukasz Muślewski <sup>1</sup>

Michał Pająk <sup>2</sup>

Bogdan Landowski <sup>1</sup>

Bogdan Żółtowski <sup>1</sup>

<sup>1</sup> University of Science and Technology in Bydgoszcz, Poland

<sup>2</sup> University of Technology in Radom, Poland

## ABSTRACT

*Ship large-power steam boiler may serve as an example of complex critical technical system. A basis for rational control of operation of such system is knowledge on its capability of fulfilling the tasks to which it was intended. In order to make it possible to apply computer aiding to operational decision-making the capability should be described analytically. In this paper it was proposed to express the capability of ship steam boiler (considered a complex system) to perform service tasks, by calculating components of its usability potential in a given instant  $t$ . To this end, was distinguished a set of steam boiler fundamental features which formulate space of its technical states. Values and characteristic intervals of the features were defined and this way sub-spaces of serviceability and non-serviceability states of the object in question were determined. Next, in the considered space, technical state of the boiler and its usability potential was determined. Owing to this it become possible to quantitatively express the steam boiler functioning capability which served as a basis for elaborating an algorithm for controlling the operational processes of a complex technical system under action. In this paper is also described a way of application of the presented method to calculation of ship steam boiler usability potential, which may be especially instrumental in the case of operational control of the boilers of the kind, equipped with interstage reheaters, i.e. those operating with high values of operational parameters.*

**Keywords:** Ship steam boilers, operation management, complex technical systems, usability potential.

## INTRODUCTION

There are two fundamental groups of processes which have place in operational phase of any technical system, hence also that of ship steam boiler, namely: operational processes and serviceability-ensuring processes called also maintenance ones. The main aim of operational use is to execute the tasks to fulfilling which a given technical system (boiler) was built. Execution of operational use aims changes features which describe such system, as a result of action of forcing factors dependent on and independent of operation of the system [19]. If values of boiler features reach their limits then its further operation may cause failures. For this reason steam boiler is to be subjected to maintenance processes. During the maintenance processes values of boiler features

are so changed as to make useful operating the boiler further possible. Changes in any boiler features force changes in its technical state, which consequently causes change in its capability of fulfilling operational tasks for which it was fitted in design and production phases. The capability is defined in the form of usability potential of steam boiler considered to be a technical system [14].

In the case of critical technical objects [22] for which occurrence of a failure is associated with high cost as well as hazard to health and life of people the problem of rational operation consists in such operational use of them as to maximize effects of its operation and prevent non-serviceability state to occur. Steam boilers (not only shipboard ones) and other main devices being a part of steam

and machine power plants on sea-going ships, may serve as such technical objects. Additionally, both steam boilers and other technical devices operating in sea conditions cannot be subjected to renewal processes in an arbitrary instant. The instant must be therefore assigned in advance (service life strategy) and in such a way as to ensure, by ship main power subsystems, executing ship's transport tasks possible up to the assigned instant. And, the only operational strategy which makes it possible to satisfy the condition of preventing against non-serviceability state, is the state-based strategy [21]. However it does not satisfy requirements dealing with necessity of in-advance assigning the instant of qualifying a boiler or other system for renewal. Moreover, for execution of operational processes in accordance with the state-based strategy it is necessary to determine a state of the boiler in question (considered to be a technical system) which constitutes an important issue for all complex technical systems.

The consideration presented in this paper deals with large-power steam boilers. Boilers of the kind are presently used as main boilers on large sea-going ships, especially tankers and passenger ships [8,10,12]. Aspiration for increasing efficiency of boilers results in increasing their power and degree of complexity of their structure by introducing additional heating surfaces in the form of interstage reheaters. Such boilers operate at large values of steam working parameters (12MPa, 565°C – UTR-II Kawasaki) [2], that makes them critical technical objects.

In the case of the considered technical objects it becomes necessary to make an operational decision answering the question whether a ship may begin its voyage or its boiler should be renewed or replaced. A basis for making such decision is determination of quantity of usability potential present in the considered technical object in a given instant.

During literature research it has been found out that accurate determination of usability potential of complex technical system meets many difficulties. The first problem is definition of the notion of usability potential itself. A detail analysis of the problem is contained in [18]. As results from the publication, to apply a new approach to the problem is necessary in order to unambiguously specify notions in the considered domain. Another research problem is association of usability potential with technical state of ship boilers. To accurately determine technical state of a boiler is not possible without its shutting down. Moreover even in the case of making diagnosis determination of some parameters of boiler elements is not possible by means of non-destructive methods. As an example may serve state of material of which steam boiler drum is built. It is common knowledge that it works under brittle fracture conditions and model of the process has not been fully so far identified that leads to necessity of performing mechanical tests on specimens taken from boiler drum. To determine usability potential of ship steam boiler in an arbitrary instant of its service it is necessary to know a model of wastage process not only of its units as it takes into account only additive features of boiler operational system, but also a model of its

wastage as a technical system owing to this both additive and constitutive features of such system are taken into account.

A detail analysis of usefulness of existing analytical and probabilistic models for representing changes in state of a complex technical system is given in the literature source [16]. As results from the publication, in present there is a lack of mathematical models which could make it possible to determine usability potential of complex technical systems such as ship steam boilers. Therefore, in this work is presented a way for the modelling of state of ship steam boilers considered to be technical systems as well as their usability potential, within a determined space of technical states of the systems. The described way has been next used to analyze usability potential of a selected large-power boiler considered to be a complex system.

## SPACE OF TECHNICAL STATES OF A SYSTEM

For an arbitrary feature  $x_i$  which describes a given system it is possible to define the variability interval  $X_{iZM}$  as a set of values which this feature may take. The variability interval is constrained by the minimum value  $x_{imin}$  and maximum value  $x_{imax}$  of the feature in question. Within the feature variability interval, depending on an assumed criterion for assessing value of the feature, the minimum limit value  $x_{igrmin}$  and maximum limit value  $x_{igrmax}$  establishing the range of permissible values, can be determined. A subset of permissible values is formed by suboptimum values contained in the interval between the minimum suboptimum value  $x_{isomin}$  and the maximum suboptimum value  $x_{isomax}$ . Among suboptimum values the optimum value  $x_{io}$  can be distinguished. The above specified values and ranges are defined to be characteristic values and intervals of a feature.

It has been also defined that the set of cardinal features is the least numerous set of features considered significant for a given problem, whose instantaneous values unambiguously identify system's state [24]. The system's state described by vector of cardinal features is a point in  $n$ -dimensional space, where  $n$  stands for power of the set of cardinal features, and the space is that of system's features.

If points of system's feature space are taken as states of the system then characteristic intervals of features which describe the system determine, in the system's feature space,  $n$ -dimensional hyper-fields of system's states: the field of non-permissible states  $S_{ND}$ , field of permissible states  $S_D$  and field of suboptimum states  $S_{SO}$ , respectively. The fields of system's features in the space of features are formulated as a cartesian product which is a common part of cylindrical extensions corresponding to relevant intervals of feature values [16].

If the set of cardinal features contains physical features of the system, for which characteristic values and intervals have been distinguished with respect to possible execution of system's service aims then in the space of system's features, are obtained hyper-fields of reliability states of the system. Such space is called the space of technical states of the system.

For the features which are dimensions of the defined space, exactly determined, i.e. such that the interval of suboptimum values coincides with the interval of permissible values, then one obtains such split of the variability range of features that in the considered space of system's features, hyper-fields of serviceability and non-serviceability states, are formed (Fig.1) [5].

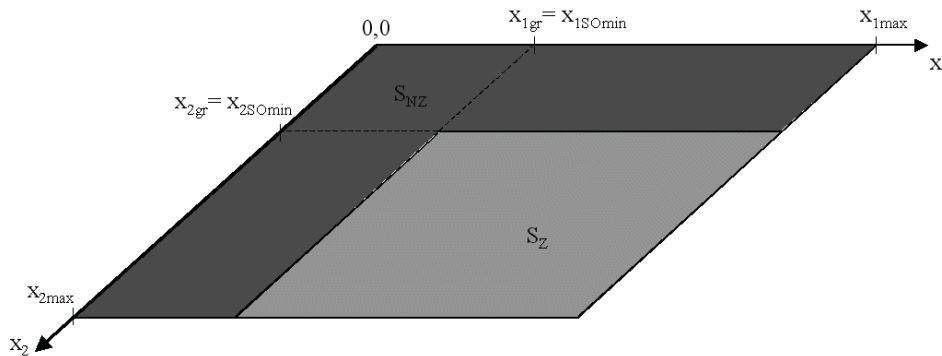


Fig. 1 – Location of fields of serviceability and non-serviceability states in the strictly determined space of technical states of an arbitrary system R2

In the strictly determined space of technical states [17] a system remains in the serviceability state if values of all cardinal features are contained within their respective intervals of permissible values (1):

$$s_R(x_1, x_2, \dots, x_n) \in S_Z \Leftrightarrow \forall x_i \in X \wedge i = 1, 2, \dots, n : x_i \in X_{iD} \quad (1)$$

where:

$s_R$  – real state of the system,

$x_i$  – i-th cardinal feature of the system,

$S_Z$  – hyper-field of serviceability states,

$X_{iD}$  – interval of permissible values of i-th feature which describes the system.

The system is in a non-serviceability state if value of at least one of the cardinal features which form the space of technical states of the system is contained within the interval of non-permissible values (2) [10]:

$$s_R(x_1, x_2, \dots, x_n) \in S_{NZ} \Leftrightarrow \exists X_k \subset X : \text{card}(X_k) \geq 1 \wedge \forall x_i \in X_k : x_i \in X_{iND} \quad (2)$$

where:

$S_{NZ}$  – hyper-field of non-serviceability states of the system.

The set of points which form the boundary of hyper-field of serviceability states is a representation of the system's limit states sgr [26].

If for the analyzed object in question, i.e. a ship steam boiler, the general coordinates used in Fig. 1, are replaced by steam pressure and temperature at outlet from heat exchanger (interstage reheater) then at assumed constant steam load, constant inlet steam parameters as well as constant amount of heat in exhaust gas, one obtains the space of reliability states of the considered exchanger. If values of outlet steam parameters drop below the determined ones (usually, temperature equal to that of life steam, 5K, and pressure reduced below a half

of that of life steam) then the exchanger will be considered as being in non-serviceability state [12].

It should be stressed that the conducted considerations have a detail character for relatively simple systems such as steam boilers on sea-going ships, nevertheless the presented method may be implemented also for assessing more complex technical objects or operational systems.

## USABILITY POTENTIAL AND ITS CHANGES OCCURRING IN OPERATIONAL PHASE

In the considered space the system's real state  $s_R$  is represented in the form of a point of coordinates equal to instantaneous values of its cardinal features. Quantity of usability potential contained in the system is function of its technical state. Therefore it was assumed that the usability potential contained in the system is a vector with its origin placed in the origin of the coordinate frame and the end in the point which represents the system's real state  $s_R$ . Quantity of the usability potential contained in the system is equivalent to length of the vector (3) [4]:

$$Pu(s_R) = \sqrt{\sum_{i=1}^n (x_{Ri})^2} \quad (3)$$

where:

$Pu(s_R)$  – quantity of the usability potential contained in the system in the state  $s_R$ .

The vector whose origin is placed in the point belonging to the boundary of the hyper-field of serviceability states and the end in the point representing system's real state, is interpreted to be the usability potential of quantity possible to be transformed as a result of operation of the system, contained in the system in a given instant  $t$ . The quantity was calculated as the vector length (4) [18]:

$$\delta Pu = \begin{cases} 0 \wedge s_R \in S_{NZ} \\ \sqrt{\sum_{i=1}^n (x_{Ri} - x_{BNZDi})^2} \wedge s_R \in S_Z \end{cases} \quad (4)$$

where:

$\delta Pu$  – available quantity of usability potential,

$x_{Ri}$  – value of  $i$ -th feature of real state of the system,

$x_{BNZDi}$  – value of  $i$ -th feature of system's state represented by a point which belongs to the boundary of the hyper-field of serviceability states,

$S_{NZ}$  – hyper-field of non-serviceability states,

$S_Z$  – hyper-field of serviceability states.

During conducting operational processes technical object is subjected to action of forcing factors both dependent upon and independent of functioning the object. The action of forcing factors onto technical object introduces changes in values of its cardinal features [15]. As technical state of the system is represented in the form of a point of coordinates equal to instantaneous values of cardinal features then the process of changes in system's states may be presented in the form of a trajectory whose every point represents system's state in the instant  $t$ ,  $t \in [t_1, t_2]$  [20]. By determining the quantity of usability potential contained in the system (3), for the beginning point of the trajectory,  $s_1 = s(t_1)$ , and the end point of the trajectory,  $s_2 = s(t_2)$ , one can calculate the change in quantity of usability potential, which occurs during realization of the considered operational process, as the length of the vector of change in usability potential (5)

$$\Delta Pu = |\overrightarrow{\Delta Pu}| : \overrightarrow{\Delta Pu} = \overrightarrow{\Delta Pu}(s_1) - \overrightarrow{\Delta Pu}(s_2) \quad (5)$$

By assuming the selected limit state  $s_{gr}$  as a point with respect to whom quantity of available usability potential is determined, one is able to determine the quantity for the beginning point and end point of the analyzed trajectory. Difference of the determined vectors for the beginning point and end point is the vector of change in quantity of available usability potential of the system, and its length is the change in the quantity,  $\Delta \delta Pu$  (6):

$$\Delta \delta Pu = |\overrightarrow{\Delta \delta Pu}| : \overrightarrow{\Delta \delta Pu} = \overrightarrow{\delta Pu}(s_1) - \overrightarrow{\delta Pu}(s_2) \quad (6)$$

where:

$\Delta \delta Pu$  – change in quantity of available usability potential.

It should be noticed that for the points not belonging to the hyper-field of non-serviceability states the usability potential vector is a sum of usability potential vector of the selected limit state  $s_{gr}$  and the available quantity of usability potential determined with respect to the selected limit state described by the relation (7) and illustrated in Fig. 2.

$$\forall s_R \notin S_{NZ} : \overrightarrow{Pu}(s_R) = \overrightarrow{Pu}(s_{gr}) + \overrightarrow{\delta Pu}(s_R) \quad (7)$$

As the sum is constant for a determined real state, hence by selecting (for the calculations) such limit state for which quantity of usability potential is the least, the largest quantity of available usability potential is obtained. Such state is determined to be the optimum limit state.

### ANALYSIS OF CHANGES IN USABILITY POTENTIAL OF A SELECTED SUBSYSTEM OF FLOATING UNIT

During conducting the investigations, a large-power steam boiler system fitted with interstage reheater, used on a selected floating unit, was analyzed. Such object is a critical technical object hence one of the most important aims of its service is not to permit a non-serviceability state to occur, that is in line with the main aim of ship service [9]. However, because of complex structure and multi-dimensional relations between elements of the system in question, to describe numerically the discussed service aim is really very difficult.

Prevention against occurrence of a non-serviceability state requires to determine an available quantity of usability potential contained in a crucial (from the point of view of operation) element, subsystem or complex system, in a given instant  $t$ . Hence, to make the investigations complete it is necessary to determine technical state of the boiler. The technical state results from technical state of particular boiler subsystems, including boilers, shafts and steam turbines themselves, but taken as a state of multi-dimensional complex technical system, it does not result directly from them. Simultaneously, state of particular elements is not monitored in a continuous way.

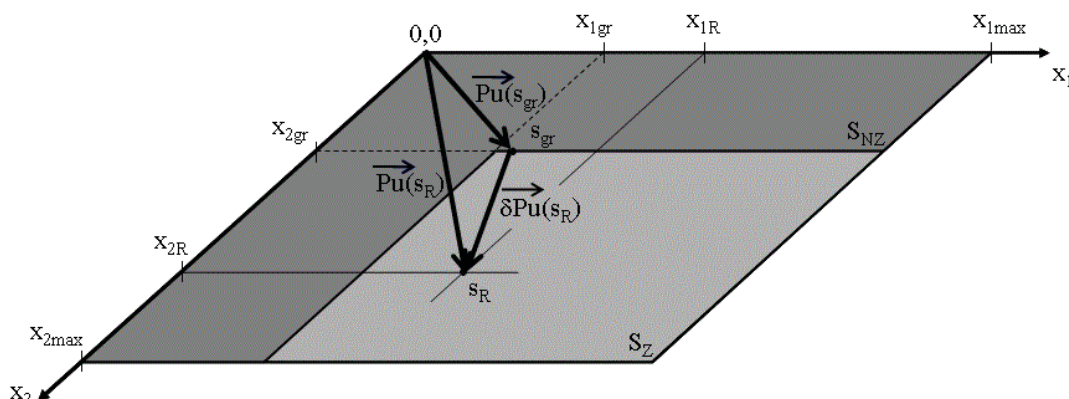


Fig.2 – The usability potential  $\overrightarrow{Pu}(s_R)$  expressed as a sum of the usability potential of limit state  $\overrightarrow{Pu}(s_{gr})$  and the vector of available quantity of usability potential  $\overrightarrow{\delta Pu}(s_R)$  in the space of technical states of an arbitrary system,  $R^2$ .

State of boiler proper piping or reheaters and heaters as well as a degree of their scaling is not directly monitored but it can be only determined by measuring values of outlet steam parameters. Simultaneously, any measurement of the kind, e.g. steam pressure at outlet from the boiler, is influenced by many elements of steam-water circuit of the boiler, which, in conditions of varying steam load, is very important but particularly difficult to be verified. Thus, the first issue is to numerically determine technical state of particular elements of the boiler. In addition, interrelations between boiler elements make accurate determining the whole system not possible even if state of its particular elements is known. Since it is hard to find cause of a drop in temperature of superheated steam despite the same amount of combusted fuel. Because it may be a problem connected with fuel quality, technical state of burners, state of boiler proper piping, reheater or quality of combustion process. It seems therefore that the most rational approach is to consider the boiler to be a power machine and relate its technical state expressed indirectly by efficiency of transformation of fuel chemical energy into thermal energy of outlet steam, to amount of energy consumed in operational process [1,3,6,7,11,23,25].

Taking the above given conclusion into account, the way of description of system's technical state presented in this work, was applied to solving the problem. The features simultaneously describe quality of system's operation [13]. For this reason was performed identification of cardinal features which form dimensions of the space of technical states, within the set of deviations enumerated in TKE ? method of operational quality control of steam boiler system. The method is commonly used for assessment of operational quality of devices of power units [15]. In these considerations the method was applied to analyzing quality of steam boiler operation.

As a result of the performed analyses were selected the deviations directly associated with boiler operation quality, namely:

- $q3$  – deviation ( dealing with heat consumption per 1 kWh, determined on the basis of temperature of interstage superheated steam [kJ/kWh]),
- $q4$  – deviation ( dealing with heat consumption per 1 kWh, determined on the basis of steam throttling in the interstage reheater [kJ/kWh]),
- $q5$  – deviation (dealing with heat consumption per 1 kWh, determined on the basis of injection of water into interstage superheated steam [kJ/kWh]) and
- $q8$  – deviation ( dealing with heat consumption per 1 kWh, determined on the basis of decreased efficiency of the boiler [kJ/kWh])

– all are considered to be cardinal features which determine the space of technical states of the boiler in question. Moreover, it was assumed that – from the point of view of technical state of the system – the interval of permissible values for the distinguished features coincides with that for suboptimum values, which means that the features are strictly determined.

On the basis of measurement results obtained from tests of a steam boiler installed on an existing ship, instantaneous values of particular selected deviations were calculated and functional relationships of the particular deviation values in function of time were next obtained by using multinomial approximation. For each of the achieved approximation multinomial value of derivative was calculated within its determination interval. On this basis it was stated that each of the multinomials is a constantly increasing function. This proves the assumption that values of cardinal features of the investigated operational system, which determine the space of its technical states in operational process, should vary in a strictly monotonous way. For each of the multinomials, minimum and maximum value was also calculated, which, together with the strictly increasing character of the runs, defines their values at the beginning and end of the determination interval. On this basis was proved the assumption that values of the analyzed deviations decrease in steps as a result of performed serviceability assurance processes. In means that all the assumed cardinal features of ship boiler operational system are renewal-dependent in the serviceability assurance process.

Next, fields of serviceability and non-serviceability states of boiler system were defined in the space of its features, which are described by limit values of the system's features. In the case of the considered system the space of features is described by the deviations :  $q3, q4, q5, q8$ . For the analysis are appropriate the values of the deviations corresponding to boiler operation at a given speed of the ship, as only then the interstage reheater is under operation. Therefore periods of boiler operation during port manoeuvres or ship going under reduced speed should be excluded from the analysis.

During the tests in service, limit values of the deviations were determined to be maximum ones which occur in the end of boiler operation periods just before passing it to renewal. The values are interpreted to be the biggest at which there is no hazard of occurrence of a non-serviceability state ( 0%). Simultaneously, minimum values of the deviations recorded in the beginning of before-repair periods, were taken the smallest.

Tab. 1 – Characteristic values of the deviations

Deviation	Smallest value before repair [kJ/kWh]	Biggest value before repair [kJ/kWh]	Smallest value after transposition [kJ/kWh] – minimum limit value of non-permissible value interval	Biggest value after transposition [kJ/kWh] – maximum limit value of non-permissible value interval
A	B	C	D	E
$q3$	-43.78	16.88	0	60.66
$q4$	-27.95	41.13	0	69.08
$q5$	-22.63	31.94	0	54.57
$q8$	-45.76	98.92	0	144.68

In order to obtain split of the variability range of features of the boiler considered to be a system, appropriate for strictly

determined space of technical states, transposition of the coordinate frame was performed. This way the hyper-field of non-serviceability states (Col. D and E, Tab.1) as well as the coordinates of optimum limit point (Col. E, Tab. 1), were determined.

On the basis of the determined coordinates of the hyper-fields of serviceability and non-serviceability states it is possible to analyze degree of use of available usability potential of ship boiler after every completed transport task. In Tab. 2, values of usability potential quantity in the beginning of transport task and the end of it, as well as values of changes in the available quantity, are presented for exemplary transport tasks.

Tab. 2 – Changes in available usability potential – operational processes

No.	Available quantity of usability potential in the beginning of operational period	Available quantity of usability potential in the end of operational period	Change in available usability potential
-	[kJ/kWh]	[kJ/kWh]	[kJ/kWh]
1.	767.25	391.71	375.54
2.	525.46	54.29	471.17
3.	820.28	468.75	351.53
4.	467.81	70.89	396.92
5.	326.16	13.96	312.20
6.	736.89	325.21	411.68
Mean value			386.51

Comparing available quantities of usability potential of the boiler, which remain after completion of every transport task, and mean value of change in available usability potential, which results from fulfilment of the tasks by the ship, one is able to determine whether the remaining quantity of usability potential is sufficient for undertaking a subsequent transport task. Basing on the data presented in Tab. 2, one can plan further carrying out transport tasks in the cases represented by the data given in Row 1 and 3 of the table.

## SUMMARY

Operational management of ship steam boilers representing complex technical objects, requires, because of degree of their complicity and multi-dimensional relationships between their components, to implement an approach based on general theory of systems. Such approach is especially favourable in the case of the so critical objects operating in sea conditions as ship steam boilers which are subjected to special limitations as to the carrying out of operational processes and ensuring of their serviceability. In this work is presented a system method of description of usability potential and its changes in the space of technical states of an arbitrary system. The method was applied to analyzing usability potential of a steam boiler operating on an existing ship and its changes occurring in operational processes of the considered object of investigations. Consequently, the space of technical states of an arbitrary boiler was formulated together with

its hyper-fields of serviceability and non-serviceability states, as well as the optimum limit point, quantities of available usability potential and its changes which occurs during execution of transport tasks, were also determined. On this basis, premises were reached for deciding on whether to pass the object to maintenance operations or to conduct its use further. The proposed method is a unique approach to the issue of determination of usability potential of complex technical objects, which makes it possible to take into account system relationships in modelling operational processes. Application of the method to determination of usability potential of ship large-power steam boilers makes it possible to perform analysis of operational state of the boiler analytically, owing to this one can strictly calculate whether a given propulsion unit will be able to reliably carry out a subsequent operational task or it should be subjected to maintenance operations. Such decision-making is an important issue in the case of sea-going ships where any failures and necessary repairs during voyage seriously endanger their safety and serviceability as well as constitute source of possible financial losses.

Further planned research will be aimed at the representing of relationships of change in available usability potential of the boiler in function of the conditions in which shipping tasks are conducted, i.e. sea conditions, ship service speed and quantity and rate of changes in boiler load.

## BIBLIOGRAPHY

1. Balcerski A.: Ship power plants. Fundamentals of thermodynamics, engines and main propulsions, auxiliary devices, installations ( in Polish). Gdansk University of Technology, Gdańsk 1990
2. Bucknall R.W.G., Attah E. E.: Energy use onboard LNG steam ships. Proceedings of the Low Carbon Shipping Conference, London 2013
3. Charchalis A., Krefft J.: Main dimensions selection methodology of the container vessels in a preliminary stage, KONES, Journal of Power train and Transport, 2009, Vol. 16, No. 2
4. Dorst L., Fontijne D., Mann S.: Geometric algebra for computer science. Elsevier 2007
5. Downarowicz O.: Operation systems. Management of engineering resources. in Polish) . Instytut Technologii Eksploatacji ( Institute of Operation Technology), Radom 2005
6. Gardzilewicz A., Obrzut D., Szymaniak M.: Polish aspects in the modern design solutions of steam turbine flow systems. Polish Maritime Research, Special issue 2009/S1
7. Grzędziela A., Musiał J., Muślewski Ł., Pająk M.: A method for identification of non-coaxiality in engine shaft lines of a selected type of naval ships. Polish Maritime Research.

Vol. 22 No. 1(85), 2015

8. Górski Z., Perepeczko A.: Ship steam boilers ( in Polish). Gdynia Maritime University, Gdynia 2013
9. Górski W., Burciu Z.: Identification of main parameters which impact fuel consumption on ships in real operational conditions ( in Polish). *Logistyka* 4/2011, Poznań 2011
10. Harrington R.L.: *Marine Engineering : ...? The Society of Naval Architects and Marine Engineers*, New York 1971
11. Samsung Heavy Industry : Machinery operating manual, 300 000 DWT Crude Oil Tanker. Publ. Samsung HI Co., South Korea, October 2000.
12. Molland A.F.: *The Maritime Engineering Reference Book, A Guide to Ship Design, Construction and Operation*. Butterworth 2013
13. Muślewski Ł.: Evaluation Method of Transport Systems Operation Quality. *Polish Journal of Environmental Studies*. Vol. 18, No. 2A, Hard ? Olsztyn 2009
14. Oziemski S.: *Man in machine* (in Polish). Instytut Technologii Eksploatacji (Institute of Operation Technology), Radom 2004
15. Pająk M.: Fuzzy extension of TKE method for determining operation process quality of power units ( in Polish). *Zagadnienia Eksploatacji Maszyn* 4/2007, Instytut Technologii Eksploatacji ( Institute of Operation Technology), Radom 2007
16. Pająk M.: The Analysis of Usefulness of Operational Potential Consumption Models to Control Complex Technical Systems Maintenance. *Journal of KONES Power train and Transport* vol. 17 No. 2, Warsaw 2010
17. Pająk M.: The technical states' space in the modelling process of operation tasks of a complex technical system. *Maintenance Problems* 1/2014, Instytut Technologii Eksploatacji ( Institute of Operation Technology), Radom 2014
18. Pająk M.: Operational potential of a complex technical system. *Maintenance Problems* 4/2015, Instytut Technologii Eksploatacji ( Institute of Operation Technology), Radom 2015
19. Pająk M., Muślewski Ł.: Fuzzy model for assessment of operation quality control of complex operational system ( in Polish). *Problemy Eksploatacji* 3/2005, Instytut Technologii Eksploatacji ( Institute of Operation Technology), Radom 2005
20. Pająk M., Muślewski Ł.: Computerisation of systems operation quality assessment. 10th International Conference on Computer Systems' Aided Science, Industry and Transport – Transcomp, Zakopane 2006
21. Pająk M., Woropay M.: Maintenance strategy by controlled consumption of operational potential. *Journal of KONES Power train and Transport* vol. 16 No. 4, Warsaw 2009
22. Pihowicz W.: *Technical safety engineering. Fundamental problems* ( in Polish), WNT ( Technical Scientific Publishers) Warsaw 2008
23. Rodríguez C., Antelo F., De Miguel A., Carbia J.: Study of possibilities of using a steam plant type “reheat” and mixed boilers of coal and fuel-oil for the propulsion of bulk carriers. *Journal of Maritime Research*, Vol. VIII. No. 2, Santander 2011
24. Woropay M., Muślewski Ł.: Quality in system formulation ( in Polish). Instytut Technologii Eksploatacji ( Institute of Operation Technology), Radom 2005
25. Yi Y-S., Watanabe Y., Kondo T., Kimura H., Sato M.: Oxidation Rate of Advanced Heat-Resistant Steels for Ultra-Supercritical Boilers in Pressurized Superheated Steam. *Journal of Pressure Vessel Technology*, Vol. 123, 2001
26. Zdoński M., McGeough J.A., Szpytko J.: On the use of maintenance developments to improve inherent reliability. *Engineering achievements across the global village. International Journal of INGENIUM*, Cracow – Glasgow 2005

#### CONTACT WITH THE AUTHOR

Łukasz Muślewski

*e-mail: l.muslewski@wp.pl*

University of Science and Technology in Bydgoszcz  
Al. Prof. S. Kaliskiego 7  
85-796 Bydgoszcz

**POLAND**

# EXPERIMENTAL AND MATHEMATICAL INVESTIGATIONS ON UNCONFINED COMPRESSIVE BEHAVIOUR OF COSTAL SOFT SOIL UNDER COMPLICATED FREEZING PROCESSES

Wei Wang<sup>1</sup>

Na Li<sup>1</sup>

Fang Zhang<sup>1</sup>

Aizhao Zhou<sup>2</sup>

Snow Chi<sup>3</sup>

<sup>1</sup> School of Civil Engineering, Shaoxing University, Shaoxing, China

<sup>2</sup> School of architectural and Civil Engineering, Jiangsu University of Science and Technology, Zhenjiang, China

<sup>3</sup> Melbourne School of Design, Melbourne University, Victoria, Australia

## ABSTRACT

*In order to properly understand the effect of freezing-thawing circle (FTC) to mechanical behavior of costal soft soil (CSS), unconfined compressive test is conducted. Six kind FTC times are designed from zero to five. The tested data show that: (1) unconfined compressive strength of CCS decreases nonlinearly with more FTC, and the strength after five FTC times becomes about 22% of its original strength without any freezing-thawing experience; (2) stress-strain curves of all unconfined compressive samples can be well fitted by three-parameter hyperbolic model; (3) and relationship between two parameters and FTC times can be fitted by exponent function, while another parameter can be considered as 0.95. Consequently, one composite hyperbolic- exponent empirical formula is established in order to describe freezing-thawing-dependent stress-strain behavior of CSS. Finally, good agreements have been found between tested data and simulated results.*

**Keywords:** costal soft soil, stress-strain curve model, unconfined compressive behavior, freezing-thawing circle

## INTRODUCTION

This paper is aimed at well understanding the freezing-thawing-dependent unconfined compressive behavior by laboratory test and establishing an empirical formula to simulate unconfined compressive stress-strain curves of CSS.

Unconfined compressive behavior of soil is one basic subject to geotechnical engineering. Lots of effort has been devoted to it considering different kind soil. The work team of Liu<sup>1</sup> conducted the assessment of unconfined compressive strength of cement stabilized marine clay. Effect of suction on unconfined compressive strength in partly saturated soils was discussed<sup>2</sup> and the unconfined compressive strength of compacted granular soils by using inference systems was discussed<sup>3,4</sup>. In some case, soil foundation or slope may experience freezing-thawing circle (FTC) process due to nature season change, day and night temperature difference, or artificial freezing engineering, which would make big difference to unconfined compressive strength of soil<sup>5,6</sup>.

People should properly understand this difference before corresponding engineering construction in order to assure its work function and engineering safety. Research work on the soil slope stability based on soil strength deterioration in seasonal frozen areas was made by Ge<sup>7</sup>. Experiment study on unconfined compressive strength before and after thaw of the forth layer silt clay in shanghai was presented by the work team of Song<sup>8</sup>. As to saturated silty clay, its shear strength properties influenced by freeze-thaw was put forward<sup>9</sup>. Wang<sup>10</sup> conducted the testing study of freezing-thawing strength of unsaturated undisturbed loess considering influence of moisture content. Freezing-thawing behavior of fine-grained soils reinforced with polypropylene fibers was presented by Zaimoglu<sup>11</sup>. Now, some attention had been paid to the effect of freezing-thawing cycles on performance of fly ash stabilized expansive soil<sup>12</sup>. Although lots of work had been done and many study paper had been presented, study work on coastal soft soil (CSS) is not too much.

## EXPERIMENTAL PART AND METHODOLOGY

Laboratory test soil is CSS from Shaoxing Ctiy, China. It is grey color and with 30% moisture content. In order to study freezing-thawing-dependent unconfined compressive behavior, this test consist three main steps.

First step is to prepare initial soil samples. According to Chinese laboratory test code, twelve column shape soil samples are made with 81.0 mm height and 39.1 mm diameter, where six is for designed unconfined compressive test and other six is for additional remedy and repeated test.

Second step is to carry out different freezing-thawing circles test. Freezing-thawing box in Shaoxing University is used to complete this work. For one FTC, its freezing temperature is designed as -12°C and its thawing temperature is designed as 15°C; both freezing time and thawing time are all 24 hours. As to above ten column shape samples, this step is conducted as following:

(1) Two samples should be taken out previously for unconfined compressive test without any FTC, and these samples are denoted as s0.

(2) The rest ten samples are put into the freezing-thawing box to experience first one 48 hours FTC, then another two samples should be taken out for designed unconfined compressive test, and these two samples are denoted as s1.

(3) As this way, samples with FTC from 2 to 5 can be archived denoted by s2, s3, s4 and s5 until all twelve samples are all used.

Third step is to choose the laboratory apparatus and determine its loading procedure. In this test, one unconfined compressive apparatus with no. DW-1 is used made by Shangyu Survey and Geotechnical Instrumentation Company. Axial loading of it is automatically conducted by axial displacement with 0.1 mm/s. Test of all samples is finished and ended with the same axial strain reaching 8%.

According to loading procedure designed in above section, six series stress-strain data for different samples from s0 to s5 are obtained, shown as in Fig. 1, where q and ε denote axial stress and axial strain, respectively.

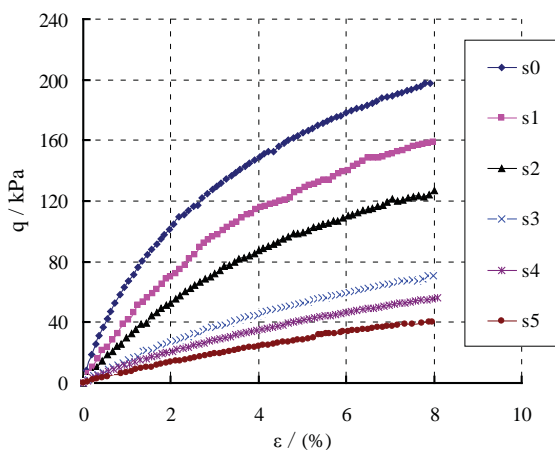


Fig. 1. Tested stress-strain data of different samples

From Fig. 1, unconfined compressive stress of all soil samples with various FTC and axial strain can be obtained, shown as in Table 1. It is evident that:

Tab. 1: Unconfined compressive stress with different FTC /kPa

FTC	ε=1%	ε=2%	ε=3%	ε=5%	ε=7%
0	67.5	101.2	129.8	164.5	189.7
1	41.0	70.1	96.2	129.3	150.3
2	30.0	52.7	72.1	99.5	121.2
3	15.2	26.9	36.8	53.0	65.0
4	10.2	21.1	28.3	41.4	51.2
5	7.1	13.6	19.2	28.7	37.3

(1) Whatever the FTC might be, the unconfined compressive stress increase nonlinearly with its increasing axial strain. For example, it increases from 67.5 kPa when ε=1% to 189.7 kPa when ε=7% with FTC=0.

(2) If axial strain is fixed, unconfined compressive stress decreases drastically with increasing FTC. For example, it changes from 164.5 kPa to 28.7 kPa with ε=5%.

In order to describe the FTC effect on unconfined compressive stress, normalized stress factor K is employed to express it:

$$K = \frac{q_i}{q_0} \times 100\% \quad (1)$$

Wherein,  $q_i$  denotes the compressive stress with FTC=i and  $i=0, 1, \dots, 5$ ;  $q_0$  denotes the compressive stress with FTC=0, namely it denotes the compressive stress of sample without any FTC process.

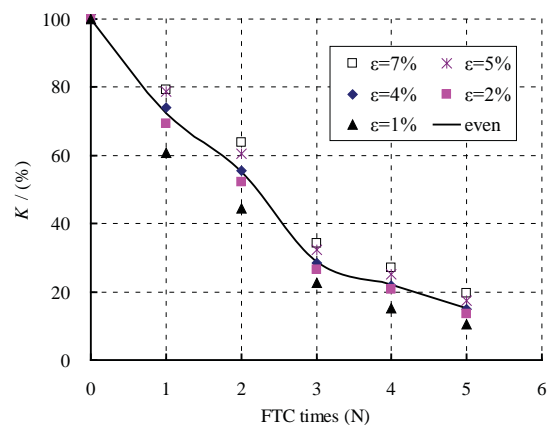


Fig. 2. Normalized stress factor K of different samples

Normalized stress factors of all samples and their even values are list in Fig. 2. From this figure, following conclusions can be drawn:

(1) If FTC is fixed, normalized stress factor K is not sensitive to axial strain ε. So, K can denote basic change law of the unconfined compressive strength of CSS, because it has nothing to do with axial strain which is selected to decide unconfined compressive strength.

(2) Normalized stress factor K becomes smaller and smaller

with increasing FTC. Even values of K with FTC from 0 to 5 are 100%, 72%, 55%, 29%, 22%, 15%, respectively.

(3) Differences between two close even values of K are 28%, 17%, 23%, 7%, 7%. It is to say, the sensitive area of FTC for unconfined compressive strength is from 0 to 3; after four FTC times, the change of unconfined compressive strength of CSS can be neglected to some degree.

## RESULTS AND DISCUSSION

It is shown from Fig.1 that, no matter what FTC is, the stress-strain curve of CSS consistently appear same shape to two-parameter hyperbolic model<sup>13</sup>, so it can be empirically written as:

$$q = \frac{A\varepsilon}{B + \varepsilon} \quad (2)$$

After using Eq. 2 to fit or describe investigated stress-strain data, many researchers have found the inferior of two-parameter hyperbolic model<sup>14</sup>. In order to improve the two-parameter hyperbolic model, we propose following formula to describe the stress-strain curve:

$$q = \frac{A\varepsilon^k}{B + \varepsilon^k} \quad (3)$$

In Eq. 2 and Eq. 3, A, B and k are three undetermined soil parameters. Because of having three parameters, Eq. 3 is called as three-parameter hyperbolic model in following discussion. There is no denying the fact that three-parameter hyperbolic model is superior to two-parameter hyperbolic model.

After fitting the six stress-strain curves in the Fig.1 using Eq. 3, corresponding values of A, B and k with various FTC can be archived and list as in Table 2.

Tab. 2: Fitted values of the model parameters with various FTC

FTC	0	1	2	3	4	5
A/kPa	340.20	262.02	223.58	169.38	206.35	135.77
B	4.18	5.37	6.41	10.34	15.21	17.70
k	0.85	1.02	1.01	0.96	0.86	0.98

Table 2 demonstrates that, with higher FTC times, values of parameter A decrease monotonically but that of parameter B exhibits a process of strict increasing. At the same time, FTC almost makes no difference to the value of parameter k, shown as in Fig. 3, so we can simply use average value 0.95 as the model parameter:

$$k = g_1(N) = 0.95 \quad (4)$$

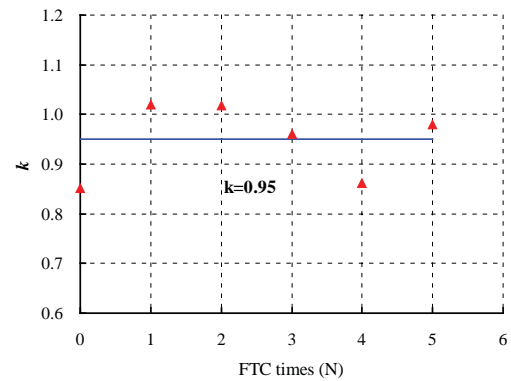


Fig. 3. Relationship between parameter k and FTC

Two exponent functions are used to fit and build empirical expression for A and B, and the best fitted empirical functions for them are negative and positive exponent functions, respectively. The fitted diagram are shown as Fig. 4 and Fig. 5, and the empirical functions can be expressed as:

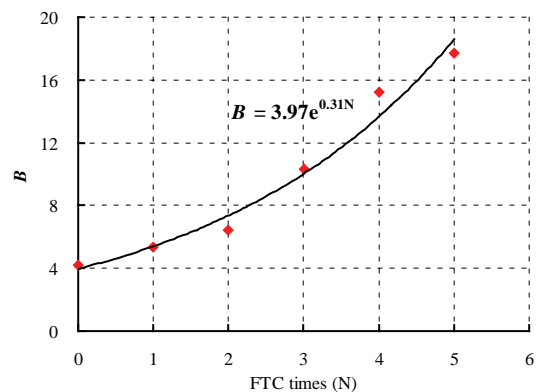


Fig. 4. Relationship between parameter A and FTC

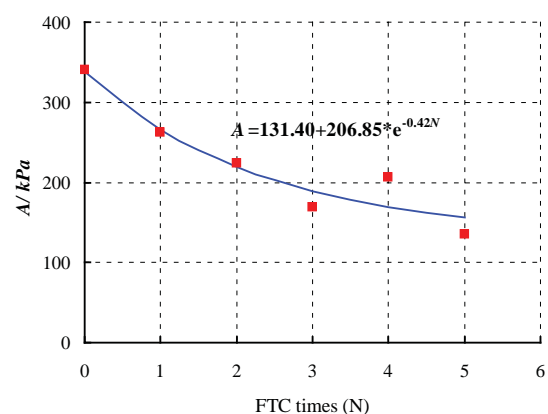


Fig. 5. Relationship between parameter B and FTC

$$A = g_2(N) = 131.40 + 206.85e^{-0.42N} \quad (5)$$

$$B = g_3(N) = 3.97e^{0.31N} \quad (6)$$

Based on Eq. 3, Eq.4, Eq.5 and Eq. 6, empirical formula for CCS stress-strain curve considering different FTC times can be deduced as:

$$q = \frac{A\varepsilon^k}{B + \varepsilon^k} = \frac{g_2(N)\varepsilon^{g_1(N)}}{g_3(N) + \varepsilon^{g_1(N)}} = \frac{(131.40 + 206.85e^{-0.42N})\varepsilon^{0.95}}{3.97e^{0.31N} + \varepsilon^{0.95}} \quad (7)$$

Eq. 7 can well describe the relationship among the axial stress, axial strain and FTC of CSS, and it is a three-parameter hyperbolic function with axial strain and a power function with FTC. So Eq. 7 can be considered as an empirical composite hyperbolic-exponent function formula (CHE formula).

Put  $N=0, 1, 2, 3, 4$  and  $5$  into Eq. 7, simulated stress-strain curve of CCS can be obtained and shown as in Fig. 6.

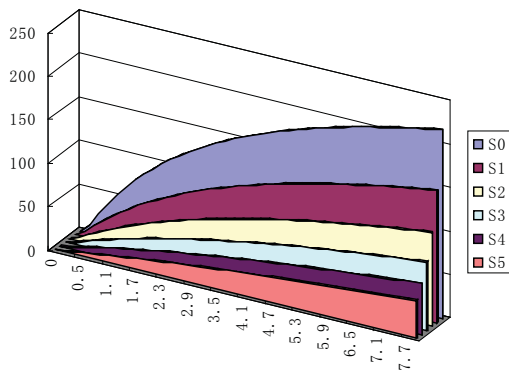


Fig. 6. Simulated stress-strain curve of CCS

In order to verify applicable ability of the presented CHP formula, comparisons between laboratory test and CHE formula simulating are conducted by taking s1 and s4 as example, and results are shown as Fig. 7.

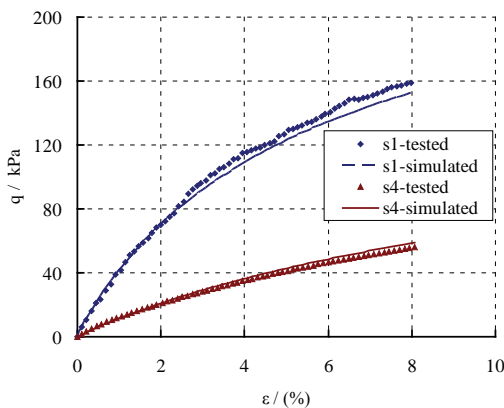


Fig. 7: Tested and simulated  $q$ - $\varepsilon$  curves

To further analyze the accuracy of CHE formula, the definition of the relative simulating error RD is presented:

$$RD = \frac{q_{\text{test}} - q_{\text{simu.}}}{q_{\text{test}}} \times 100\% \quad (8)$$

Wherein:  $q_{\text{test}}$  represents the tested data and  $q_{\text{simu.}}$  represents the simulated data. The relative simulating errors of the CHE

formula were calculated by equation (8), shown as in Fig. 8.

Fig. 7 indicates that CHE formula can well simulate the tested stress-strain curves of s1 and s4 samples. Fig. 8 indicates that relative simulating error of CHE formula is very small, especially, this error is just about 5% when  $\varepsilon > 1\%$ . According to Fig. 7 and Fig. 8, we can make conclusion that CHE formula can offer good agreements with the unconfined compressive stress-strain curves of CSS experienced various FTC times.

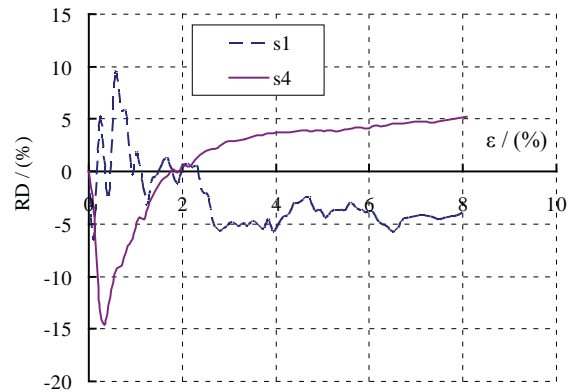


Fig. 8: Relative simulating error of CHE formula

Although above, following problems should be noted:

- (1) Tested samples of this work are relatively small and not enough to express the general law of soil. In order to archive it, laboratory test on different kind soils should be conducted.
- (2) Conclusions of this work are limited to present tested data and its mathematical analysis, micro-mechanical study considering FTC-dependent soil structural behavior should be further conducted by using scanning electron microscope.
- (3) Although the empirical CHE formula can well simulate the tested stress-strain curves, its simulating error is bigger to some degree when  $\varepsilon < 1\%$ . It would be better for us to establish more precise formula based on more samples tests.

## CONCLUSIONS

FTC effect on unconfined compressive behavior of CSS is studied in details, and basic work and conclusions are as follows.

- (1) Unconfined compressive stress decreases drastically with increasing FTC.
- (2) Whatever the FTC might be, the unconfined compressive stress increase nonlinearly with its increasing axial strain. If FTC is fixed, normalized stress factor  $K$  is not sensitive to axial strain.
- (3) Based on hyperbolic model, one three-parameter hyperbolic model and one empirical CHE formula are presented and proposed to describe the unconfined compressive  $q$ - $\varepsilon$  curves with various FTC times. Good agreements have been found between CHP formula simulating and tested data.

## ACKNOWLEDGMENTS

The authors thank the reviewers who gave a thorough and careful reading to the original manuscript. Their comments are greatly appreciated and have help to improve the quality of this paper. This work is supported in part by the National Natural Science Foundation of China (NO. 41202222), and by the Ministry of Housing and Urban-Rural Development of China (NO. 2012-k3-4, NO. 2015-k3-020, NO. 2015-k4-003). Some Laboratory tests were carried out by Li-sha Ma, Qiao-yuan Chi, Miao Li, Peng Jin and Yi-qi Tu.

## REFERENCES

1. S. Y. LIU, D. W. ZHANG, Z. B. LIU: Assessment of unconfined compressive strength of cement stabilized marine clay. *Marine Georesources and Geotechnology*, 26, 19(2008).
2. J. CHAE, B. KIM, S. PARK, S. KATO: Effect of suction on unconfined compressive strength in partly saturated soils. *KSCE Journal of Civil Engineering*, 14(3), 281(2010).
3. E. KALKAN, S. AKBULUT, A. TORTUM, A. CELIK: Prediction of the unconfined compressive strength of compacted granular soils by using inference systems. *Environ. Geol.*, 8, 1429(2009).
4. X. Q. CHEN, C. H. LI, W. WANG, X. ZHANG: Active geotechnical treatment technology for permafrost embankment of Qinghai-Tibet railway. *The Electronic Journal of Geotechnical Engineering*, 17(Y), 3635(2012).
5. Y. FENG, J. L. HE, L. LIANG: Experimental study of the shear strength characteristics of fine-grained soil under freezing and thawing cycles. *Journal of Glaciology and Geocryology*, 30(6): 1013(2008).
6. Z. Q. ZHANG, Z. P. HU, J. ZHAO: Strength properties of lime-fly ash loess under freezing-thawing cycles. *Journal of Traffic and Transportation Engineering*, 11(6): 24(2011).
7. Q. Ge, H. Wu, Y. F. Gong: Research on the soil slope stability based on soil strength deterioration in seasonal frozen areas. *Advanced Materials Research*, 243: 4270(2011).
8. Z. G. SONG, Y. Q. TANG, J. HONG: Experiment study on unconfined compressive strength before and after thaw of the forth layer silt clay in shanghai. *Low Temperature Architecture Technology*, 31(12): 85(2009).
9. L. L. YU, X. Y. XU, M. Q. LI, P. F. LI, Z. L. YAN: Influence of freeze-thaw on shear strength properties of saturated silty clay. *Rock and Soil Mechanics*, 31(8): 2448(2010).
10. T. H. WANG, S. F. LUO, X. J. LIU. Testing study of freezing-thawing strength of unsaturated undisturbed

loess considering influence of moisture content. *Rock and Soil Mechanics*, 31(8): 2378(2010).

11. ZAIMOGLU A. SAHINL. Freezing-thawing behavior of fine-grained soils reinforced with polypropylene fibers. *Cold Regions Science and Technology*, 60(1): 63(2010).
12. BIN-SHAFIQUE SAZZAD, RAHMAN, K., AZFAR IREEN: The effect of freezing-thawing cycles on performance of fly ash stabilized expansive soil subbases. *Geotechnical Special Publication*, 211: 697(2011).
13. J. J. GUO, W. WANG, X. N. WANG: Improved hyperbolic model for harden/soften stress-strain curve of Yangtze River soil. *The Electronic Journal of Geotechnical Engineering*, 17(L): 1675(2012).
14. W. WANG, X. J. SONG, H. LING, T. H. LU, G. W. ZHOU: Composite exponential-hyperbolic model for stress-strain curve of seashore soft soil. *Chinese Journal of Geotechnical Engineering*, 32(9): 1455(2010).

## CONTACT WITH THE AUTHOR

Wei Wang

*e-mail: wangwells@qq.com*

School of Civil Engineering  
Shaoxing University  
Shaoxing

**CHINA**

# DESIGN METHODOLOGY OF STRENGTH VERIFICATION OF PLATFORM DURING LOAD OUT OF THE ARKUTUN DAGI SE-TOPSIDE 43.800 MT

Magdalena Kaup <sup>1</sup>

Wojciech Jurczak <sup>2</sup>

Janusz Kaup <sup>3</sup>

<sup>1</sup> The West Pomeranian University of Technology, Szczecin, Poland

<sup>2</sup> Polish Naval Academy, Poland

<sup>3</sup> Westcon Design Poland, Szczecin, Poland

## ABSTRACT

*This paper presents the methodology of strength verification during load out of the heavy cargo, in this case Arkutun Dagi SE-Topside platform. General methodology of making calculation models and load algorithms has been presented. Paper shows results of verification of global shear forces and bending moments using self-developed algorithms to modify centre of gravity, fill tanks and hydrostatically balance a 3D finite element model with commercial hydrostatic code. The NAPA and ANSYS codes were used to calculate hydrostatic pressures and to apply to 3D-FE models and to carry out strength calculation of barge construction.*

**Keywords:** Strength verification, transport of offshore structures, load out analysis, ANSYS automation

## NOMENCLATURE

LC	Load case
ANSYS	FE strength analysis software
NAPA	Stability calculation software
DSF	Deck support frame
GD	Genfer Design
WDP	Westcon Design Poland
SE	South east
NE	North east
Fr	Frame
LBHd	Longitudinal bulkhead
TBHd	Transverse bulkhead
FE	Finite element
CoG	Centre of gravity
AD Topside	Arkutun Dagi Topside 43800 mT
PS	Portside
SB	Starboard
SWSF	Still water shear force
SWBM	Still water bending moment
SWTORSION	Still water torsion moment

## INTRODUCTION

A large number of transport operations of offshore heavy structures and increased requirements for strength calculations during load out and transport, cause an increased demand for complex strength analyses [3, 12]. The barges used for those operations need strength analysis for each cargo separately [4, 7, 11]. Methodology for performing such analyses was successfully introduced by Genfer Design (currently Westcon Design Poland) for analysis of load out of heavy structures from quay to oceangoing barge. The same technique has also been applied in inland transport. This paper is based on one of the heaviest offshore cargo load out analysis which has been carried out by GD/WDP. Subject of this analysis was a strength verification of the barge under the AD Topside 43.800 mT during load out in the harbour and seagoing transport from the harbour to destination place. The paper focuses only on load out in the harbour.

Transport of AD Topside has been contracted by Heerema Marine Contractors on offshore barge H-851, one of the biggest offshore barges in the world [2, 9]. Main dimensions of the barge have been shown in table 1.1.

Tab. 1.1. Principal dimensions of H-851 barge

Length (moulded)	= 260.0 m
Breadth (moulded)	= 63.0 m (42.0 m narrow forward part)
Depth (moulded)	= 15.0 m
Maximum Summer Load Draft	= 10.674 m

The general view of 3D-FE model with cargo (DSF and Topside of offshore platform) has been shown on figure 1.1.

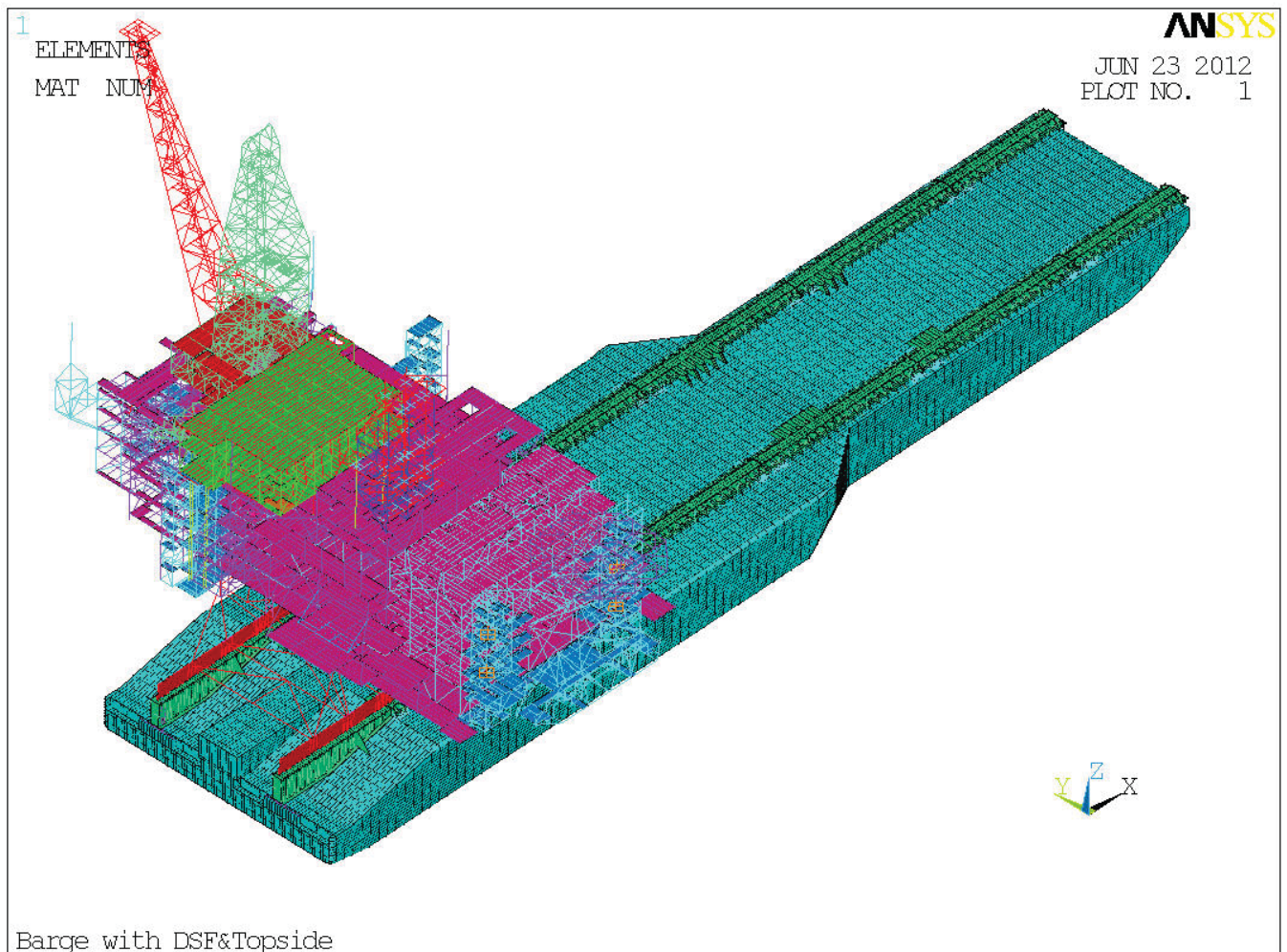


Fig. 1.1. 3D-FE model of H-851 barge, DSF with AD Topside, general view

Presented load out operation consisted of the transportation of the main cargo – AG Topside with deck supporting frame (DSF) on skid beam (steel part of the barge on deck used for cargo skidding) from quay onto barge. The load out operation has been shown on figure 1.2.

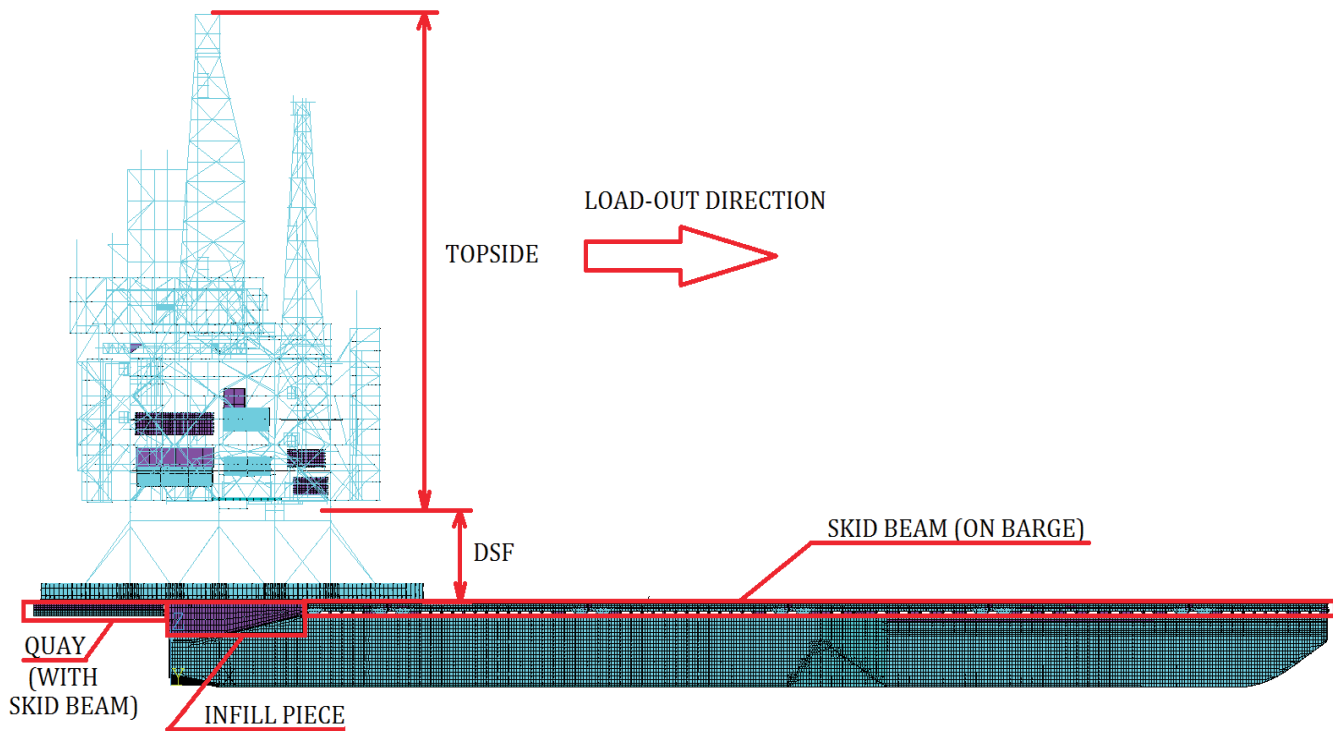
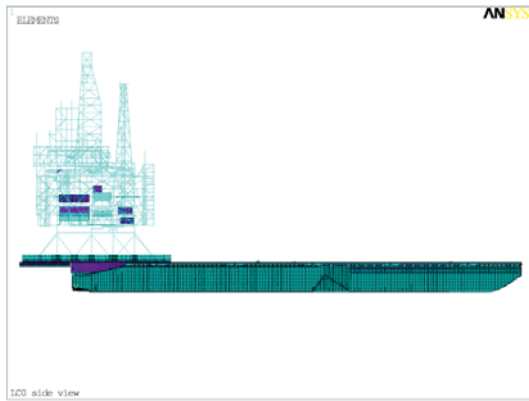


Fig. 1.2. Barge H-851 and DSF with AD Topside on skid beam during load-out operation

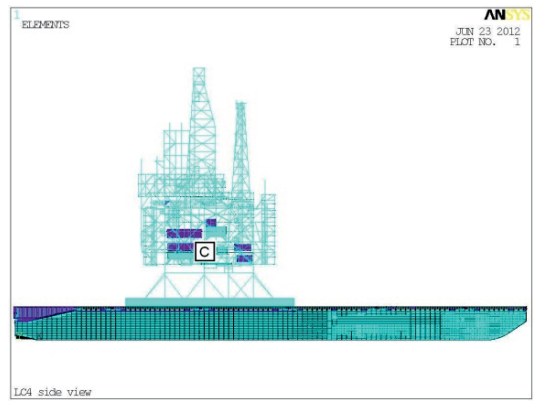
For the purpose of load out operation analysis, nine load cases were defined by position of Row C of DSF&AD Topside on barge (see table 1.2 and figure 1.3.):

Tab. 1.2. Load cases defined by the position of DSF Row C with respect to the barge

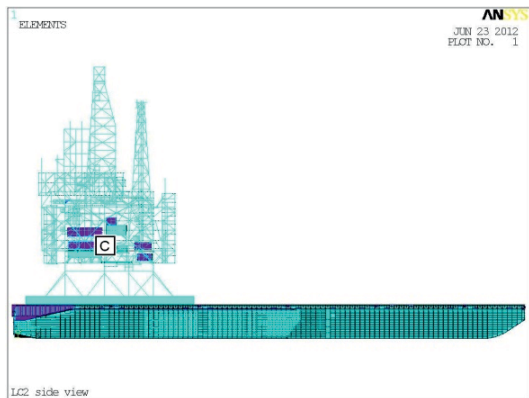
Load Case	Position Row C		Remarks
	Frame	X [m] <sup>1)</sup>	
LC0 fr5-NE_plus25 and LC0 fr5-NE_min25	5	11.5	Assumed 2/3 of DSF and topsides weight supported by barge (two LCs with +/-25mm differences between level of barge and quay). NE Topside
LC1 fr16-NE	16.5	40	NE topside & DSF fully on barge – most aft
LC2 fr19-NE	19	46.25	NE topside & DSF fully on barge – Row C on fr.19, i.e. on TBHd
LC3 fr29-NE	29	71.25	NE topside & DSF fully on barge – Row C on fr.29, i.e. on TBHd
LC4 fr39-NE	39	96.25	NE topside & DSF fully on barge – Row C on fr.39, i.e. on TBHd
LC5 fr44-NE	44	108.75	NE topside & DSF fully on barge – Row C on fr.44, i.e. between TBHds
LC6 fr54-NE	54	133.75	NE topside & DSF fully on barge – Row C on fr.54, i.e. between TBHds
LC7 fr71-SE	71.5	177.5	SE topside & DSF in transport position (harbour)
LC8 fr71-SE	71.5	177.5	SE topside & DSF in transport position (before sea voyage on calm water) – another draft and ballast distribution than in LC7



LC. 0



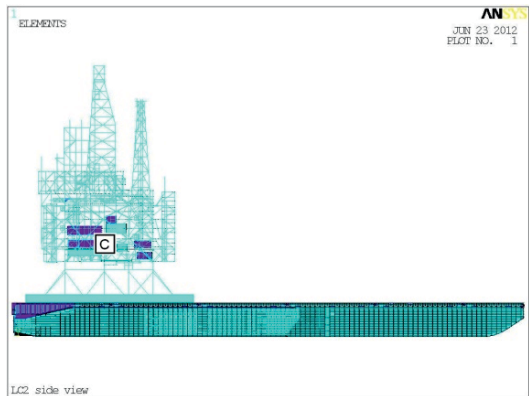
LC. 4



LC. 1



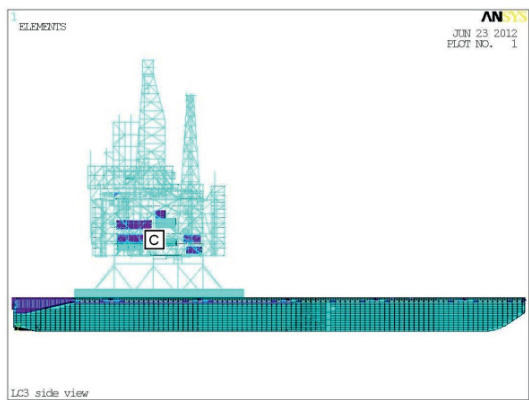
LC. 5



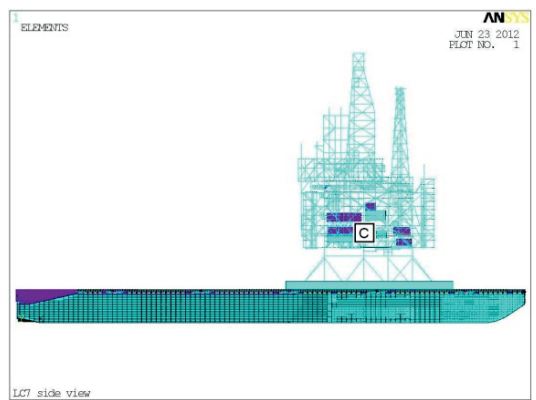
LC. 2



LC. 6



LC. 3



LC. 7 & LC. 8

Fig. 1.3. Graphical presentations of selected load cases defined by the position of DSF Row C with respect to the barge

# CALCULATION METHODOLOGY

## GENERAL ALGORITHM OF ANALYSIS

During load out operation the AD Topside with DSF was transported on skid beam by continuously pulling hydraulic cylinders. In analysis quasi-static move along step-by-step has been assumed, therefore as many 3D-FE models as load cases were required (each model for each analysed topside position). Topside FE model [8] has been delivered by the client (where beam and shell elements have been used) in transport position (LC7). Due to design modification during project, the model had different mass and centre of gravity than expected (and many constrain equation). 3D-FE model of barge has been made by GD/WDP. Because of idealization of the structure and neglected barge equipment this model also had different mass and centre of gravity than required.

The second part of the calculation (transport load cases) requires accurate mass and CoG position because of acting accelerations (directional and angular). DSF is lying on skid beam with layer of wood is mounted in-between (for reduction of local pressure due to barge stiffness distribution). There is no fixed connection between DSF and barge, therefore frictional contact connections between the wood and DSF as well as the wood and skid beam have to be defined in each position of Topside (see figures 2.1.1 and 2.1.2).

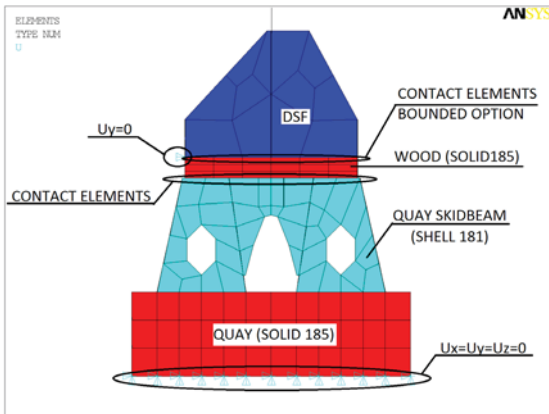


Fig. 2.1.1. Connection of quay with DSF by contact on skid beam

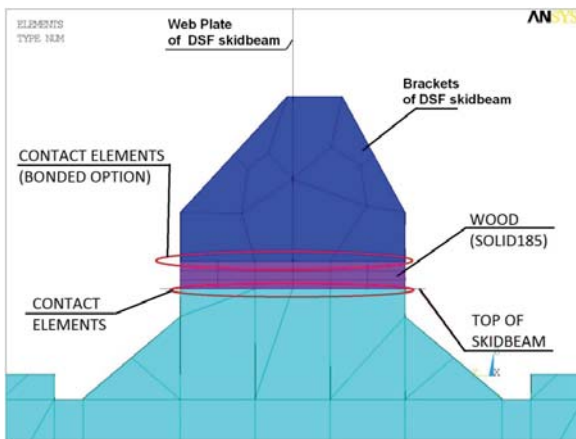


Fig. 2.1.2. Connection of barge with DSF by contact on skid beam

Due to required modification of existing structure, (after checking results of strength analysis) the process of complete calculation had to be repeated. For reducing the overall design time, calculation process had to be automated. General algorithm of analysis has been shown on figure 2.1.3.

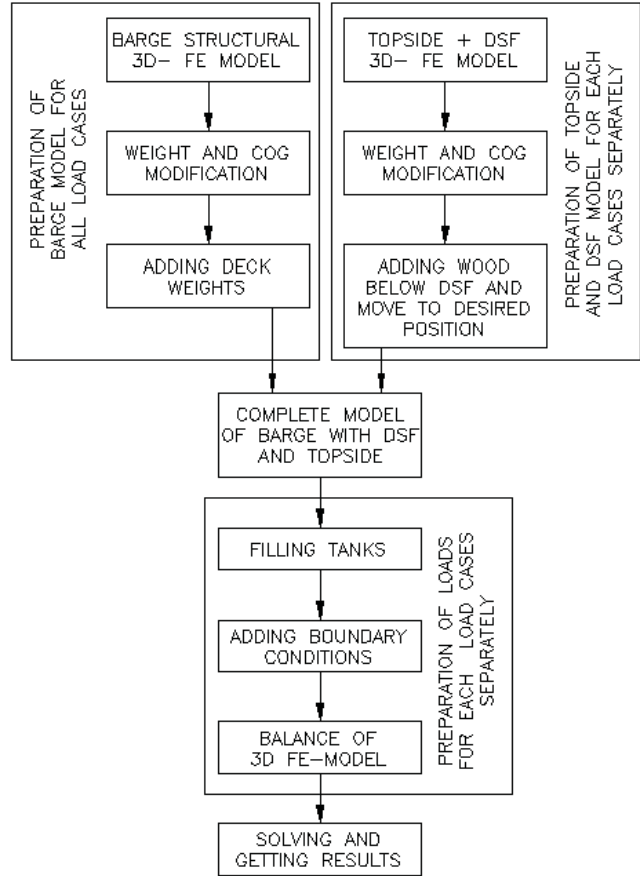


Fig. 2.1.3. General algorithm of analysis

Because of geometric complexity of barge structure and detailed modelling, barge has been divided into twelve parts. Geometry of each part has been modelled and meshed separately. In the next step the complete 3D-FE model of barge has been assembled from all the parts (without geometry, i.e. only finite elements). This approach is faster than operation on the complete model because it allows to use only partial geometry for modification. The other reason to use this approach is a fact, that ANSYS APDL (version 13) has problems with large, complex geometries (but problems not occur with FE models) [1].

The next difficulty was to achieve a required mass and CoG of barge, Topside and DSF. There are few known methods of solving such a problem. The easiest way is to change the density of material. This approach allows to achieve required mass easily, but introduces difficulties with achieving correct CoG in X, Y and Z direction.

To obtain required mass and CoG of 3D-FE model of the barge the other method has been used. The solution was to

add the mass elements (Mass21 in ANSYS) on each node of FE web frame. Total required mass of those mass elements was computed as a difference between the mass required and the mass calculated from 3D-FE model (for each web frame separately). Using this method allows to achieve correct longitudinal mass distribution and to obtain shear forces and bending moments comparable with the results from hydrostatic software.

Next phase of making the barge model consists of adding concentrated masses on deck (as containers, outfit equipment, etc.). It has been done using mass elements in CoG of each concentrated mass and contact elements for connection of with relevant deck area.

In the same time the 3D-FE model of Topside with DSF has been modified, i.e. it's mass and CoG has been checked and corrected. The layer of wood below DSF has been added into 3D-FE model and it has been moved to required position (defined by analysed load case).

By connecting models of barge and Topside with DSF the complete 3D-FE model has been built. The next phase was to prepare applied loads such as tanks filling hydrostatic pressure, buoyancy hydrostatic pressure and residual loads for final balance. Each block of general algorithm (mass and CoG modification, filling tanks, and balance of model) has been described in more detailed manner in subsections below.

### ALGORITHM OF MODIFICATION OF MASS AND CENTER OF GRAVITY

Algorithm used to modify mass and CoG for barge has been shown on figure 2.2.1 Algorithm of modification of the mass and CoG of AG Topside with DSF uses very similar procedure and has not been shown separately.

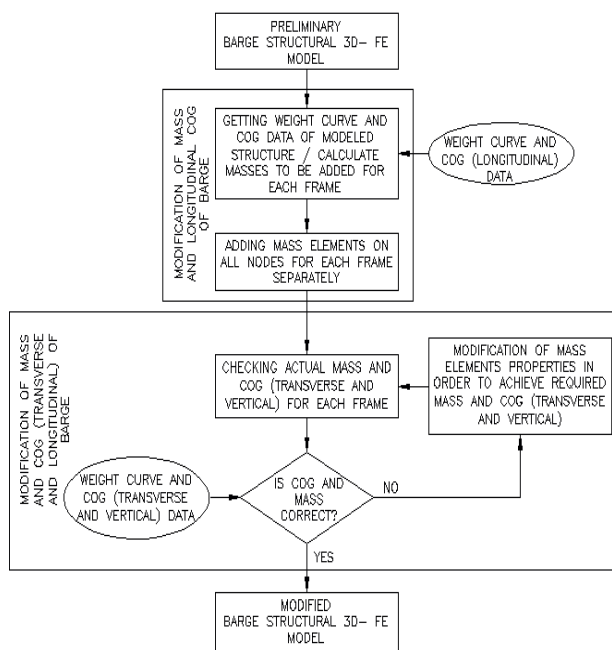


Fig. 2.2.1. Algorithm of weight and centre of gravity modification

Currently this procedure is semiautomatic, which means that modification of transverse and vertical CoG position requires an iterative process of changing the coefficients. The current version of the algorithm requires the expert to modify the coefficients, which is planned to be automated in the future.

### ALGORITHM OF FILLING AND CHECKING MASS OF TANKS

Tanks' contents have been defined by client for each load case to achieve equilibrium position of barge (no heel and trim position). Because CoG of Topside is not in the centreline of barge, filling of tanks is not symmetrical. The example of tanks' filling for one load case has been presented on figure 2.3.1.



Fig. 2.3.1. Example of ballast tanks used in load cases LC0 fr05-NE

There are a few ways to add tank loads to 3D-FE model. The easiest way is to add mass element in CoG of liquid in each tank and connect this element's mass by contact with boundary walls of tank. This approach does not give correct distribution of pressure on tank's walls. It is better to use internal liquid tank pressure instead of equivalent mass element. In this way we can take into consideration the trim, heel and dynamic accelerations (sea-going cases are not described in this paper) without local peak stresses caused by numerical inaccuracy. Internal liquid pressures of filled tanks have been found using following algorithm (see figure 2.3.2).

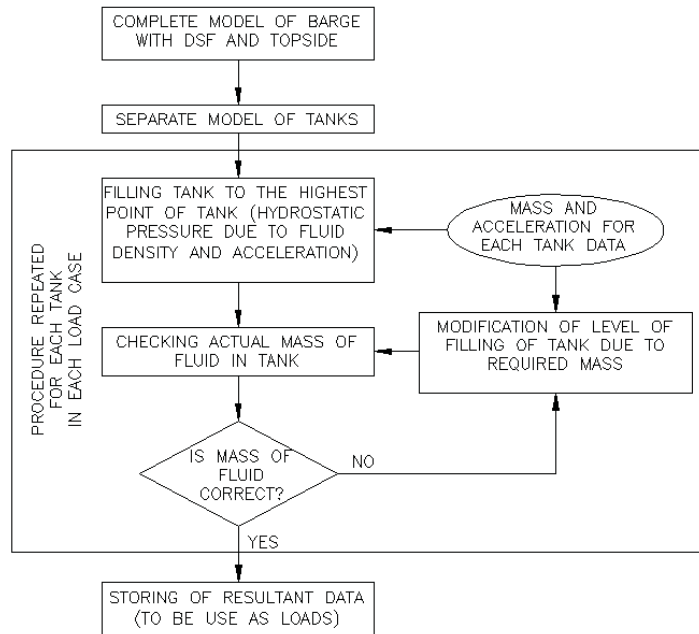


Fig. 2.3.2. Algorithm of filling of tanks

Internal liquid tank pressure application procedure adopted in 3D-FE model is based on ABS Guide for ‘SAFEHULL-Dynamic Loading Approach’ for Vessels [5].

Static and dynamic pressures exerted on completely filled and/or partially filled tanks are considered in analysis assuming that there is no relative motion between the tank and the contained liquid. No sloshing effects are considered, i.e. not included in the procedure.

The loads are calculated by applying a hydrostatic pressure distribution in the accelerated reference frame fixed with respect to the tank. The tanks are modelled by assigning the pressure load to those surfaces which are the walls of the tanks.

The filling of the tanks is controlled by assigning pressure load only to the wet part of the tank walls (see figure 2.3.3). Internal pressure head in direction of resultant acceleration vector is found iteratively in order to achieve user specified filled volume of tank with assumed accuracy.

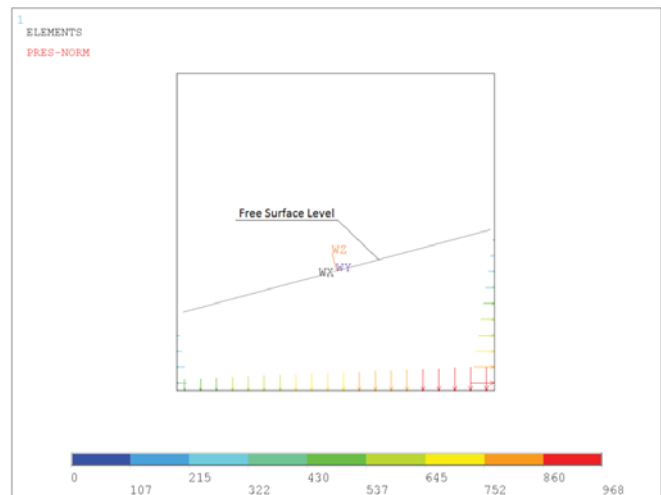


Fig. 2.3.3. Internal liquid tank pressure distribution

Procedure described above allows to find level, position (heel and trim) and pressure distribution taking into account relative acceleration vector.

## ALGORITHM OF BALANCING THE COMPLETE 3D-FE MODEL

Last step of preparing of loads for particular load cases is to add buoyancy pressure on shell of barge. This pressure can be taken as hydrostatic pressure for waterline calculated in hydrostatic software, but it introduces significant reaction forces in places where boundary condition are added. It is because of numerical differences in definition of barge shell in NAPA [9] and finite element model in ANSYS [1]. Those high reactions forces cause peaks of stresses and inaccurate distribution of shear forces and non-zero bending moments on ends of barge. To avoid the difficulties with significant reaction forces described above it is important to make very accurate hydrostatic balance.

General algorithm of model balancing has been shown on figure 2.4.1. Separate model of shell has been extracted from complete 3D-FE model (i.e. barge, AD Topside and DSF) and has been used to calculate balance hydrostatic pressure due to smaller model size and faster calculation time.

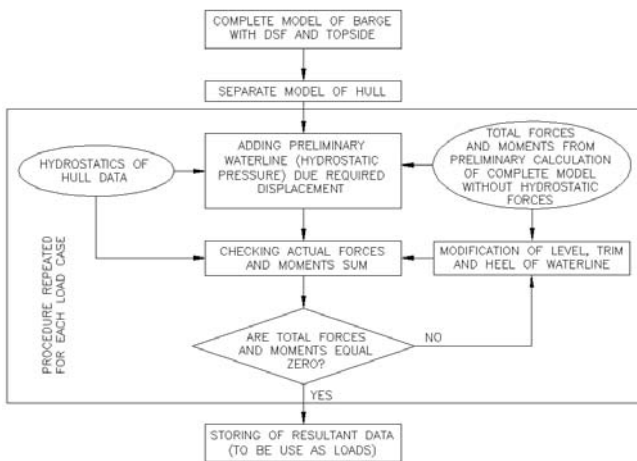


Fig. 2.4.1. Algorithm of balance of 3D-FE model

In the first step complete model has been calculated with all loads except buoyancy hydrostatic pressure. Loads and additional masses taken into consideration in those calculations are as follows:

- structural weight of hull and skid beam,
- DSF & Topside,
- infill-piece,
- mooring equipment and other deck masses,
- fenders,
- liquids in tanks,
- gravity loads (in sea-going load cases also dynamic accelerations).

Reactions forces obtained from those calculations act as inputs to calculations with separate model of hull. The purpose of the above algorithm is to find correct waterline (balanced hydrostatic pressure).

In the case of ANSYS 3D-FE model, static trim is computed by iteratively adjusting the variables: draught, trim angle and heel angle until hydrostatic equilibrium is achieved, i.e. until

the balance of buoyancy and lightweight distributions is met.

This approach gives very low unbalanced reactions forces which can be neglected from strength analysis point of view (below 0.1% of displacement).

## RESULTS

### COMPARISON OF SHEAR FORCES AND BENDING MOMENTS OBTAINED FROM ANSYS AND NAPA

On the basis of ballast and weight distribution (the AD Topside positions have been shown in chapter 1) for harbour LCs the static equilibrium of barge has been computed in NAPA and compared with ANSYS results. Distributions of bending moments in all harbour load cases obtained from ANSYS have been shown on figure 3.1.1.

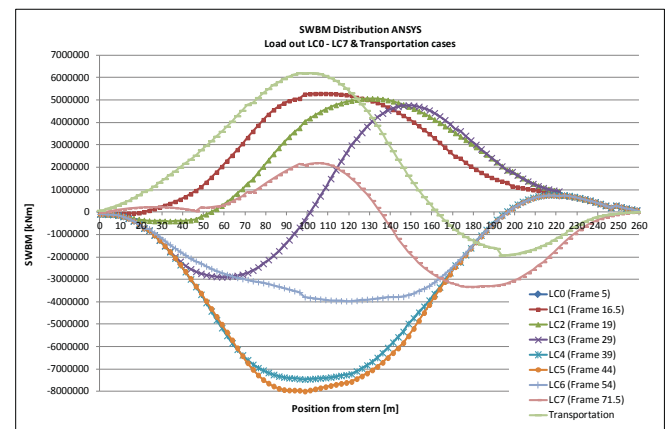


Fig. 3.1.1. Bending moments distribution in all harbour load cases

Analysis algorithm has been verified by checking the shear forces, bending moments and torsion moments acquired from NAPA and from ANSYS. Results of comparison for selected load cases (LC0, LC4 and LC8) have been shown on figures 3.1.2 to 3.1.10.

Values from ANSYS were captured only from structure of barge and skid beam (i.e. only from elements that are taken into consideration in longitudinal strength) but effect of DSF with AD Topside is included in the results. Because of this, maximum values of bending moments are equal or lower from those computed in NAPA. DSF is about 85m long and its stiffness has influence on whole structure (BARGE+DSF).

The next important thing is a construction of DSF. There are a few columns on each side of DSF. In hydrostatic software, weight of DSF with Topside is taken into account as triangle distributed load (to achieve required mass and centre of gravity). In ANSYS distribution of weight is resultant of DSF stiffness and barge condition (hogging or sagging) and stiffness. This situation is observed on figures 3.1.2 to 3.1.10. In place of DSF shear forces obtained from ANSYS are different from those obtained from NAPA. Outside of DSF the values and distributed curves are very close from both programs.

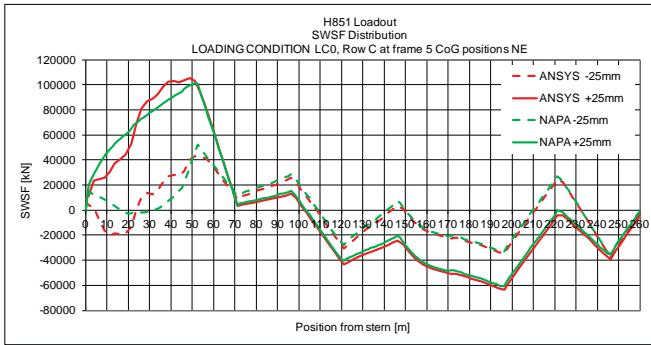


Fig. 3.1.2. LC0 – Comparison of shear forces obtained from ANSYS and NAPA

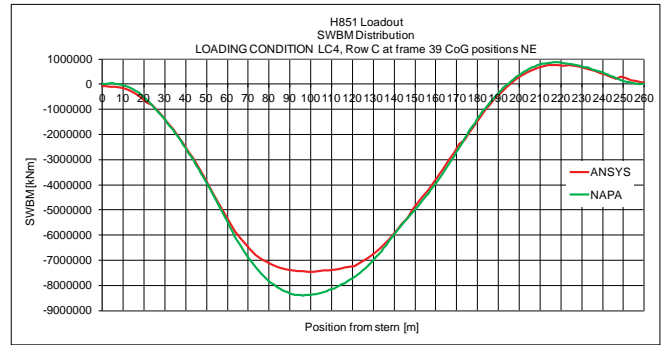


Fig. 3.1.6. LC4 – Comparison of bending moments obtained from ANSYS and NAPA

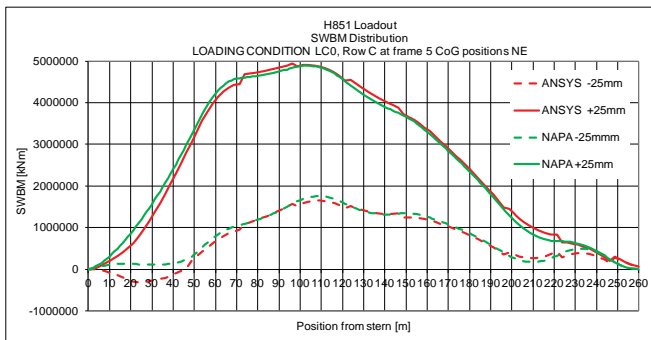


Fig. 3.1.3. LC0 – Comparison of bending moments obtained from ANSYS and NAPA

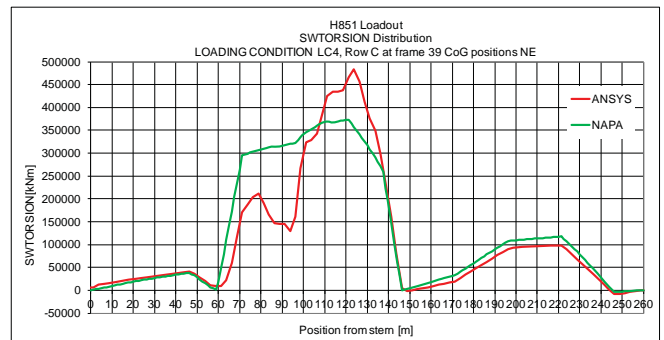


Fig. 3.1.7. LC4 – Comparison of torsion moments obtained from ANSYS and NAPA

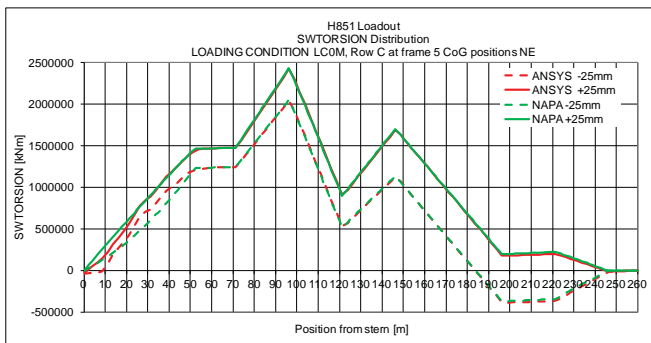


Fig. 3.1.4. LC0 – Comparison of torsional moments obtained from ANSYS and NAPA

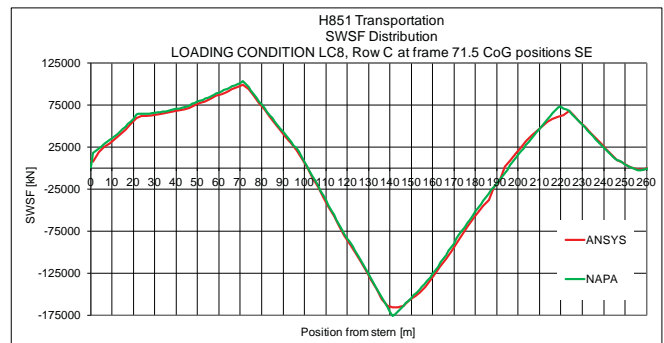


Fig. 3.1.8. LC8 – Comparison of shear forces obtained from ANSYS and NAPA

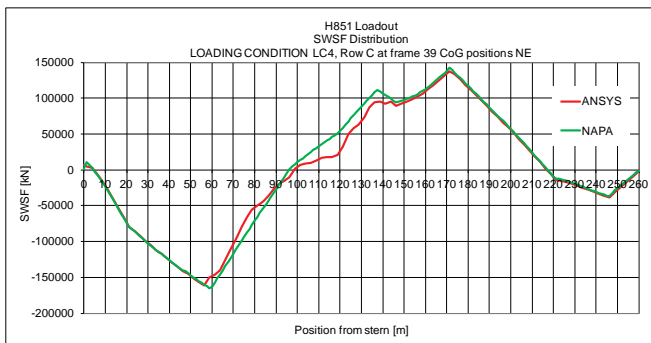


Fig. 3.1.5. LC4 – Comparison of shear forces obtained from ANSYS and NAPA

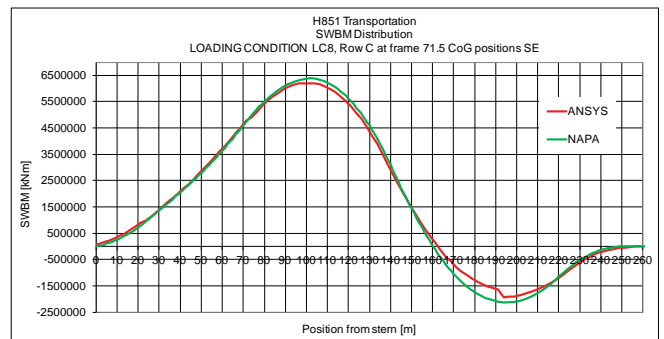


Fig. 3.1.9. LC8 – Comparison of bending moments obtained from ANSYS and NAPA

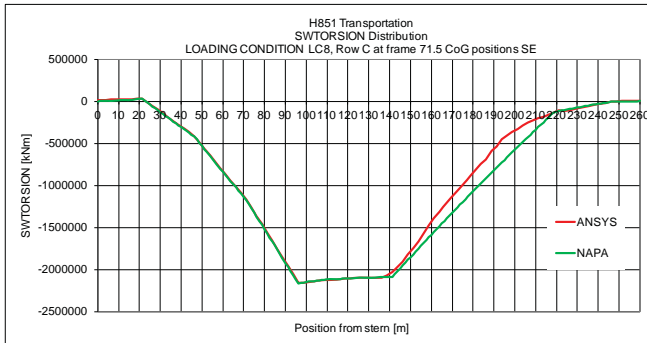


Fig. 3.1.10. LC8 – Comparison of torsion moments obtained from ANSYS and NAPA

### SELECTED RESULTS OF ANALYSIS

Complex strength analysis of load out of AD Topside against Lloyd’s Register rules [10] has been performed. Complete stresses distribution images have been captured, but not presented in this paper. Only selected results have been shown. Because of wood installed below DSF it was important to know forces acting on skid beam. During load out from quay to barge in part of time DSF is partially on quay and barge (see figure 3.2.1).

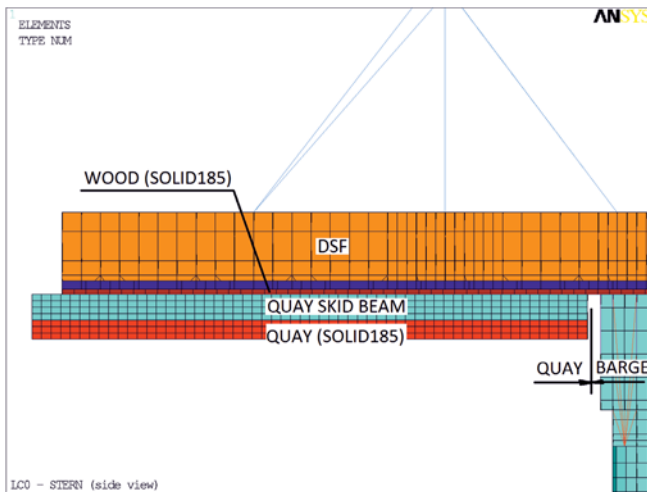


Fig. 3.2.1. LC0 – DSF partially on quay and barge (vertical position of barge can be controlled in range of +/- 25 mm)

Vertical position of barge can be controlled in range +/- 25mm. This means that the edge end of the quay will have a peak of pressure when the top of skid beam of barge is 25 mm below the skid beam of quay. On the other hand if the top of skid beam of barge is above the top of skid beam of the quay, it will cause a peak of pressure on barge structure. Because a stiffness of the quay is significantly higher than stiffness of barge structure the peak of Z-forces on the quay (see figures 3.2.2 and 3.2.3) is higher than peak of Z-forces on barge (see figures 3.2.4 and 3.2.5). The next thing that can be observed is the gap (no contact) between skid beam and DSF. The gap occurs on barge or quay due to barge position (+/- 25mm). Those figures have shown that contact elements allow for

separation of the skid beam and DSF skid and interaction of transverse forces between barge and DSF by friction.

Reaction forces on skid beam have been also shown for LC4 and LC8. The maximum values of reaction forces, observed in this LCs, are lower than in LC0. The most uniform distribution of reaction forces is observed in LC8.

No symmetrical distribution of reaction forces and moments on skid beam gives bending and torsion of barge structure. Deflection in one of load cases (LC8) has been shown on figure 3.2.6. Deflections have occurred on top deck lines of longitudinal bulkheads (Y=0m, Y=10.5m, Y=18.75m and Y=21m, both sides PS and SB).

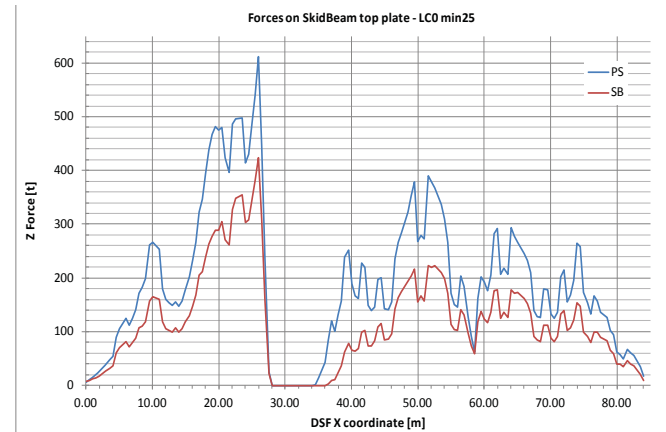


Fig. 3.2.2. LC0 (minus 25mm) – Reaction forces on PS/SB skid beams (top of skid beam on barge below top of skid beam on quay), peak of force on end of quay observed

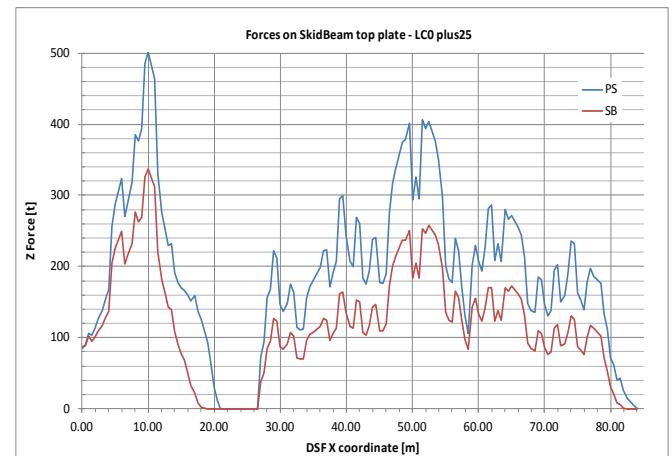


Fig. 3.2.3. LC0 (plus 25mm) – Reaction forces on PS/SB skid beams (top of skid beam on barge above top of skid beam on quay)

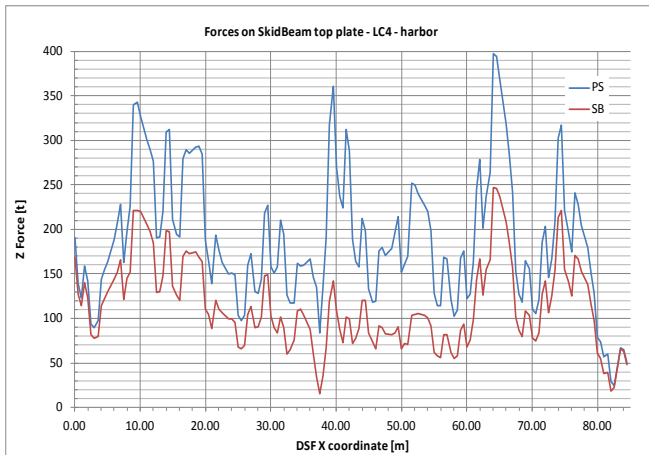


Fig. 3.2.4. LC4 – Reaction forces on PS/SB skid beams

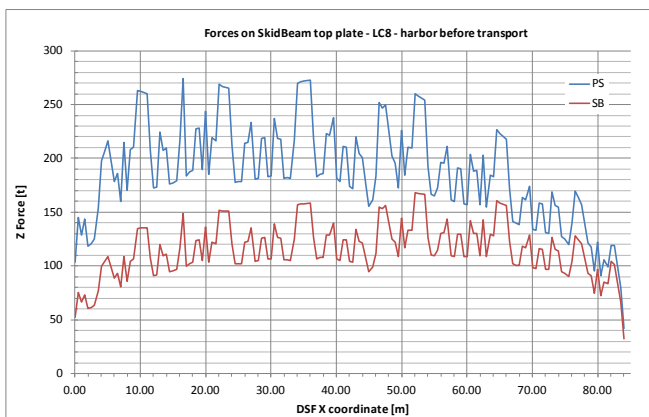


Fig. 3.2.5. LC8 – Reaction forces on PS/SB skid beams

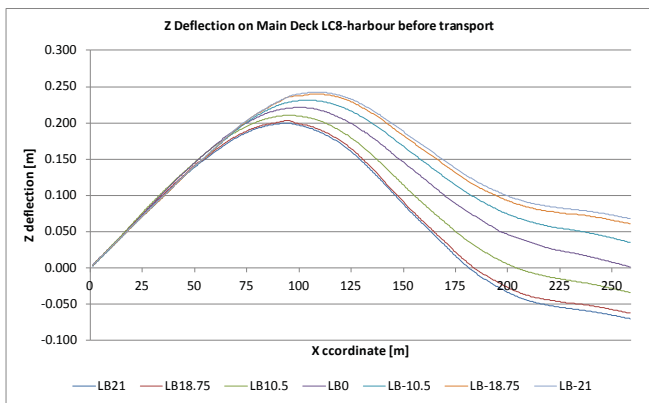


Fig. 3.2.6. LC8 – Deflections of deck lines on longitudinal sections (top of longitudinal bulkheads)

## CONCLUSION

Design methodology of strength verification of platform during load out has been presented. The NAPA and ANSYS codes were used to calculate hydrostatic pressures and to apply them to 3D-FE models and to carry out strength calculation of barge structure. Presented results show a very good convergence of shear forces, bending and torsion moments with results

obtained from NAPA. Due to a different definition of vertical loads used in codes of ANSYS and NAPA small differences in results has been observed. Hydrostatic software such as NAPA does not take into account influence of stiffness of deck load (AD topside with DSF). The use of 3D-FE model allowed to include that stiffness and therefore reduce stresses during load out of barge. More accurate results lead to reduction of a range of modification of skid beam and decrease the operation costs. Because time required to obtain accurate balance with self-developed algorithm in ANSYS is much longer than using NAPA, barge ballast procedure and balance were always prepared in NAPA. Only final hydrostatic balance was prepared in ANSYS.

Neither NAPA nor ANSYS currently takes into account changes of hydrostatics due to barge deflection. Implementation of this phenomenon in own algorithms is currently under consideration. Deflected waterline has a positive effect on hull deflection and stress level. This effect can reduce deflections and calculated stresses during similar harbour operations.

## ACKNOWLEDGMENT

The paper was funded in the course of science propagation at The Faculty of Mechanical and Electrical Engineering Polish Naval Academy.

## REFERENCES

1. ANSYS, Inc. Southpointe 275 Technology Drive Canonsburg, PA 15317, USA
2. Bokhorst J., Willemsse O., Zoontjes R.: Float-Over Analysis For World's Largest Float-Over Barge, OMAE2011-49462
3. Cheunga L. Y., Foonga K. G.: Design considerations of a load out skid frame for a 14,000-ton upper hull structure, The IES Journal Part A: Civil & Structural Engineering, Vol. 1, pp.93-95, 2008
4. GL Noble Denton, Guidelines for Float-over Installations, 0031/ND Rev 0
5. Guide for 'Safe hull-Dynamic Loading Approach' for vessels, American Bureau of Shipping, 2013
6. Hamilton J., French R., Rawstron P., Topsides and Jacket Modelling for Float-over Installation Design, OTC 19227
7. Kenney, J. J., Knoll, D. A., Brooks, A. M. , Crimmins, D. M.: Loadout of Auger Deck and Hull-Deck Mating Operations, 26th Annual conference, Vol 3: Construction and installation, pp. 409-418, Houston 1994

8. NAPA, The Naval Architecture Package, NAPA Oy, 2012
9. Rozeboom M., Design considerations for the modifications of the H-851 into a float-over vessel”, DOT 2008
10. Rules and Regulations for the Classification of Ships, Lloyd`s Register, 2014
11. Smith P.L., Hodges S.B., Digre K.A., Sarwono B.A., Schipper H., Ursa TLP hull design, fabrication and transportation, OCT '99 - 31st Annual Offshore Technology Conference, pp. 161-173, Houston, US, 1999
12. Yang Y.T., Park B.N., Ha S.S.: Development of load-out design methodology and numerical strength evaluation for on-ground-build floating storage and offloading system, Ocean Engineering 32, pp 986–1014, 2005

## CONTACT WITH THE AUTHOR

Wojciech Jurczak

*e-mail: wjurczak@amw.gdynia.pl*

Polish Naval Academy  
Śmidowicza Street 69  
81-127 Gdynia

**POLAND**

## EXPERIMENTAL METHOD FOR PLOTTING S-N CURVE WITH A SMALL NUMBER OF SPECIMENS

Przemysław Strzelecki, PhD

Janusz Sempruch, Prof.

University of Science and Technology in Bydgoszcz, Poland

### ABSTRACT

*The study presents two approaches to plotting an S-N curve based on the experimental results. The first approach is commonly used by researchers and presented in detail in many studies and standard documents. The model uses a linear regression whose parameters are estimated by using the least squares method. A staircase method is used for an unlimited fatigue life criterion. The second model combines the S-N curve defined as a straight line and the record of random occurrence of the fatigue limit. A maximum likelihood method is used to estimate the S-N curve parameters. Fatigue data for C45+C steel obtained in the torsional bending test were used to compare the estimated S-N curves. For pseudo-random numbers generated by using the Mersenne Twister algorithm, the estimated S-N curve for 10 experimental results plotted by using the second model, estimates the fatigue life in the scatter band of the factor 3. The result gives good approximation, especially regarding the time required to plot the S-N curve.*

**Keywords:** high-cycles fatigue, S-N curve, fatigue tests, number of specimens

### INTRODUCTION

To determine a fatigue life or fatigue limit of structural components, the inter-dependencies resulting from the material data of one of the S-N curves, are used. The S-N curves are used in calculations for both limited and unlimited fatigue life regimes.

For the limited fatigue life regime, it is most often represented by the coefficient  $m$  defined by the following equation:

$$\log(N) = m \log(S) + c \quad (1)$$

where  $N$  is the number of load cycles,  $S$  is a stress amplitude, and  $c$  is an absolute constant term in the expression. The recommendations on selecting value of the coefficient  $m$

are available in the literature. A critical analysis of the recommended values is shown in Tab.1, based on a set of values of the coefficient  $m$  taken from the literature (based on 91 material data sets for steel). Fig. 1 shows the histogram for the available material data. The average recommended values are considered accurate although significant deviations can be observed in some cases. The deviations are related to a large scatter of the coefficient  $m$ . Based on the estimated gamma distribution (shown in Fig. 1) a (9.51÷15.26) scatter can be observed for 50% probability. For 95% probability, the scatter is greater and amounts to 5.61÷22.51, which can pose serious problems with accurate determination of a correct value.

A complete S-N curve can be plotted by using an analytical method. Selected methods [1,2,3,4,5] were verified by the

authors of this study. Fig. 2 shows the histogram of error distribution of fatigue life estimation for both methods. Sign “+” indicates that the estimated values are on the safe side. Sign “-” indicates the opposite. In case the curve shifts from safe to unsafe side, “+/-” sign is assigned. The opposite is marked with “/+” sign. Based on the results of Fig. 2 the practical implementation of the analytical methods does not only affect modelling accuracy but also the quality of determining the position of the estimated fatigue life in relation to the actual fatigue life. The methods may result in over-estimation or under-estimation of the fatigue life, which is very difficult to anticipate a priori.

Tab. 1 Guidelines for selection of recommended number of specimens

Value of the coefficient $m$	Probability of getting $m$ -value
5÷20 acc. [1]	92,6%
6÷20 acc. [2]	90,4%
8÷12 acc. [3]	35,3%
5,61÷22,51	95% (estimated from histogram of Fig. 1)
9,51÷15,26	50% (estimated from the histogram of Fig. 1)

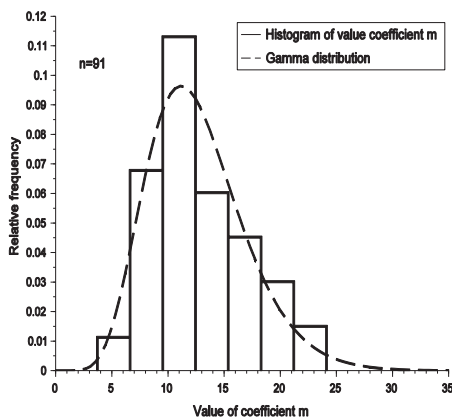


Fig. 1. Distribution of the coefficient  $m$  for smooth specimen of constructional steel under normal stress

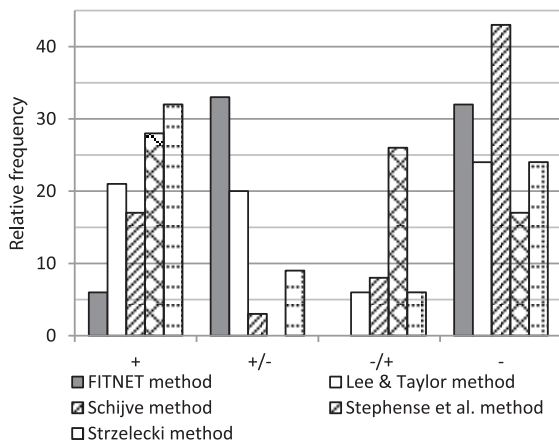


Fig. 2. Distribution of the coefficient  $m$  for smooth specimen of constructional steel under normal stress

Although there is an average characteristic error for the method, see Fig. 3, the scatter of error still remains significant, and to determine the correction factor (as a safety factor) to reduce the estimation inaccuracy, is still difficult.

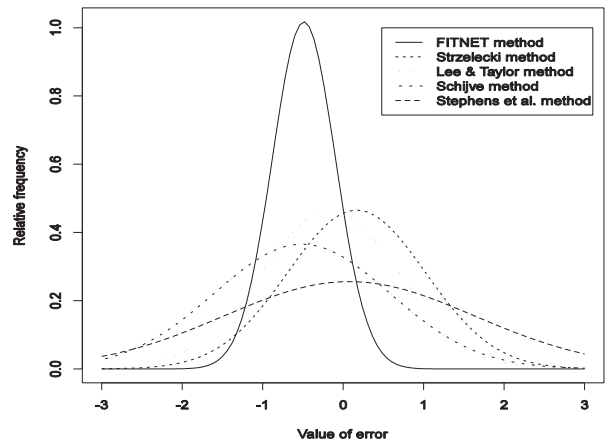


Fig. 3. Distribution of the coefficient  $m$  for smooth specimen of constructional steel under normal stress

The study [8] discusses that along with the strictly experimental methods (considered accurate) and the analytical methods (burdened with uncertainty as shown below) a hybrid solution is available by combining the available knowledge on analytical and experimental methods. Similar approach is discussed in study [9]. Fig. 4 shows an example of how in the fatigue tests the amount of work spent for experimental support of the analytical method, affects the error of fatigue life estimation. The points marked with numbers in Fig. 4 correspond to the following values: 1 – analytical method error where material values are determined by using tensile test, 2 – analytical/experimental method error determined by using tensile test and fatigue test for three specimens at 105 load cycles, 3 – analytical/experimental method error determined by using tensile test and the fatigue limit  $Z_{go}$  by using Locati method, 4 – scatter of results obtained by using the method described in [10] at 95% confidence level.

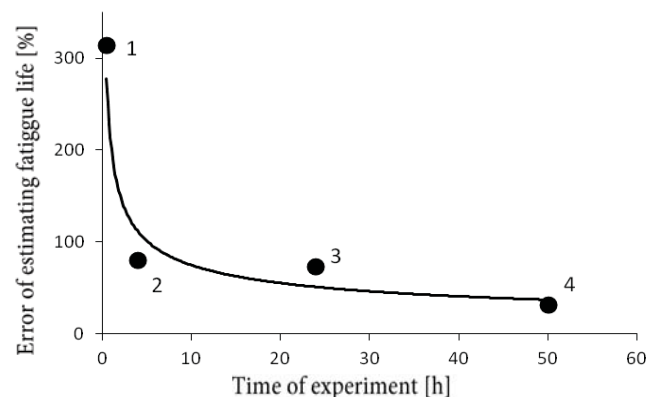


Fig. 4. Diagram of value of fatigue life estimating error according to time of carrying out the test [7] – a proposal of idea

Results for experimental verification of the approach were obtained at the torsional bending test stand shown in Fig. 5

(described and verified in [11]). Based on the graph shown in Fig. 5 the hybrid approach is preferred to determine the fatigue life of a notched specimen considered to be a model of a structural component.

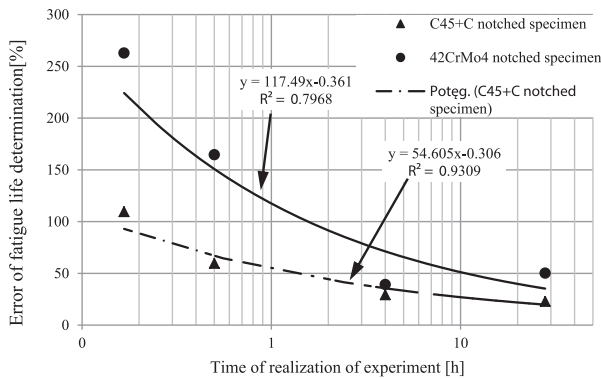


Fig. 5. The analytical method error versus the number of experimental values [8] – verification of idea

Only experimental tests yield results with an anticipated probability of the correct value estimation. Costly (due to the required time) fatigue tests can be significantly reduced with the new concepts.

The purpose of the study is to determine the fatigue life and fatigue limit modelling process for limited and unlimited fatigue life regime by experimental plotting the S-N curve with a small number of specimens.

## S-N CURVE ESTIMATION METHODS

Fig. 6 shows an estimation diagram for S-N curve based on the experimental data. The most common method to describe the relationship between the fatigue life and the load amplitude for a limited fatigue life regime is a linear regression, as given by Eq. (1). The equation parameters are commonly determined by using the least squares method described in detail in [12]. The equations to estimate the parameters of Eq.(1) are as follows:

$$\hat{m} = \frac{\sum_{i=1}^k (X_i - \bar{X})(Y_i - \bar{Y})}{\sum_{i=1}^k (X_i - \bar{X})^2}, \quad (2)$$

$$\hat{c} = \bar{Y} - \hat{m}\bar{X}, \quad (3)$$

where Y is log(N), X is log(S), and k is the sample size.  $\hat{c}$  stands for an estimated parameter, and  $\bar{m}$  stands for an average value. Standard deviation is calculated by means of the following formula,[12]:

$$\sigma = \sqrt{\frac{\sum_{i=1}^k (Y_i - \hat{Y})^2}{k - 2}}. \quad (4)$$

Standard requirements define various numbers of specimens. 15 specimens at 5 load levels are recommended as a minimum, by [10]. Study [13] recommends to initially determine the S-N curve for 5 specimens, one for each load level and further tests to increase the S-N curve accuracy, although

it does not specify a recommended number of specimens. Another study [14] recommends to determine the S-N curve for at least 28 specimens. For preliminary tests, it recommends to carry out 7 tests, but it does not specify a required number of load levels. It only includes a reference to [12] where the relation to replication percentage is defined:

$$PR = 100 \left[ 1 - \left( \frac{Sl}{n_a} \right) \right] [\%] \quad (5)$$

where Sl is the number of load levels and  $n_a$  is a total number of specimens.

The standard recommends to achieve the replication percentage as shown in Tab. 2.

Tab.2 Guidelines for recommended percent replication for various tests [12]

Type of tests	Percent replication
Preliminary and exploratory (research and development tests)	17 to 33
Research and development testing of components and specimens	33 to 50
Design allowable data	50 to 75
Reliability data	75 to 88

When determining fatigue limit for unlimited fatigue life regime, a staircase method is often used based on Dixon and Mood concept discussed in [3,5]. The method requires a minimum of 15 specimens. The staircase method consists in tests at constant load, constant load frequency and uniform temperature. The number of load cycles is measured until failure or until a specified number of cycles  $N_G$  (e.g. 5·10<sup>6</sup>) is reached. A limit number of cycles is selected based on the type of used material. For the initial specimen stress amplitude is selected below the anticipated fatigue limit. For the subsequent specimen the load is reduced following the failure of the initial specimen. Otherwise (without specimen failure, or when the specimen reaches the limit number of cycles) the load is increased. The difference between the load levels are determined lower than or equal to 0,05· $Z_G$ . Example test procedure using the staircase method is shown in Fig. 6 - in the bottom left corner.

Fatigue limit is calculated by means of the following formula [3,5]:

$$Z_G = S_0 + S_i \left( \frac{A}{F} \pm \frac{1}{2} \right) \quad (6)$$

where:  $S_0$  is an initial stress amplitude,

$S_i$  - the stress amplitude between subsequent load levels,

F - a total value of less frequent events,

A is defined as:

$$A = \sum_{i=1}^n i \cdot f \quad (7)$$

where  $i$  is the ordinal number of the load level, for  $S_0$  it is 0, and  $f$  is the number of less frequent events at the  $i$ -th level, and  $n$  is the total number of load levels. Sign “+” in Eq. (7) indicates that the more frequent event is specimen failure, whereas “-” indicates that the failure is a less frequent event. Standard deviation is calculated as:

$$s = 1,62 \cdot \sigma_i \left( \frac{FB - A^2}{F^2} + 0,029 \right), \quad (8)$$

where:

$$B = \sum_{i=1}^n i^2 \cdot f. \quad (9)$$

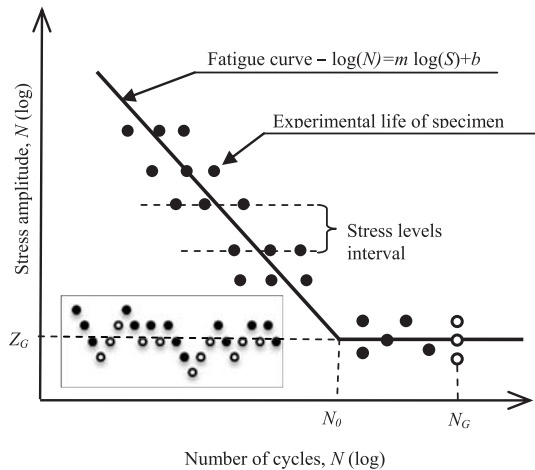


Fig. 6. Scheme of estimated fatigue curve in high cycle range and fatigue limit

Plotting the S-N curve by using linear regression and staircase method is referred to as the classic approach and the first model ( Model I)

Based on the assumptions presented in [15], an alternative approach is referred to as the second model ( Model II ) , presented below. The advantage of the second model is the ability to plot the complete S-N curve with a smaller number of specimens. The basis for the procedure is as follows: Eq. (1) is expressed as:

$$\log(N)=m \log(S)+c+\varepsilon_n \quad (10)$$

where  $\varepsilon_n$  is a random component of fatigue life with normal distribution. The density function can be expressed as:

$$f(N) = \frac{1}{\sqrt{2\pi\sigma_n^2}} \exp \left( -\frac{(\log(N) - (m \log(S) + b))^2}{\sigma_n^2} \right) \quad (11)$$

where  $\sigma_n$  is standard deviation.

The fatigue limit can be expressed as:

$$S_i = Z_G + \varepsilon_s \quad (12)$$

where  $\varepsilon_s$  is a random component of fatigue limit with normal distribution. The density function can be expressed in this case as follows:

$$f(S) = \frac{1}{\sqrt{2\pi\sigma_s^2}} \exp \left( -\frac{(S - Z_G)^2}{\sigma_s^2} \right) \quad (13)$$

where  $\sigma_s$  is standard deviation.

It can be assumed that the failure can occur as a result of a stress higher than the limit value  $Z$  or after the fatigue life higher than or equal to that defined by Eq. (10), is reached. Since the values are random it can be assumed that the probability of failure will be equal to the probability of value satisfying Eq. (11) and (13). With this assumption, the probability of failure for limited and unlimited fatigue life regime can be expressed as follows, [16]:

$$P(N < N_i) = \Phi \left( \frac{\log N_i - (a \cdot \log S_i + b)}{\sigma_v} \right) \cdot \Phi \left( \frac{S_i - Z_s}{\sigma_s} \right) = q \quad (14)$$

where  $\Phi$  is the normal distribution function and  $q$  is the probability of specimen failure.

The maximum likelihood method is used to determine the parameters in Eq. (14). The method can be applied to the specimens that reached the limit number of cycles. The likelihood function is expressed as follows, [15]:

$$L(\theta) = \prod_{j=1}^k [f_n(N_j; S_j, \theta)]^{\delta_j} [1 - F_n(N_j; S_j, \theta)]^{1-\delta_j}, \quad (15)$$

where

$$\delta_j = \begin{cases} 1 & \text{if } N_i \text{ is a failure} \\ 0 & \text{if } N_i \text{ is a censored observation.} \end{cases} \quad (16)$$

The maximum likelihood function is expressed as:

$$L(\theta) = \phi \left( \frac{\log N_i - (a \cdot \log S_i + b)}{\sigma_v} \right)^{\delta_i} \cdot \Phi \left( \frac{S_i - S_{xe}}{\sigma_{xe}} \right)^{\delta_i} \cdot \left( 1 - \left( \Phi \left( \frac{\log N_i - (a \cdot \log S_i + b)}{\sigma_v} \right) \cdot \Phi \left( \frac{S_i - S_{xe}}{\sigma_{xe}} \right) \right) \right)^{1-\delta_i}, \quad (17)$$

where  $\Phi$  is the normal distribution density function.

## VERIFICATION OF THE METHOD

Data from the fatigue tests of S45+C steel were used to verify both models. The fatigue test was carried out on the test stand as presented in [11]. Tab. 3. shows values of static properties of the tested material. The specimens were prepared from the drawn bar in as - delivered state. Fig. 7 shows the specimen geometry.

Tab. 3 Properties of C45+C material used for calculation [11]

Ultimate strength Su [MPa]	826
Yield stress Sy [MPa]	647
Hardness HB	232

Fig. 8 shows experimental test results for C45+C steel with S-N curves plotted by using Model I and Model II. The tests were performed on 31 specimens in limited fatigue life regime and 19 specimens in unlimited fatigue life regime (7 specimens failed and 12 specimens reached the limit number of cycles NG). All S-N curves were plotted at 50% probability of failure. All calculations were performed by using R software ,version 3.1.3 , [17].

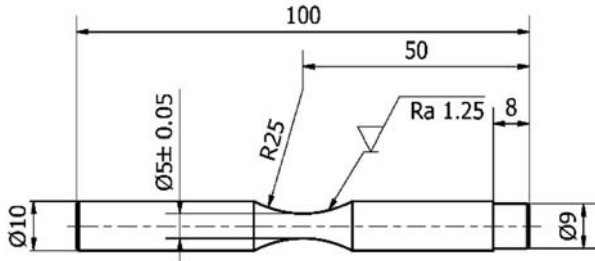


Fig. 7. Specimen used for tests  
C45+C

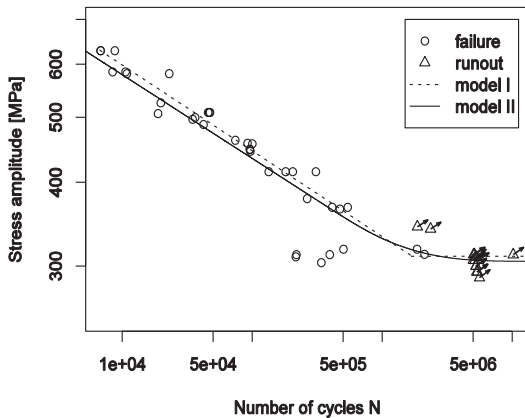


Fig. 8. Fatigue data of C45+C steel and fitted fatigue characteristics by using model I and model II

The equations for Model I are shown below.

$$\log(N_i) = -7.8 \log(S_i) + 59.2 \pm 0.28 \quad (18)$$

$$Z_G = 310.3 \pm 11.4 \quad (19)$$

The equation according to Model II is presented by means of the formula (20).

$$\Phi\left(\frac{\log N_i - (-8 \cdot \log S_i + 60.2)}{0.67}\right) \cdot \Phi\left(\frac{S_i - 304.9}{20}\right) = q \quad (20)$$

Fig. 9 shows the results obtained by using the staircase method.

The coefficients obtained by using Model I and Model II vary to each other. The differences can be observed in the S-N curves shown in Fig. 8. Since the S-N curve for Model II

is shifted to the left resulting in the under-estimation of the fatigue life, the situation can be considered safe. Standard deviations for limited and unlimited fatigue life regimes are higher for the Model II equation (0.67 to 0.28 and 20 to 11.4, respectively) due to the higher scatter of specimen fatigue life near the fatigue limit.

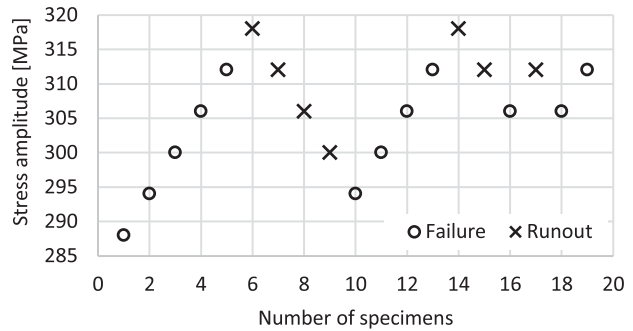


Fig. 9. Fatigue data from staircase method

## SMALL NUMBER OF SPECIMENS TO PLOT THE S-N CURVE

A predefined number of specimens was used in Model I, [9,12,13]. No explicit number of tests was specified for Model II. How far can the number of specimens be reduced in Model II allowing for the number of specimens used in the tests based on Model I?

An existing set of 50 test results was used to verify Model II for a small number of specimens by random generating smaller subsets with the use of the following method. Ten (10) random specimens were generated. Five (5) specimens were generated for the tests using the staircase method (shown in Fig. 9) and 5 for a limited fatigue life (stress amplitude from 341 MPa to 628 MPa). The test results were divided into 5 groups by stress amplitude before generating random specimens for a limited fatigue life. One specimen was randomly selected for each range. The selected specimens are shown in Fig. 10, 11, 12, 13, 14 and 15. A rectangular distribution with the density function defined by Eq. [17] was used to generate the pseudo-random numbers:

$$f(x) = 1/(max - min). \quad (21)$$

Pseudo-randomness has been achieved by using the Mersenne Twister algorithm.

Fig. 16 shows gamma distribution of the coefficient  $m$ , previously shown in Fig. 1, as well as the modal value of the distribution and the value obtained by using Model I. A range of the obtained value for Model II for the randomly generated specimens is also included. The values of the coefficient  $m$  estimated by using the maximum likelihood method were lower than 7.8 (i.e. the value estimated by using Model I), where

the generated test results were within the unlimited fatigue life range at the number of cycles below 106. It caused the S-N curve to shift to the left. This can be observed in Fig. 10, 11, 14 and 15. It is clearly visible for the 5th and 6th generated random number .

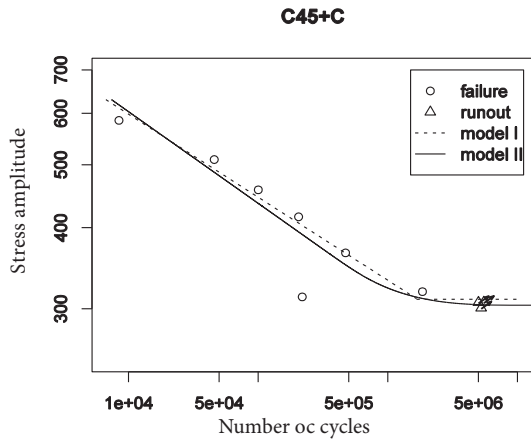


Fig. 10. Fatigue data of C45+C steel from 1st generated random number of specimens and fitted fatigue characteristics by using Model II and Model I described by Eq. (18) and (19), respectively.

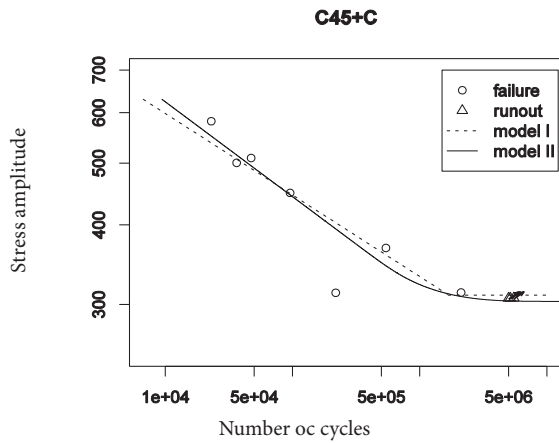


Fig. 11. Fatigue data of C45+C steel from 2nd generated random number of specimens and fitted fatigue characteristics by using Model II and Model I described by Eq. (18) and (19), respectively.

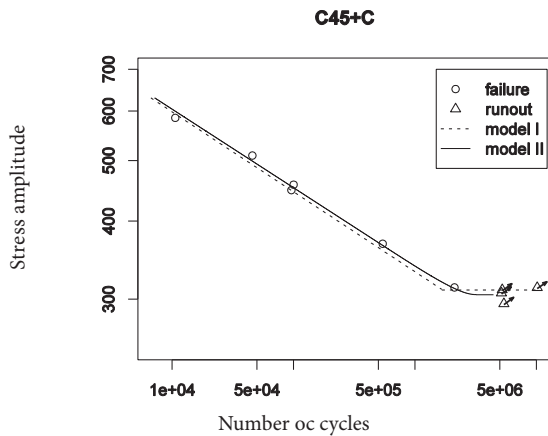


Fig. 12. Fatigue data of C45+C steel from 3rd generated random number of specimens and fitted fatigue characteristics by using Model II and Model I described by Eq. (18) and (19), respectively.

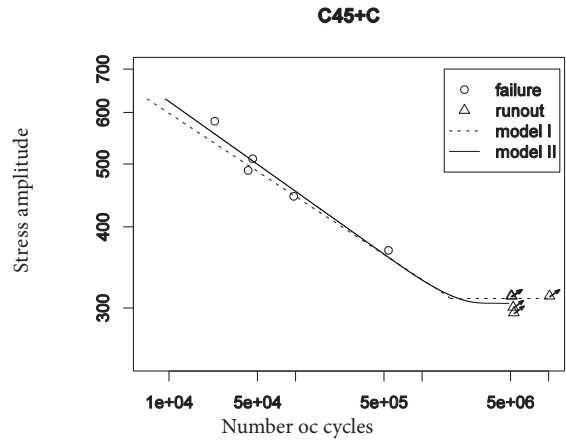


Fig. 13. Fatigue data of C45+C steel from 4th generated random number of specimens and fitted fatigue characteristics by using Model II and Model I described by Eq. (18) and (19), respectively.

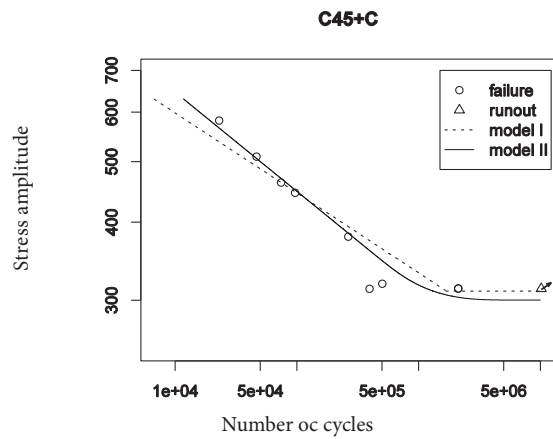


Fig. 14. Fatigue data of C45+C steel from 5th generated random number of specimens and fitted fatigue characteristics by using Model II and Model I described by Eq. (18) and (19), respectively.

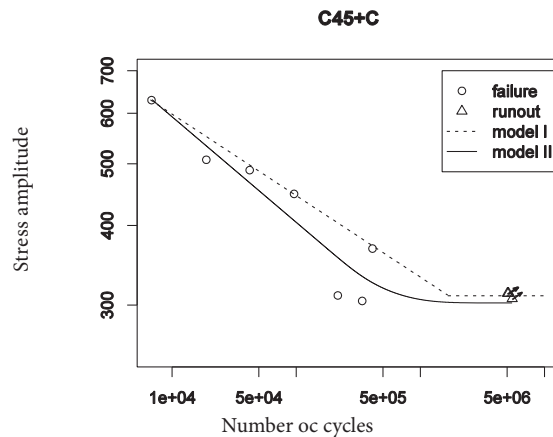


Fig. 15. Fatigue data of C45+C steel from 6th generated random number of specimens and fitted fatigue characteristics by using Model II and Model I described by Eq. (18) and (19), respectively.

Tab. 4 Values of coefficients for Model II estimated from the data generated by pseudo-random procedure

No.	$a$	$b$	$\sigma_v$	$Z_s$	$\sigma_s$
1	-7.1	54.6	0.71	303.7	19.4
2	-6.7	52.4	0.69	303.3	19.4
3	-8	60.1	0.13	304.9	20
4	-7.2	55.7	0.51	305	20
5	-6.3	50	0.51	301.5	17.4
6	-6	47.8	0.55	302.4	19.8

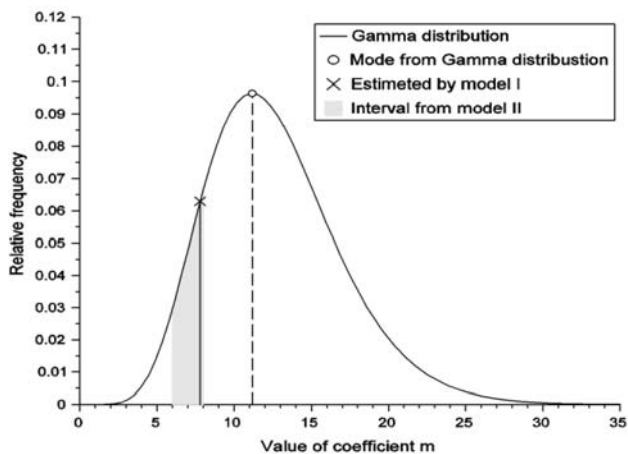


Fig. 16. Distribution of the coefficient  $m$  for smooth specimen of constructional steel under normal stress (from Fig. 1) and its estimated value from Model I and II.

Fig. 17 shows comparison of the fatigue life determined by using experimental method and that estimated by using Model I. Fig. 18, Fig. 19 and Fig. 20 show comparison of fatigue life determined from S-N curve obtained by using Model I and Model II for all specimens and two randomly generated data.

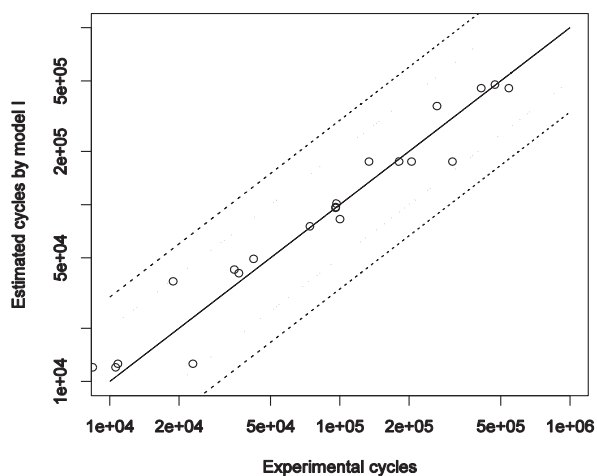


Fig. 17. Comparison of experimental value of fatigue cycles and that calculated by using Model I

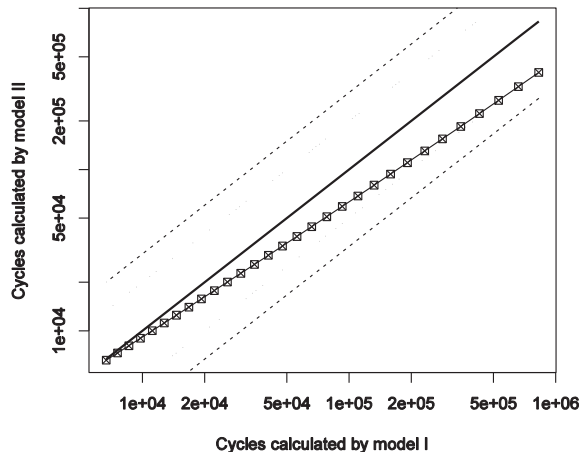


Fig. 18. Comparison of fatigue cycles calculated by using Model I and II for all specimens

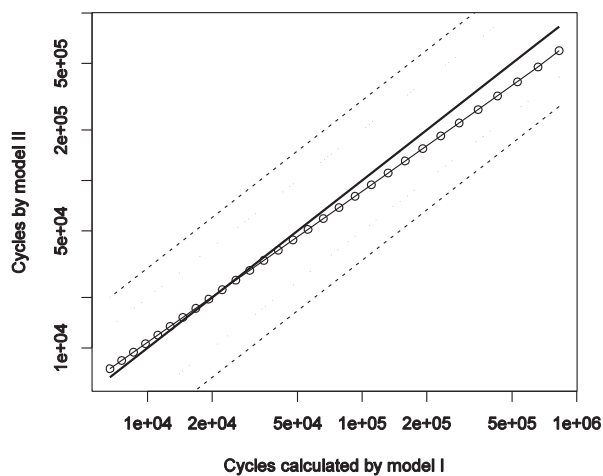


Fig. 19. Comparison of fatigue cycles calculated by using Model I and II for pseudo-random 1

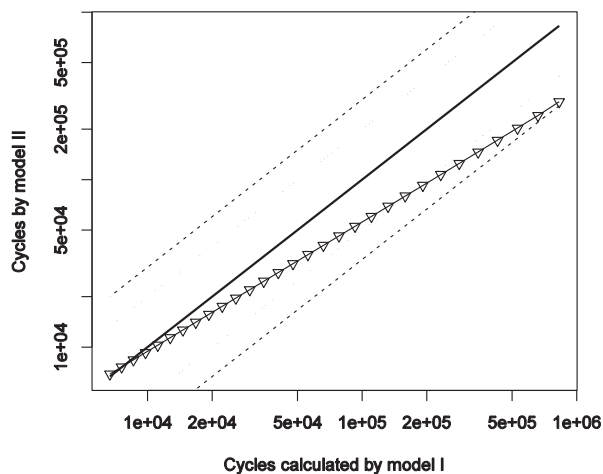


Fig. 20. Comparison of fatigue cycles calculated by model I and II for pseudo-random 6 – the least favorable generated pseudo-random

## ANALYSIS AND SUMMARY

The S-N curves estimated by means of Model I and Model II are similar to each other for all specimens. The difference in the estimated fatigue life shown in Fig. 18. Fig. 18 is within

the band 2. It means that the difference is small considering the scatter of test results compared to the fatigue life estimated from the S-N curve based on Model I (Fig. 17). For the S-N curves determined by using pseudo-random-generated data, the difference in estimated fatigue life are within the band 3. For the estimated fatigue limit value, the difference between Model I and Model II is 5.4 MPa. The maximum difference for pseudo-random-generated data is 8.8 MPa.

The following conclusions have been drawn from the study:

1. The differences in the fatigue life estimated from the S-N curve based on Model I and Model II differ by no more than the scatter band of the experimental results.
2. The differences between the estimated fatigue limit values for Model I and II, for all results and pseudo-random results, are within the standard deviation expressed by Eq. (19).
3. Standard deviations for the fatigue limit were higher for the S-N curve estimated from Model II, which is most likely due to allowing for ? the specimens that have reached the base number of cycles.
4. The advantage of Model II compared to Model I is the ability to determine a complete S-N curve by using the least number of specimens. The S-N curve was determined by using Model II and allowed fatigue life to be estimated with a satisfactory accuracy for 10 specimens. According to standard requirements the number of specimens is to be 30.
5. Standard deviation values for S-N curve estimated from Model II (see Eq. (20) and Tab. 4) were, in most cases, higher than those estimated from Model I (see Eq.(18)).
6. Considering the above presented conclusions, Model II can be used to determine a complete S-N curve when the set of experimental results contains less data than required by the standards.
7. Since the obtained results are of particular interest, similar verifications are recommended for other structural materials.

## BIBLIOGRAPHY

1. I. Stephens, Ralph, A. Fatemi, R. Stephens, Robert, O. Fuchs, Henry: *Metal Fatigue in Engineering* (1980), John Wiley and Sons, 2001.
2. Z. Dyląg, Z. Orłoś,: *Fatigue strength of materials* (in Polish), Wydawnictwo Naukowe-Techniczne, 1962.
3. S. Kocańda, J. Szala: *Basic methods for fatigue calculations* (in Polish), (1997)
4. M. Kocak, S. Webster, J. Janosch, J., A. Ainsworth, R., R. Koers: *FITNET Fitness-for-Service PROCEDURE – FINAL DRAFT MK7*, 2006.
5. Y.L. Lee, J. Paw, B. Hathaway, Richard, E. Barkey, Mark: *Fatigue Testing and Analysis - Theory and Practice*, Elsevier Butterworth-Heinemann, 2005.
6. J. Schijve : *Fatigue of structures and materials*, Second Edition , Springer Science+Business Media, 2009.
7. P. Strzelecki: *Analytical method for determining fatigue properties of materials and construction elements in high cycle life* (in Polish), Uniwersytet Technologiczno-Przyrodniczy w Bydgoszczy, 2014.
8. P. Strzelecki, J. Sempruch, K. Nowicki: *Accuracy of Analytical-Experimental Method for Determining the Fatigue Characteristics in a Limited Life Region*, Solid State Phenom. 224 (2014) 63–68. doi:10.4028/www.scientific.net/SSP.224.63.
9. T. Tomaszewski, J. Sempruch: *Analysis of size effect in high-cycle fatigue for EN AW-6063*, Solid State Phenom. 224 (2015) 75–80. doi:10.4028/www.scientific.net/SSP.224.75.
10. PN-H-04325:1976: *Fatigue tests of metals -- Basic definition and general guidelines for the preparation of samples and tests*, 1976.
11. P. Strzelecki, J. Sempruch: *Experimental Verification of the Analytical Method for Estimated S-N Curve in Limited Fatigue Life*, Mater. Sci. Forum. 726 (2012) 11–16. doi:10.4028/www.scientific.net/MSF.726.11.
12. ASTM E-739-91: *Standard Practice for Statistical Analysis of Linear or Linearized Stress-Life (S-N) and Strain-Life Fatigue Data*, 2006.
13. PN-EN-3987: *Aerospace series - Test methods for metallic materials - Constant amplitude force-controlled high cycle fatigue testing*, 2010.
14. ISO-12107: *Metallic materials - fatigue testing - statistical planning and analysis of data*, 2003.
15. F.G. Pascual, W.Q. Meeker: *Estimating Fatigue Curves with the Random Fatigue-Limit Model*, Technometrics. 41 (1999) 277–290. doi:10.2307/1271342.
16. S. Lorén, M. Lundström: *Modelling curved S-N curves*, Fatigue Fract. Eng. Mater. Struct. 28 (2005) 437–443. doi:10.1111/j.1460-2695.2005.00876.x.
17. R Core Team: *R: A language and environment for statistical computing*, (2015). <http://www.r-project.org/>.

**CONTACT WITH THE AUTHOR**

Paweł Strzelecki

Janusz Sempruch

University of Science and Technology in Bydgoszcz  
Al. Prof. S. Kaliskiego 7  
85-796 Bydgoszcz

**POLAND**

# APPLICATION OF TWO-PARAMETER FATIGUE CHARACTERISTICS IN FATIGUE PERSISTENCE CALCULATIONS OF STRUCTURAL COMPONENTS UNDER CONDITIONS OF A BROAD SPECTRUM OF LOADS

Grzegorz Szala

University of Science and Technology in Bydgoszcz, Poland

## ABSTRACT

*The paper presents an original method of calculation of the fatigue persistence based on the adoption of the load spectrum in the form of a correlation table, two-parameter fatigue characteristics and the linear hypothesis of fatigue damage summation. The calculation results by the proposed method were compared with the results of fatigue tests programmed for node-seal construction. On the basis of a comparative analysis of the test results and calculations conclusions regarding the usefulness of the proposed method to evaluate the fatigue persistence of components have been reached.*

**Keywords:** fatigue persistence, linear hypothesis of fatigue damage summation, fatigue tests

## INTRODUCTION

Research and analysis of the two-parameter fatigue characteristics carried out in recent years [1] enabled the development of new, effective methods of calculation of the fatigue persistence of components subjected to loads with a wide spectrum of operating conditions.

Loads of this type are loads typical for structural components of means of transport (motor vehicles, airplanes, etc.) including ocean engineering objects, e.g. offshore drilling platforms [2] and shipbuilding [3] and [4]. In [3] the basic assumptions of methods of calculation of the fatigue persistence of ship structure elements have been given. The assumptions show that in these calculations should take into account: the cyclic property (fatigue) of the analysed structural element designated

under load conditions of constant amplitude [1], variable loads in the form of a load spectrum (the set of cycles with variable values, maximum and minimum or variable amplitudes and average values of cycles) [5] and the corresponding hypothesis of summing damage [6]. In [4] are examples of calculations of elements of ship structures.

Development of load spectra requires a suitable method of counting cycles [7], which is also described in the monograph [8]. Dedicated cycles of duty operation of a random broad-spectrum is conveniently summarized in a table of coordinates:  $S_{\min}$ ,  $S_{\max}$  [3], or  $S_{ai}$ ,  $S_{mi}$  [5]. In this paper the second embodiment has been used since it is compatible with the system adopted in the description of two-parameter fatigue characteristics [1].

The complexity of the material properties, the structure and geometry of the bonded components, which include ship structures [9] and [10] causes the cyclical properties are designated on the so-called elementary nodes and not on core materials, as is done in the elements of machines with the uniform structure of the material [8]. This type of method to describe the cyclic properties has been adopted by the International Institute of Welding (IIW) publishing a catalogue of *S-N* curves (Wöhler diagrams) for welded joints [11], also described in [12].

These data were used in the calculation according to the original method based on the adoption of the load spectrum in the form of a table of correlation ( $S_{mj}, S_{ai}$ ) [5], a modified two-parameter characteristics of fatigue IM model (model I modified) [13] and the linear hypothesis summation of fatigue damage of Palmgren-Miner [6].

The aim of the study is a comparative analysis of the results of calculation of the fatigue persistence of the proposed method with the results of experimental studies on the example of node-seal construction.

The work includes: formulation of the problem, a description of the fatigue properties of the node, an analysis of operational loads and description of the spectrum load persistence calculations and comparative analysis of the calculation results and programmable fatigue tests.

## FORMULATION OF THE PROBLEM

According to the linear hypothesis of summation of fatigue damage by Palmgren-Miner, the damage caused by one cycle of parameters  $S_{ai}, S_{mj}$  is:

$$D_{1(i,j)} = \frac{1}{N_{ij}(S_{ai}, S_{mj})} \quad (1)$$

where:

$N_{ij}(S_{ai}, S_{mj})$  – is the number of cycles for fatigue crack growth under constant amplitude and sinusoidal load parameters  $S_{ai}, S_{mj}$ .

For random loads with a wide spectrum, the basic hypothesis of linear form is given by:

$$\sum_{i=1}^k \sum_{j=1}^l \frac{n_{ij}}{N_{ij}} = 1 \quad (2)$$

where:

$i = 1, 2, \dots, k$  – number of amplitude level of stress cycle  $S_{ai}$ ,  
 $j = 1, 2, \dots, l$  – the number of levels of the average stress cycle  $S_{mj}$

$n_{ij}$  – number of sinusoidal load cycles in a spectrum with parameters  $S_{ai}, S_{mj}$

$N_{ij}$  – number of sinusoidal cycles of constant amplitude  $S_{ai}$  and mean value  $S_{mj}$  till fatigue crack.

Introducing a frequency of cycles with defined parameters in the stress spectrum

$$\alpha_{ij} = \frac{n_{0ij}}{n_0} = \frac{n_{cij}}{n_c} \quad (3)$$

where:

$n_{0ij}$  – the number of cycles in the load spectrum with parameters

$S_{ai}, S_{mj}$

$n_0$  – the total number of cycles in the load spectrum

$$n_0 = \sum_{i=1}^k \sum_{j=1}^l n_{0ij},$$

$n_{cij}$  – number of programmed load cycles with parameters  $S_{ai}, S_{mj}$  till fatigue crack,

$n_c$  – the total number of programmed load cycles till fatigue crack – fatigue persistence.

one gets:

$$n_c = \frac{1}{\sum_{i=1}^k \sum_{j=1}^l \frac{\alpha_{ij}}{N_{ij}}} \quad (4)$$

$N_{ij}$  – is determined from the two-parameter fatigue characteristics.

## RESEARCH DESCRIPTION

### RESEARCH OBJECT

For calculations and tests of the fatigue persistence a soldered construction node was selected as shown in Fig. 1.

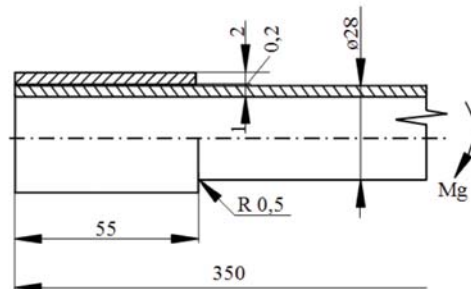


Fig. 1. The construction node made of steel pipe welding

Construction node made of steel pipes (10BX steel) of the following chemical composition: 0,13 C, (0,4÷0,6) Mn, maximum: 0,003 Si, 0,004 P and 0,0045 S, connected with a LM63 solder. The tensile strength of the pipe  $R_m = 363$  MPa, the yield strength  $R_{0,2} = 310$  MPa.

### SERVICE LOADS

Part of the stress graph in the structural element measured by the strain gauge in service, and basic parameter estimates and the statistical functions shown in Fig. 2.

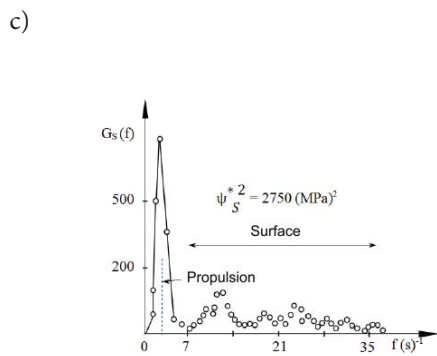
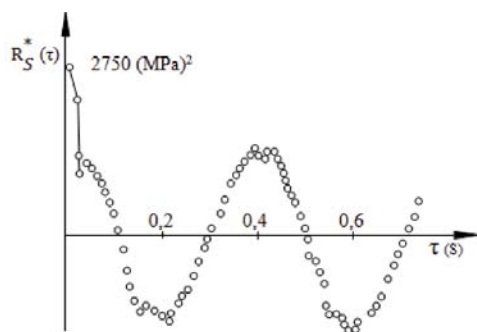
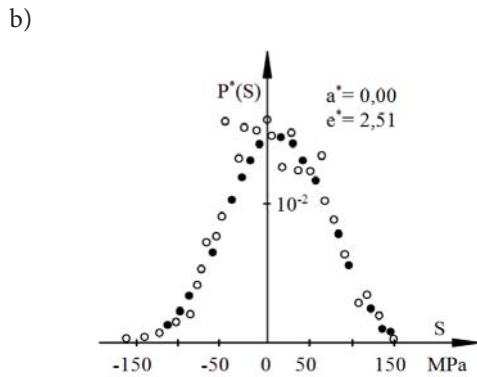
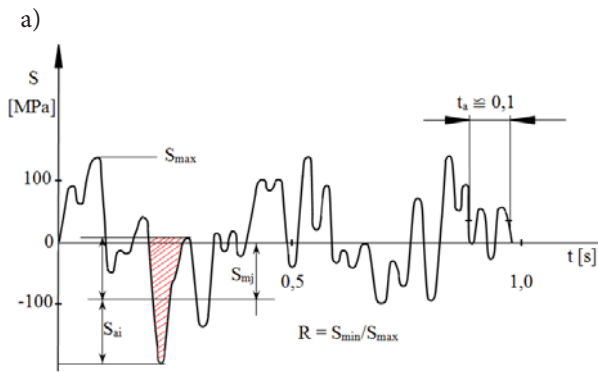


Fig. 2. Service stresses in the construction node: a – part of the chart, b – probability density function, c – autocorrelation function, d – the function of spectral density power

From the statistical functions shown in fig. 2 it is clear that the analysed load is the realization of a stochastic process with a broad spectrum and complex structure. The component load

with a frequency of about 3,5 Hz arises from the impact of the user on the drive system and a wide frequency range is applied resulting from the impact of road surface irregularities.

The analysis of methods for the development of stress spectrum described in [5] and [8] it is clear that in this case, from among the known methods of counting cycles, the following methods are recommended: counting complete cycles (full cycles counting method), and the method of envelope (rain-flow counting method). In this work, to develop a spectrum of stress in a table of correlation in the system of relative values  $S_{ai}/S_{max}$ ,  $S_{mj}/S_{max}$  the method of full cycles has been selected. The data on stress spectrum are shown in Table 1. The fields of Table 1 include the relative value of numbers of cycles  $\alpha_{ij} = n_{0ij}/n_0$ . The table field is divided into four fields, depending on the range of variation of the asymmetry factor cycles:

- 1)  $0 < R < 1,0$ ; 2)  $-1,0 \leq R \leq 0$ ; 3)  $-\infty < R < -1,0$ ; 4)  $1 < R < +\infty$ .

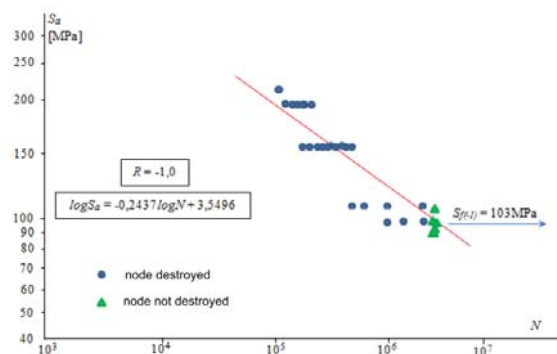
Tab. 1. The spectrum of the stress of the structural element  $\alpha_{ij} \cdot 10^3$

$S_{ai}/S_{max}$ \ $S_{mj}/S_{max}$	0,8	0,7	0,6	0,5	0,4	0,3	0,2	0,1	$\alpha_j$
0,4 \ 1			2		4,33		21,65	1	26
0,3 \ 2					8,66	8,66	65	47,62	129,97
0,2 \ 3	8,66		4,33	4,33	4,33	47,62	90,91		203,46
0,1 \ 4		13	17,32	30,30	34,63	17,32	65	47,62	225,11
0 \ 5			8,66	34,63	26	21,65	90,91	21,65	203,46
-0,1 \ 6	4,33		4,33		8,66	8,66	56,28	26	108,23
-0,2 \ 7					4,33	8,66	26	21,65	60,6
-0,3 \ 8						8,66	13	21,65	43,29
-0,4 \ 9								4	
$\alpha_k$	13	13	34,63	69,26	90,91	121,2	428,5	229,4	1000

## CYCLIC PROPERTIES OF THE RESEARCH OBJECT

The determination of fatigue characteristics of two-parameter model by IM requires the designation of Wöhler charts ( $S_{ai} - N$ ) for the swinging load ( $R = -1,0$ ) and the variable unilateral load ( $R = 0$ ). These charts are shown in Fig. 3.

a)



b)

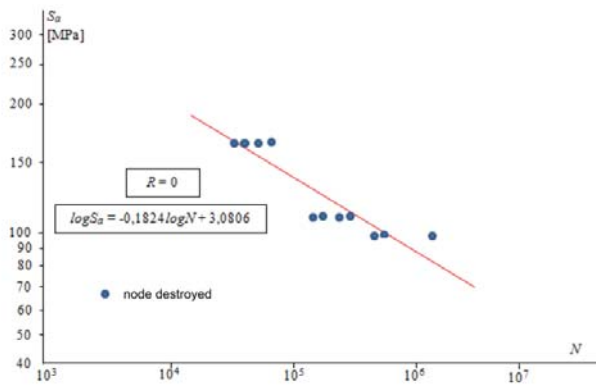


Fig. 3. Wöhler fatigue charts: a) for  $R = -1, 0$ , b) for  $R = 0$   
These charts are described by formulas:

$$\log S_a = -\frac{1}{m_0} \log N + c_0 \quad (5)$$

and

$$\log S_a = -\frac{1}{m} \log N + c \quad (6)$$

On the basis of formulas (5) and (6) a two-parameter fatigue characteristic has been determined in the form:

- for area 1

$$N_{ij} = N_0 \left[ \frac{S_{f(-1)} \cdot (R_m + S_{ai} - S_{mj})}{S_{ai} \cdot R_m \cdot (1 + \psi_N)} \right]^{m_0} \quad (7)$$

for  $0 < R < 1$

- for area 2

$$N_{ij} = N_0 \frac{S_{f(-1)}^{m_0}}{(S_{ai} + \psi_N \cdot S_{mj})^{m_0}} \quad (8)$$

for  $-1 \leq R \leq 1$

- for area 3

$$N_{ij} = N_0 \frac{S_{f(-1)}^{m_0}}{(S_{ai} - \psi_N \cdot S_{mj})^{m_0}} \quad (9)$$

for  $-\infty \leq R \leq -1$

- for area 4

$$N_{ij} = N_0 \left[ \frac{S_{f(-1)} \cdot (R_m + S_{ai} + S_{mj})}{S_{ai} \cdot R_m \cdot (1 + \psi_N)} \right]^{m_0} \quad (10)$$

for  $1 < R < +\infty$

where  $\psi_N$  is the coefficient of sensitivity to the asymmetry of the cycle  $R$ .

The chart of two-parameter fatigue characteristics of the construction element being analyzed and of selected lines of stability constants  $N = \text{const}$ , has been shown in Fig. 4.

### CALCULATIONS OF FATIGUE PERSISTENCE

In Table 2, which has a similar arrangement as Table 1, in the respective fields, number of cycles for fatigue crack  $N_{ij}$  calculated from the formulas (7) to (10) depending on the value  $S_{ai}$  and  $S_{mj}$ , were specified.

From the data in Tables 1 and 2 and the formula (4) one may firstly calculate the value of ratios  $\alpha_{ij}/N_{ij}$  in each field, and then the sum of the damage and and fatigue persistence and its number of cycles  $n_c$ .

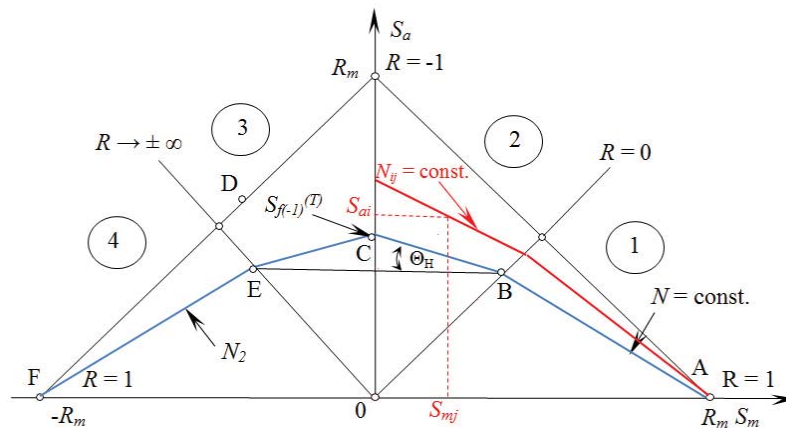


Fig. 4. A diagram of two-parameter characteristics of fatigue in the schematic view

Tab. 2. Numbers of cycles  $N_{ij} - S_{max} = 160$  MPa

$S_{mj} \setminus i$		$S_{ai}$							
		128	112	96	80	64	48	32	16
$j$	$i$	1	2	3	4	5	6	7	8
64	1					$9,5 \cdot 10^6$		$2,5 \cdot 10^8$	
48	2					$1,0 \cdot 10^7$	$7,0 \cdot 10^7$	$2,5 \cdot 10^8$	$7,0 \cdot 10^8$
32	3	$8,5 \cdot 10^5$		$2,5 \cdot 10^6$	$4,5 \cdot 10^6$	$1,5 \cdot 10^7$	$7,5 \cdot 10^7$	$2,5 \cdot 10^8$	
16	4		$2,5 \cdot 10^6$	$5,0 \cdot 10^6$	$7,5 \cdot 10^6$	$2,5 \cdot 10^7$	$7,5 \cdot 10^7$	$2,5 \cdot 10^8$	$7,0 \cdot 10^8$
0	5			$5,2 \cdot 10^6$	$8,0 \cdot 10^6$	$2,0 \cdot 10^7$	$7,5 \cdot 10^7$	$2,5 \cdot 10^8$	$7,0 \cdot 10^8$
-16	6	$9,0 \cdot 10^5$		$5,0 \cdot 10^6$		$2,5 \cdot 10^7$	$7,5 \cdot 10^7$	$2,5 \cdot 10^8$	$7,0 \cdot 10^8$
-32	7					$1,5 \cdot 10^7$	$7,5 \cdot 10^7$	$2,5 \cdot 10^8$	$7,0 \cdot 10^8$
-48	8						$7,0 \cdot 10^7$	$2,5 \cdot 10^8$	$7,0 \cdot 10^8$
-64	9								

$S_{max} = 200$  MPa

$S_{mj} \setminus i$		$S_{ai}$							
		160	140	120	100	80	60	40	20
$j$	$i$	1	2	3	4	5	6	7	8
80	1					$5,5 \cdot 10^6$		$8,5 \cdot 10^7$	
60	2					$6,0 \cdot 10^6$	$1,5 \cdot 10^7$	$9,5 \cdot 10^7$	$3,5 \cdot 10^8$
40	3	$4,0 \cdot 10^5$		$9,0 \cdot 10^5$	$2,5 \cdot 10^6$	$6,5 \cdot 10^6$	$2,0 \cdot 10^7$	$1,0 \cdot 10^8$	
20	4		$7,5 \cdot 10^5$	$9,5 \cdot 10^5$	$3,0 \cdot 10^6$	$7,0 \cdot 10^6$	$2,5 \cdot 10^7$	$1,0 \cdot 10^8$	$5,0 \cdot 10^8$
0	5			$1,0 \cdot 10^6$	$4,5 \cdot 10^6$	$8,0 \cdot 10^6$	$3,0 \cdot 10^7$	$1,0 \cdot 10^8$	$5,0 \cdot 10^8$
-20	6	$5,0 \cdot 10^5$		$9,5 \cdot 10^5$		$7,0 \cdot 10^6$	$2,5 \cdot 10^7$	$1,0 \cdot 10^8$	$5,0 \cdot 10^8$
-40	7					$6,5 \cdot 10^6$	$2,0 \cdot 10^7$	$1,0 \cdot 10^8$	$4,0 \cdot 10^8$
-60	8						$1,5 \cdot 10^7$	$9,5 \cdot 10^7$	$3,5 \cdot 10^8$
-80	9								

$S_{max} = 240$  MPa

$S_{mj} \setminus i$		$S_{ai}$							
		192	168	144	120	96	72	48	24
$j$	$i$	1	2	3	4	5	6	7	8
96	1					$1,0 \cdot 10^6$		$4,5 \cdot 10^7$	
72	2					$1,5 \cdot 10^6$	$7,5 \cdot 10^6$	$6,0 \cdot 10^7$	$2,0 \cdot 10^8$
48	3	$0,1 \cdot 10^5$		$5,5 \cdot 10^5$	$9,0 \cdot 10^5$	$2,5 \cdot 10^6$	$8,5 \cdot 10^6$	$7,0 \cdot 10^7$	
24	4		$3,0 \cdot 10^5$	$6,0 \cdot 10^5$	$9,5 \cdot 10^5$	$4,5 \cdot 10^6$	$8,5 \cdot 10^6$	$7,5 \cdot 10^7$	$4,5 \cdot 10^8$
0	5			$7,5 \cdot 10^5$	$1,0 \cdot 10^6$	$5,0 \cdot 10^6$	$9,5 \cdot 10^6$	$7,5 \cdot 10^7$	$4,0 \cdot 10^8$
-24	6	$1,5 \cdot 10^5$		$6,0 \cdot 10^5$		$4,5 \cdot 10^6$	$8,5 \cdot 10^6$	$7,5 \cdot 10^7$	$4,5 \cdot 10^8$
-48	7					$2,5 \cdot 10^6$	$8,5 \cdot 10^6$	$7,0 \cdot 10^7$	$2,5 \cdot 10^8$
-72	8						$7,5 \cdot 10^6$	$6,0 \cdot 10^7$	$2,0 \cdot 10^8$
-96	9								

Tab. 3: Ratio values  $\alpha_{ij}/N_{ij}$  for: a)  $S_{max} = 160$  MPa, b)  $S_{max} = 200$  MPa, c)  $S_{max} = 240$  MPa

a)

$j \setminus i$		0,8	0,7	0,6	0,5	0,4	0,3	0,2	0,1
$j$	$i$	1	2	3	4	5	6	7	8
0,4	1					$0,45 \cdot 10^{-9}$		$8,66 \cdot 10^{-11}$	
0,3	2					$8,66 \cdot 10^{-10}$	$1,23 \cdot 10^{-10}$	$26 \cdot 10^{-11}$	$6,8 \cdot 10^{-11}$
0,2	3	$1,01 \cdot 10^{-8}$		$1,73 \cdot 10^{-9}$	$0,96 \cdot 10^{-9}$	$2,88 \cdot 10^{-10}$	$6,34 \cdot 10^{-10}$	$36,36 \cdot 10^{-11}$	
0,1	4		$5,2 \cdot 10^{-9}$	$3,46 \cdot 10^{-9}$	$4,04 \cdot 10^{-9}$	$13,8 \cdot 10^{-10}$	$2,3 \cdot 10^{-10}$	$26 \cdot 10^{-11}$	$6,8 \cdot 10^{-11}$
0	5			$1,66 \cdot 10^{-9}$	$4,32 \cdot 10^{-9}$	$13,0 \cdot 10^{-10}$	$2,88 \cdot 10^{-10}$	$36,36 \cdot 10^{-11}$	$3,09 \cdot 10^{-11}$
-0,1	6	$0,48 \cdot 10^{-8}$		$0,86 \cdot 10^{-9}$		$3,46 \cdot 10^{-10}$	$1,15 \cdot 10^{-10}$	$22,51 \cdot 10^{-11}$	$3,71 \cdot 10^{-11}$
-0,2	7					$2,88 \cdot 10^{-10}$	$1,15 \cdot 10^{-10}$	$10,4 \cdot 10^{-11}$	$3,09 \cdot 10^{-11}$
-0,3	8						$1,23 \cdot 10^{-10}$	$5,2 \cdot 10^{-11}$	$3,09 \cdot 10^{-11}$
-0,4	9								

b)

$j \setminus i$		0,8	0,7	0,6	0,5	0,4	0,3	0,2	0,1
		1	2	3	4	5	6	7	8
0,4	1					$0,78 \cdot 10^{-9}$		$2,54 \cdot 10^{-10}$	
0,3	2					$1,44 \cdot 10^{-9}$	$5,77 \cdot 10^{-10}$	$6,84 \cdot 10^{-10}$	$13,6 \cdot 10^{-11}$
0,2	3	$2,16 \cdot 10^{-8}$		$0,48 \cdot 10^{-8}$	$1,73 \cdot 10^{-9}$	$0,66 \cdot 10^{-9}$	$23,8 \cdot 10^{-10}$	$90,91 \cdot 10^{-11}$	
0,1	4		$1,73 \cdot 10^{-8}$	$1,82 \cdot 10^{-8}$	$10,1 \cdot 10^{-9}$	$4,94 \cdot 10^{-9}$	$6,92 \cdot 10^{-10}$	$65 \cdot 10^{-11}$	$9,52 \cdot 10^{-11}$
0	5			$8,66 \cdot 10^{-9}$	$7,69 \cdot 10^{-9}$	$3,25 \cdot 10^{-9}$	$7,21 \cdot 10^{-10}$	$90,91 \cdot 10^{-11}$	$4,33 \cdot 10^{-11}$
-0,1	6	$0,86 \cdot 10^{-8}$		$0,45 \cdot 10^{-8}$		$1,23 \cdot 10^{-9}$	$3,46 \cdot 10^{-10}$	$56,28 \cdot 10^{-11}$	$5,2 \cdot 10^{-11}$
-0,2	7					$0,66 \cdot 10^{-9}$	$4,33 \cdot 10^{-10}$	$26 \cdot 10^{-11}$	$5,41 \cdot 10^{-11}$
-0,3	8						$5,77 \cdot 10^{-10}$	$1,36 \cdot 10^{-10}$	$6,18 \cdot 10^{-11}$
-0,4	9								

c)

$j \setminus i$		0,8	0,7	0,6	0,5	0,4	0,3	0,2	0,1
		1	2	3	4	5	6	7	8
0,4	1					$4,33 \cdot 10^{-9}$		$4,81 \cdot 10^{-10}$	
0,3	2					$5,77 \cdot 10^{-9}$	$1,15 \cdot 10^{-9}$	$10,81 \cdot 10^{-10}$	$23,81 \cdot 10^{-11}$
0,2	3	$8,66 \cdot 10^{-8}$		$0,78 \cdot 10^{-8}$	$0,48 \cdot 10^{-8}$	$1,73 \cdot 10^{-9}$	$5,6 \cdot 10^{-9}$	$12,98 \cdot 10^{-10}$	
0,1	4		$4,33 \cdot 10^{-8}$	$2,88 \cdot 10^{-8}$	$3,18 \cdot 10^{-8}$	$7,69 \cdot 10^{-9}$	$2,03 \cdot 10^{-9}$	$8,66 \cdot 10^{-10}$	$10,58 \cdot 10^{-11}$
0	5			$1,15 \cdot 10^{-8}$	$34,6 \cdot 10^{-9}$	$5,2 \cdot 10^{-9}$	$2,27 \cdot 10^{-9}$	$12,12 \cdot 10^{-10}$	$5,41 \cdot 10^{-11}$
-0,1	6	$2,88 \cdot 10^{-8}$		$0,72 \cdot 10^{-8}$		$1,92 \cdot 10^{-9}$	$1,01 \cdot 10^{-9}$	$7,5 \cdot 10^{-10}$	$5,77 \cdot 10^{-11}$
-0,2	7					$1,73 \cdot 10^{-9}$	$1,01 \cdot 10^{-9}$	$3,71 \cdot 10^{-10}$	$8,66 \cdot 10^{-11}$
-0,3	8						$1,15 \cdot 10^{-9}$	$2,16 \cdot 10^{-10}$	$10,82 \cdot 10^{-11}$
-0,4	9								

Ratio figures  $\alpha_j/N_{ij}$  were summarized in Table 3 and the results of calculation of the fatigue persistence  $n_c$  according to formula (4) are shown in Table 4. The persistence chart has been shown in Fig. 5 according to the description provided in the form of a mathematical model (12).

Table 4: The results of calculation of fatigue persistence of the soldered construction node

$S_{max}$ [MPa]	160	200	240
$n_c$	$2,19 \cdot 10^7$	$7,89 \cdot 10^6$	$8,18 \cdot 10^5$

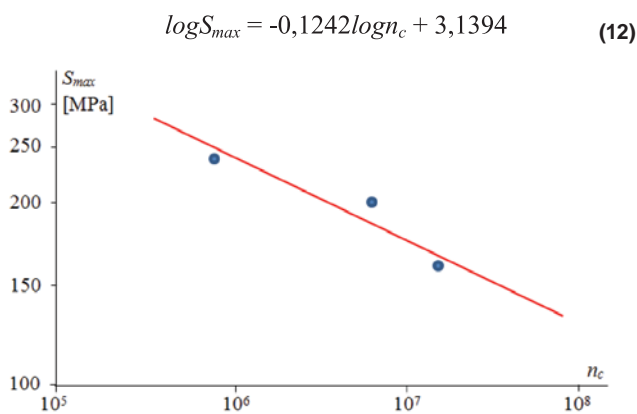


Fig. 5. Fatigue persistence chart according to data from Table 4.

## RESEARCH ON FATIGUE PERSISTENCE OF THE CONSTRUCTION ELEMENT

The studies of fatigue persistence of the construction element were performed with the use of programmable research method. The load program in the fatigue tests corresponded to the load of the calculation described in section 4. Results of programmable studies were summarized in Table 5, and the fatigue persistence chart has been shown in Fig. 6.

Tab. 5: Results of fatigue persistence studies  $n_c^{Ex}$

$S_{amax}$ [MPa]	$n_c^{Ex}$					
	1	2	3	4	5	6
240	$5,8 \cdot 10^5$	$1,36 \cdot 10^6$	$2,05 \cdot 10^6$	$9,15 \cdot 10^5$	$9,86 \cdot 10^5$	$2,43 \cdot 10^6$
200	$2,62 \cdot 10^6$	$4,23 \cdot 10^6$	$6,13 \cdot 10^6$	$5,13 \cdot 10^6$	$8,95 \cdot 10^6$	$1,45 \cdot 10^7$
160	$1,83 \cdot 10^7$	$2,79 \cdot 10^7$	$8,52 \cdot 10^7$	$1,15 \cdot 10^7$	$2,41 \cdot 10^7$	$5,8 \cdot 10^7$
120	$8,95 \cdot 10^7$	$2,15 \cdot 10^8$	$3,45 \cdot 10^8$	$1,52 \cdot 10^8$	$2,75 \cdot 10^8$	$5,34 \cdot 10^8$

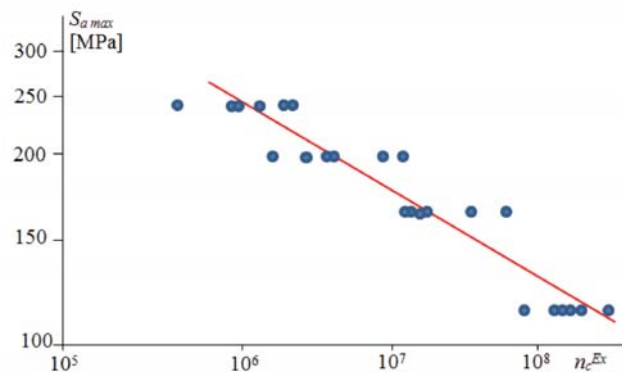


Fig. 6. Chart of fatigue persistence in terms of programmable load

The chart of fatigue persistence determined based on the experimental data described by the formula (13).

$$\log S_{max} = -0,1227 \log n_c + 3,1219 \quad (13)$$

## COMPARATIVE ANALYSIS OF TEST RESULTS AND CALCULATION AND CONCLUSIONS

A comparison of formulas (12) and (13) shows a significant compliance of fatigue persistence determined experimentally according to the results of the calculation methods described in point 2 of this work. The compliance is the result of carefully selected methods to develop a load program, two-parameter characteristics of fatigue and summation hypotheses of fatigue damage.

For loads of a broad spectrum, adopting the method of counting complete cycles proved to be appropriate and in line with the general recommendations in this area [8]. Similarly, the adoption of two-parameter characterization of fatigue IM [13] verified experimentally for construction steel favoured the compatibility of the calculation of the test results. Basing calculations on the load spectrum in the form of a table of correlation [5] and two-parameter characterization of fatigue avoided the reduction of asymmetric cycles to symmetric cycles ( $R = -1,0$ ) which is associated with considerable simplifications affecting the accuracy of the calculations.

Relative positions of the graphs of the fatigue persistence determined by means of calculations and experimental tests are shown in Fig. 7. The relative differences in the stability of the graphs calculated extremities are:

- for  $S_{max} = 150$  MPa

$$\delta = \frac{n_{cobl} - n_{cex}}{n_{cobl}} = \frac{5,7892 \cdot 10^7 - 5,1082 \cdot 10^7}{5,7892 \cdot 10^7} = 0,1176 \quad (14)$$

- for  $S_{max} = 300$  MPa

$$\delta = \frac{n_{cobl} - n_{cex}}{n_{cobl}} = \frac{2,1454 \cdot 10^5 - 1,7994 \cdot 10^5}{2,1454 \cdot 10^5} = 0,1612 \quad (15)$$

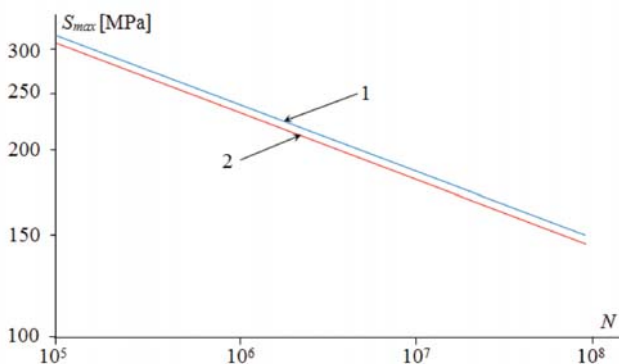


Fig. 7. The relative position of persistence charts: 1 – as determined by the calculation method, 2 – as determined by programmable testing method

From the above calculations, the formulas (14) and (15) show that the relative differences in results determined by the stability calculation and programmed methods are respectively: for  $S_{max} = 150$  MPa – 11,76 %, for  $S_{max} = 300$  MPa – 16,12 %. Taking into account the natural considerable dispersion of results of fatigue tests, especially soldered construction elements, these differences are insignificant.

The above analysis shows that in the case of structural components made of steel, subject to the conditions of random service loads of a broad spectrum, an appropriate method of calculation of the fatigue persistence is the method of application in the field:

- development of load spectra method of counting complete cycles or envelope method,
- selection of fatigue characteristics – the adoption of two-parameters characteristics of fatigue IM according to [13],
- summation hypothesis of fatigue damage– the adoption of the linear hypothesis of fatigue damage summation by Palmgren-Miner.

## BIBLIOGRAPHY

1. LIGAJ B., SZALA G.: Experimental verification of two-parameters models of fatigue characteristics by using the tests of S55J0 steel as an example, Polish Maritime Research, 1(63) 2010, Vol. 17 pp.39-50
2. API: Recommended Practice for Planning, Designing and Constructing, Fixed Offshore Platforms – Loads and Resistance Factor Design, American Petroleum Institute, Washington DC, 1993
3. FRICKE W., PETERSHAGEN H., PAETZOLD H.: Fatigue Strength of Ship Structures – Part I: Basic Principles, published by Germanischer Lloyd and Institute of Naval Architecture of the Hamburg University, Hamburg, 1997
4. FRICKE W., PETERSHAGEN H., PAETZOLD H.: Fatigue Strength of Ship Structures – Part II: Examples, published by Germanischer Lloyd and Institute of Naval Architecture of the Hamburg University, Hamburg, 1998
5. LIGAJ B.: The influence of loadings programmes elaborated on the base on correlation chart steel 18G2A fatigue live, Problemy Eksploatacji – Zeszyty Naukowe 3/2007 (66), str. 129-146
6. SZALA J.: Hipotezy sumowania uszkodzeń zmęczeniowych, Wydawnictwo Uczelniane Akademii Techniczno-Rolniczej, Bydgoszcz, 1998
7. ASTM: Standard Practises for Cycle Counting in Fatigue Analysis, ASTM Designation E 1049-85, American Society for Testing and Materials, New York
8. KOCAŃDA S., SZALA J.: Podstawy obliczeń zmęczeniowych, Wydanie III, Wydawnictwa Naukowe PWN, Warszawa, 1997
9. KOZAK J.: Selected problems on application of steel sandwich panels to marine structures, Polish Maritime Research, 4(62) 2009, Vol. 16, 2009
10. KOZAK J.: Fatigue life of steel laser – welded panels, Polish Maritime Research, Special Issue S1, 2006

11. HOBACHER A.: Recommendations for fatigue design of welded joints and components, IIW document XIII-1965-03/XV-1127-3, 2004
12. JANOSCH J.-J.: FITNET MK7 (European Fitness for Service Network), Section 7, Fatigue Module, Caterpillar, France, 2006
13. SZALA G.: The modification of the generalized two-parametric fatigue characteristics based on High diagram conception. Scientific Problems of Machines Operation and Maintenance nr 2/2010, Radom, 2010

#### **CONTACT WITH THE AUTHOR**

Grzegorz Szala

University of Science and Technology in Bydgoszcz  
Al. Prof. S. Kaliskiego 7  
85-796 Bydgoszcz

**POLAND**